

PATH INTEGRAL MONTE CARLO STUDIES OF  
ULTRACOLD FEW-ATOM SYSTEMS

By  
YANGQIAN YAN

A dissertation submitted in partial fulfillment of  
the requirements for the degree of

DOCTOR OF PHILOSOPHY

WASHINGTON STATE UNIVERSITY  
Department of Physics and Astronomy

MAY 2016

©Copyright by YANGQIAN YAN, 2016  
All Rights Reserved

©Copyright by YANGQIAN YAN, 2016  
All Rights Reserved

To the Faculty of Washington State University:

The members of the Committee appointed to examine the dissertation of  
YANGQIAN YAN find it satisfactory and recommend that it be accepted.

---

Doerte Blume, Ph.D., Chair

---

Peter Engels, Ph.D.

---

Mark G. Kuzyk, Ph.D.

## Acknowledgement

I would like to express my special thanks to my advisor Professor Doerte Blume, who has been selfless in dedicating so much of her time to her students. She is critical and insightful to my research questions and patient with my writing. She always has a broad picture but also pays attention to details in research, writing, and presentations. She provided me many opportunities for attending conferences, workshops, and visiting other institutions. Her advices on presentations and communications could not be more helpful. She has always been thoughtful and I learned many different things other than physics. She also introduced me to the beautiful world of GNU/LINUX, which is a great environment for everything. It would be hard to imagine my daily life without it.

My gratitude also goes to our past and present group members: Kevin Daily, Debraj Rakshit, Qingze Guan, and Jethin Jacob with whom I had many fruitful discussions, and Seyed Ebrahim Gharashi and Xiangyu Yin, with whom I also shared close collaborations. I would like to especially thank my past and present office mates Xiangyu Yin and Qingze Guan. I bothered them with all kinds of questions and thoughts. They also dedicated a lot of time helping me with my writing.

I also benefited a lot from the weekly journal club that we have been holding together with Dr. Chuanwei Zhang's group (now at UT Dallas), Dr. Peter Engels's group, and Dr. Michael Forbes's group at Washington State University. My physics knowledge would have been much narrower without it.

I want to thank my parents and friends, who have been understanding and supportive.

I wish to thank the staff at the department of physics and astronomy and the XSEDE help desk. They have always been helpful and their responses have always been timely.

Lastly, I would like to acknowledge the financial support by the NSF through grant PHY-1205443 and PHY-1415112. I have also benefited from the computational resources at WSU

HPC and the XSEDE.

PATH INTEGRAL MONTE CARLO STUDIES OF  
ULTRACOLD FEW-ATOM SYSTEMS

Abstract

by Yangqian Yan, Ph.D.  
Washington State University  
May 2016

Chair: Doerte Blume

Motivated by the fact that ultracold atomic systems can nowadays be realized experimentally with varying number of particles, this thesis explores the transition from few- to many-body physics in ultracold matter via the path-integral Monte Carlo (PIMC) technique. The PIMC approach, which accounts for the particle statistics and yields thermodynamic observables, can be applied to both small and large systems.

We determine the energy, Tan's contact, various structural properties, the superfluid fraction and density, and the condensate fraction of small harmonically trapped bosonic and fermionic systems as functions of the temperature and  $s$ -wave scattering length. We find that the superfluid fraction of fermions is negative for certain parameter combinations and develop a microscopic understanding of this, at first sight, surprising behavior. We further illustrate that the superfluid fraction and condensate fraction are distinct quantities by performing finite temperature two-body calculations.

A simple model that can be used to extract the ground state energy of  $N$ -boson droplets from finite temperature calculations is proposed. This approach, combined with a novel two-body zero-range propagator, is used to explore the generalized Efimov scenario at unitarity. For three bosons, Efimov predicted the existence of an infinite series of geometrically spaced

bound states. Whether the  $N$ -boson energy is fully determined by three-body physics or dependent on higher-body properties has long been debated in the literature. We find that the  $N$ -body ground state energies display a notable model-dependence, suggesting that corrections to Efimov universality become increasingly more important with increasing  $N$ . For van der Waals systems, a weaker universality is found.

The equation of state (EOS) of spin-balanced equal-mass two-component Fermi gases at unitarity has been determined in cold atom experiments. At high temperature or low density, the virial expansion provides a good description of the EOS. While the second- and third-order virial coefficients have been calculated theoretically and verified experimentally, theory and experiment do not yet agree on the fourth-order virial coefficient. Our *ab initio* determination of the fourth-order virial coefficient agrees with experiments, thereby settling an ongoing debate in the literature.

# Table of Contents

	Page
Acknowledgement . . . . .	iii
Abstract . . . . .	v
List of Tables . . . . .	xi
List of Figures . . . . .	xiv
Related Publications . . . . .	xxxii
<b>1 Introduction . . . . .</b>	<b>1</b>
<b>2 Path integral Monte Carlo method . . . . .</b>	<b>22</b>
2.1 Introduction . . . . .	22
2.2 General scheme . . . . .	23
2.3 Partition function and density matrix . . . . .	27
2.3.1 Trotter formula . . . . .	33
2.3.2 Pair product approximation . . . . .	37
2.3.3 Comparison of the two approximations . . . . .	39
2.4 Permutations . . . . .	40
2.5 Sampling . . . . .	47
2.5.1 General scheme: Importance sampling . . . . .	47

2.5.2	General background on Monte Carlo methods . . . . .	50
2.5.3	“Naive move” . . . . .	60
2.5.4	“Wiggle move” . . . . .	62
2.5.5	“Permute move” . . . . .	68
2.5.6	“Pair distance move” . . . . .	74
2.5.7	“Whole path move” . . . . .	74
2.5.8	“Center-of-mass move” . . . . .	76
2.6	Estimators . . . . .	76
2.6.1	Energy estimator . . . . .	80
2.6.2	Structural properties . . . . .	84
2.7	Brief summary . . . . .	86
<b>3</b>	<b>Harmonically trapped Fermi gas: Temperature dependence of the Tan contact</b> . . . . .	<b>88</b>
3.1	Harmonically trapped Fermi gas: Temperature dependence of the Tan contact	89
3.2	Appendix . . . . .	98
3.2.1	Basis set expansion approach . . . . .	98
3.2.2	Path integral Monte Carlo approach . . . . .	98
3.2.3	(1,1) system with zero-range interactions . . . . .	99
3.2.4	(2,1) system with zero-range interactions . . . . .	101
3.2.5	Cluster expansion in canonical ensemble and connection to virial equation of state in grandcanonical ensemble . . . . .	105
3.2.6	Note on the temperature scales . . . . .	108
<b>4</b>	<b>Abnormal superfluid fraction of harmonically trapped few-fermion systems</b>	<b>109</b>
4.1	Abnormal superfluid fraction of harmonically trapped few-fermion systems .	110

<b>5</b>	<b>Temperature-dependence of small harmonically trapped atom systems with Bose, Fermi and Boltzmann statistics</b>	<b>120</b>
5.1	Introduction	121
5.2	Theoretical background	123
5.2.1	System Hamiltonian and observables	123
5.2.2	Efimovian states of three identical bosons in a trap	128
5.2.3	PIMC approach	132
5.3	Condensate and superfluid fractions of the two-body system	136
5.4	$N$ -body systems	144
5.4.1	$N$ identical bosons	144
5.4.2	Single-component gas with a single impurity	154
5.5	Conclusions	159
<b>6</b>	<b>Incorporating exact two-body propagators for zero-range interactions into <math>N</math>-body Monte Carlo simulations</b>	<b>162</b>
6.1	Introduction	163
6.2	$N$ -body density matrix	164
6.3	Two-body relative density matrix	166
6.3.1	One-dimensional system	167
6.3.2	Three-dimensional system	172
6.4	One-dimensional tests	176
6.5	Three-dimensional tests	180
6.6	Conclusion	187
<b>7</b>	<b>Energy and structural properties of <math>N</math>-boson clusters attached to three-body Efimov states: Two-body zero-range interactions and the role of the three-body regulator</b>	<b>189</b>

7.1	Introduction . . . . .	190
7.2	Three-body system at unitarity . . . . .	195
7.3	$N$ -body clusters at unitarity: Overview of literature results . . . . .	200
7.4	$N$ -body results at unitarity for the model 2bZR+3bRp . . . . .	203
7.5	Results for other interaction models . . . . .	213
7.6	Conclusions . . . . .	216
7.7	Supplemental material . . . . .	218
<b>8</b>	<b>Path integral Monte Carlo determination of the fourth-order virial coefficient for unitary two-component Fermi gas with zero-range interactions</b> . . . . .	<b>220</b>
8.1	Introduction . . . . .	221
8.2	Virial expansion framework . . . . .	223
8.3	Contradicting literature results for $b_4$ . . . . .	224
8.4	Customized PIMC algorithm . . . . .	225
8.5	PIMC results . . . . .	227
8.6	Conclusion . . . . .	231
8.7	Supplemental material . . . . .	231
	8.7.1 Literature values of $b_4$ . . . . .	231
	8.7.2 Pair product approximation and zero-range density matrix . . . . .	232
	8.7.3 Extrapolation to the $\tau \rightarrow 0$ limit and selected raw data . . . . .	233
<b>9</b>	<b>Conclusions . . . . .</b>	<b>237</b>
	<b>Bibliography . . . . .</b>	<b>242</b>

# List of Tables

2.1	Definitions of PIMC terminology used in this thesis. Columns 1-3 show the term, symbol, and explanation, respectively. . . . .	30
2.2	Definitions of Monte Carlo sampling terminology used in this thesis. Columns 1-3 show the symbol, name, and related equation number, respectively. The configuration $\mathbf{x}$ is defined by $\mathbf{x} = \{\mathbf{R}_0, \dots, \mathbf{R}_{n-1}\}$ . . . . .	49
3.1	Contact $C_{2,1}$ as a function of temperature for $s$ -wave zero-range interactions at unitarity. . . . .	103
3.2	High-temperature expansion coefficients $c_{1,1}^{(i)}$ and $c_{2,1}^{(i)}$ for the cluster expansion in the canonical ensemble. . . . .	105
3.3	High-temperature expansion coefficients $c_{\text{gc};1,1}^{(i)}$ and $c_{\text{gc};2,1}^{(i)}$ extracted from the contact determined in the grand canonical ensemble. . . . .	107
5.1	Relative zero-temperature energy $E_{\text{droplet}}$ for $N$ bosons interacting through the Gaussian potential $V_G$ with diverging $s$ -wave scattering length. The energies in columns 2 and 5 are obtained by extrapolating the PIMC results to $T = 0$ . The energies are expressed in units of the short-range energy scale $E_{\text{sr}}$ , $E_{\text{sr}} = \hbar^2/(mr_0^2)$ . Column 3 reports the energies from Ref. [1]; no errorbars are reported in that reference. For comparison, our basis set expansion approach (see Ref. [2] for a discussion of the approach) yields $E_{\text{droplet}}/E_{\text{sr}} = -0.11923(1)$ and $-0.70173(5)$ for $N = 3$ and $4$ , respectively. . . . .	149

7.1	Summary of potential models considered in this work. For each model, the two-body potential $V_{2b}$ and the three-body potential $V_{3b}$ are listed. $V_{2b}$ for 2bZR+3bZR, 2bZR+3bHC, and 2bZR+3bRp is the Fermi-Huang pseudopotential [3]; $a_s$ is set to infinity. $V_{ZR}(R)$ for 2bZR+3bZR is treated as a zero-range boundary condition. $V_{HC,R_0}(R)$ is the hardcore repulsive potential; $V_{HC,R_0}(R) = 0$ for $R > R_0$ and $V_{HC,R_0}(R) = \infty$ for $R < R_0$ . $V_0$ and $r_0$ for 2bG, $c_{12}$ and $c_6$ for 2bLJ, $c_{10}$ and $c_6$ for 2b10-6, and $c_8$ and $c_6$ for 2b8-6 are chosen such that the $s$ -wave scattering length is infinitely large and the two-body system supports one zero-energy $s$ -wave bound state. . . . .	193
7.2	PIMC energies for the model 2bZR+3bRp for $N = 4 - 15$ . Columns 2-4 show the scaled energy $E_N/N/(E_3/3)$ for $p = 5, 6$ , and $7$ , respectively. The error bars (not explicitly reported) are around 3%. . . . .	204
7.3	Summary of the definitions of length scales. The van der Waals length $L_{vdW}$ is defined in Ref. [4]. $L_p$ for $p = 6$ agrees with $L_{vdW}$ if $m$ is replaced by the reduced two-body mass $m/2$ . . . . .	207
7.4	DMC energies for the Hamiltonian with two-body van der Waals interactions for $N = 4 - 15$ . Columns 2-4 show the scaled energy $E_N/N/(E_3/3)$ for the models 2bLJ, 2b10-6, and 2b8-6, respectively. The error bars (not explicitly reported) are around 1%. . . . .	215
7.5	PIMC energies for the model 2bZR+3bRp for $N = 5 - 15$ . Columns 2-6 show the scaled energy $E_N/N/(E_3/3)$ for $p = 4-8$ , respectively. The error bars (not explicitly reported) are around 6%. . . . .	219
7.6	DMC energies for the Hamiltonian with two-body van der Waals interactions for $N = 4 - 15$ . Columns 2-3 show the scaled energy $E_N/N/(E_3/3)$ for the models He-He(scale) and He-He(arctan), respectively. The error bars (not explicitly reported) are around 1%. . . . .	219

8.1	Summary of literature results. The value reported in the respective reference is underlined. The conversion to other “representations” is done using Eqs. (8.10)-(8.12). The column labeled “Ref.” refers to the bibliography of the main text. . . . .	232
8.2	Selected PIMC raw data. Columns 1 and 2 show the inverse temperature $E_{\text{ho}}/(k_B T)$ and the number of imaginary time slices $N$ , respectively. Columns 3 and 4 show the observables $Q_{3,1}^{\text{ni}}/Q_{3,1}$ and $Q_{2,2}^{\text{ni}}/Q_{2,2}$ for the (3,1) and (2,2) systems, respectively. . . . .	235
8.3	Selected extrapolated PIMC results. Columns 1 and 2 show the inverse temperature $E_{\text{ho}}/(k_B T)$ and the order used in the extrapolation, respectively. Columns 3 and 5 show the extrapolated $\tau \rightarrow 0$ observables $Q_{3,1}^{\text{ni}}/Q_{3,1}$ and $Q_{2,2}^{\text{ni}}/Q_{2,2}$ for the (3,1) and (2,2) systems, respectively. Columns 4 and 6 show the resulting subcluster contributions $b_{3,1}$ and $b_{2,2}/2$ , respectively, to the fourth-order virial coefficient. . . . .	236

# List of Figures

1.1	The superfluid fraction $\rho_s$ of liquid helium-4 under saturated vapor pressure as a function of the temperature $T$ . The data are taken from Ref. [5]. . . .	2
1.2	Illustration of the zero-momentum scattering solutions for finite-range and zero-range interaction potentials. The thick dashed, solid, and dotted lines in panels (a), (b), and (c) show the Gaussian interaction potential $V_g(r)$ with $d = 0.8, 1.342$ , and $1.7$ , respectively. The thin dashed, solid, and dotted lines in panels (a), (b), and (c) show the corresponding unnormalized zero-momentum scattering solutions $u_0(r)$ . The circles, squares, and diamonds in panels (a), (b), and (c) show the zero-momentum solution for the zero-range potentials with the scattering length adjusted to be the same as those for the Gaussian potentials. Note, the zero-momentum solutions for the zero-range potential and the Gaussian potential coincide at large $r$ . . . . .	8
1.3	Illustration of a three-body recombination process. . . . .	12
1.4	Illustration of the cluster expansion. The filled circles show the atoms in an ultracold gas. The two-body, three-body, and four-body subsystems are illustrated by solid, dotted, and dashed circles. . . . .	15
1.5	Superfluid fraction $\rho_s$ of two identical bosons with zero-range interaction at unitarity in a harmonic trap with trapping frequency $\omega$ as a function of the temperature $k_B T / (\hbar\omega)$ . . . . .	16

2.1	World-line representation for a single particle in a one-dimensional harmonic trap. The temperature is set to $T = \hbar\omega/k_B$ . Panels (a), (b), (c), and (d) show paths for $n = 2, 4, 8,$ and $16,$ respectively. . . . .	29
2.2	Isomorphism between path integrals for a single free particle in two-dimensional space and classical particles connected by springs. In the path integral interpretation, the circles and wiggly lines depict the beads and (single-particle) links of a single particle, respectively. Panels (a), (b), and (c) are for low, medium, and high temperatures. In the classical mechanics formulation, the circles and wiggly lines depict particles and springs, respectively. . . . .	31
2.3	Isomorphism between path integrals for two interacting particles in two-dimensional space and classical particles connected by springs. In the path integral interpretation, the circles and wiggly lines depict the beads and links of a single particle, respectively. Dotted lines depict the two-body interaction between beads with the same imaginary time index. Panels (a), (b), and (c) are for low, medium, and high temperatures. In the classical mechanics formulation, the circles and wiggly lines depict particles and springs, respectively. Dotted lines depict the two-body interaction between selective particles. Earlier in the text, position vectors of the $k$ th particle are denoted by $\mathbf{r}_{k,j}$ . Using this notation, one has $\mathbf{r}_k = \mathbf{r}_{k,0}$ , $\mathbf{r}'_k = \mathbf{r}_{k,1}$ , and $\mathbf{r}''_k = \mathbf{r}_{k,2}$ . . . . .	36
2.4	Illustration of paths corresponding to the identity permutation $\hat{1}$ [panel (a)] and the permutation $\hat{P}_{12}$ [panel (b)] for Eq. (2.54). The circles and wiggly lines show beads and single-particle density matrices, respectively, for two free particles. Orange circles denote the head beads $\mathbf{r}_1$ and $\mathbf{r}_2$ . . . . .	46
2.5	Correlation coefficient $r_k$ as a function of the lag $k$ for a sample of 800 random numbers uniformly distributed between 0 and 1. The upper and lower solid lines show the 95% confidence interval. . . . .	51

2.6	Ratio of volumes of a $d$ -dimensional hypersphere with unit radius and a $d$ -dimensional hypercube with edge length of 2. . . . .	54
2.7	Illustration of the equilibration process for a Markov chain (crosses) for the Gaussian probability density function $p_G(x)$ (solid line). The graph employs dimensionless units. The starting point of the Markov chain is at $-5$ . The $x$ and $y$ axes correspond to the value and the configuration index, respectively. . . . .	55
2.8	Correlation coefficient $r_k$ as a function of the lag $k$ for the Markov chain discussed in Fig. 2.7. The equilibration stage (configuration index 1 to 25 in Fig. 2.7) is not considered here, i.e., the series of points $\{x_{26}, \dots, x_{100}\}$ is considered. The upper and lower solid lines denote the 95% confidence interval. . . . .	59
2.9	Illustration of the naive move for a single particle in a one-dimensional harmonic trap for $n = 32$ beads. Black circles depict the old bead positions. The red circle shows the proposed bead position for the 16-th time slice index. It can be seen that only two links (namely those involving the 15-th and 16-th beads and the 16-th and 17-th beads) are changed. . . . .	62
2.10	Illustration of the wiggle move for a single particle in a one-dimensional harmonic trap. Black and red circles depict the old and proposed new configurations, respectively. It is assumed that the construction of the new path segment was continued after the construction of the first midpoint bead, the next two midpoint beads, and so on. . . . .	67
2.11	Illustration of the permute move for two particles in a one-dimensional harmonic trap. Black and red circles depict the old and proposed new configurations, respectively. . . . .	71
2.12	Young diagrams for (a) the 3-cycle permutation, (b) the 2-cycle permutation, and (c) the identity permutation. . . . .	73

2.13	Illustration of the whole path move for a single particle in a one-dimensional harmonic trap. Black and red circles depict the old and new configurations, respectively. . . . .	75
2.14	Histogram of samples of an observable $O$ [the ratio of the partition function of the non-interacting (3,1) system and the partition function of the (3,1) system at unitarity at $\beta\hbar\omega = 0.7$ ]. The simulation is done on 480 processors and each processor produces 80 samples. The red solid line shows the unnormalized normal distribution with mean value 0.658547 and standard deviation 0.00415146. . . . .	79
2.15	Correlation coefficient $r_k$ as a function of the lag $k$ for the sample and observable considered in Fig. 2.14. The results for a single processor are considered, i.e., a series of 80 data points is analyzed. The upper and lower solid lines show the 95% confidence interval. . . . .	80
3.1	(a) The dotted, dashed, dash-dotted and dash-dot-dotted lines show the scaled pair distribution function $r^2 P_{12}(r)$ for $k_B T / (\hbar\omega) = 0, 0.6, 1.2$ and $2$ , respectively, for the (3,1) system interacting through $V_G$ with $r_0 = 0.06a_{ho}$ . The $T = 0$ curve is determined using the basis set expansion approach while the finite $T$ curves are determined using the PIMC approach. The thick solid lines in the inset of panel (a), which is a blow-up of the small $r$ region, show the extrapolation to $r = 0$ . (b) The solid and dotted lines show the relative energy of the ground state with $L^\Pi = 1^-$ and first excited state with $L^\Pi = 0^+$ of the (2,1) system interacting through $V_G$ with $r_0 = 0.06a_{ho}$ as a function of $-1/a_s$ . . . . .	92

- 3.2 Contact  $C_{N_1, N_2}$  as a function of  $k_B T / E_{\text{ho}}$  for the (a) (1, 1), (b) (2, 1), (c) (3, 1), and (d) (2, 2) systems. The circles, squares and triangles show  $C_{N_1, N_2}$  for  $V_G$  with  $r_0 / a_{\text{ho}} = 0.06, 0.08$  and  $0.1$  obtained using the PIMC approach. The solid lines show  $C_{N_1, N_2}$  for  $V_G$  with  $r_0 = 0.06 a_{\text{ho}}$  obtained using the basis set expansion approach. For comparison, the dotted lines in panels (a) and (b) show  $C_{N_1, N_2}$  obtained using  $V_F$ . (a) The dashed line shows the first-order Taylor expansion at high temperature. (b) The dashed line shows the cluster expansion, i.e., the quantity  $2C_{1,1}$ . (c)/(d) The dashed and dash-dotted lines show the leading order term of the cluster expansion and the full cluster expansion, respectively. The insets of panels (a) and (b) show blow-ups of the low temperature regions. . . . . 93
- 3.3 Circles, squares, crosses and triangles show  $C_{N_1, N_2}$  for the (1, 1), (2, 1), (3, 1) and (4, 1) systems, respectively, interacting through  $V_G$  with  $r_0 = 0.06 a_{\text{ho}}$  as a function of  $T$  [6]. Dotted lines serve as a guide to the eye. Inset: Crosses, squares and circles show the contact of the (3, 1) system for Fermi, Boltzmann and Bose statistics, respectively. . . . . 96
- 3.4 Range dependence of the contact  $C_{1,1}$  for  $r_0 = 0.06 a_{\text{ho}}$  as a function of  $k_B T / E_{\text{ho}}$ . The circles show the difference between the finite-range contact calculated using approach (i) and the zero-range contact, normalized by the zero-range contact. The solid line shows the difference between the finite-range contact calculated using approach (ii) and the zero-range contact, normalized by the zero-range contact. In the large  $T$  limit, the difference approaches zero from below. In approach (ii),  $r_{\text{eff}} = 0.12178 a_{\text{ho}}$ —corresponding to  $V_G$  with  $r_0 = 0.06 a_{\text{ho}}$ —has been used. . . . . 100

- 3.5 (a) The solid, dotted, dashed and dash-dotted lines show the weight factor  $\exp[-E_j^{\text{rel}}/(k_B T)]/Z^{\text{rel}}$  (see right axis) as a function of the relative energy for  $k_B T/E_{\text{ho}} = 0.2, 0.4, 0.6$  and  $0.8$ , respectively. The circles show the zero-temperature contact  $\bar{C}_{2,1}$  (see left axis) for states with  $E_j^{\text{rel}} < 5E_{\text{ho}}$ . (b) The dots show the zero-temperature contact  $\bar{C}_{2,1}$  as a function of the relative energy for  $E_j^{\text{rel}} \lesssim 30E_{\text{ho}}$ . The solid (dashed) line connects the contacts of  $L = 1$  ( $L = 0$ ) states, which are characterized by the same  $s_{L,\nu}$  value but different  $q$  values; the  $s_{L,\nu}$  values chosen are the smallest ones for both  $L = 1$  and  $0$ . . . . . 104
- 4.1 Superfluid properties of the non-interacting trapped single-component gas as a function of  $k_B T/E_{\text{ho}}$ . (a) From top to bottom at  $k_B T = E_{\text{ho}}$ , the alternating solid and dashed lines show  $n_s$  for the Fermi gas with  $N = 1 - 10$ . (b) From bottom to top, alternating solid and dashed lines show  $n_s$  for the Bose gas with  $N = 1 - 10$ . (c) The dashed and solid lines replot  $n_s$  for  $N = 2$  and  $3$ , respectively. For comparison, symbols show  $n_s$  obtained using the PIMC approach. The errorbars are smaller than the symbol size. (d) The dashed and solid lines show the scaled radial total and superfluid density for  $N = 2$ . 113
- 4.2 Properties of the interacting trapped  $(2, 1)$  system as a function of  $k_B T/E_{\text{ho}}$ . (a) The lines from bottom to top show  $n_s$  for  $a_{\text{ho}}/a_s = 0, 0.2, \dots, 2$ . (b)/(c) The lines from top to bottom show  $I_c$  and  $I_q$ , respectively, for  $a_{\text{ho}}/a_s = 0, 0.2, \dots, 2$ . . . . . 116

4.3 Properties of the trapped (2, 2) system. (a) The dotted, solid, dashed, and dash-dotted lines show  $n_s$  as a function of  $k_B T/E_{\text{ho}}$  for  $a_s/a_{\text{ho}} = 0, -0.2, -1,$  and  $\infty$ , respectively. The squares, circles, and diamonds show  $n_s$  obtained by the PIMC approach for  $a_s/a_{\text{ho}} = -0.2, -1,$  and  $\infty$ , respectively. (b) and (c) show blowups of the high-temperature region. (d) The thin dotted and dashed lines show  $I_c$  for  $a_s = 0$  and  $-a_{\text{ho}}$ , respectively; the thick dotted and dashed lines show  $I_q$  for  $a_s = 0$  and  $-a_{\text{ho}}$ , respectively. The dashed curves are obtained by the microscopic approach (using  $r_0 = 0.06a_{\text{ho}}$ ) for  $k_B T/E_{\text{ho}} \leq 0.5$  and by the PIMC approach (using  $r_0 = 0.1a_{\text{ho}}$ ) for  $k_B T/E_{\text{ho}} \geq 0.6$ . (e) The solid, dotted, dashed, dash-dash-dotted, dash-dotted, and dash-dot-dotted lines show  $\rho_s r^2$  for  $a_s = -0.2a_{\text{ho}}$  and  $k_B T/E_{\text{ho}} = 0.5, 0.6, 0.8, 1, 1.4,$  and  $2,$  respectively. . . . . 117

5.1 Relative energy spectrum as a function of the three-body phase  $\theta_b$  for three identical bosons in a harmonic trap interacting through zero-range potentials with infinite  $s$ -wave scattering lengths. The circle, square, and triangle show the ground state energy for the Gaussian two-body interaction with range  $r_0/a_{\text{ho}} = 0.06, 0.08,$  and  $0.1,$  respectively. The inset shows the negative energy regime on a log scale. The spacing between the energy levels for fixed  $\theta_b$  is very close to 515, i.e., very close to the free-space scaling factor. . . . . 130

5.2	Hyperradial density $P_{\text{hyper}}(R)$ for three identical bosons at unitarity. Solid and dotted lines show the PIMC results at $k_B T/E_{\text{ho}} = 0.4$ for the Gaussian model potential with $r_0/a_{\text{ho}} = 0.06$ and $0.1$ , respectively (in the main panel, the curves are indistinguishable on the scale shown). The main panel and the inset show the same data but use a different scaling: The main panel uses units derived from the energy of the three-boson system at $T = 0$ while the inset employs harmonic oscillator units. For comparison, the dashed line shows the hyperradial density obtained using the zero-range pseudopotential with $\kappa_*$ determined by the relative energy of the finite-range potential. . . .	131
5.3	Statistical factor $S$ for the $(N - 1, 1)$ system with interspecies potential $V_G$ with $r_0 = 0.06a_{\text{ho}}$ and $1/a_s = 0$ . Squares, crosses, triangles, and circles show the statistical factor $S$ as a function of (a) the temperature $T$ and (b) the inverse temperature $T^{-1}$ for $N = 3, 4, 5$ , and $6$ , respectively. . . . .	135
5.4	The lines show (a) the condensate fraction $n_c$ and (b) the superfluid fraction $n_s$ as a function of the temperature $T$ for two Boltzmann particles with zero-range interaction for various $a_s$ . The solid, dotted, dashed, dash-dotted, dash-dot-dotted, and dash-dash-dotted lines are for $a_{\text{ho}}/a_s = -\infty, -2, 1, 0, 1$ , and $2$ , respectively. In panel (b), the dependence on $a_s$ is small. The insets compare (a) the condensate fraction $n_c$ and (b) the superfluid fraction $n_s$ for two Boltzmann particles (lines; these are the same data as shown in the main parts of the figure) and two identical bosons (squares and circles correspond to $a_{\text{ho}}/a_s = -\infty$ and $0$ , respectively) as a function of the temperature. . . .	139

5.5	Panels (a) and (b) show radial densities for two identical non-interacting fermions. Solid, dotted, and dashed lines show (a) the scaled radial total density and (b) the scaled radial superfluid density, for $k_B T/E_{\text{ho}} = 0.5, 0.26459,$ and $0.2,$ respectively. In panel (a), the dotted line is hardly distinguishable from the dashed line. The solid lines in panels (c), (d), and (e) show (c) the superfluid fraction $n_s,$ (d) the classical moment of inertia $I_c,$ and (e) the quantum mechanical moment of inertia $I_q$ as a function of the temperature $T.$ The diamond, square and circle mark the temperatures considered in panels (a) and (b). . . . .	142
5.6	Energies as a function of the temperature $T$ for three identical bosons at unitarity interacting through $V_G$ with different $r_0.$ Circles and squares show the PIMC results for $r_0/a_{\text{ho}} = 0.06$ and $0.08,$ respectively. For comparison, the solid and dotted lines show the result obtained using the droplet state plus center of mass excitations. The dashed line shows the thermally averaged energy for three identical non-interacting bosons. Dash-dot-dotted and dash-dotted lines show results obtained using the simple combined model for $r_0/a_{\text{ho}} = 0.06$ and $0.08$ (see the text for discussion). . . . .	144
5.7	Phase transition like feature for $N$ identical harmonically trapped bosons interacting through $V_G$ with $1/a_s = 0.$ (a) Circles and squares show the energy obtained by the PIMC approach for $r_0 = 0.1a_{\text{ho}}$ and $N = 3$ and $4,$ respectively, as a function of the temperature $T.$ The dotted, solid, and dashed lines show the energies for $N = 3, 4,$ and $5$ obtained using the simple combined model. (b) The dotted, solid and dashed lines show the heat capacity $C_v$ for $N = 3, 4,$ and $5,$ respectively, as a function of $T.$ . . . . .	146

- 5.8 Transition temperature  $T_{\text{tr}}$  for  $N$  identical bosons in a harmonic trap at unitarity as a function of  $N$ . The transition temperature is calculated using the simple combined model. The circles show  $T_{\text{tr}}$  using the droplet energies for the Gaussian two-body interaction model employed in this work. For comparison, the squares show  $T_{\text{tr}}$  using the droplet energies for a model Hamiltonian with attractive two-body and repulsive three-body interactions [7] (to obtain the squares, the three-body eigen energy  $E_{\text{droplet}} = E_{\text{trimer}}$  is chosen such that it agrees with that for the Gaussian two-body interaction model, i.e., the circle and the square agree for  $N = 3$ ). . . . . 148
- 5.9 Hyperradial density  $P_{\text{hyper}}(R)$  for three identical bosons at unitarity interacting through  $V_{\text{G}}$  with  $r_0 = 0.06a_{\text{ho}}$  for various temperatures  $T$ . Dash-dash-dotted, solid, dotted, dashed, and dash-dotted lines are for  $k_B T/E_{\text{ho}} = 3, 4, 5, 6,$  and  $7,$  respectively. Panel (a) shows the small  $R$  region while panel (b) shows the large  $R$  region. Note that panels (a) and (b) have different scales for the  $x$ -axis and the  $y$ -axis. . . . . 150
- 5.10 Superfluid fraction  $n_s$  as a function of the temperature  $T$  for  $N$  identical bosons at unitarity. The circles and squares show the PIMC results for the Gaussian potential  $V_{\text{G}}$  with  $r_0 = 0.1a_{\text{ho}}$  for  $N = 3$  and  $4,$  respectively. The errorbars are smaller than the symbol size. For comparison, the solid line shows the result obtained using a single-particle model (see text for discussion). . . 151

- 5.11 Scaled pair distribution functions  $r_{j4}^2 P_{\text{pair}}(r_{j4})$  ( $j < 4$ ) for the (3, 1) system with interspecies interaction  $V_G$  with  $r_0 = 0.06a_{\text{ho}}$  and diverging interspecies scattering length  $a_s$  at temperature (a)  $k_B T/E_{\text{ho}} = 0.6$ , (b)  $k_B T/E_{\text{ho}} = 1.2$ , (c)  $k_B T/E_{\text{ho}} = 2$ , and (d)  $k_B T/E_{\text{ho}} = 3$ . Dashed, solid, and dotted lines are for systems with Fermi, Boltzmann, and Bose statistics, respectively. The error bars are comparable to or smaller than the line widths. In panel (a), the solid and dotted lines are hardly distinguishable. In panel (d), all three lines nearly coincide. . . . . 156
- 5.12 Superfluid fraction  $n_s$  as a function of the temperature  $T$  for the (3, 1) system with interspecies potential  $V_G$  with  $r_0 = 0.06a_{\text{ho}}$  and  $1/a_s = 0$ . The circles, crosses, and squares are obtained from the PIMC simulations with Bose, Boltzmann, and Fermi statistics, respectively. The error bars are only shown when they are larger than the symbol size. For comparison, dotted, solid, and dashed lines show the superfluid fraction for the non-interacting (3, 1) systems with Bose, Boltzmann, and Fermi statistics, respectively. . . . 157
- 6.1 PIMC results for  $N$  harmonically trapped distinguishable one-dimensional particles with two-body zero-range interactions of infinite strength at temperature  $T = \hbar\omega/k_B$ . (a) The symbols show the energy obtained by the PIMC approach as a function of the number of particles  $N$ . For comparison, the dotted line shows the exact thermally averaged energy. (b) Symbols show the energy difference  $\Delta E$  between the PIMC energies and the exact results. As a reference, the dotted line shows the  $\Delta E = 0$  curve. In (a) and (b), the circles and squares are calculated using 8 and 128 time slices, respectively. . . . . 177

6.2	PIMC results for harmonically trapped one-dimensional bosons interacting through two-body zero-range interactions with coupling constant $g = \hbar^2/(\sqrt{2}\mu a_{\text{ho}})$ at temperature $T = \hbar\omega/(32k_B)$ . The dashed and dotted lines show the pair distribution function obtained by the PIMC approach for $N = 2$ and 3 bosons, respectively. For comparison, the solid lines show the asymptotic short-range behavior obtained by alternative means (see text). . . . .	180
6.3	Scaled pair distribution functions $4\pi P_{12}(r)r^2$ for two distinguishable particles of mass $m$ in a harmonic trap at $k_B T/(\hbar\omega) = 1$ . The solid and dashed lines are for two particles with infinitely large $s$ -wave scattering length interacting through the zero-range potential and a Gaussian potential with effective range $r_e \approx 0.0861a_{\text{ho}}$ , respectively. For comparison, the dotted line is for the non-interacting system. . . . .	181
6.4	Scaled pair distribution function $4\pi P_{12}(r)r^2$ for three identical harmonically trapped three-dimensional bosons with two-body zero-range interactions with infinitely large $s$ -wave scattering length and repulsive $1/R^6$ three-body potential. The solid line and squares are calculated by the zero-temperature PIGS approach and the PIMC approach at $T = \hbar\omega/k_B$ . For comparison, the circles show the scaled pair distribution function obtained by sampling the exact ground state density using the Metropolis algorithm. . . . .	185
6.5	PIMC energies for $N = 5$ harmonically trapped three-dimensional bosons with two-body zero-range interactions with infinite scattering length and and repulsive $1/R^6$ three-body interaction at temperature $T = \hbar\omega/k_B$ as a function of the time step $\tau$ . The circles (lower-lying data set) and squares (higher-lying data set) show the energy obtained using the second- and fourth-order scheme, respectively. The error bands are obtained by fitting the data for different $\tau$ intervals. . . . .	186

6.6	Free-space $N$ -boson ground state energy $E_{\text{cluster}}$ as a function of $N$ for infinitely large two-body $s$ -wave scattering length. The circles with errorbars are extracted from our PIMC simulations. The dotted line shows the energies reported in Ref. [7]. . . . .	187
7.1	Schematic illustration of the energy spectrum for four identical bosons. The x marks the $(1/a_s, E) = (0, 0)$ point. The dotted line shows the energy of the weakly-bound dimer. The solid lines show different Efimov trimer states, which become unbound on the positive scattering length side at the atom-dimer threshold. The dashed lines show “ground state” and “excited state” tetramers that are attached to each Efimov trimer. These tetramer states hit the dimer-dimer threshold on the positive scattering length side (the energy of the two dimers is shown by the dash-dotted line). It should be noted that the excited tetramer state turns into a virtual state for a certain region of positive scattering lengths [8]; this detail is not reflected in the plot. . . . .	192
7.2	Breaking of the scale invariance for the three-boson system at unitarity with three-body hardcore regulator. The circles show the difference between the binding momentum ratio $\kappa_3^{(n)}/\kappa_3^{(n+1)}$ of the $n$ th and $(n + 1)$ th states for the model 2bZR+3bHC and the ratio $\exp(\pi/ s_0 ) = 22.6944$ for the model 2bZR+3bZR as a function of $n$ . The solid line shows a fit to the data points. The breaking of the scale invariance becomes weaker with increasing $n$ . . . . .	196

7.3	Binding momentum characteristics for the three-boson system with three-body power law regulator at unitarity. The circles show the ratio of the binding momentum of two consecutive states for the model 2bZR+3bRp as a function of $p$ . Panel (a) shows the binding momentum ratio for the ground and the first excited states while panel (b) shows the ratio for the first and the second excited states. The solid and dashed lines show the binding momentum ratio for the models 2bZR+3bZR and 2bZR+3bHC, respectively. . . . .	197
7.4	Angular distributions for three identical bosons at unitarity. The circles, triangles and squares show the angular distributions $P_{\text{tot}}(\theta)$ , $P_{\text{min}}(\theta)$ , and $P_{\text{max}}(\theta)$ for the model 2bZR; these distributions are identical to those for the models 2bZR+3bHC and 2bZR+3bRp. The solid, dotted, and dashed lines show the angular distributions $P_{\text{tot}}(\theta)$ , $P_{\text{min}}(\theta)$ , and $P_{\text{max}}(\theta)$ for the model 2bG. . . .	199
7.5	Radial density $\rho(r)$ for three identical bosons at unitarity ( $r$ is measured relative to the center of mass of the three-body system). The dashed and solid lines show $\rho(r)$ for the models 2bZR+3bZR and 2bZR+3bRp with $p = 6$ , respectively. . . . .	200

7.6	<p>Energy per particle of <math>N</math>-boson clusters at unitarity. (a) Summary of literature results. The dashed and dotted lines show the analytical prediction by Gattobigio and Kievsky [1] and Nicholson [9], respectively. The triangles show the diffusion Monte Carlo (DMC) energies for a Hamiltonian with two-body square well interaction and repulsive three-body hardcore regulator [7]. The diamonds show the energy for the model 2bG [10]. (b) Summary of our PIMC calculations. The circles and pluses are for the model 2bZR+3bRp with <math>p = 4</math> and 8, respectively; the error bars (not shown) are of the order of the symbol sizes. The squares, diamonds, and triangles are for the model 2bZR+3bRp with <math>p = 5, 6,</math> and <math>7,</math> respectively; the error bars (not shown) are smaller than the symbol sizes. (c) Summary of our calculations for two-body van der Waals models. The circles, crosses, and squares show our DMC results for the models 2bLJ, 2b10-6, and 2b8-6, respectively. . . . .</p>	201
7.7	<p>Comparison of our PIMC energies (left) and literature results (right) for selected <math>N</math>. Panels (a), (b), and (c) show our PIMC energy per particle for <math>N</math>-boson clusters interacting through the model 2bZR+3bRp as a function of <math>p</math> for <math>N = 6, 10,</math> and <math>13,</math> respectively. For comparison, panels (d), (e), and (f) show the energy per particle from the literature for the same <math>N</math>. The triangles, diamonds, and squares are from von Stecher [7], Nicholson [9], and Gattobigio <i>et al.</i> [1]. Since the work by Nicholson is restricted to even <math>N</math>, comparison for <math>N = 13</math> cannot be made. . . . .</p>	205

- 7.8 Expectation value  $\bar{r}$  of the pair distance as a function of  $N$  for  $N$ -boson systems interacting through various models. (a) The squares are for the model 2bZR+3bRp with  $p = 6$ . (b) The triangles are for the model 2bG. (c) The circles are for the model 2bLJ. The error bars show the variance of the pair distance. The pair distances are plotted using two different units: (i) the inverse three-body binding momentum (left axis) and (ii) the characteristic length scale of the model Hamiltonian (right axis). . . . . 208
- 7.9 (a) Expectation value  $\bar{R}$  of the sub-three-body hyperradius (triple size) as a function of  $N$  for  $N$ -boson systems interacting through the model 2bZR+3bR6. The error bars show the variance of the triple size. (b) Triple distribution function  $P_{\text{triple}}(R)$  for the  $N = 13$  cluster scaled using the three-body binding momentum  $\kappa_3$ . The solid lines from top to bottom at  $\kappa_3 R = 0.6$  are for the model 2bZR+3bRp with  $p = 4, 5, 6, 7$ , and 8. The inset replots the triple distribution functions using the binding momentum  $\kappa_{13}$  of the  $N = 13$  droplet. In these units, the triple distribution functions for different  $p$  collapse. . . . 209
- 7.10 (a) Maximum density  $\rho_{\text{max}}$  as a function of  $N$  for  $N$ -boson systems interacting through various models. The circles, squares, and diamonds are for the model 2bZR+3bRp with  $p = 5$  (lowest data set), 6, and 7 (highest data set), respectively. For comparison, the line is for the model 2bG. (b) Same data as in (a) but replotted as the minimum average interparticle distance  $(\rho_{\text{max}})^{-1/3}$ . The right axis shows the data for the model 2bZR+3bR6 in units of  $L_6$ . . . 210

7.11	Scaled pair distribution function $4\pi r^2 P_{\text{pair}}(r)$ for $N = 13$ bosons interacting through various models. (a) The solid lines from top to bottom at $\kappa_3 r = 0.8$ are for the model 2bZR+3bRp with $p = 4-8$ , scaled using the three-body binding momentum $\kappa_3$ . The inset replots the pair distribution functions scaled using the binding momentum $\kappa_{13}$ of the $N = 13$ droplet. In these units, the pair distribution functions for different $p$ collapse. (b) The dashed and dotted lines show the scaled distribution functions for the models 2bLJ and 2bG, respectively, using the three-body binding momentum $\kappa_3$ . . . . .	211
7.12	Angular distribution $P_{\text{tot}}(\theta)$ for $N$ -boson clusters interacting through the model 2bZR+3bRp with $p = 6$ . The lines from top to bottom at $\theta = 0$ are for $N = 5, 6, 7, 9$ , and 13. . . . .	213
7.13	Assessing the applicability of Eq. (7.4) for $N$ -boson systems with two-body finite-range interactions at unitarity. Circles and triangles show the normalized difference $(\kappa_N^{\text{appr}} - \kappa_N)/\kappa_N$ for the models 2bG and 2bLJ, respectively, as a function of the number of particles $N$ . . . . .	216
8.1	Benchmarking our PIMC results (circles) for the (2,1) system at unitarity through comparison with sum-over-states results. (a) The observable $Q_{2,1}^{\text{ni}}/Q_{2,1}$ as a function of the imaginary time step $\tau$ at $k_B T = E_{\text{ho}}$ . The circles show our PIMC results. The error bars (not shown) are smaller than the symbol size. The solid line shows the fourth-order polynomial fit of the form $a + b\tau^2 + c\tau^4$ . The dashed line shows the sum-over-states results. (b) $b_3$ as a function of $1/(k_B T)$ . The circles show our PIMC results while the solid line shows the sum-over-states results. . . . .	228

8.2	PIMC determination of the fourth-order virial coefficient. Circles in panels (a), (b), and (c) show $b_{3,1}$ , $b_{2,2}/2$ , and $b_4$ , respectively, determined by our PIMC approach. The crosses in (a) and (b) show the $T \rightarrow \infty$ limit of the two-parameter fit (dashed line) to the PIMC data at the four highest temperatures. The dashed line and the cross in (c) show the sum of the fits from (a) and (b). The error bar in (c) is obtained by error propagation. The diamond with error bar shows the experimental result from Ref. [11]. . . . .	229
8.3	Benchmarking our PIMC results (circles) for the (2,1) system at unitarity through comparison with sum-over-states results. The observable $Q_{2,1}^{\text{ni}}/Q_{2,1}$ as a function of the imaginary time step $\tau$ at temperature $k_B T = 2E_{\text{ho}}$ . The error bars (not shown) are smaller than the symbol size. In (a), the time steps correspond to $N = 2, 3, 4$ , and 6. In (b), the time steps correspond to $N = 3, 4, 6$ , and 8. The solid line shows the fourth-order polynomial fit of the form $a + b\tau^2 + c\tau^4$ . The dashed line shows the sum-over-states results. . . . .	234

# Related Publications

1. Y. Yan and D. Blume: Path integral Monte Carlo determination of the fourth-order virial coefficient for unitary two-component Fermi gas with zero-range interactions, arXiv: 1602.02328 (2016).
2. Y. Yan and D. Blume: Energy and structural properties of  $N$ -boson clusters attached to three-body Efimov states: Two-body zero-range interactions and the role of the three-body regulator, Phys. Rev. A **92**, 033626 (2015).
3. Y. Yan and D. Blume: Incorporating exact two-body propagators for zero-range interactions into  $N$ -body Monte Carlo simulations, Phys. Rev. A **91**, 043607 (2015)
4. S. E. Gharashi, X. Y. Yin, Y. Yan, and D. Blume: One-dimensional Fermi gas with a single impurity: Perturbative description of the upper branch, Phys. Rev. A **91**, 013620 (2015).
5. D. Blume and Y. Yan: Generalized Efimov Scenario for Heavy-Light Mixtures, Phys. Rev. Lett. **113**, 213201 (2014).
6. Y. Yan and D. Blume: Temperature dependence of small harmonically trapped atom systems with Bose, Fermi, and Boltzmann statistics, Phys. Rev. A **90**, 013620 (2014).
7. Y. Yan and D. Blume: Abnormal Superfluid Fraction of Harmonically Trapped Few-Fermion Systems, Phys. Rev. Lett. **112**, 235301 (2014).
8. Y. Yan and D. Blume: Harmonically trapped Fermi gas: Temperature dependence of the Tan contact, Phys. Rev. A **88**, 023616 (2013).

# Chapter 1

## Introduction

Helium-4 exists, at standard atmosphere and room temperature, in the form of a gas. As the temperature  $T$  drops below 4K, it undergoes a first-order phase transition and forms a (normal) liquid [12]. Similar to water, the viscosity of the helium normal fluid is finite. However, as  $T$  drops below 2.17K, helium-4 undergoes a second-order phase transition to a superfluid. The superfluid phase was discovered in 1938 through the observation of a sudden drop of the viscosity [13, 14]. Other remarkable characteristics of a superfluid include the existence of quantized vortices [15].

Superfluidity can be explained phenomenologically by Landau's two fluid model [12], that is, the system can be separated into two components: the normal fluid and the superfluid. Each component has its own density and velocity. The normal fluid has a finite viscosity and follows the classical hydrodynamic equation of motion while the superfluid component has zero viscosity. The fraction of the superfluid component in the total system defines the superfluid fraction  $\rho_s$ . Figure 1.1 shows the superfluid fraction of helium-4 under saturated vapor pressure [5]. The superfluid fraction at zero temperature is 1, decreases as  $T$  increases, and drops to 0 sharply at  $T = 2.17\text{K}$ .

The fermionic isotope helium-3 also exhibits a superfluid phase but at a much lower temperature than the bosonic isotope helium-4, namely at 3mK [16–18]. Differences between

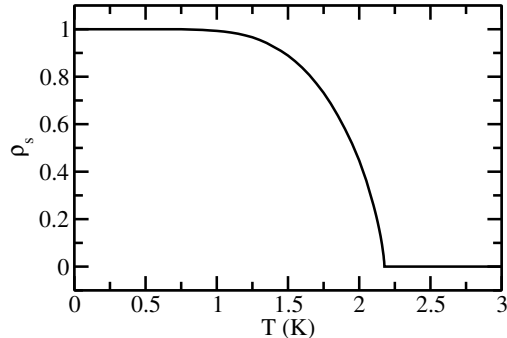


Figure 1.1: The superfluid fraction  $\rho_s$  of liquid helium-4 under saturated vapor pressure as a function of the temperature  $T$ . The data are taken from Ref. [5].

helium-3 and helium-4 isotopes exist in the mass and the particle statistics. The differences between the two-body van der Waals interaction potentials for two helium-4 atoms and two helium-3 atoms due to the relativistic corrections are too small to be responsible for the vastly different transition temperatures. Since the difference in the atomic masses is only around 25%, the huge change of the transition temperature can be attributed to, at least primarily, the particle statistics. The particle statistics becomes important when the temperature is so low that the wave nature of the particles becomes important, i.e., the de Broglie wave length  $\lambda$  becomes comparable to the interparticle spacing. Here  $\lambda$  is defined by

$$\lambda = \frac{h}{\sqrt{3mk_B T}}, \quad (1.1)$$

where  $k_B$  and  $h$  are the Boltzmann constant and Planck's constant, respectively. In the language of path integrals, using the canonical ensemble, each particle is represented by a path that is closed [19, 20]. The “size” spanned by each particle's path is determined by  $\lambda$ . When  $\lambda$  is comparable to the interparticle spacing, the paths of different particles overlap. In this case, exchange effects can happen: The paths of two or more particles can “join together” to form a larger loop. It can be shown that the superfluid fraction is proportional to the thermal average of the square of the projected areas of the paths [19]. To have a closed path with a large projected area, many particles must join together. This means that

the appearance of superfluidity is related to the dominance of exchange effects.

To further illuminate the importance of the particle statistics, we first consider bosons. The many-body wave function of  $N$  identical bosons is symmetric under the exchange of any two bosons; note, the exchange refers to the exchange of the position vectors, the spin degrees of freedom, and any other degrees of freedom needed to characterize the bosons. It was predicted in the 1920s that non-interacting bosons undergo a transition at a critical temperature  $T_c$  [21, 22]. Below the critical temperature, a large fraction of the bosons occupies the same state. This phenomenon is termed Bose-Einstein condensation (BEC). Gaseous helium-4 atoms in the metastable  $2^3S_1$  state have been brought to BEC in 2001 [23, 24]. In the BEC phase, the de Broglie wavelength  $\lambda$  is larger than the interparticle spacing  $\bar{r}$ . At the critical temperature  $T_c = 4.7\mu\text{K}$  (this number is for a typical experimental realization of gaseous helium-4),  $\lambda$  is about twice as large as the interparticle spacing  $\bar{r}$ :  $\lambda \approx 11,000a_0$  and  $\bar{r} \approx 5,600a_0$ . Here  $a_0$  denotes the Bohr radius. The  $s$ -wave scattering length, which characterizes the strength of the interaction, is  $141a_0$  for two helium atoms in the metastable state [25]. This scattering length, as well as the range  $r_{\text{vdW}}$  ( $r_{\text{vdW}} \approx 5.35a_0$  [4, 26]) of the two-body van der Waals interaction [4, 27], are much smaller than the interparticle spacing  $\bar{r}$ . This implies that the system is very weakly-interacting (close to the non-interacting regime) and that the condensate fraction, i.e., the fraction of atoms occupying the same state, is almost 100% at the lowest temperature realized experimentally.

The behavior of gaseous metastable helium and liquid helium-4 is very different. At the critical temperature of 2.17K, the de Broglie wavelength  $\lambda$  of atoms in liquid helium-4 is also about twice as large as the interparticle spacing  $\bar{r}$ :  $\lambda \approx 16a_0$   $\bar{r} \approx 7a_0$  [5]. However, unlike in the gaseous system, the van der Waals length  $r_{\text{vdW}}$  of two liquid helium atoms in the ground state (i.e., in the  $1^1S_0$  state) is comparable to the interparticle spacing:  $r_{\text{vdW}} \approx 5.08a_0$  [4, 28] and  $\bar{r} \approx 7a_0$ . Moreover, the interactions in liquid helium-4 are deemed strong since the  $s$ -wave scattering length  $a_s$ ,  $a_s \approx 170a_0$  [28], is much larger than the interparticle spacing.

Because of this strong interaction, the condensate is largely depleted and the condensate fraction of liquid helium-4 is only around 10% even at zero temperature [12].

Formally, the condensate fraction is defined by the largest occupation number of all the single-particle natural orbitals divided by the number of particles [29–31]. Following this definition, only non-interacting systems at zero temperature have a condensate fraction of 1. If the interactions are turned on or the temperature is increased, the total wave function of the system can, in general, no longer be written as a product of single-particle natural orbitals. In general, to get the natural orbitals, one has to diagonalize the one-body density matrix. The one-body density matrix  $\rho(\mathbf{r}, \mathbf{r}')$  in position space reads

$$\rho(\mathbf{r}, \mathbf{r}') = \int_{\mathbf{r}_2} \dots \int_{\mathbf{r}_N} \psi^*(\mathbf{r}, \mathbf{r}_2, \dots, \mathbf{r}_N) \psi(\mathbf{r}', \mathbf{r}_2, \dots, \mathbf{r}_N) d\mathbf{r}_2 \dots d\mathbf{r}_N, \quad (1.2)$$

where  $\psi(\mathbf{r}_1, \mathbf{r}_2, \dots, \mathbf{r}_N)$  is the many-body wave function. The definition here applies to zero temperature and can be generalized to finite temperature [19]. In terms of the field operators  $\hat{\psi}(\mathbf{r})$  and  $\hat{\psi}^\dagger(\mathbf{r})$ , which, respectively, destroy and create a particle at position  $\mathbf{r}$ , the one-body density matrix reads

$$\rho(\mathbf{r}, \mathbf{r}') = \langle \hat{\psi}^\dagger(\mathbf{r}') \hat{\psi}(\mathbf{r}) \rangle, \quad (1.3)$$

where  $\langle \dots \rangle$  indicates the average either over a state (at zero temperature) or a thermal average of states (at finite temperature).

For homogeneous systems, the total momentum operator commutes with the Hamiltonian if the Hamiltonian is translationally invariant. The one-body density matrix in momentum space can be written as  $\langle \hat{a}_{\mathbf{k}'}^\dagger \hat{a}_{\mathbf{k}} \rangle$ , where  $\hat{a}_{\mathbf{k}}$  and  $\hat{a}_{\mathbf{k}'}^\dagger$  are the annihilation and creation operators of a particle with momentum  $\mathbf{k}$  and  $\mathbf{k}'$ , respectively. It can be shown that the off-diagonal terms with  $\mathbf{k} \neq \mathbf{k}'$  are zero because of the momentum conservation. This means that the one-body density matrix in momentum space is diagonal and that the natural orbitals are plane wave states. Since the zero-momentum state has the lowest energy, the state with the largest

occupation for homogeneous systems in thermal equilibrium is typically the zero-momentum state.

The occupation of the zero-momentum state can alternatively be obtained from the density matrix  $\rho(\mathbf{r}, \mathbf{r}')$  in position space. Specifically, the condensate fraction of homogeneous systems is proportional to  $\lim_{|\mathbf{r}-\mathbf{r}'|\rightarrow\infty} \rho(\mathbf{r}, \mathbf{r}')$ . The above quantity is referred to as off-diagonal long-range order (ODLRO). The term “off-diagonal” refers to the fact that  $\mathbf{r} \neq \mathbf{r}'$  and the term “long range” refers to the fact that one looks at large separations. For trapped systems, the total momentum operator does not commute with the Hamiltonian, implying that the zero-momentum state is no longer the most occupied state; in fact, the one-body density matrix in momentum space is, in general, not diagonal. Because of the trap, the ODLRO is zero. The condensate fraction is, however, not necessarily zero. To obtain the condensate fraction of inhomogeneous systems, one needs to diagonalize the one-body density matrix. In general, this is much more challenging than considering the  $|\mathbf{r} - \mathbf{r}'| \rightarrow \infty$  limit.

As we discuss now, the low temperature behavior of fermions is very different from that of bosons. Because of the Pauli exclusion principle, two identical fermions cannot occupy the same state. It follows immediately that identical fermions cannot, at least not in the traditional sense (see below), form a condensate. However, when fermions are brought to low enough temperature, the de Broglie wave length  $\lambda$  can be much larger than the interparticle spacing. As in the boson case, this is the regime where the quantum statistics plays a dominant role. Fermionic matter for which  $\lambda \gtrsim \bar{r}$  is termed degenerate Fermi gas (DFG). For a single-component Fermi gas (assuming that spin flips are absent), two identical fermions cannot occupy the same position. Thus, two-body  $s$ -wave contact interactions have no impact on the system’s wave function. The simplest interaction that a single-component Fermi gas “feels” is a  $p$ -wave interaction; while interesting,  $p$ -wave interactions will not be discussed in this thesis. To realize  $s$ -wave interactions, one needs at least two components (again, assuming that spin flips are absent).

Let us consider a two-component Fermi gas with interspecies  $s$ -wave interactions [32]. For small and positive scattering length, two fermions in different hyperfine states can form a dimer whose size is much smaller than the interparticle spacing. The dimer can thus be treated as a composite boson. The dimers can undergo a transition to BEC, much like bosons in a Bose gas. For small and negative scattering length, two fermions in different hyperfine states do not form a weakly-bound state. Nevertheless, the two-body density matrix shows non-vanishing ODLRO at sufficiently low temperature. Note, the one-body density matrix does not show a non-vanishing ODLRO, indicating that the condensation observed is associated with the formation of Cooper pairs [30, 32]. In both the  $a_s < 0$  and  $a_s > 0$  cases, the two-component gas is superfluid at sufficiently low temperature.

The first experimental realization of atomic BECs and DFGs was achieved using bosonic  $^{87}\text{Rb}$  in 1995 [33] and using fermionic  $^{40}\text{K}$  in 1999 [34], respectively. The typical interparticle spacings for the  $^{87}\text{Rb}$  atoms in the BEC were  $\bar{r} \approx 14,000a_0$  and those for the  $^{40}\text{K}$  atoms in the DFG were  $\bar{r} \approx 2,000a_0$ . Similar to the metastable helium gas experiments discussed above, these average interparticle spacings are much larger than the van der Waals lengths,  $r_{\text{vdW}} \approx 82.58a_0$  and  $64.9a_0$  for  $^{87}\text{Rb}$  and  $^{40}\text{K}$ , respectively. Because of this separation of scales, the interactions in ultracold atom experiments can typically be simulated by zero-range potentials. In the low energy limit, the interaction potential is characterized by the  $s$ -wave scattering length  $a_s$  [35],

$$a_s = -\lim_{k \rightarrow 0} \frac{\tan(\delta_s(k))}{k}, \quad (1.4)$$

where  $\delta_s(k)$  is the  $s$ -wave phase shift. Here and in the following, we assume that the  $p$ -wave interactions and higher partial wave interactions are negligibly small. It follows that many, though not all, properties of cold atom gases are governed by the  $s$ -wave scattering length.

To introduce the concept of the zero-range potential, we consider the two-body problem in free space. We assume that the two particles interact through a spherically symmetric

interaction potential  $V(r)$  that falls off faster than  $1/r^3$  at large interparticle distance  $r$ . Both finite-range and zero-range potentials will be considered. We perform a partial wave decomposition and focus on the  $s$ -wave channel. The relative scaled radial Hamiltonian  $H_r$  for the  $s$ -wave channel reads

$$H_r = \frac{-\hbar^2}{2\mu_m} \frac{\partial^2}{\partial r^2} + V(r), \quad (1.5)$$

where  $\mu_m$  is the reduced two-body mass. The solution for a given  $k$ , where  $k = \sqrt{2\mu_m E}/\hbar^2$  and  $E$  is the energy, is denoted by  $u_k(r)$ . Since the interaction potential is assumed to be short-ranged, the asymptotic behavior of  $u_k(r)$  at large  $r$  is determined by the kinetic energy term. It can be written as  $u_k^{\text{asym}}(r) = A \sin(kr + \delta_s(k))$ , where  $A$  is a constant. By matching  $u_k^{\text{asym}}(r)$  and  $u_k(r)$  at large  $r$  (i.e., in the regime where the potential can be neglected), we determine the energy-dependent phase shift  $\delta_s(k)$  for arbitrary  $k$ . Taking the  $k \rightarrow 0$  limit [see Eq. (1.4)], we obtain the  $s$ -wave scattering length  $a_s$ .

As an example, we consider two particles interacting through a finite-range Gaussian potential  $V_g(r)$  with range  $r_0$  and depth  $d$ ,

$$V_g(r) = -\frac{\hbar^2 d}{2\mu_m r_0^2} e^{-\frac{r^2}{2r_0^2}}. \quad (1.6)$$

Depending on the value of  $d$  (assuming  $r_0$  and  $\mu_m$  are fixed), the potential supports 0, 1, 2, ... bound states. The thick lines in Fig. 1.2 show the interaction potential for three different depths  $d$  as a function of  $r/r_0$ . We numerically solve the scaled radial Schrödinger equation for the zero-momentum scattering state  $u_0(r)$ . The thin lines in Fig. 1.2 show the result. In the zero  $k$  limit, the asymptotic wave function can be simplified, using Eq. (1.4), to  $A(r - a_s)$ . The scattering lengths for the above potentials can be read off from the intersection of the asymptotic large  $r$  behavior with the  $x$ -axis. The  $s$ -wave scattering lengths corresponding to the potentials with  $d = 0.8, 1.342$ , and  $1.7$  are negative, infinite, and positive, respectively.

In the low-energy limit, the interaction potential  $V(r)$  can be characterized by the  $s$ -wave

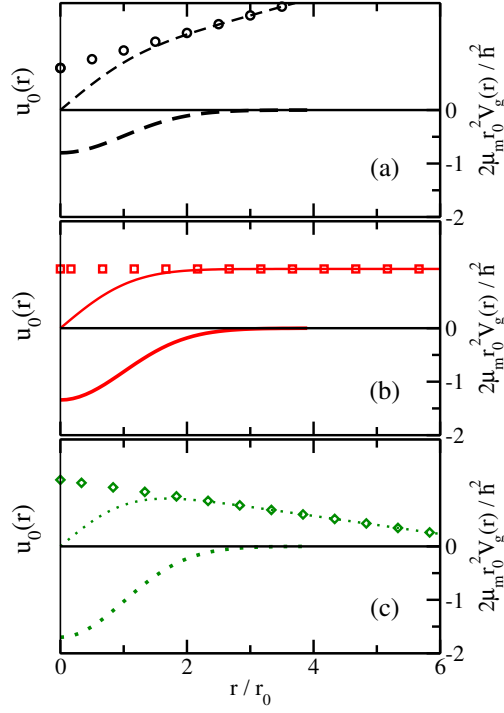


Figure 1.2: Illustration of the zero-momentum scattering solutions for finite-range and zero-range interaction potentials. The thick dashed, solid, and dotted lines in panels (a), (b), and (c) show the Gaussian interaction potential  $V_g(r)$  with  $d = 0.8, 1.342,$  and  $1.7,$  respectively. The thin dashed, solid, and dotted lines in panels (a), (b), and (c) show the corresponding unnormalized zero-momentum scattering solutions  $u_0(r)$ . The circles, squares, and diamonds in panels (a), (b), and (c) show the zero-momentum solution for the zero-range potentials with the scattering length adjusted to be the same as those for the Gaussian potentials. Note, the zero-momentum solutions for the zero-range potential and the Gaussian potential coincide at large  $r$ .

scattering length. For many purposes, the true interaction potential can be replaced by the zero-range pseudo potential  $2\pi \frac{\hbar^2}{\mu_m} a_s \delta(\mathbf{r}) \frac{\partial}{\partial r} r$  [3]. The two-body Schrödinger equation for this zero-range potential can be solved analytically. In free space, there exists no bound state when  $a_s < 0$ , a zero-energy bound state when  $a_s = \infty$ , and a single bound state when  $a_s > 0$ . The zero-momentum scattering solution reads  $A(r - a_s)$ , which is identical to the asymptotic behavior of the scattering wave function for a finite-range potential with the same  $s$ -wave scattering length. Instead of accumulating the phase shift up to a few times of  $r_0$  —as is the case for a finite-range potential—, all the phase shift is, for the zero-range potential, accumulated at  $r = 0$ , i.e., the asymptotic behavior extends to  $r = 0$ . The circles, squares, and diamonds in Fig. 1.2 show the zero-momentum wave functions for the zero-range potential for the same three scattering lengths as those for the Gaussian potential. In the regime  $r \lesssim r_0$ , the wave functions for the zero- and finite-range potentials differ. This short-range regime corresponds to “high-energy physics”. In the regime  $r \gtrsim r_0$ , the wave functions for the finite-range potential are reproduced accurately by the wave functions for the zero-range pseudo potential. It is this large- $r$  behavior of the two-body wave function that determines, at least in a zeroth-order approximation, a number of characteristics of ultracold gases. For the zero-range pseudo potential to provide a faithful description, all length scales, including the interparticle spacing and the de Broglie wave length, must be much larger than the range of the true interaction potential.

The only length scale provided by the zero-range potential is the  $s$ -wave scattering length  $a_s$ . When  $a_s$  equals zero or diverges, there is no length scale associated with the two-body interaction potential. In the absence of external forces, this means that the system is scale invariant. A scale invariant Hamiltonian gives rise to scale invariant solutions, that is, an eigen state can be scaled arbitrarily and still satisfy the Schrödinger equation. Scale invariance is a powerful concept that has found applications in many areas of physics, including the study of phase transitions [36] and fractals [37]. In cold atom physics, scale invariance in

an essential ingredient for understanding anomalies of two-dimensional systems [38–40] and Efimov physics in three spatial dimensions [41].

To introduce the concept of scale invariance, we consider a single particle in one dimension in free space. The Hamiltonian is scale invariant because no length scale is provided. It follows that the corresponding eigen states are also scale invariant. We now prove this. Let the wave function  $\psi(x)$  be an eigen state of the Hamiltonian  $H(x)$ ,

$$H(x) = -\frac{\hbar^2}{2m} \frac{\partial^2}{\partial x^2}, \quad (1.7)$$

with eigen energy  $E$ , i.e.,

$$H(x)\psi(x) = E\psi(x). \quad (1.8)$$

Replacing  $x$  by  $\lambda_s x$  in Eqs. (1.8) and (1.7), we have

$$H(\lambda_s x)\psi(\lambda_s x) = E\psi(\lambda_s x) \quad (1.9)$$

and

$$H(\lambda_s x) = \lambda_s^{-2} H(x); \quad (1.10)$$

here  $\lambda_s$  is an arbitrary scaling factor. Substituting  $H(\lambda_s x)$ , Eq. (1.10), into Eq. (1.9), we have

$$H(x)\psi(\lambda_s x) = E\lambda_s^2\psi(\lambda_s x). \quad (1.11)$$

This means that if  $\psi(x)$  is an eigen state of  $H$  with eigen energy  $E$ , then  $\psi(\lambda_s x)$  is also an eigen state of  $H$  with eigen energy  $E\lambda_s^2$ .

Non-interacting scale invariant systems are simple and solutions can be found in textbooks [42]. Non-trivial scale invariant systems are provided by three-dimensional Bose and Fermi gases with zero-range interactions and infinite  $a_s$  (i.e., at unitarity). The unitary Bose gas turns out to be unstable due to the Thomas collapse [43], which will be discussed in more

detail later. The unitary Fermi gas, in contrast, is stable since the Pauli exclusion principle plays the role of a repulsive force that prevents the system from collapsing. Homogeneous ultracold Fermi gases at unitarity thus provide an ideal experimentally realizable system with which to explore the implications of scale invariance.

An important aspect of ultracold atoms is that the  $s$ -wave scattering length, in many cases, can be tuned via a Feshbach resonance [4]. This allows one to realize the scale invariant regimes discussed above. In addition, the use of Feshbach resonances allows one to explore the entire regime of interaction strengths, from weakly-interacting to strongly-interacting, both effectively repulsive and effectively attractive. For broad  $s$ -wave Feshbach resonances, a single-channel model describes the physics very well and many aspects of ultracold gases have been explained using single-channel zero-range models. Zero-range interactions have also been used to model nuclear [44, 45], atomic and atom-laser interactions [46–48].

Tan’s contact plays a central role in systems with zero-range interactions [49–51]. Observables such as energies, radio-frequency spectra, and pair and momentum distributions are related through one single quantity, i.e., the contact (for short-range potentials, Tan’s relations still hold approximately). The contact has been measured experimentally [52–56] and calculated theoretically [57–67] for various cold atom systems. Recently, the concept of the contact has been generalized to nuclei [68, 69].

The BECs and DFGs routinely generated in experiments typically consist of tens of thousands of atoms, i.e., they are many-body systems. Despite of the large number of atoms in these systems, a good number of properties are determined by the interactions of just two or three particles. Intuitively, this can be understood by realizing that typical BECs and DFGs are very dilute, implying that the likelihood of finding more than a few particles within another particle’s interaction range is very small. In the following, we discuss a number of examples that highlight the connections between few-body and many-body physics from different perspectives. In addition, we discuss a number of few-body phenomena that can

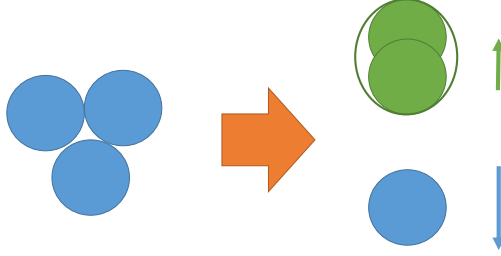


Figure 1.3: Illustration of a three-body recombination process.

be studied using cold atoms.

*Atom losses in and stability of Bose and Fermi gases:* As already mentioned, the unitary Bose gas is unstable while the unitary Fermi gas is stable. This unstable versus stable behavior is due to the different behavior of the respective three-body systems. In ultracold atomic experiments, atoms leave the trap if they have too much energy or if they form dimers, trimers, ... that are not trapped. The formation of a bound dimer requires the presence of a third atom. Two particles cannot form a bound dimer in the absence of a third particle, since the binding energy gained has to be turned into kinetic energy. Without a third particle, this would violate momentum conservation. Thus, the main loss mechanism is three-body recombination (see Fig. 1.3). For three bosons, e.g., two form a bound dimer, the dimer and the third particle carry the same kinetic energy, and fly out of the trap in opposite directions. Intuitively, the three-body loss rate increases as  $|a_s|$  increases. It is found that the three-body loss rate scales as  $|a_s|^4$  [70]. The many-boson system suffers from three-body losses if  $|a_s|$  is large, rendering it challenging to create degenerate unitary Bose gases in thermal equilibrium. For equal-mass two-component Fermi gas, the situation is different due to the Pauli exclusion principle. In this case, three fermions cannot occupy the same spatial position, suppressing three-body losses. It is found that the three-body loss rate scales as  $a_s^6$  for  $a_s > 0$  and  $|a_s|^{2.455}$  for  $a_s < 0$  [71, 72]. As a result, the atom loss is such that large samples of fermionic atoms in two spin states can be created. A question that occupied researches for quite a while is then whether the fermionic atoms undergo a Bosenova-like collapse or form a stable gas. It is now understood that two-component Fermi

gas at unitarity are stable [32, 73]. Multi-component Fermi gas, in contrast, have been predicted to undergo a Bosenova-type collapse [74].

*Three-body Efimov effect:* For two-body zero-range potentials, the three-body problem has been solved using the hyperspherical coordinate approach [41, 75, 76], which divides the coordinates into 5 hyperangles and 1 hyperradius  $R$ . The hyperangular and hyperradial degrees of freedom separate for  $a_s = 0$  and  $a_s = \infty$ . In these two cases, the hyperradial Hamiltonian  $H_R$  reads

$$H_R = \frac{-\hbar^2}{2m_R} \frac{\partial^2}{\partial R^2} + \frac{\hbar^2(s_0^2 - 1/4)}{2m_R R^2}, \quad (1.12)$$

where  $m_R$  is a conveniently chosen mass scale and  $s_0$  is the eigen value of the differential equations for the hyperangles. Replacing  $R$  by  $\lambda_s R$ , one finds that  $H_R(\lambda_s R) = \lambda_s^{-2} H_R$ . This means, following our earlier discussion, that  $H_R$  is scale invariant. Because  $\lambda_s$  can take any value, the scale invariance is continuous. For three identical bosons,  $s_0$  is approximately equal to the imaginary number  $1.006i$ . This means that the  $1/R^2$  attraction is so strong that the Hamiltonian  $H_R$  supports bound states with infinitely negative eigen energy. This, in turn, means that the energy spectrum is not bounded from below, which is unphysical. A short-range three-body regulator in the hyperradius is needed to prevent the formation of bound states with infinitely negative energies and to set the scale of the energy spectrum. In ultracold atomic systems, the three-body regulator is effectively implemented by the two-body van der Waals length [77, 78]. The van der Waals length sets a short-range length scale and cuts off the three-body energy spectrum. The short-range regulator breaks the continuous scale invariance at unitarity. If a zero-range boundary condition in the hyperradius is used as the short-range three-body regulator, then the three-body system possesses a discrete scale invariance. That is, to satisfy the zero-range boundary condition, the scaling factor  $\lambda_s$  can only take specific values. The binding momenta  $\kappa$  of the bound states form an infinite geometric series. The ratios between two binding momenta corresponding to two consecutive states is around 22.7. It can be shown [41] that, even though the scale invari-

ance is broken for finite  $a_s$ , the energy spectrum as a function of  $1/a_s$  is fully determined by the  $s$ -wave scattering length and the three-body parameter introduced by the zero-range boundary condition in the hyperradius. Specifically, the spectrum follows Efimov's radial scaling law [41].

Three bosons with negative  $a_s$  can form a three-body bound state even though the two-body subsystems are not bound. This is frequently depicted symbolically by three Borromean rings. The scattering lengths at which the zero-energy three-body bound states appear are denoted by  $a_-$ . The  $a_-$  also form a geometric series, with the ratio between consecutive  $a_-$  being 22.7, i.e., the same as the binding momentum ratios at unitarity. When the scattering length is equal to  $a_-$ , three free atoms with zero kinetic energy can couple to the zero-energy Efimov trimer, which opens up a rapid decay path into deeply bound dimer states [79]. Thus the three-body loss is resonantly enhanced. This enhanced three-body loss has been observed in ultracold atomic gas experiments. In fact, the measurement of the scattering lengths at which enhanced losses occur on the negative scattering length side is the first experimental evidence of the existence of Efimov trimer states [80].

*Extended Efimov scenario:* No true Efimov effect exists for four or more bosonic particles [81]. That is, there exists no infinite series of  $N$ -body bound states in the vicinity of a scattering length at which a zero-energy  $(N - 1)$ -body bound state exists. Nevertheless, the three-body Efimov scenario has been generalized to more than three particles. The  $N$ -body bound states have been found to be universal and fully determined by three-body physics, i.e, a four-body parameter is found to be unnecessary [41, 82, 83]. Two four-body states are attached to each Efimov trimer with fixed ratio of energies. Specifically, for each  $a_-$  in the three-body energy spectrum, there exist two scattering lengths at which four-body bound states emerge. At these scattering lengths, the loss rates are enhanced. The experimentally determined four-body loss enhancement positions [84] agree with the results from numerical four-body calculations [85]. Similarly, one can also find  $N$ -body bound states attached to

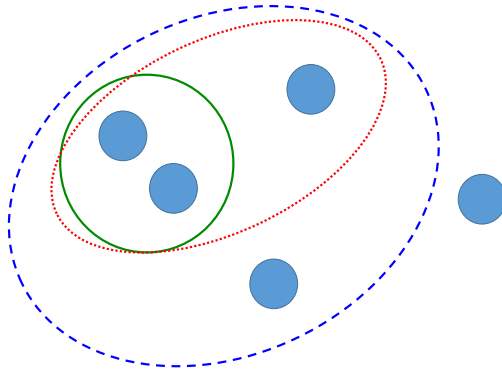


Figure 1.4: Illustration of the cluster expansion. The filled circles show the atoms in an ultracold gas. The two-body, three-body, and four-body subsystems are illustrated by solid, dotted, and dashed circles.

three-body trimer states. The measured five-body loss enhancement rate agrees qualitatively with the theoretical prediction based on five-body calculations [86]. Since five-body events are much rarer than three- and four-body events, the current experimental precision is unfortunately not good enough to determine the scattering lengths at which the five-body Borromean states occur accurately.

*Unitary Fermi gas and cluster expansion:* While the behavior of the unitary Bose gas at zero temperature depends on the three-body parameter, that of the unitary two-component Fermi gas does not. At finite temperature, the only energy scales of the unitary two-component Fermi gas are the chemical potential  $\mu$  and the thermal energy  $k_B T$ . This means that the thermodynamic properties depend only on the ratio  $\mu/(k_B T)$ .

At high temperature, the grand canonical thermodynamic potential  $\Omega$  can be expanded in terms of the fugacity  $z = \exp[-\mu/(k_B T)]$ . This approach is known as cluster expansion [87–89]. The  $n$ -th expansion coefficient, i.e., the  $n$ -th order virial coefficient  $b_n$ , can be determined by the partition functions of clusters with  $n$  or fewer particles. Figure 1.4 schematically illustrates the cluster expansion. The grand canonical thermodynamic potential  $\Omega$  at high temperature and low density can be described perturbatively through the virial coefficients even though the two-body interaction is infinitely strong. To leading order,  $\Omega$  can be approximately described by the non-interacting system. The second-order virial coef-

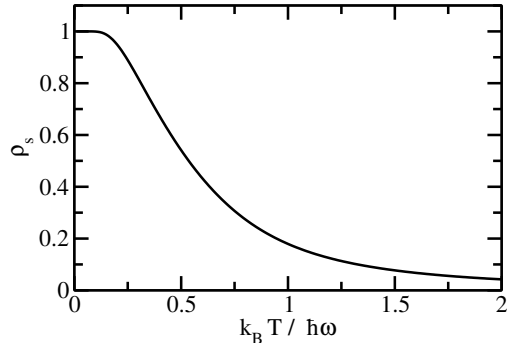


Figure 1.5: Superfluid fraction  $\rho_s$  of two identical bosons with zero-range interaction at unitarity in a harmonic trap with trapping frequency  $\omega$  as a function of the temperature  $k_B T / (\hbar \omega)$ .

ficient, calculated by studying two-body physics, gives rise to the first-order correction to  $\Omega$  (illustrated by the solid circle in Fig. 1.4). Studying  $n$ -body systems thus provides  $(n - 1)$ th order corrections. From  $\Omega$ , thermodynamic properties such as the pressure and the density can be determined. Virial coefficients, which can be calculated from the properties of few-body Hamiltonian, are thus crucial for our understanding of the many-body unitary Fermi gas in the normal phase (i.e., at temperatures above the transition temperature). Moreover, precision measurements in table-top ultracold atomic experiments can provide insights into the thermal properties of neutron stars.

*Smearred out phase transitions:* Phase transitions exist, strictly speaking, only in the thermodynamic limit, i.e., in the infinite number of particles limit. Sharp phase transitions do not exist in few-body systems. Instead, observables change smoothly with the temperature. Often times, though, finite- $N$  systems exhibit remnants of phase transitions, so-called smeared out phase transitions. Figure 1.5 illustrates a smeared out phase transition. The solid line shows the superfluid fraction  $\rho_s$  of two bosons with zero-range interaction at unitarity in a harmonic trap with trapping frequency  $\omega$  as a function of the temperature  $k_B T / (\hbar \omega)$ . Unlike the superfluid fraction for bulk helium (see Fig. 1.1), the superfluid fraction of the two-boson system varies smoothly as a function of the temperature. By studying the dependence on the number of particles, few-body results can provide estimates of the transition temperature

and insights into the nature of the phase transition of the corresponding many-body system.

As will hopefully become clear throughout this thesis, few-body systems are also interesting in their own right. Experimentally, few-body systems in one dimension have been prepared with high fidelity [90–93]. Few-body systems are also interesting with a view point towards applications. For example, carefully designed few-body systems have the potential to serve as a platform for quantum computing.

The continuous-space path integral Monte Carlo (PIMC) algorithm has been widely used to determine thermodynamic properties of bulk helium [19], pristine and doped droplets [94, 95], nanotubes [96], and other systems. The PIMC technique is capable of treating the canonical ensemble of particles with Bose or Fermi statistics. The canonical ensemble implies finite temperature and fixed number of particles. Thus, the PIMC technique can bridge our understanding of the quantum behavior at zero temperature and the classical behavior at high temperature. One of the strengths of the PIMC algorithm is that it can be used to treat few-body systems and many-body systems, therefore providing a consistent framework for studying the transition between the two. The PIMC approach can treat bosonic systems with large number of particles because the complexity scales polynomially with the number of particles [19]. For fermions, in contrast, the applicability of the PIMC approach is complicated by the Fermi sign problem [97–99]. The complexity for fermionic systems scales at least exponentially with the number of particles. Other close variants of the PIMC technique used in this work include the path integral ground state approach (PIGS) [100, 101], which treat systems at zero temperature, and the path integral Monte Carlo worm algorithm, which can treat the canonical and grand canonical ensemble [102].

The PIMC technique has not been applied very much to cold atom systems, even though other variants of Monte Carlo methods [103] such as continuous-time lattice Monte Carlo [104], diagrammatic Monte Carlo [105, 106], and diffusion Monte Carlo [32, 107] have been applied fairly extensively. Continuous-space PIMC studies of cold atom systems are

challenging because of the short-range nature of the atom-atom interaction. The algorithm has to discretize the imaginary time so fine that both the interaction potential and the physics that occurs on the trap scale can be resolved. To realize large  $s$ -wave scattering lengths using two-body short-range interactions, one must consider length scales that are largely separated, which complicates the problem. A possible way around this is the use of zero-range interactions. In three spatial dimensions, the  $\delta$ -function potential introduces a singularity, which prohibits the “direct” use of this type of potential in position space implementations. As discussed in Chapter 6, this problem can be solved by using the zero-range propagator, which incorporates the potential directly.

This thesis used the PIMC approach to investigate both zero and finite temperature properties of few-body systems. We determined the energy, contact, pair distribution function, superfluid and condensate fractions, and other properties as a function of the temperature for various systems and elucidated the role of the particle statistics. A negative superfluid fraction for imbalanced few-fermion systems at low temperature was found for certain scattering lengths. A scheme to incorporate zero-range interactions into PIMC simulations was developed. Using this scheme, we treated the unitary Bose gas with two-body zero-range interactions and three-body repulsive interactions. The energy and the structural properties of the  $N$ -boson ground states were determined. The structural properties for various  $N$  were found to be linked universally if a scaling that uses the  $N$ -body energy was employed. We also treated four fermions at unitarity and determined the fourth-order virial coefficient. Ours is the first numerical calculation that agrees with experimental results.

The remainder of this thesis is organized as follows. Chapter 2 introduces the PIMC algorithm and illustrates its workings through example applications to ultracold few-atom systems. During the course of my Ph.D., I developed the PIMC code used to generate the PIMC results presented in Chapters 3-8 from scratch. The code was parallelized so that it could be run on computer clusters. Chapter 2 introduces some of the basic ideas behind

the PIMC algorithm, which samples the partition function of the system of interest. Several approximations to the partition function are introduced. The “moves” utilized to sample the partition function are explained. “Estimators” for the energy, structural distribution functions, and the superfluid fraction are discussed.

Chapter 3 contains the manuscript that has been published in Physical Review A [“Harmonically trapped Fermi gas: Temperature dependence of the Tan contact”, Y. Yan and D. Blume, Phys. Rev. A **88**, 023616 (2013)]. This chapter considers trapped unitary two-component Fermi gases with short-range interactions. We employ the PIMC and explicitly correlated Gaussian (ECG) algorithms. The Tan contact is determined for up to four particles as a function of temperature. A cluster expansion for the few-body system that provides an accurate description of the Tan contact in the high temperature regime is developed. In this work, I performed the PIMC calculations and Blume performed the ECG calculations. Both Yan and Blume contributed to the writing of the first draft of the manuscript.

Chapter 4 contains the manuscript that has been published in Physical Review Letters [“Abnormal Superfluid Fraction of Harmonically Trapped Few-Fermion Systems”, Y. Yan and D. Blume, Phys. Rev. Lett. **112**, 235301 (2014)]. We consider a trapped two-component Fermi gas and determine the superfluid fraction and density for up to four fermions as a function of the temperature and scattering length. We find a negative superfluid fraction and density for certain parameter combinations. The calculations for systems with up to three particles are performed using zero-range interactions and by explicitly summing over all eigen states. The results for the four-body system are obtained using the PIMC approach at high temperature and the ECG approach at low temperature. In this work, I performed the PIMC calculations, analyzed all the raw data, and wrote the first draft of the manuscript. Blume performed the ECG calculation.

Chapter 5 contains the manuscript that has been published in Physical Review A [“Temperature dependence of small harmonically trapped atom systems with Bose, Fermi, and

Boltzmann statistics”, Y. Yan and D. Blume, Phys. Rev. A **90**, 013620 (2014)]. One focus of this paper is on a comparative study of systems with different particle statistics. We determine the condensate fraction, superfluid fraction and superfluid density as a function of the temperature and scattering length for two atoms with zero-range interaction. We present the energies, structural properties, and superfluid fraction as a function of the temperature for trapped particles with Bose and Fermi statistics interacting via short-range potentials. The role of the particle statistics is analyzed carefully. Finally, we study the trapped  $N$ -boson system with Gaussian interactions and introduce a simple model that describes the transition from the ground liquid-like state to the “gas-like” state. In this work, Blume provided the ECG energies. I performed all other calculations, analyzed all the results, and wrote the first draft of the manuscript.

Chapter 6 contains the manuscript that has been published in Physical Review A [“Incorporating exact two-body propagators for zero-range interactions into  $N$ -body Monte Carlo simulations”, Y. Yan and D. Blume, Phys. Rev. A **91**, 043607 (2015)]. We develop a general scheme to incorporate zero-range interactions into PIMC simulations and provide several benchmark tests. In this work, I performed all the calculations and wrote the first draft of the manuscript.

Chapter 7 contains the manuscript that has been published in Physical Review A [“Energy and structural properties of  $N$ -boson clusters attached to three-body Efimov states: Two-body zero-range interactions and the role of the three-body regulator”, Y. Yan and D. Blume, Phys. Rev. A **92**, 033626 (2015)]. Using the scheme developed in Chapter 6, we study the energy and structural properties of the ground state of  $N$ -boson clusters with two-body zero-range interactions and three-body repulsive interactions. The  $N$ -body energy is found to be not universally (at least not fully) determined by the three-body parameter. Instead, we find that the structural properties can be linked universally if a scaling that uses the  $N$ -body energy was employed. For comparison, we consider systems with two-body van

der Waals interactions without a three-body regulator. The ground state of the  $N$ -body clusters is found to be fairly universal for the interactions considered. In this work, Blume performed the calculation for the systems with van der Waals interactions. I performed all other calculations and wrote the first draft of the manuscript.

Chapter 8 contains the manuscript entitled “Path integral Monte Carlo determination of the fourth-order virial coefficient for unitary two-component Fermi gas with zero-range interactions” (Y. Yan and D. Blume, arXiv:1602.02328). Using the zero-range propagator developed in Chapter 6 together with an “on-the-fly antisymmetrization” scheme, we develop a general PIMC framework for treating fermions with zero-range interactions. Utilizing this customized PIMC approach, we study the unitary four-fermion system. Specifically, we determine the fourth-order virial coefficient. In this work, I performed all the calculations and wrote the first draft of the manuscript.

Finally, Chapter 9 concludes and provides an outlook.

# Chapter 2

## Path integral Monte Carlo method

### 2.1 Introduction

This chapter discusses the path integral Monte Carlo (PIMC) method [19]. The PIMC approach is a finite temperature method that can connect classical statistical mechanics, which considers point-like particles in thermal equilibrium, and quantum mechanics, which considers zero-temperature wave functions. It is an *ab initio* method, which, in principle, does not employ approximations. The PIMC method can be used to calculate many thermodynamic properties of systems with bosonic, fermionic or mixed particle statistics. The concept of path integrals goes back to Richard Feynman, who successfully used them to interpret the wave nature of particles and to explain the double-slit experiment [108]. The path integral formalism provides an alternative to the Schrödinger equation and connects classical and quantum mechanics in an intuitive manner. Since most readers are familiar with the Schrödinger equation, we base our derivations on the Schrödinger equation and statistical mechanics.

Since the PIMC approach is based on stochastic sampling, the statistical error of observables calculated by the PIMC approach can be controlled by adjusting the length of the simulation. To achieve small statistical error bars for “complicated” systems, e.g., strongly

correlated systems, long simulation times are oftentimes needed. One advantage of Monte Carlo techniques is that simultaneous simulations can be run on separate computers with essentially no communication. In parallel computing, this feature is known as “embarrassingly parallel” or “perfectly parallel”. As a result, different models of parallel computing such as MapReduce (divide the work in a predefined manner to different “workers” and combine at the end) and Scatter/Gather (one “master” continuously distributes work to “slaves”) can be applied on a variety of architectures of computer resources, including clusters (equally fast computers on the same network) and distributed computing resources (computers with varying speed on different networks). The simulations presented in this thesis were mainly run on computer clusters. We use the model of MapReduce and, specifically, primarily the Reduce function defined in Message Passing Interface.

The remainder of the chapter is organized as follows. Section 2.2 discusses the general scheme of the PIMC approach. Section 2.3 discusses approximations to the partition function, which plays a key role in PIMC simulations. Section 2.4 discusses how to deal with the exchange statistics if identical particles are present. Section 2.5 lists a number of methods to sample the partition function. Last, Sec. 2.6 discusses selected estimators that are used to extract thermodynamic properties from the sampled paths.

## 2.2 General scheme

We consider  $N$  interacting particles under external confinement described by the Hamiltonian  $\hat{H}$  at finite temperature  $T$ . We define the “inverse temperature”  $\beta$ ,  $\beta = 1/(k_B T)$ , which has the unit of inverse energy. We work in position space, where the interaction potential and external potentials are local (i.e., potentials that only depend on the position vectors and not on the momentum vectors as would be the case if spin-orbit coupling terms were present). The kinetic energy, however, is non-local (see below). The position vector for the  $j$ -th particle is denoted by  $\mathbf{r}_j$  and we collectively denote the positions of all the particles by  $\mathbf{R}$ ,

$\mathbf{R} = \{\mathbf{r}_1, \mathbf{r}_2, \dots, \mathbf{r}_N\}$ . A key quantity that describes the system under study at temperature  $T$  is the density matrix operator  $\hat{\rho}$ ,  $\hat{\rho} = \exp(-\beta\hat{H})$  [87]. In position space, the density matrix operator reads

$$\rho(\mathbf{R}, \mathbf{R}'; \beta) = \langle \mathbf{R} | \exp(-\beta\hat{H}) | \mathbf{R}' \rangle. \quad (2.1)$$

We refer to the representation of the density matrix operator in position space as density matrix. The diagonal term  $\rho(\mathbf{R}, \mathbf{R}; \beta)$  of the density matrix gives the non-normalized probability to find the particles in  $3N$ -dimensional space, i.e., at  $\mathbf{R}$ . The off-diagonal terms  $\rho(\mathbf{R}, \mathbf{R}'; \beta)$  with  $\mathbf{R} \neq \mathbf{R}'$  give the coherences, i.e., higher-order spatial correlations of the system. Intuitively, if the Hamiltonian contains only simple  $\mathbf{R}$ -dependent potential terms  $V(\mathbf{R})$  and no kinetic energy terms, then the density matrix in position space will be diagonal because the position vector  $\mathbf{R}$  commutes with the Hamiltonian,

$$\langle \mathbf{R} | \exp(-\beta\hat{V}) | \mathbf{R}' \rangle = \exp(-\beta V(\mathbf{R})) \delta(\mathbf{R} - \mathbf{R}'). \quad (2.2)$$

Thus, the off-diagonal terms are introduced by the kinetic energy; for now, we exclude the possibility of zero-range interactions, which cannot be expressed as a simple function of  $\mathbf{R}$ . Using Schrödinger quantum mechanics, the density matrix can be obtained by inserting the identity

$$\sum_n |\psi_n\rangle \langle \psi_n| = \hat{1}, \quad (2.3)$$

where  $\{\psi_1, \psi_2, \dots\}$  is a complete set of eigen states of the Hamiltonian  $\hat{H}$  and  $\hat{1}$  the unit operator, into Eq. (2.1),

$$\rho(\mathbf{R}, \mathbf{R}'; \beta) = \sum_n \psi_n^*(\mathbf{R}) \exp(-\beta E_n) \psi_n(\mathbf{R}'), \quad (2.4)$$

where  $E_n$  is the eigen energy associated with state  $\psi_n$ .

The trace of the density matrix operator gives the partition function  $Z$  [87],

$$Z = \text{Tr} \exp(-\beta \hat{H}) = \int_{\mathbf{R}} \rho(\mathbf{R}, \mathbf{R}; \beta) d\mathbf{R}, \quad (2.5)$$

where the integration goes over all  $3N$  Cartesian coordinates. The partition function is a key quantity in many thermodynamic relations. For example, the thermodynamic expectation value of the Hamiltonian  $\hat{H}$ , the energy  $E$ , can be written as [19]

$$\langle E \rangle = -\frac{\partial \ln Z}{\partial \beta} = -Z^{-1} \frac{\partial Z}{\partial \beta} \quad (2.6)$$

and the heat capacity  $C_v$  is defined through [19]

$$C_v = \frac{\partial \langle E \rangle}{\partial T} = \frac{1}{k_B T^2} \frac{\partial^2 \ln Z}{\partial \beta^2}. \quad (2.7)$$

Since Eqs. (2.6) and (2.7) are derived from thermodynamic relations, they are referred to as thermodynamic estimator relations. Moreover, the partition function  $Z$  serves as a normalization constant, i.e., the probability to find the system in state  $\psi_n$  is given by  $\exp(-\beta E_n)/Z$ . Using  $Z$  as a normalization constant, the thermal expectation value for a general operator  $\hat{\mathcal{O}}$  can be written as [87]

$$\langle \mathcal{O} \rangle = \frac{\text{Tr}(e^{-\beta \hat{H}} \hat{\mathcal{O}})}{Z}. \quad (2.8)$$

Since this is derived from quantum mechanics, we refer to Eq. (2.8) as quantum estimator relation.

In PIMC simulations, one samples the density matrix and extracts observables either through thermodynamic estimator relations [such as those given in Eqs. (2.6) and (2.7)] or through quantum estimator relations [Eq. (2.8)]. In practice, the problem is two-fold: (i) In general, we do not know the density matrix and we have to develop an approximate expression that has a controlled accuracy. (ii) We have to come up with an efficient scheme

to sample the density matrix, i.e., to visit different configurations with a probability that is proportional to the density matrix. Aspects (i) and (ii) will be addressed in Secs. 2.3 and 2.5, respectively.

One might wonder why we choose to work with the inverse temperature  $\beta$  instead of the temperature  $T$  in our discussion above. The answer is two-fold. i) The density matrix operator  $\hat{\rho}$ ,  $\hat{\rho} = \exp(-\beta\hat{H})$ , can be Taylor expanded around  $\beta = 0$ , i.e.,  $\beta$  can be treated as a small parameter. This suggests that one might be able to obtain an approximate, yet accurate, description of the density matrix at small  $\beta$  or large temperature. Indeed, different schemes to approximate the high-temperature density matrix will be discussed in Sec. 2.3. ii) The inverse temperature allows one to formally connect statistical mechanics and quantum mechanical time evolution. The density matrix operator  $\exp(-\beta\hat{H})$  is formally identical to the time evolution propagator  $\exp(-it\hat{H}/\hbar)$  if the inverse temperature  $\beta$  is replaced by  $it/\hbar$ . Real time propagation can be interpreted as particles following different paths, with the phase adding up either constructively or destructively. In imaginary time propagation, particles also follow different paths but with the probability being determined by the Boltzmann factor. Thus, we often refer to the inverse temperature as imaginary time and to the density matrix operator as imaginary time propagator.

It is worth mentioning that if we propagate an arbitrary initial wave packet (which has finite overlap with the ground state wave function) to infinite imaginary time, it will lose energy and, assuming the absence of degeneracies, eventually decay to the ground state of  $\hat{H}$ . This imaginary time propagation scheme is the key idea behind the DMC [107] and PIGS algorithms [100]. In PIMC simulations, in contrast, the propagation stops at a finite  $\beta$ , namely the temperature of physical interest.

## 2.3 Partition function and density matrix

In the infinite temperature limit, i.e., for  $\beta = 0$ ,  $\hat{\rho} = \exp(-\beta\hat{H})$  becomes the identity operator. This implies that the density matrix is simply a  $\delta$ -function in position space,

$$\rho(\mathbf{R}, \mathbf{R}'; 0) = \delta(\mathbf{R} - \mathbf{R}'). \quad (2.9)$$

To propagate to finite temperature, one can solve the Bloch equation [19]

$$\frac{\partial \hat{\rho}}{\partial \beta} = -\hat{H}\hat{\rho}, \quad (2.10)$$

which is obtained by taking the partial derivative of the density matrix operator with respect to  $\beta$ . Equation (2.10) can be interpreted as a diffusion equation in the inverse temperature  $\beta$ . If the kinetic energy operator  $\hat{K}$  is zero, the density matrix operator  $\hat{\rho} = \exp(-\beta\hat{V})$  can be readily solved for. Similarly, if the potential energy operator  $\hat{V}$  is zero, the density matrix operator can also be solved for. In this case, the solution  $\rho_0$  corresponds to free particles diffusing in space and is a product of single-particle Gaussians,

$$\rho_0(\mathbf{R}, \mathbf{R}'; \beta) = (4\pi\lambda_m\beta)^{-3N/2} \exp\left(-\frac{(\mathbf{R} - \mathbf{R}')^2}{4\lambda_m\beta}\right), \quad (2.11)$$

where  $\lambda_m$  is equal to  $\hbar^2/(2m)$ . Equation (2.11) shows that the off-diagonal  $\mathbf{R} \neq \mathbf{R}'$  terms of  $\rho_0$  are non-zero. This shows explicitly that the kinetic energy operator is non-local in position space. If  $\hat{V}$  and  $\hat{K}$  are both non-zero, then the density matrix at finite  $T$  is known only for a few simple problems such as non-interacting particles in a harmonic trap [20] and two particles with zero-range interactions. In general, the density matrix is not known analytically. If it were known, it would be unnecessary to perform a numerical PIMC simulation.

There exist many ways to approximate the density matrix. Most of the approaches are based on the following idea. The density matrix operator at low temperature (large  $\beta$ ) can

be written as a product of density matrix operators at high temperature (small  $\beta$ ),

$$\exp(-\beta\hat{H}) = [\exp(-\beta\hat{H}/n)]^n. \quad (2.12)$$

Inserting the identity

$$\int_{\mathbf{R}} |\mathbf{R}\rangle \langle \mathbf{R}| d\mathbf{R} = \hat{1} \quad (2.13)$$

$n - 1$  times into Eq. (2.12),

$$\begin{aligned} \langle \mathbf{R}_0 | e^{-\beta\hat{H}} | \mathbf{R}_n \rangle &= \langle \mathbf{R}_0 | e^{-\beta\hat{H}/n} \underbrace{\int_{\mathbf{R}_1} |\mathbf{R}_1\rangle \langle \mathbf{R}_1| d\mathbf{R}_1}_{=\hat{1}} e^{-\beta\hat{H}/n} \underbrace{\int_{\mathbf{R}_2} |\mathbf{R}_2\rangle \langle \mathbf{R}_2| d\mathbf{R}_2}_{=\hat{1}} \times \dots \\ &\times \underbrace{\int_{\mathbf{R}_{n-1}} |\mathbf{R}_{n-1}\rangle \langle \mathbf{R}_{n-1}| d\mathbf{R}_{n-1}}_{=\hat{1}} e^{-\beta\hat{H}/n} | \mathbf{R}_n \rangle, \end{aligned} \quad (2.14)$$

we obtain

$$\begin{aligned} \rho(\mathbf{R}_0, \mathbf{R}_n; \beta) &= \int_{\mathbf{R}_1} \int_{\mathbf{R}_2} \dots \int_{\mathbf{R}_{n-1}} \rho(\mathbf{R}_0, \mathbf{R}_1; \beta/n) \rho(\mathbf{R}_1, \mathbf{R}_2; \beta/n) \times \dots \\ &\times \rho(\mathbf{R}_{n-1}, \mathbf{R}_n; \beta/n) d\mathbf{R}_1 d\mathbf{R}_2 \dots d\mathbf{R}_{n-1}. \end{aligned} \quad (2.15)$$

The problem of integrating over the density matrix at the desired temperature  $\beta$  [i.e., integrating the Bloch equation, Eq. (2.10)] has been converted to integrating over many density matrices at  $n$  times larger temperature. As  $n$  approaches infinity, the high-temperature density matrix becomes exact (since  $\hat{\rho}$  approaches the unit operator) and so does the final answer. The key point is that one can typically find a fairly accurate but approximate high-temperature density matrix for finite  $n$ , requiring  $n - 1$  “auxiliary” integrations that can be performed by Monte Carlo techniques.

Each set of coordinates  $\mathbf{R}_j$  inserted in Eq. (2.14) is referred to as a “time slice”. In addition,  $\mathbf{R}_0$  and  $\mathbf{R}_n$  are considered as two extra time slices if  $\mathbf{R}_0$  is not equal to  $\mathbf{R}_n$  and

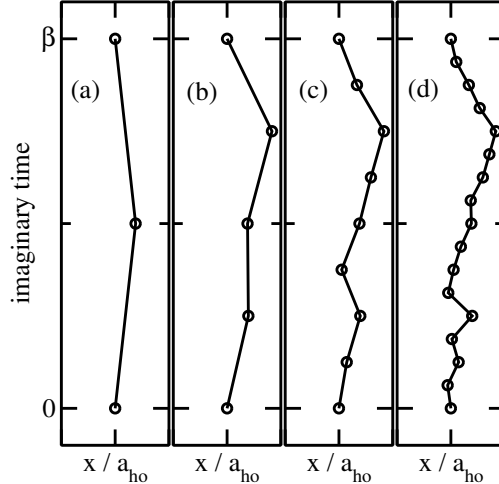


Figure 2.1: World-line representation for a single particle in a one-dimensional harmonic trap. The temperature is set to  $T = \hbar\omega/k_B$ . Panels (a), (b), (c), and (d) show paths for  $n = 2, 4, 8,$  and  $16$ , respectively.

$\mathbf{R}_0$  is considered as one extra time slice if  $\mathbf{R}_0$  is equal to  $\mathbf{R}_n$ . The position vector  $\mathbf{r}_{k,j}$  of the  $k$ -th particle in the set of coordinates  $\mathbf{R}_j$  is referred to as a “bead”. Thus, a single particle is represented by  $n$  beads if  $\mathbf{R}_0 = \mathbf{R}_n$  and by  $n + 1$  beads if  $\mathbf{R}_0 \neq \mathbf{R}_n$ . The density matrix that “connects” two consecutive time slices is referred to as a “link”. The inverse temperature corresponding to this link is  $\tau$ , where  $\tau = \beta/n$ . The density matrix that “connects” two consecutive beads is referred to as a “single-particle link”. If  $\mathbf{R}_0$  is equal to  $\mathbf{R}_n$ , the number of beads  $n$  for a single particle is equal to the number of time slices. In addition, for closed paths, the set of all time slices  $\{\mathbf{R}_0, \dots, \mathbf{R}_{n-1}\}$  is referred to as a configuration. The definitions are summarized in Table 2.1.

The determination of many observables requires the full trace of the density matrix. This implies that the zeroth time slice  $\mathbf{R}_0$  and the time slice  $\mathbf{R}_n$  have to be the same, i.e., all paths need to be closed. The conclusions (Sec. 9) contain a short discussion of open paths. The particle statistics, which will be discussed in Sec. 2.4, changes the picture of the closed paths a bit; however, even in the presence of permutations, there exist no open ends (at least not in the applications pursued in this thesis).

Figure 2.1 shows the world-line representation of a single particle in a one-dimensional

Table 2.1: Definitions of PIMC terminology used in this thesis. Columns 1-3 show the term, symbol, and explanation, respectively.

bead	$\mathbf{r}_{k,j}$	a single coordinate of the $k$ th particle at the $j$ th imaginary time index
time slice	$\mathbf{R}_j$	a set of beads at the $j$ th imaginary time index
configuration	$\{\mathbf{R}_0, \dots, \mathbf{R}_{n-1}\}$	the set of all time slices
link	$\rho(\mathbf{R}_j, \mathbf{R}_{j+1}; \tau)$	the density matrix connecting two consecutive time slices
single-particle link	$\rho(\mathbf{r}_{k,j}, \mathbf{r}_{k,j+1}; \tau)$	the density matrix connecting two beads

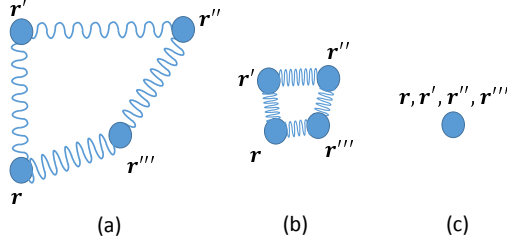


Figure 2.2: Isomorphism between path integrals for a single free particle in two-dimensional space and classical particles connected by springs. In the path integral interpretation, the circles and wiggly lines depict the beads and (single-particle) links of a single particle, respectively. Panels (a), (b), and (c) are for low, medium, and high temperatures. In the classical mechanics formulation, the circles and wiggly lines depict particles and springs, respectively.

harmonic trap. World lines move in position space ( $x$ -axis) and imaginary time ( $y$ -axis). The position vector  $\mathbf{r}_0$  of the initial bead ( $\tau = 0$ ) and the position vector  $\mathbf{r}_n$  ( $\tau = \beta$ ) are the same, as required for closed paths. Panels (a), (b), (c), and (d) show paths for  $n = 2, 4, 8,$  and  $16$  beads, respectively. As  $n$  increases, the path is resolved in more detail (each link is more accurate) and observables calculated based on the sampled paths become more accurate.

Figure 2.2 depicts a single particle (the Hamiltonian only contains the kinetic energy term) in two-dimensional space [109]. Two consecutive beads (circles in Fig. 2.2) are connected by a single-particle link (wiggly line in Fig. 2.2). The kinetic energy is “carried” by the density matrices represented by the links. The expression for the density matrix in free space reads [Eq. (2.11) for a single particle with position vector  $\mathbf{r} = (x, y)$ ]

$$\rho_0(\mathbf{r}, \mathbf{r}'; \beta) = (4\pi\lambda_m\beta)^{-1} \exp\left(-\frac{(\mathbf{r} - \mathbf{r}')^2}{4\lambda_m\beta}\right). \quad (2.16)$$

The action  $S$  [19],

$$S = -\ln[\rho_0(\mathbf{r}, \mathbf{r}'; \beta)], \quad (2.17)$$

of the single-particle link that connects the beads labeled  $\mathbf{r}$  and  $\mathbf{r}'$  reads

$$S = \ln(4\pi\lambda_m\beta) + \frac{(\mathbf{r} - \mathbf{r}')^2}{4\lambda_m\beta}. \quad (2.18)$$

It can be seen that the action  $S$  has the same form as that of a “spring potential”  $V_s(\mathbf{r}-\mathbf{r}')$  for two classical particles with position vectors  $\mathbf{r}$  and  $\mathbf{r}'$  connected via Hooke’s law. The density matrix can thus be interpreted as being proportional to the Boltzmann factor  $\exp(-\beta V_s)$  of a classical system of springs. Note that  $\mathbf{r}$  and  $\mathbf{r}'$  in Eqs. (2.16) and (2.18) correspond to position vectors of consecutive beads for one single particle while  $\mathbf{r}$  and  $\mathbf{r}'$  in the classical isomorphism correspond to position vectors of two different particles. Thus, we can interpret the PIMC simulation of a single particle at finite temperature as a simulation of a chain of classical particles connected by springs (or a polymer with nearest neighbor interactions). Figures 2.2(a), (b), and (c) are for low, medium, and high temperatures, respectively. The stiffness of the springs is determined by the temperature  $1/\tau$  of the links. The size of the path is large at low temperature, decreases with increasing temperature and approaches the point-particle limit at infinite temperature.

We now consider the opposite limit, i.e., we neglect the kinetic energy and only consider the potential energy. As discussed before, the potential energy is usually local and appears in the diagonal part of the density matrix in position space. Thus the potential energy is carried by the beads (circles in Fig. 2.2) and not by the links. In this potential-energy-only scenario, the beads are sitting at the same location for all imaginary times, i.e., Fig. 2.2(c) represents the path for a single particle in the absence of the kinetic energy term at all temperatures. Intuitively, this can be understood by realizing that the delocalization of the particles is introduced by the kinetic energy.

The following two sections introduce two different approaches for approximating the high-temperature density matrix.

### 2.3.1 Trotter formula

One way to approximate the high-temperature density matrix is to use the Trotter formula [110]. At high temperature (small  $\tau$ ,  $\tau = \beta/n$ ), the kinetic energy contribution  $\hat{K}$  and the potential energy contribution  $\hat{V}$  to the density matrix can be split,

$$\exp[-\tau(\hat{K} + \hat{V})] = \exp(-\tau\hat{K}) \exp(-\tau\hat{V}) + \mathcal{O}(\tau^2), \quad (2.19)$$

where the notation  $\mathcal{O}(\tau^2)$  indicates that the leading-order error scales, in general, as  $\tau$  to the power of 2. More specifically, by Taylor expanding the exponentials, one can prove that the leading-order error is  $\frac{1}{2}\tau^2[\hat{K}, \hat{V}]$ , where  $[\hat{K}, \hat{V}]$  is the commutator between  $\hat{K}$  and  $\hat{V}$ ,  $[\hat{K}, \hat{V}] = \hat{K}\hat{V} - \hat{V}\hat{K}$ . In the infinite  $n$  limit, the Trotter formula becomes exact,

$$\exp[-\tau(\hat{K} + \hat{V})] = \lim_{n \rightarrow \infty} [\exp(-\tau\hat{K}/n) \exp(-\tau\hat{V}/n)]^n. \quad (2.20)$$

In practice  $n$  cannot be infinitely large. Thus, we perform calculations for different  $n$  and extrapolate the observables of interest to the infinite  $n$  limit.

Importantly, the Trotter formula can be extended to higher orders. We can readily adopt a  $\mathcal{O}(\tau^3)$  scheme by further splitting the kinetic energy term or the potential energy term,

$$\exp[-\tau(\hat{K} + \hat{V})] = \exp(-\tau\hat{K}/2) \exp(-\tau\hat{V}) \exp(-\tau\hat{K}/2) + \mathcal{O}(\tau^3) \quad (2.21)$$

or

$$\exp[-\tau(\hat{K} + \hat{V})] = \exp(-\tau\hat{V}/2) \exp(-\tau\hat{K}) \exp(-\tau\hat{V}/2) + \mathcal{O}(\tau^3). \quad (2.22)$$

In practice, Eq. (2.22), which is accurate up to second order [the error is  $\mathcal{O}(\tau^3)$ ], is easier to

use than Eq. (2.21). In position space, Eq. (2.22) reads

$$\rho(\mathbf{R}, \mathbf{R}'; \tau) = \exp[-\tau V(\mathbf{R})/2] \exp[-\tau V(\mathbf{R}')/2] \rho_0(\mathbf{R}, \mathbf{R}'; \tau) + \mathcal{O}(\tau^3), \quad (2.23)$$

where  $\rho_0$  [see Eq. (2.11)] is the density matrix that accounts for the kinetic energy term.

One can reach successively higher accuracy by the repeated use of the Baker-Campbell-Hausdorff formula [111]

$$e^{\epsilon \hat{A}} e^{\epsilon \hat{B}} = e^{\hat{C}}, \quad (2.24)$$

where

$$\begin{aligned} \hat{C} = \epsilon(\hat{A} + \hat{B}) + \frac{1}{2}[\hat{A}, \hat{B}]\epsilon^2 + \frac{1}{12}([\hat{A}, [\hat{A}, \hat{B}]] + [\hat{B}, [\hat{B}, \hat{A}]])\epsilon^3 \\ - \frac{1}{24}[\hat{B}, [\hat{A}, [\hat{A}, \hat{B}]]]\epsilon^4 + O(\epsilon^5). \end{aligned} \quad (2.25)$$

Using Eqs. (2.24) and (2.25) twice, we obtain [112]

$$e^{\epsilon \hat{B}} e^{\epsilon \hat{A}} e^{\epsilon \hat{B}} = e^{\hat{D}}, \quad (2.26)$$

where

$$\hat{D} = \epsilon(\hat{A} + 2\hat{B}) - \frac{1}{6}\epsilon^3[\hat{A}, [\hat{B}, \hat{A}]] + \frac{1}{6}\epsilon^3[\hat{B}, [\hat{A}, \hat{B}]] + O(\epsilon^5). \quad (2.27)$$

Applying Eqs. (2.26) and (2.27) twice to

$$\exp\left(-\tau \frac{\hat{V}}{6}\right) \exp\left(-\tau \frac{\hat{K}}{2}\right) \exp\left(-\tau \frac{2\tilde{V}}{3}\right) \exp\left(-\tau \frac{\hat{K}}{2}\right) \exp\left(-\tau \frac{\hat{V}}{6}\right), \quad (2.28)$$

we can check that the fourth-order factorization [112]

$$\begin{aligned} \exp \left[ -\tau(\hat{K} + \hat{V}) \right] &= \exp \left( -\tau \frac{\hat{V}}{6} \right) \exp \left( -\tau \frac{\hat{K}}{2} \right) \times \\ &\exp \left( -\tau \frac{2\tilde{V}}{3} \right) \exp \left( -\tau \frac{\hat{K}}{2} \right) \exp \left( -\tau \frac{\hat{V}}{6} \right) \\ &\quad + O(\tau^5), \end{aligned} \tag{2.29}$$

where  $\tilde{V}$  is given by  $\hat{V} + \tau^2[\hat{V}, [\hat{K}, \hat{V}]]/48$ , holds. The term  $[\hat{V}, [\hat{K}, \hat{V}]]$  in position space can be simplified to  $(\hbar^2/m) \sum_{i=1}^N |\nabla_i V|^2$  (the term  $|\nabla_i V|^2$  corresponds to the square of the force on the  $i$ th particle). The gradient  $\nabla_i$  in three spatial dimensions can be written as

$$\nabla_i = \hat{x} \frac{\partial}{\partial x_i} + \hat{y} \frac{\partial}{\partial y_i} + \hat{z} \frac{\partial}{\partial z_i}, \tag{2.30}$$

where  $\hat{x}$ ,  $\hat{y}$  and  $\hat{z}$  are unit vectors pointing in the  $x$ ,  $y$ , and  $z$  directions, respectively. Care needs to be taken in evaluating the derivatives, since  $V$  usually contains a double sum over two-body potentials or even a triple sum over three-body potentials. In most cases, the evaluation of the force terms cannot be simplified analytically, implying that the evaluation of double commutators involves double or triple sums over  $N$ , making the numerical evaluation comparatively expensive. Note that Eq. (2.29) is not the only form of the fourth-order factorization [112]. Specifically, the exponentials containing the potential energy can have different numerical factors.

Using the Trotter formula, the isomorphism of a single particle in free space and the classical spring system can be extended to multiple particles with interactions. Figure 2.3 depicts two interacting particles in two-dimensional space (the particles do not feel a single-particle potential). In this case, the density matrix for the link that connects the beads

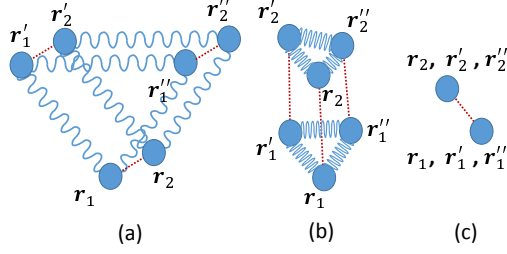


Figure 2.3: Isomorphism between path integrals for two interacting particles in two-dimensional space and classical particles connected by springs. In the path integral interpretation, the circles and wiggly lines depict the beads and links of a single particle, respectively. Dotted lines depict the two-body interaction between beads with the same imaginary time index. Panels (a), (b), and (c) are for low, medium, and high temperatures. In the classical mechanics formulation, the circles and wiggly lines depict particles and springs, respectively. Dotted lines depict the two-body interaction between selective particles. Earlier in the text, position vectors of the  $k$ th particle are denoted by  $\mathbf{r}_{k,j}$ . Using this notation, one has  $\mathbf{r}_k = \mathbf{r}_{k,0}$ ,  $\mathbf{r}'_k = \mathbf{r}_{k,1}$ , and  $\mathbf{r}''_k = \mathbf{r}_{k,2}$ .

labeled  $\mathbf{r}_1, \mathbf{r}'_1, \mathbf{r}_2,$  and  $\mathbf{r}'_2$  reads [see Eq. (2.22)]

$$\rho(\{\mathbf{r}_1, \mathbf{r}_2\}, \{\mathbf{r}'_1, \mathbf{r}'_2\}; \tau) = e^{-\tau V_{2b}(\mathbf{r}_1 - \mathbf{r}_2)/2} e^{-\tau V_{2b}(\mathbf{r}'_1 - \mathbf{r}'_2)/2} \rho_0(\mathbf{r}_1, \mathbf{r}'_1; \tau) \rho_0(\mathbf{r}_2, \mathbf{r}'_2; \tau), \quad (2.31)$$

where  $V_{2b}$  denotes the two-body interaction potential between particles 1 and 2 and  $\rho_0(\mathbf{r}_k, \mathbf{r}'_k; \tau)$  the single-particle density matrix of the  $k$ th particle [see Eq. (2.16)]. As in Fig. 2.2, two consecutive beads for the same particle (circles in Fig. 2.3) are connected by single-particle links, which represent the density matrices  $\rho_0$  (wiggly lines in Fig. 2.3). Since the two-body interaction (dotted lines in Fig. 2.3) is diagonal in position space [see the exponentials on the right hand side of Eq. (2.31)], it connects beads of different particles with the same index, i.e., it connects  $\mathbf{r}_1$  and  $\mathbf{r}_2$ ,  $\mathbf{r}'_1$  and  $\mathbf{r}'_2$ , and  $\mathbf{r}''_1$  and  $\mathbf{r}''_2$  (or  $\mathbf{r}_{k,j-1}$  and  $\mathbf{r}_{k,j}$ ). Figures 2.3(a), (b), and (c) are for low, medium, and high temperatures, respectively. Each particle in the PIMC simulation corresponds to  $n$  classical particles connected by springs. The classical particles corresponding to different chains interact only if they have the same bead index. The action  $S$  of the paths corresponds to the total energy  $E_{\text{tot}}$  of the corresponding classical system. Correspondingly, the density matrix of the system treated

in the PIMC simulation corresponds to the Boltzmann factor  $\exp(-\tau E_{\text{tot}})$  of the classical system.

### 2.3.2 Pair product approximation

For the pairwise additive potential model

$$V(\mathbf{R}) = \sum_{j=1}^{N-1} \sum_{k=j+1}^N V_{2b}(\mathbf{r}_{jk}), \quad (2.32)$$

the high-temperature density matrix can be evaluated using the pair product approximation [19]. To introduce the pair product approximation, we define the two-body kinetic energy operator  $\hat{K}_{jk}$  in position space,

$$\hat{K}_{jk} = -\frac{\hbar^2}{m} \nabla_{\mathbf{r}_{jk}}^2, \quad (2.33)$$

and assume the absence of single-particle potentials. The relative non-interacting and interacting two-body Hamiltonian are  $\hat{K}_{jk}$  and  $\hat{K}_{jk} + \hat{V}_{2b}(\mathbf{r}_{jk})$ , respectively. The pair product approximation considers two-body correlations explicitly, but not higher-body correlations, and writes the many-body density matrix as a product over single-particle density matrices and two-body density matrices,

$$\rho(\mathbf{R}, \mathbf{R}'; \tau) \approx \rho_0(\mathbf{R}, \mathbf{R}'; \tau) \left( \prod_{j < k}^N \bar{\rho}^{\text{rel}}(\mathbf{r}_{jk}, \mathbf{r}'_{jk}; \tau) \right), \quad (2.34)$$

where  $\bar{\rho}^{\text{rel}}$ ,

$$\bar{\rho}^{\text{rel}}(\mathbf{r}_{jk}, \mathbf{r}'_{jk}; \tau) = \frac{\langle \mathbf{r}_{jk} | \exp[-\tau(\hat{K}_{jk} + \hat{V}_{2b}(\mathbf{r}_{jk}))] | \mathbf{r}'_{jk} \rangle}{\langle \mathbf{r}_{jk} | \exp(-\tau \hat{K}_{jk}) | \mathbf{r}'_{jk} \rangle}, \quad (2.35)$$

is the reduced pair density matrix. The denominator of the reduced pair density matrix coincides with the known relative non-interacting two-body density matrix. Thus the only

“non-trivial input” is the relative density matrix of the interacting two-body system. One can readily see that the pair product approximation is exact for two particles at any temperature because the center of mass and relative degrees of freedom separate in this case. In some cases such as for the two-body zero-range interaction potential, the exact reduced pair density matrix is known analytically [113–116]. In other cases such as for the two-body hardcore potential, the approximate reduced pair density matrix is known analytically in closed form [117, 118]. If the reduced density matrix is not known analytically, one can perform a partial wave decomposition and obtain a numerical representation of the reduced two-body density matrix [19].

In dilute gases or weakly-bound droplets, two systems considered in this thesis, the interparticle spacing is typically so large that two-body collisions dominate over three- and higher-body collisions. Moreover, the importance of three- and higher-body collisions decreases with increasing temperature. The leading-order error of the pair product approximation is determined by the importance of three-body correlations. For two-component equal-mass Fermi gases with two-body zero-range interactions, three-body correlations are suppressed by the Pauli exclusion principle. For this system, we found that the pair product approximation provides an extremely good description of the density matrix. Specifically, we obtain accurate simulation results for a small number of beads (see Ch. 8 for details). For bosons, in contrast, three-body correlations can be significant. As a consequence, the pair product approximation is not as efficient as for two-component fermions. As discussed in Ch. 7, many of our simulations employ a large number of beads (“large” in this context means about two orders of magnitude more number of beads as in the simulations for fermions).

For the pair product approximation, we are not able to use the classical isomorphism because the kinetic and potential energy contributions are mixed. One needs to evaluate the single-particle density matrix, which can be represented by springs as in Figs. 2.2 and 2.3.

However, one also needs to evaluate the reduced two-body density matrix, which connects two consecutive beads of one particle’s path with the same consecutive beads of another particle’s path. These “four-bead connections” do not have a simple classical analog.

### 2.3.3 Comparison of the two approximations

Both methods of approximating the high-temperature density matrix have their advantages and disadvantages.

In the Trotter formula based scheme, the kinetic and the potential energy terms are treated separately. Inserting the identity  $\int_{\mathbf{R}} |\mathbf{R}\rangle \langle \mathbf{R}| d\mathbf{R} = \hat{1}$  [see Eq. (2.15)], the potential energy is diagonal in position space. This means that one can directly evaluate the potential energy term at each time slice. The kinetic energy term contains off-diagonal terms and needs to be evaluated at each link instead of at each time slice. Nevertheless, since the kinetic energy term corresponds to a simple Gaussian, one can perform the sampling according to the kinetic energy piece of the density matrix readily and, generally, efficiently (see Sec. 2.5.4 for details).

Even though the Trotter formula can formally be generalized to expressions that are accurate to order  $\tau^5$ ,  $\tau^6$ , ..., these expressions are not that useful in practice because they contain either commutators that involve rather complicated expressions or terms corresponding to negative imaginary time, which are not normalizable. There exists a multi-product expansion for the propagator [119]; however, applications thereof are still rare [120]. Thus present-day algorithms, including the algorithm developed during my Ph.D. career, employ Trotter formula based decompositions that are accurate to order  $\tau^4$ .

In the pair product approximation, the two-body reduced density matrix contains the kinetic energy and potential energy contributions. This means that the reduced two-body density matrix needs to be evaluated at each link. Because the reduced two-body density matrix is, in general, not a simple Gaussian, the sampling is generally less efficient (see

Sec. 2.5 for details). Furthermore, as shown in Sec. 2.4, the evaluation of the permutations is more involved. In general, the computational complexity of the pair product approximation is larger than that of the Trotter formula.

From our perspective, the pair product approximation has two advantages. i) Typically, the pair product approximation is more accurate than the Trotter formula based scheme, especially in cases where three-body correlations are suppressed such as in the case of the two-component Fermi gas. ii) More importantly, the pair product approximation can deal with a class of two-body potentials that the Trotter formula based scheme cannot deal with (at least no such treatment is known to us). For example, the two-body hardcore and zero-range potentials contain infinities and can thus not be treated by the Trotter formula based scheme. However, the infinities can be dealt with analytically in the pair product approximation.

## 2.4 Permutations

To account for the particle statistics, one needs to ensure the proper behavior of the density matrix under particle permutations. For Boltzmann particles, the sum over the eigen states in Eq. (2.4) is “unrestricted”. For bosons and fermions, in contrast, the sum includes only eigen states with the proper exchange properties. Said differently, the Hilbert space for identical bosons or identical fermions is restricted compared to that of Boltzmann particles described by the same Hamiltonian. The high-temperature approximations for the density matrix that are discussed in Sec. 2.3 apply to Boltzmann particles. To properly symmetrize or anti-symmetrize the density matrix operator  $\hat{\rho}$ , we introduce the symmetrizer  $\hat{\mathcal{P}}$  [19]. For the single-component Bose and Fermi systems ( $N$  identical particles),  $\hat{\mathcal{P}}$  can be written as [121]

$$\hat{\mathcal{P}} = \frac{1}{N!} \sum_{\sigma} (\pm 1)^{N_1(\sigma)} \hat{P}_{\sigma}, \quad (2.36)$$

where  $\sigma$  denotes the permutation of particle indices,  $N_I(\sigma)$  the number of inversions in  $\sigma$  [122], and  $\hat{P}_\sigma$  the corresponding permutation operator. For example, the symmetrizers for two and three identical fermions are  $\hat{\mathcal{A}}_2$  and  $\hat{\mathcal{A}}_3$ ,  $\hat{\mathcal{A}}_2 = \frac{1}{2}(1 - \hat{P}_{12})$  and  $\hat{\mathcal{A}}_3 = \frac{1}{6}(1 - \hat{P}_{12} - \hat{P}_{13} - \hat{P}_{23} + \hat{P}_{123} + \hat{P}_{132})$ , respectively. Here,  $\hat{P}_{ijk\dots l}$  replaces the identity of particle  $i$  (i.e., its entire “information”, including spatial coordinates, spin degrees of freedom, ...) with that of particle  $j$ , that of particle  $j$  with that of particle  $k$ , ..., and that of particle  $l$  with that of particle  $i$ . The symmetrizer  $\hat{\mathcal{P}}$  commutes with  $\hat{P}_{ij}$  if the  $i$ -th and  $j$ -th particles are identical. In the previous examples,  $\hat{\mathcal{A}}_2$  commutes with  $\hat{P}_{12}$  and  $\hat{\mathcal{A}}_3$  commutes with  $\hat{P}_{12}$ ,  $\hat{P}_{13}$ , and  $\hat{P}_{23}$ . The definition of the symmetrizer  $\hat{\mathcal{P}}$  can be generalized to multi-component Bose and Fermi systems as well as Bose-Fermi mixtures. In these cases, the total symmetrizer is written as a product of symmetrizers for each component. For example, the symmetrizer for the mixture of two identical bosons (particles 1 and 2) and two identical fermions (particles 3 and 4) reads  $\frac{1}{4}(1 + \hat{P}_{12})(1 - \hat{P}_{34})$ .

The symmetrizer  $\hat{\mathcal{P}}$  also commutes with the Hamiltonian  $\hat{H}$  and the density matrix operator  $\hat{\rho}$ .  $\hat{\mathcal{P}}$  serves the purpose of projecting out the wave functions that satisfy the proper exchange symmetry, i.e., it divides the Hilbert space into two parts: i) If  $\psi_s$  is an eigenstate with the proper symmetry, then one has  $\hat{\mathcal{P}}\psi_s = \psi_s$ . ii) If, in contrast,  $\psi_{ns}$  is an eigen state that does not have the proper exchange symmetry, then we have  $\hat{\mathcal{P}}\psi_{ns} = 0$ . We note that the eigen values of the symmetrizer  $\hat{\mathcal{P}}$  are either 0 and 1 while the eigen values of the two-particle permute operator  $\hat{P}_{12}$  are  $-1$  and  $1$ . Since the eigen values of  $\hat{\mathcal{P}}$  are either 0 or 1, we have

$$\hat{\mathcal{P}}^2 = \hat{\mathcal{P}}. \quad (2.37)$$

To prove Eq. (2.37), we introduce a unitary matrix  $\mathcal{U}$  that diagonalizes the Hermitian symmetrizer  $\hat{\mathcal{P}}$ , i.e.,  $\hat{\mathcal{D}} = \mathcal{U}\hat{\mathcal{P}}\mathcal{U}^{-1}$  is diagonal. Because  $\hat{\mathcal{P}}$  and  $\hat{\mathcal{D}}$  are connected by a unitary transformation,  $\hat{\mathcal{D}}$  and  $\hat{\mathcal{P}}$  share the same eigen values. As the eigen values of  $\hat{\mathcal{D}}$  are either 0

or 1,  $\hat{\mathcal{D}}$  is diagonal with diagonal elements 0 or 1. This implies

$$\hat{\mathcal{D}}^2 = \hat{\mathcal{D}}. \quad (2.38)$$

We now rewrite  $\hat{\mathcal{P}}^2$  using  $\hat{\mathcal{P}} = \mathcal{U}^{-1}\hat{\mathcal{D}}\mathcal{U}$ ,

$$\hat{\mathcal{P}}^2 = \mathcal{U}^{-1}\hat{\mathcal{D}}\mathcal{U}\mathcal{U}^{-1}\hat{\mathcal{D}}\mathcal{U} \quad (2.39)$$

$$= \mathcal{U}^{-1}\hat{\mathcal{D}}\hat{\mathcal{D}}\mathcal{U} \quad (2.40)$$

$$= \mathcal{U}^{-1}\hat{\mathcal{D}}\mathcal{U} \quad (2.41)$$

$$= \hat{\mathcal{P}}. \quad (2.42)$$

Thus,  $\hat{\mathcal{P}}^2 = \hat{\mathcal{P}}$  and we have proven Eq. (2.37).

The symmetrized density matrix operator reads  $\hat{\rho}_{\text{unsymm}}\hat{\mathcal{P}}$ , where  $\hat{\rho}_{\text{unsymm}}$  is the unsymmetrized density matrix operator, i.e., the density matrix operator for the corresponding system with Boltzmann particles. In position space, the symmetrized density matrix operator can be written as [19]

$$\langle \mathbf{R} | \exp(-\beta\hat{H})\hat{\mathcal{P}} | \mathbf{R}' \rangle = \langle \mathbf{R} | \exp(-\beta\hat{H}) | \hat{\mathcal{P}} \mathbf{R}' \rangle = \rho(\mathbf{R}, \hat{\mathcal{P}} \mathbf{R}'; \beta). \quad (2.43)$$

We now prove Eq. (2.43). In Schrödinger quantum mechanics, the symmetrized density matrix in position space reads

$$\langle \mathbf{R} | \exp(-\beta\hat{H}) \sum_j |\psi_{\text{symm},j}\rangle \langle \psi_{\text{symm},j} | \mathbf{R} \rangle, \quad (2.44)$$

where  $\{\psi_{\text{symm},j}\}$  is the complete set of symmetrized eigen states. The complete set of unsymmetrized eigen states of  $\hat{H}$ , i.e., the set of eigen states for Boltzmann particles is denoted by  $\{\psi_{\text{unsymm},j}\}$ . Recall that the  $\hat{\mathcal{P}}$  operator can be diagonalized using the matrix  $\mathcal{U}$ .  $\mathcal{U}$

“reorganizes” the eigen states  $\psi_{\text{unsymm},j}$  such that the new eigen states are also eigen states of  $\hat{\mathcal{P}}$ . The resulting eigen states  $\psi_{r,j}$ ,

$$\psi_{r,j} = \sum_l \mathcal{U}_{jl} \psi_{\text{unsymm},l}, \quad (2.45)$$

either have the proper symmetry, i.e.,  $\hat{\mathcal{P}}\psi_{r,j}$  is equal to  $\psi_{r,j}$  (in this case, the eigen value of  $\hat{\mathcal{P}}$  is 1) or  $\hat{\mathcal{P}}$  acting on  $\psi_{r,j}$  gives zero (in this case, the eigen value of  $\hat{\mathcal{P}}$  is 0). The set of eigen states  $\{\psi_{r,j}\}$  for which  $\hat{\mathcal{P}}\psi_{r,j} = \psi_{r,j}$  coincides with the complete set of symmetrized eigen states. This process of constructing a set of properly symmetrized eigen states from a set of unsymmetrized eigen states is known as post-symmetrization. We are now ready to prove Eq. (2.43). Starting with the left hand side of Eq. (2.43) and replacing  $\hat{\mathcal{P}}$  by  $\hat{\mathcal{P}}^2$ , we find

$$\langle \mathbf{R} | \exp(-\beta \hat{H}) \hat{\mathcal{P}} | \mathbf{R}' \rangle = \langle \mathbf{R} | \exp(-\beta \hat{H}) \hat{\mathcal{P}} \hat{\mathcal{P}} | \mathbf{R}' \rangle. \quad (2.46)$$

Inserting  $\mathcal{U}\mathcal{U}^{-1} = \hat{1}$ , we find

$$\langle \mathbf{R} | \exp(-\beta \hat{H}) \hat{\mathcal{P}} | \mathbf{R}' \rangle = \langle \mathbf{R} | \exp(-\beta \hat{H}) \hat{\mathcal{P}} \mathcal{U} \mathcal{U}^{-1} \hat{\mathcal{P}} | \mathbf{R}' \rangle. \quad (2.47)$$

Using

$$\sum_l |\psi_{\text{unsymm},l}\rangle \langle \psi_{\text{unsymm},l}| = \hat{1}, \quad (2.48)$$

we find

$$\langle \mathbf{R} | \exp(-\beta \hat{H}) \hat{\mathcal{P}} | \mathbf{R}' \rangle = \langle \mathbf{R} | \exp(-\beta \hat{H}) \hat{\mathcal{P}} \mathcal{U} \sum_l |\psi_{\text{unsymm},l}\rangle \langle \psi_{\text{unsymm},l}| \mathcal{U}^{-1} \hat{\mathcal{P}} | \mathbf{R}' \rangle. \quad (2.49)$$

Using Eq. (2.45) and reordering sums, we obtain the auxiliary identity

$$\mathcal{U} \sum_l |\psi_{\text{unsymm},l}\rangle \langle \psi_{\text{unsymm},l}| \mathcal{U}^{-1} = \sum_l |\psi_{r,l}\rangle \langle \psi_{r,l}|. \quad (2.50)$$

Using Eq. (2.50) in Eq. (2.49), we find

$$\langle \mathbf{R} | \exp(-\beta \hat{H}) \hat{\mathcal{P}} | \mathbf{R}' \rangle = \langle \mathbf{R} | \exp(-\beta \hat{H}) \hat{\mathcal{P}} \sum_l |\psi_{r,l}\rangle \langle \psi_{r,l}| \hat{\mathcal{P}} | \mathbf{R}' \rangle. \quad (2.51)$$

Using  $\hat{\mathcal{P}} \sum_l |\psi_{r,l}\rangle \langle \psi_{r,l}| \hat{\mathcal{P}} = \sum_l |\psi_{\text{symm},l}\rangle \langle \psi_{\text{symm},l}|$ , we finally arrive at

$$\langle \mathbf{R} | \exp(-\beta \hat{H}) \hat{\mathcal{P}} | \mathbf{R}' \rangle = \langle \mathbf{R} | \exp(-\beta \hat{H}) \sum_l |\psi_{\text{symm},l}\rangle \langle \psi_{\text{symm},l}| \mathbf{R}' \rangle. \quad (2.52)$$

Since the right hand side of Eq. (2.52) is equal to the right hand side of Eq. (2.43) [see also Eq. (2.44)], we have proven that  $\hat{\rho}_{\text{unsymm}} \hat{\mathcal{P}}$  is the symmetrized density matrix.

For single-component bosons or fermions, the symmetrized density matrix can be expanded as follows [see Eq. (2.36)]:

$$\rho(\mathbf{R}, \hat{\mathcal{P}} \mathbf{R}'; \beta) = \frac{1}{N!} \sum_{\sigma} (\pm 1)^{N_I(\sigma)} \rho(\mathbf{R}, \hat{P}_{\sigma} \mathbf{R}'; \beta). \quad (2.53)$$

An important point is that the density matrix can be evaluated stochastically provided each term in the sum is real. This is the case if  $\hat{H}$  is independent of time and Hermitian. The positive terms on the right hand side of Eq. (2.53) naturally correspond to a probability. The negative terms on the right hand side of Eq. (2.53), in contrast, can be evaluated using their magnitude for the sampling and separately keeping track of the sign. To account for the permutations in the low-temperature density matrix, we write the low-temperature density matrix as integrals over products of high-temperature density matrices as before.

The symmetrized density matrix operator  $\hat{\rho}_{\text{unsymm}}\hat{\mathcal{P}}$  in position space reads

$$\rho(\mathbf{R}_0, \hat{\mathcal{P}}\mathbf{R}_n; \beta) = \int_{\mathbf{R}_1} \int_{\mathbf{R}_2} \dots \int_{\mathbf{R}_{n-1}} \rho(\mathbf{R}_0, \mathbf{R}_1; \beta/n) \rho(\mathbf{R}_1, \mathbf{R}_2; \beta/n) \dots \rho(\mathbf{R}_{n-1}, \hat{\mathcal{P}}\mathbf{R}_n; \beta/n) d\mathbf{R}_1 d\mathbf{R}_2 \dots d\mathbf{R}_{n-1}. \quad (2.54)$$

Here,  $\hat{\mathcal{P}}$  is applied to  $\mathbf{R}_n$ . Because  $\hat{\mathcal{P}}$  commutes with the high-temperature density matrix, the time slice index is arbitrary, i.e., the operator  $\hat{\mathcal{P}}$  could be applied to  $\mathbf{R}_{n-1}$  or  $\mathbf{R}_{n-2}$  or ... instead of  $\mathbf{R}_n$ .

Alternatively, we can rewrite, using Eq. (2.37), the symmetrized density matrix operator  $\hat{\rho}_{\text{unsymm}}\hat{\mathcal{P}}$  as  $\hat{\rho}_{\text{unsymm}}\hat{\mathcal{P}}^j$ , where  $j$  is a positive integer. Choosing  $j$  to be equal to the number of time slices  $n$  and applying each of the symmetrizers to a different  $\mathbf{R}_j$ , we obtain

$$\rho(\mathbf{R}_0, \hat{\mathcal{P}}\mathbf{R}_n; \beta) = \int_{\mathbf{R}_1} \int_{\mathbf{R}_2} \dots \int_{\mathbf{R}_{n-1}} \rho(\mathbf{R}_0, \hat{\mathcal{P}}\mathbf{R}_1; \beta/n) \rho(\mathbf{R}_1, \hat{\mathcal{P}}\mathbf{R}_2; \beta/n) \dots \rho(\mathbf{R}_{n-1}, \hat{\mathcal{P}}\mathbf{R}_n; \beta/n) d\mathbf{R}_1 d\mathbf{R}_2 \dots d\mathbf{R}_{n-1}. \quad (2.55)$$

The advantage of Eq. (2.54) is that it contains “only”  $N!$  terms for a single-component system while Eq. (2.55) contains  $N! \times n$  terms. Because of this, Eq. (2.54) is usually the preferred choice.

For  $N$  identical bosons, the  $N!$  permutations are sampled stochastically. In practice (see Sec. 2.5.5 for details), this means that  $\hat{\mathcal{P}}\mathbf{R}_n$  on the right hand side of Eq. (2.54) gets replaced by  $\hat{\mathcal{P}}_\sigma\mathbf{R}_n$ , where  $\hat{\mathcal{P}}_\sigma$  is one of the possible permutations. During the simulation, one needs to keep track of the permutation status of the current configuration. Using the Trotter formula, the bead  $\mathbf{r}_{k,j}$  is connected by single-particle links to  $\mathbf{r}_{k,j\pm 1}$  for  $0 < j < n - 1$ , to  $\mathbf{r}_{k,n-2}$  and  $\mathbf{r}_{\hat{\mathcal{P}}_\sigma k,0}$  for  $j = n - 1$ , and to  $\mathbf{r}_{k,1}$  and  $\mathbf{r}_{\hat{\mathcal{P}}_\sigma k,n-1}$  for  $j = 0$ . Here,  $\hat{\mathcal{P}}_\sigma$  is the permutation of the current configuration.

As discussed in Ch. 1, for fermions with zero-range interactions, the Pauli exclusion

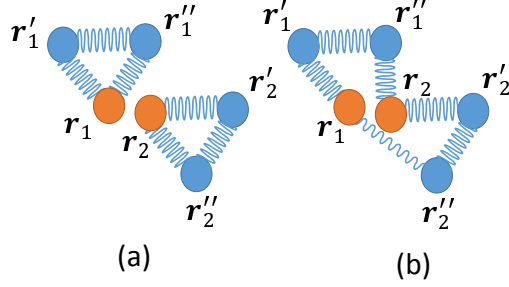


Figure 2.4: Illustration of paths corresponding to the identity permutation  $\hat{1}$  [panel (a)] and the permutation  $\hat{P}_{12}$  [panel (b)] for Eq. (2.54). The circles and wiggly lines show beads and single-particle density matrices, respectively, for two free particles. Orange circles denote the head beads  $\mathbf{r}_1$  and  $\mathbf{r}_2$ .

principle prevents the Thomas collapse. As a consequence, the symmetrizer  $\hat{\mathcal{P}}$  needs to be applied to every link. If one did not do this, the non-symmetrized link would undergo Thomas collapse, rendering the entire simulation meaningless. In contrast to Eq. (2.54), the permutation scheme used in Eq. (2.55) applies the symmetrizer to every link explicitly. Using the Trotter formula, the bead  $\mathbf{r}_{k,j}$  is connected by single-particle links to all  $\mathbf{r}_{\hat{\mathcal{P}}_\sigma k, j \pm 1}$ , where  $\hat{\mathcal{P}}_\sigma$  runs through all possible permutations. Therefore, it makes no sense to associate a fixed permutation status with a configuration.

Figures 2.4(a) and (b) illustrate the paths for a two-particle system corresponding to the identity permutation  $\hat{1}$  and corresponding to the permutation  $\hat{P}_{12}$ , respectively. The paths are based on Eq. (2.54), which means that the permutation operator is applied to  $\mathbf{R}_n$ . For paths corresponding to the identity permutation, the second bead of the first particle is connected to the zeroth bead of the first particle, i.e.,  $\mathbf{r}''_1$  is connected to  $\mathbf{r}_1$ , and the same for the second particle. For paths corresponding to the permutation  $\hat{P}_{12}$ , the second bead of the first particle is connected to the zeroth bead of the second particle, i.e.,  $\mathbf{r}''_1$  is connected to  $\mathbf{r}_2$ , and the second bead of the second particle is connected to the zeroth bead of the first particle, i.e.,  $\mathbf{r}''_2$  is connected to  $\mathbf{r}_1$ . Orange circles depict the ‘‘head’’ beads, i.e., beads belonging to the zeroth time slice. Figure 2.4(b) shows that the permuted path is closed; however, as opposed to two separate closed paths as in Fig. 2.4(a), we have a single (but

larger) closed path. Compared to Fig. 2.4(a), the last single-particle link (which connects time slice indices  $n - 1$  and  $0$ ) of the first particle in Fig. 2.4(b) is cut open and a new single-particle link between the second bead of the first particle ( $\mathbf{r}_1''$ ) and the zeroth bead of the second particle ( $\mathbf{r}_2$ ) is created. This can be summarized by saying that the tail of the first particle becomes the head of the second particle and that the tail of the second particle becomes the head of the first particle.

If Eq. (2.54) is used, the stochastic sampling of the permutations requires a move that helps with “hopping” between different permutations. If Eq. (2.55) is used, no such move is needed. The permutation sampling is discussed in detail in Sec. 2.5.5.

## 2.5 Sampling

### 2.5.1 General scheme: Importance sampling

Equation (2.15) writes the density matrix as a high-dimensional integral over a product of high-temperature density matrices. This section discusses the Monte Carlo sampling of these high-dimensional integrals for closed paths with  $\mathbf{R}_n = \mathbf{R}_0$  (there are  $3 \times n \times N$  independent variables if we are considering three spatial dimensions). Equation (2.5) can be rewritten in a “democratic manner”,

$$Z = \int_{\mathbf{R}_0} \dots \int_{\mathbf{R}_{n-1}} \pi(\mathbf{R}_0, \dots, \mathbf{R}_{n-1}) d\mathbf{R}_0 \dots d\mathbf{R}_{n-1}, \quad (2.56)$$

where

$$\pi(\mathbf{R}_0, \dots, \mathbf{R}_{n-1}) = \rho(\mathbf{R}_0, \mathbf{R}_1; \tau) \rho(\mathbf{R}_1, \mathbf{R}_2; \tau) \dots \rho(\mathbf{R}_{n-1}, \mathbf{R}_0; \tau). \quad (2.57)$$

In Eq. (2.57), the order of the density matrices does not matter. This implies that  $\mathbf{R}_0$ ,  $\mathbf{R}_1$ ,  $\dots$ , and  $\mathbf{R}_{n-1}$  are treated on equal footing, i.e., there exists no starting or ending point of the chain. In Fig. 2.2, for example, one can pick any of the beads as the initial bead. We denote

the configuration  $\{\mathbf{R}_0, \dots, \mathbf{R}_{n-1}\}$  by  $\mathbf{x}$  and the probability distribution  $\pi(\mathbf{R}_0, \dots, \mathbf{R}_{n-1})$  by  $\pi(\mathbf{x})$ . The notation of these and other quantities are summarized in Tables 2.1 and 2.2. The expectation value  $\langle \mathcal{O} \rangle$  of an arbitrary observable  $\mathcal{O}$  can be written as

$$\langle \mathcal{O} \rangle = \frac{\int_{\mathbf{x}} w(\mathbf{x}) \pi(\mathbf{x}) d\mathbf{x}}{Z} = \frac{\int_{\mathbf{x}} w(\mathbf{x}) \pi(\mathbf{x}) d\mathbf{x}}{\int_{\mathbf{x}} \pi(\mathbf{x}) d\mathbf{x}}, \quad (2.58)$$

where the integration goes over  $3 \times n \times N$  coordinates and the weight function  $w(\mathbf{x})$  needs to be calculated, as will be discussed in Sec. 2.6, for each observable. To see the structure of  $\langle \mathcal{O} \rangle$  more clearly, we rewrite Eq. (2.58),

$$\langle \mathcal{O} \rangle = \int_{\mathbf{x}} w(\mathbf{x}) \frac{\pi(\mathbf{x})}{\int_{\mathbf{x}'} \pi(\mathbf{x}') d\mathbf{x}'} d\mathbf{x}. \quad (2.59)$$

Defining the probability density function  $p(\mathbf{x})$ ,

$$p(\mathbf{x}) = \frac{\pi(\mathbf{x})}{\int_{\mathbf{x}'} \pi(\mathbf{x}') d\mathbf{x}'}, \quad (2.60)$$

Eq. (2.59) can be rewritten as

$$\langle \mathcal{O} \rangle = \int_{\mathbf{x}} w(\mathbf{x}) p(\mathbf{x}) d\mathbf{x}. \quad (2.61)$$

In contrast to the probability distribution  $\pi(\mathbf{x})$ , the probability density function  $p(\mathbf{x})$  is normalized;  $w(\mathbf{x})$  represents the weight contributed to the observable by the configuration  $\mathbf{x}$  and  $p(\mathbf{x})$  the normalized probability to be in configuration  $\mathbf{x}$ . Equation (2.61) provides the basis of importance sampling: Configurations are not blindly distributed evenly in space but instead distributed according to  $p(\mathbf{x})$ . The advantage of importance sampling is that most computer time is used to sample configurations that are physically relevant and little time to sample configurations that do not contribute significantly to  $\langle \mathcal{O} \rangle$ .

The general idea of the PIMC algorithm is to generate configurations  $\mathbf{x}$  according to  $p(\mathbf{x})$

Table 2.2: Definitions of Monte Carlo sampling terminology used in this thesis. Columns 1-3 show the symbol, name, and related equation number, respectively. The configuration  $\mathbf{x}$  is defined by  $\mathbf{x} = \{\mathbf{R}_0, \dots, \mathbf{R}_{n-1}\}$ .

$\pi(\mathbf{x})$	probability distribution	Eq. (2.57)
$p(\mathbf{x})$	probability density function	Eq. (2.60)
$w(\mathbf{x})$	weight function (observable specific)	Eqs. (2.58)-(2.61) and Sec. 2.6
$P(\mathbf{x} \rightarrow \mathbf{x}')$	transition probability	Eq. (2.71)
$G(\mathbf{x} \rightarrow \mathbf{x}')$	proposal distribution (selected by simulator)	discussion around Eqs. (2.71) and (2.72)
$A(\mathbf{x} \rightarrow \mathbf{x}')$	acceptance distribution	Eq. (2.72)
$g(\mathbf{x})$	guiding function (selected by simulator)	Eq. (2.75)
$a(\mathbf{x})$	acceptance function	Eq. (2.75)

and to use the generated configurations to accumulate the weight functions  $w(\mathbf{x})$  for a set of observables. Thus, it is crucial to have correct and efficient sampling schemes that explore the full configuration space without rejection rates close to 100% or getting stuck around a local maximum. Section 2.5.2 reviews the basics of selected Monte Carlo methods and the rest of this section details various sampling methods.

## 2.5.2 General background on Monte Carlo methods

This section is for general readers who are not familiar with Monte Carlo methods and gives an introduction to the method. We briefly introduce the random number generator, the generation of non-uniform random variables, Markov chains, and Metropolis sampling.

To generate samples from a given probability density function, we need a random number generator to generate random numbers uniformly between 0 and 1. Various random number generators that generate pseudo random numbers exist (i.e., according to a specific sequence) [123]. All good random number generators need to pass a variety of tests, which ensure that the random numbers drawn are independent of each other and uniformly distributed.

One of the tests, known as autocorrelation (or serial correlation) test [124], examines the autocorrelation of the random numbers. Given a series of random numbers  $\{x_1, \dots, x_M\}$ , the lag  $k$  correlation coefficient  $r_k$ , which measures the correlation of the series of numbers  $\{x_1, \dots, x_{M-k}\}$  and  $\{x_{k+1}, \dots, x_M\}$ , is given by [125]

$$r_k = \frac{\sum_{j=1}^{M-k} (x_j - \bar{x})(x_{j+k} - \bar{x})}{\sum_{j=1}^M (x_j - \bar{x})^2}. \quad (2.62)$$

For a series of independent random numbers generated from a given probability density function, the mean value of  $r_k$  is equal to  $-1/M$ .  $r_k$  approximately follows a normal distribution for sufficiently large  $M - k$  and the variance of  $r_k$  is approximately  $1/M$ . The probability

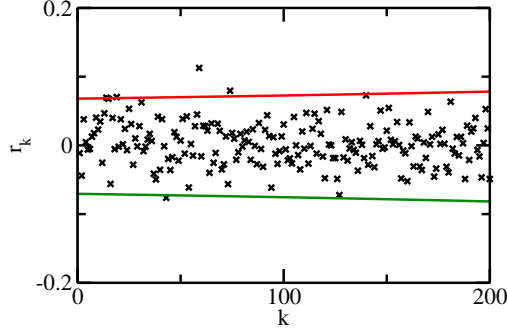


Figure 2.5: Correlation coefficient  $r_k$  as a function of the lag  $k$  for a sample of 800 random numbers uniformly distributed between 0 and 1. The upper and lower solid lines show the 95% confidence interval.

that  $r_k$  falls into the window

$$\left[ \frac{-1 - 1.96\sqrt{M - k - 1}}{M - k}, \frac{-1 + 1.96\sqrt{M - k - 1}}{M - k} \right] \quad (2.63)$$

is 95% [125]. Based on hypothesis testing theory [126], we claim, with 95% confidence level, that a sample is correlated if  $r_k$  falls outside the window given in Eq. (2.63) (based on a single test for one  $k$ ).

Figure 2.5 plots the correlation coefficient  $r_k$  as a function of the lag  $k$  for a sample of 800 random numbers. The upper and lower solid lines show the 95% confidence interval. 5 points fall outside the 95% confidence band. If we were to apply the test for  $k = 14, 19, 43, 59$  or  $74$ , i.e., the values of  $k$  for which  $r_k$  falls outside the confidence interval, we would conclude that the sample, and thus the random number generator, is correlated. However, we should keep in mind that the number of  $k$  considered is large and that we expect a few points to lie outside the 95% confidence interval (5% correspond to 10 points). Since the number of points outside the confidence interval is consistent with this, we conclude that the sample passes the autocorrelation test.

Low-dimensional sampling is usually straightforward and can be done in multiple ways. As an example, we consider a one-dimensional case. Let  $p_1(x)$  be a probability density function. If the cumulative distribution function  $F_1(x)$ ,  $F_1(x) = \int_{-\infty}^x p_1(x')dx'$ , is analytically

invertible, then  $F_1^{-1}(Y)$ , where  $Y$  is chosen uniformly from between 0 and 1, complies with the probability density function  $p_1(x)$ . This scheme of generating random numbers is referred to as direct sampling. Because no trials are thrown out during the sampling, the acceptance ratio (i.e., the fraction of trials accepted) is by definition 100%. For example, to generate samples according to the Gamma probability density function  $p_g(x)$ ,

$$p_g(x) = \begin{cases} \exp(-x) & \text{for } x > 0 \\ 0 & \text{for } x \leq 0, \end{cases} \quad (2.64)$$

we first compute the cumulative distribution function  $F_g(x)$ ,

$$F_g(x) = \begin{cases} 1 - \exp(-x) & \text{for } x > 0 \\ 0 & \text{for } x \leq 0, \end{cases} \quad (2.65)$$

and then the inverse  $F_g^{-1}(x)$  of the cumulative distribution function,

$$F_g^{-1}(x) = \begin{cases} 0 & \text{for } x \leq 0 \\ -\ln(1-x) & \text{for } 0 < x < 1 \\ \infty & \text{for } x \geq 1. \end{cases} \quad (2.66)$$

If  $Y$  is randomly and uniformly drawn from between 0 and 1,  $F_g^{-1}(Y)$  obeys  $p_g(x)$ . Unfortunately, only a limited number of  $p_1(x)$  can be generated in this manner. For example, the normal distribution cannot be generated analytically in this way (of course, one can record the cumulative distribution function of the normal distribution pointwise and perform the inversion numerically).

For the normal distribution, the Box-Muller transform [127] can be used. Instead of generating one random number at a time, the Box-Muller based sampling method generates

pairs of independent random numbers. Let  $Y_1$  and  $Y_2$  be independent random numbers that are uniformly distributed between 0 and 1. Then  $Z_1$  and  $Z_2$ ,

$$Z_1 = \sqrt{-2 \ln(Y_1)} \cos(2\pi Y_2) \quad (2.67)$$

and

$$Z_2 = \sqrt{-2 \ln(Y_1)} \sin(2\pi Y_2), \quad (2.68)$$

are independent random numbers that are normally distributed. Since  $Y_1$  and  $Y_2$  are used to generate two new random numbers, the algorithm is characterized by an acceptance ratio of 100%.

One can speed up the computational effort by using the rejection method. The evaluation of cos and sin in Eqs. (2.67) and (2.68) is time consuming. Instead, we generate  $u$  and  $v$  uniformly between  $-1$  and  $1$  and discard them if  $s$  ( $s = u^2 + v^2$ ) is larger than 1. Defining  $t$  such that it satisfies  $\sqrt{s} \cos(2\pi t) = u$  and  $\sqrt{s} \sin(2\pi t) = v$ ,  $\sqrt{s}$  and  $2\pi t$  are identified as polar coordinates of the variables  $u$  and  $v$ . It can be proven that  $s$  and  $t$  are uniformly distributed between 0 and 1. Comparing with Eqs. (2.67) and (2.68), one obtains

$$Z_1 = \sqrt{-2 \ln s} \frac{u}{\sqrt{s}} \quad (2.69)$$

and

$$Z_2 = \sqrt{-2 \ln s} \frac{v}{\sqrt{s}}. \quad (2.70)$$

As before,  $Z_1$  and  $Z_2$  are normally distributed. This highly efficient approach, which has an acceptance ratio of 78.5%, is known as the Marsaglia polar method [128]. The Ziggurat algorithm [129, 130], which is more complicated, provides a factor of around 1.5 speed up compared to the Marsaglia polar method. Both methods employ rejection sampling. There exist many other sampling schemes that reject a fraction of the generated random numbers

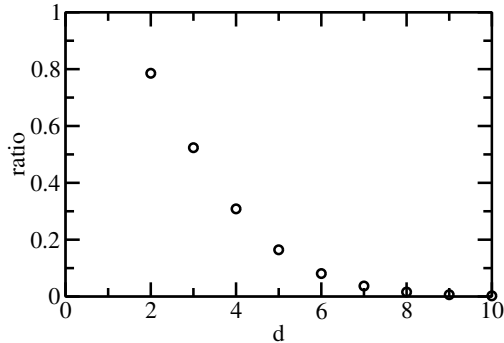


Figure 2.6: Ratio of volumes of a  $d$ -dimensional hypersphere with unit radius and a  $d$ -dimensional hypercube with edge length of 2.

to generate a distribution  $p(\mathbf{x})$ . If the scheme involves a rejection/acceptance step, we quite generally refer to the sampling scheme as “rejection sampling”.

The rejection sampling cannot be generalized efficiently to very high dimensions. The dimensionality is 2 in the Marsaglia polar method since we are effectively generating the pair  $(Z_1, Z_2)$  of random numbers ( $Z_1$  and  $Z_2$  happen to be independent of each other). The acceptance ratio of 78.5% originates from the fact that the points are generated in a 2 by 2 square (size of 4) but are accepted only if they lie in a unit circle of size  $\pi$ . To see how the acceptance ratio changes as the number of dimensions  $d$  increases, we consider a hypothetical high-dimensional rejection sampling method. Specifically, we generate points in a hypercube of volume  $2^d$  and accept the points that lie in a unit hypersphere of volume  $\pi^{d/2}/\Gamma(d/2 + 1)$ . The acceptance ratio for this hypothetical rejection sampling method is shown in Fig. 2.6 as a function of the dimension  $d$ . The acceptance ratio decreases quickly as  $d$  increases; this is known as the “curse of dimensionality” [131]. For PIMC simulations, the dimensionality can easily reach 100 or even more and the acceptance ratio would, for this simple sampling scheme, be smaller than  $10^{-69}$ . Thus, rejection sampling is not a viable approach. To avoid low acceptance ratios, Markov chain Monte Carlo methods can be used [124]. Specifically, the Metropolis (Metropolis-Hastings) algorithm is an important Markov chain Monte Carlo method for generating a sequence of random samples from the probability distribution  $\pi(\mathbf{x})$  [124]. In principle, the probability distribution can be arbitrary.

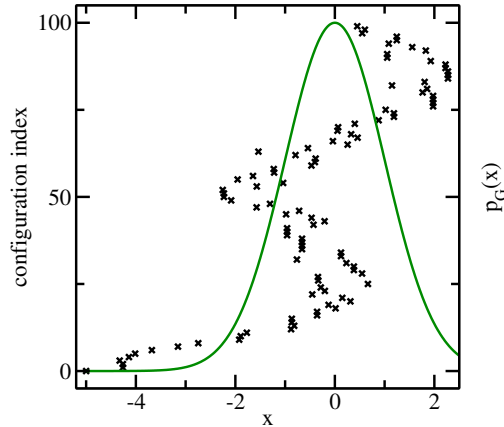


Figure 2.7: Illustration of the equilibration process for a Markov chain (crosses) for the Gaussian probability density function  $p_G(x)$  (solid line). The graph employs dimensionless units. The starting point of the Markov chain is at  $-5$ . The  $x$  and  $y$  axes correspond to the value and the configuration index, respectively.

A Markov chain is a sequence of random samples, in which the  $j$ -th sample depends only on the  $(j - 1)$ -th sample. This implies that a new sample does not have the “memory” of all previous samples but only of one other sample. If we generate a random initial configuration  $\mathbf{x}$  for which the probability distribution  $\pi(\mathbf{x})$  is small and update the configuration repeatedly with a variety of methods (such as updating a single bead, an entire path, or the center-of-mass coordinate, etc.) according to  $\pi(\mathbf{x})$ , then the algorithm reaches equilibrium after a finite number of steps. Figure 2.7 illustrates this equilibration process for a simple one-dimensional example, namely a Gaussian probability density function  $p_G(x)$  (solid line in Fig. 2.7). The algorithm used to generate the symbols in Fig. 2.7 is discussed later in the chapter; for now, we focus on the behavior of the Markov chain, i.e., on the behavior of the symbols shown in Fig. 2.7. In the example, the initial configuration is  $-5$ . The samples crawl to regimes where  $\pi(x)$  is large. It can be clearly seen that the samples have a “short-term memory”, i.e., are independent of the initial configuration. The first 25 steps or so in Fig. 2.7 correspond to the equilibration process. During the equilibration process, the configurations generated can have a small weight and may not be distributed according to  $\pi(\mathbf{x})$ . The number of steps needed to reach equilibrium varies and needs to be determined

carefully for each system under study. After equilibrium is reached, the samples generated from the Markov chain are distributed according to the probability distribution  $\pi(\mathbf{x})$ . At this point, one can take “measurements”, i.e., we can evaluate  $w(\mathbf{x})$  for the observables of interest. We return to this later in this section.

We now discuss how to update or generate the configurations using the Metropolis algorithm. A Markov process is uniquely defined by the transition probability  $P(\mathbf{x} \rightarrow \mathbf{x}')$  to go from configuration  $\mathbf{x}$  to configuration  $\mathbf{x}'$ . The Metropolis algorithm satisfies the detailed balance condition [124]

$$\pi(\mathbf{x})P(\mathbf{x} \rightarrow \mathbf{x}') = \pi(\mathbf{x}')P(\mathbf{x}' \rightarrow \mathbf{x}), \quad (2.71)$$

i.e., the flow of probability from  $\mathbf{x}$  to  $\mathbf{x}'$  is equal to that from  $\mathbf{x}'$  to  $\mathbf{x}$ . This means that there is no net flow of probability. The Metropolis algorithm needs to ensure ergodicity of the Markov process. If the process is ergodic, the Markov chain (i) returns to any previously generated configuration  $\mathbf{x}$  after a sufficiently long simulation time and (ii) is not periodic (a Markov chain of  $\{\mathbf{x}, \mathbf{x}', \mathbf{x}, \mathbf{x}', \dots\}$  is periodic). The ergodicity ensures that the probability distribution  $\pi(\mathbf{x})$  gets sampled fully. For example, as discussed in Ch. 8, if we use the traditional scheme of treating the permutations [Eq. (2.54)], for a two-component Fermi gas with zero-range interactions, the Markov process ends up with a configuration in which all particles sit on top of each other and the configuration never returns to the original configuration  $\mathbf{x}$ . This means that ergodicity is violated and that the Markov process does not generate samples according to  $p(\mathbf{x})$ . This renders the sampled configurations meaningless. We note, however, that while the detailed balance condition together with the ergodicity guarantees that the equilibrium distribution coincides with the desired probability distribution  $\pi(\mathbf{x})$ , there exist other Monte Carlo methods that do not satisfy the detailed balance condition but yield an equilibrium distribution that coincides with the desired probability distribution  $\pi(\mathbf{x})$ .

The Metropolis algorithm consists of two steps [124]: (i) the generation of a proposed configuration (or move) and (ii) the acceptance or rejection of the proposed configuration

(or move). The combination of (i) and (ii) leads to a new configuration. Starting from the configuration  $\mathbf{x}$ , we propose a new configuration  $\mathbf{x}'$  according to a proposal distribution  $G(\mathbf{x} \rightarrow \mathbf{x}')$  and accept (the new configuration would be  $\mathbf{x}'$ ) or reject the new configuration (the new configuration would be  $\mathbf{x}$ ) according to the acceptance distribution  $A(\mathbf{x} \rightarrow \mathbf{x}')$ . The Metropolis algorithm chooses  $A(\mathbf{x} \rightarrow \mathbf{x}')$  such that [124]

$$A(\mathbf{x} \rightarrow \mathbf{x}') = \min \left( 1, \frac{\pi(\mathbf{x}')G(\mathbf{x}' \rightarrow \mathbf{x})}{\pi(\mathbf{x})G(\mathbf{x} \rightarrow \mathbf{x}')} \right). \quad (2.72)$$

We verify that the detailed balance condition [Eq. (2.71)] is satisfied in the following. If  $\pi(\mathbf{x}')G(\mathbf{x}' \rightarrow \mathbf{x})$  is smaller than  $\pi(\mathbf{x})G(\mathbf{x} \rightarrow \mathbf{x}')$ , we obtain

$$P(\mathbf{x} \rightarrow \mathbf{x}') = G(\mathbf{x} \rightarrow \mathbf{x}')A(\mathbf{x} \rightarrow \mathbf{x}') = \frac{\pi(\mathbf{x}')G(\mathbf{x}' \rightarrow \mathbf{x})}{\pi(\mathbf{x})} \quad (2.73)$$

and

$$P(\mathbf{x}' \rightarrow \mathbf{x}) = G(\mathbf{x}' \rightarrow \mathbf{x})A(\mathbf{x}' \rightarrow \mathbf{x}) = G(\mathbf{x}' \rightarrow \mathbf{x}). \quad (2.74)$$

Plugging Eqs. (2.73) and (2.74) into Eq. (2.71), we confirm that Eq. (2.71) holds. Similarly, if  $\pi(\mathbf{x}')G(\mathbf{x}' \rightarrow \mathbf{x})$  is larger or equal to  $\pi(\mathbf{x})G(\mathbf{x} \rightarrow \mathbf{x}')$ , following the same logic, we confirm that Eq. (2.71) holds. Thus, we have shown that detailed balance is fulfilled.

In practice, the acceptance ratio  $A$  (which is a number and not an  $\mathbf{x}$ - and  $\mathbf{x}'$ -dependent function), i.e., the fraction of rejected moves, should be monitored. This acceptance ratio  $A$  is different from the acceptance ratio encountered in the rejection sampling. In the rejection sampling, a rejected configuration does not lead to a new configuration. In the Metropolis sampling, in contrast, a rejected configuration does lead to a new configuration. When a configuration is rejected, the old configuration becomes the new configuration.

As an example, we write the probability distribution  $\pi(\mathbf{x})$  as a product of the guiding

function  $g(\mathbf{x})$  and the acceptance function  $a(\mathbf{x})$ ,

$$a(\mathbf{x}) = \frac{\pi(\mathbf{x})}{g(\mathbf{x})}. \quad (2.75)$$

We choose the proposal distribution  $G(\mathbf{x} \rightarrow \mathbf{x}')$  such that the equilibrated probability distribution without the rejection move is proportional to  $g(\mathbf{x})$ . Using  $\pi(\mathbf{x}) \propto g(\mathbf{x})$  and  $P(\mathbf{x} \rightarrow \mathbf{x}') = G(\mathbf{x} \rightarrow \mathbf{x}')$  in Eq. (2.71), we obtain

$$\frac{G(\mathbf{x}' \rightarrow \mathbf{x})}{G(\mathbf{x} \rightarrow \mathbf{x}')} = \frac{g(\mathbf{x})}{g(\mathbf{x}')}. \quad (2.76)$$

Plugging Eqs. (2.76) and (2.75) into Eq. (2.72), the acceptance distribution  $A(\mathbf{x} \rightarrow \mathbf{x}')$  simplifies to

$$A(\mathbf{x} \rightarrow \mathbf{x}') = \min\left(1, \frac{a(\mathbf{x}')}{a(\mathbf{x})}\right). \quad (2.77)$$

The crosses in Fig. 2.7 are generated following the discussion in the previous paragraph. To generate configurations according to the Gaussian probability density function  $p_G(x)$ ,

$$p_G(x) = \frac{\exp(-\frac{x^2}{2})}{\sqrt{2\pi}}, \quad (2.78)$$

we choose  $g(x) = 1$  and  $a(x) = p_G(x)$ . To generate the uniform distribution  $g(x) = 1$ , we propose a new configuration  $x'$  randomly from the window  $[x - \delta x, x + \delta x]$ , where  $x$  denotes the current configuration. We then have

$$G(x \rightarrow x') = \begin{cases} 1 & \text{for } x - \delta x < x' < x + \delta x \\ 0 & \text{otherwise.} \end{cases} \quad (2.79)$$

The acceptance distribution is given in Eq. (2.77). Because some configurations are rejected, the positions for some consecutive configuration indices in Fig. 2.7 are the same. In the

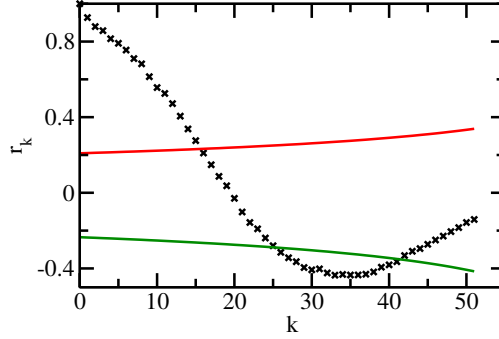


Figure 2.8: Correlation coefficient  $r_k$  as a function of the lag  $k$  for the Markov chain discussed in Fig. 2.7. The equilibration stage (configuration index 1 to 25 in Fig. 2.7) is not considered here, i.e., the series of points  $\{x_{26}, \dots, x_{100}\}$  is considered. The upper and lower solid lines denote the 95% confidence interval.

example, 20 points out of 100 points are rejected, yielding an acceptance ratio of 80%.

For most of the updates (i.e., the generation of proposed new configurations), the acceptance ratio should not be too large and not be too small. A high acceptance ratio typically implies that the deviation between the old and new configurations is, on average, small. This typically means that the configuration space is explored comparatively slowly (Fig. 2.7 belongs to this case; see also Fig. 2.8). A low acceptance ratio typically means that the Markov chain contains many identical configurations; again, this means that the configuration space is explored comparatively slowly. Both cases can result in large correlations of the sample and should be avoided. As a rule of thumb, the acceptance ratio should lie roughly between 30% and 50% [132]. In special cases, the acceptance ratio can be as high as 100% without loss of efficiency. One such move is the center-of-mass move discussed in Sec. 2.5.8. Even though this move has a high acceptance ratio, the proposed configurations deviate significantly from the previous configurations.

Even if we minimize the correlations between configurations by choosing an appropriate acceptance ratio, the samples are, in general, highly correlated. As an example, Fig. 2.8 shows the correlation coefficient  $r_k$  as a function of the lag  $k$  for the series of points shown in Fig. 2.7. If the lag  $k$  is smaller than 15,  $r_k$  lies outside the 95% confidence interval, indicating

that the sample is strongly correlated for small lag. For larger  $k$  ( $k > 41$ ), the  $r_k$  falls into the 95% confidence interval (note, only a small portion of the  $k > 41$  data is shown in Fig. 2.8). To reduce the correlations, we do not “measure” the observables for every configuration but instead “measure” observables for every  $K_s$ -th configuration.  $K_s$  should be chosen to be on the order of the correlation length. For example,  $K_s$  is around 20 for the samples used in Figs. 2.7 and 2.8. If we choose a large  $K_s$ , the samples are truly independent. Unfortunately, the use of truly uncorrelated samples wastes a huge amount of computer time since many configurations, which contain “partial information”, are not being used when accumulating observables. In practice, we choose  $K_s$  such that the correlations are not too large and not too small, that is, we weigh the computational effort involved in generating new configurations and calculating observables. For example, if an observable is “cheap” to calculate, it may be fine to choose a relatively small  $K_s$ . If, however, an observable is “expensive” to calculate, then it may be better to choose a somewhat larger  $K_s$ .

### 2.5.3 “Naive move”

The simplest move (the “naive move”) consists of shifting the position vector  $\mathbf{r}_{\text{old}}$  of a single bead by  $\delta\mathbf{r}$ , where  $\delta\mathbf{r}$  is drawn uniformly from the window  $[-\Delta\mathbf{r}, \Delta\mathbf{r}]$ . The basic idea behind this move is that the density matrix is a smooth function of  $\mathbf{x}$  and that a small change in  $\mathbf{x}$  does not introduce a huge change in the probability distribution  $\pi(\mathbf{x})$ . The size of the window  $\Delta\mathbf{r}$  can be adjusted such that the acceptance ratio of the proposed new position vector is around 50%. The proposal distribution  $G(\mathbf{x} \rightarrow \mathbf{x}')$  is a constant if only one bead  $\mathbf{r}_{\text{old}}$  is moved and the new bead lies in the window  $[-\Delta\mathbf{r} + \mathbf{r}_{\text{old}}, \Delta\mathbf{r} + \mathbf{r}_{\text{old}}]$ ; otherwise,  $G(\mathbf{x} \rightarrow \mathbf{x}') = 0$ . The guiding function  $g(\mathbf{x})$  is a constant across all space. According to Eq. (2.75), the acceptance function  $a(\mathbf{x})$  is the same as the probability distribution  $\pi(\mathbf{x})$ . Thus, the move is accepted according to

$$A(\mathbf{x} \rightarrow \mathbf{x}') = \min\left(1, \frac{\pi(\mathbf{x}')}{\pi(\mathbf{x})}\right). \quad (2.80)$$

Importantly, one cannot choose an unbalanced window like  $[-\epsilon\Delta\mathbf{r}, \Delta\mathbf{r}]$ , where  $\epsilon < 1$ , since the detailed balance condition, Eq. (2.71), is not satisfied in this case. In this example, it is possible to go from  $\mathbf{x}$  to  $\mathbf{x} + \Delta\mathbf{r}$  but it is not possible to go from  $\mathbf{x} + \Delta\mathbf{r}$  to  $\mathbf{x}$  in one move.

The algorithm for the naive move is the following: i) Let the current configuration  $\mathbf{x}$  be  $\mathbf{x} = (\mathbf{R}_0, \dots, \mathbf{R}_{n-1})$ . Randomly select a particle index  $k$  and a time slice index  $j$ . Set  $\mathbf{r}_{\text{old}} = \mathbf{r}_{k,j}$  and calculate the old probability distribution  $\pi_{\text{old}} = \pi(\mathbf{R}_0, \dots, \mathbf{R}_{n-1})$ . ii) Generate a new position  $\mathbf{r}_{\text{new}} = \mathbf{r}_{\text{old}} + \delta\mathbf{r}$ , where  $\delta\mathbf{r}$  is drawn uniformly from the window  $[-\Delta\mathbf{r}, \Delta\mathbf{r}]$ . Define  $\mathbf{R}_j^{\text{new}} = (\mathbf{r}_{1,j}, \dots, \mathbf{r}_{k-1,j}, \mathbf{r}_{\text{new}}, \mathbf{r}_{k+1,j}, \dots, \mathbf{r}_{N,j})$  and calculate the new probability distribution  $\pi_{\text{new}} = \pi(\mathbf{R}_0, \dots, \mathbf{R}_{j-1}, \mathbf{R}_j^{\text{new}}, \mathbf{R}_{j+1}, \dots, \mathbf{R}_{n-1})$ . iii) Calculate the ratio  $\pi_{\text{new}}/\pi_{\text{old}}$ . If this ratio is larger than a random number uniformly drawn from 0 to 1, accept the move and set  $\mathbf{r}_{k,j} = \mathbf{r}_{\text{new}}$ ; otherwise, reject the move and set  $\mathbf{r}_{k,j} = \mathbf{r}_{\text{old}}$ .

Although the naive move attempts to change only one bead at a time, whether the proposed move gets accepted or rejected depends on all the beads, i.e., the coordinates of all particles at all time slices, since the acceptance/rejection depends on the ratio  $\pi_{\text{new}}/\pi_{\text{old}}$ . Because the probability distribution  $\pi(\mathbf{x})$  is a product of density matrices represented by the links [Eq. (2.57)], the only contributing terms to the ratio  $\pi_{\text{new}}/\pi_{\text{old}}$  are the density matrices  $\rho(\mathbf{R}_{j-1}, \mathbf{R}_j; \tau)$  and  $\rho(\mathbf{R}_j, \mathbf{R}_{j+1}; \tau)$ . Furthermore, if one uses the second-order Trotter formula [Eq. (2.23)], which treats the potential and kinetic energy terms separately, the terms that contribute to  $\rho(\mathbf{R}_{j-1}, \mathbf{R}_j; \tau)$  and  $\rho(\mathbf{R}_j, \mathbf{R}_{j+1}; \tau)$  are the potential energy term  $\exp[-\tau V(\mathbf{R}_j)]$  and the kinetic energy terms  $\rho_0(\mathbf{r}_{k,j-1}, \mathbf{r}_{k,j}; \tau)$  and  $\rho_0(\mathbf{r}_{k,j}, \mathbf{r}_{k,j+1}; \tau)$ .

The caveat of the naive move is that the correlation length is typically long. In the best case scenario (i.e., in the case where all beads of all particles are considered exactly once and all proposed moves are accepted),  $n \times N$  moves are needed to generate a configuration in which every bead differs from the starting configuration. Thus, we calculate observables for every  $(\alpha \times n \times N)$ -th configuration, where  $\alpha$  is a constant greater than 1 that is adjusted to ensure that the observables are calculated from configurations with small correlations. In

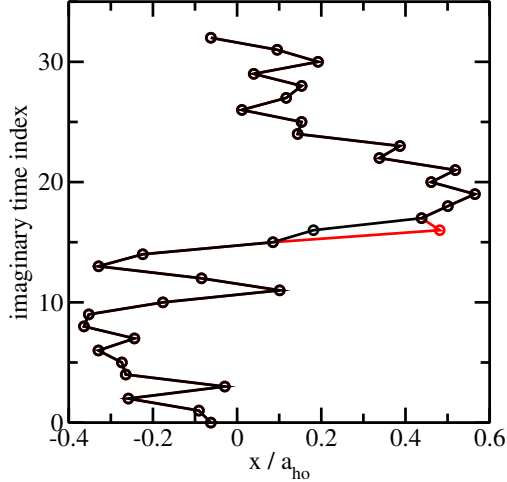


Figure 2.9: Illustration of the naive move for a single particle in a one-dimensional harmonic trap for  $n = 32$  beads. Black circles depict the old bead positions. The red circle shows the proposed bead position for the 16-th time slice index. It can be seen that only two links (namely those involving the 15-th and 16-th beads and the 16-th and 17-th beads) are changed.

practice, we find that  $\alpha$  lies between 2 and 20.

Figure 2.9 illustrates the naive move for a single particle in a one-dimensional harmonic trap. It can be seen that only one bead position is changed for the proposed move.

#### 2.5.4 “Wiggle move”

In general, the closer the guiding function  $g(\mathbf{x})$  is to the probability distribution  $\pi(\mathbf{x})$ , the more efficient the sampling method becomes. At high temperature, the systems considered in this thesis typically have a low density and are therefore described quite well by the non-interacting density matrix. Thus, we use the non-interacting density matrix as the guiding function  $g(\mathbf{x})$ . Since the non-interacting density matrix is a product of simple Gaussians both in free space [Eq. (2.11)] and in a harmonic trap [Eq. (5.22)], one can generate configurations with 100% acceptance ratio using the Box-Muller transformation or with high efficiency using the Marsaglia polar method or the Ziggurat algorithm. If the difference between the density matrix of the system to be simulated and the non-interacting density matrix is small,  $a(\mathbf{x})$

[see Eq. (2.75)] is close to 1 for all  $\mathbf{x}$ . In this case, the acceptance ratio for a move generated using the guiding function  $g(\mathbf{x})$  is high. Despite the large acceptance ratio, the correlation between consecutive configurations is small. In the non-interacting limit, the acceptance ratio is exactly 1.

We now consider an example. For the second-order Trotter formula (neglecting permutations), the kinetic energy contribution and the potential energy contribution separate naturally. Plugging Eq. (2.23) into Eq. (2.57) and choosing the non-interacting density matrix  $\rho_0(\mathbf{x})$  in free space,

$$\rho_0(\mathbf{x}) = \prod_{k=0}^{N-1} \rho_0(\mathbf{R}_k, \mathbf{R}_{k+1}; \tau), \quad (2.81)$$

as the guiding function  $g(\mathbf{x})$ , we obtain that  $a(\mathbf{x})$  contains only potential energy terms,

$$a(\mathbf{x}) = \exp \left( -\tau \sum_{k=0}^{N-1} V(\mathbf{R}_k) \right). \quad (2.82)$$

Alternatively, one could use the non-interacting density matrix in a harmonic trap [Eq. (5.22)] as the guiding function. Readers are referred to Ref. [20] to learn how to modify the equations accordingly. In the following, we use the non-interacting density matrix in free space as the guiding function. Depending on the number of beads changed simultaneously, the wiggle move is a single-bead move or a multi-bead move.

We now introduce the single-bead version of the wiggle move; the multi-bead version will be discussed in a separate step. We randomly select a particle index  $j$  and a time slice index  $k$ . Similar to the naive move, we define  $\mathbf{r}_{\text{old}} = \mathbf{r}_{j,k}$  and denote the new proposed position vector by  $\mathbf{r}_{\text{new}}$ . We define  $\mathbf{R}_k^{\text{new}} = (\mathbf{r}_{1,k}, \dots, \mathbf{r}_{j-1,k}, \mathbf{r}_{\text{new}}, \mathbf{r}_{j+1,k}, \dots, \mathbf{r}_{N,k})$ . The old and new configurations read

$$\mathbf{x} = \{\mathbf{R}_0, \dots, \mathbf{R}_{n-1}\} \quad (2.83)$$

and

$$\mathbf{x}' = \{\mathbf{R}_0, \dots, \mathbf{R}_{k-1}, \mathbf{R}_k^{\text{new}}, \mathbf{R}_{k+1}, \dots, \mathbf{R}_{n-1}\}, \quad (2.84)$$

respectively. Since the time slice index  $k$  is fixed, only the  $\rho_0(\mathbf{R}_{k'}, \mathbf{R}_{k'+1}; \tau)$  with  $k' = k$  and  $k' = k - 1$  are modified during the move. Moreover, only the bead corresponding to particle  $j$  is changed. Correspondingly, we only need to consider those pieces of  $\rho_0(\mathbf{x})$  that depend on  $\mathbf{r}_{j,k}$ ,  $\mathbf{r}_{j,k-1}$ , and  $\mathbf{r}_{j,k+1}$ . We thus write

$$\rho_0(\mathbf{x}) \propto \exp\left(-\frac{(\mathbf{r}_{j,k} - \mathbf{r}_{j,k-1})^2 + (\mathbf{r}_{j,k} - \mathbf{r}_{j,k+1})^2}{4\lambda_m\tau}\right) \quad (2.85)$$

or, rearranging the exponent,

$$\rho_0(\mathbf{x}) \propto \exp\left(-\frac{[\mathbf{r}_{j,k} - (\mathbf{r}_{j,k-1} + \mathbf{r}_{j,k+1})/2]^2}{2\lambda_m\tau}\right). \quad (2.86)$$

The right hand side of Eq. (2.86) is equal to a Gaussian whose mean value is given by the midpoint of the  $(k - 1)$ -th and the  $(k + 1)$ -th bead of the  $j$ -th particle and whose variance is  $\lambda_m\tau$ . To generate configurations according to the Gaussian guiding function  $g(\mathbf{x}) = \rho_0(\mathbf{x})$ , we choose the proposal distribution  $G(\mathbf{x} \rightarrow \mathbf{x}')$  to be

$$G(\mathbf{x} \rightarrow \mathbf{x}') \propto \exp\left(-\frac{[\mathbf{r}_{\text{new}} - (\mathbf{r}_{j,k-1} + \mathbf{r}_{j,k+1})/2]^2}{2\lambda_m\tau}\right). \quad (2.87)$$

Note that the right hand side of Eq. (2.87) involves only  $\mathbf{r}_{\text{new}}$  and not  $\mathbf{r}_{\text{old}}$ . Combining Eqs. (2.87) and (2.86), the detailed balance condition [Eq. (2.71)] is satisfied if we choose  $\rho_0(\mathbf{x})$  as the probability distribution  $\pi(\mathbf{x})$  and  $G(\mathbf{x} \rightarrow \mathbf{x}')$  as the transition probability  $P(\mathbf{x} \rightarrow \mathbf{x}')$ . This implies that the proposal distribution  $G(\mathbf{x} \rightarrow \mathbf{x}')$  given in Eq. (2.87) does generate samples according to  $g(\mathbf{x})$ . The wiggle move (i.e., the proposal distribution) generates configurations for which the bead  $\mathbf{r}_{\text{new}}$  is completely independent of the previous bead  $\mathbf{r}_{\text{old}}$ . In the non-interacting limit, the wiggle move is the best single-bead move because the acceptance ratio is 1 and the correlations are minimized. In this case, the single-bead move is analogous to the direct sampling for that bead.

The single-bead version of the wiggle move can be generalized to multiple consecutive beads. Since the multi-bead move leads to a deformation of a segment of the path, the move is called “wiggle move”. Our discussion follows Ref. [133]. We propose to change a path segment consisting of multiple beads according to  $\rho_0(\mathbf{x})$  instead of a single bead of the path. We denote the time slice indices of the two ends that are unchanged by  $k$  and  $k + s$ , where  $s$  is an integer power of 2. The case  $s < 0$  can be avoided by relabeling the beads, i.e., by choosing a different starting point of the path. The corresponding position vectors are  $\mathbf{r}_{j,k}$  and  $\mathbf{r}_{j,k+s}$ . As in the single-bead move, only a subset of the terms contributing to  $\rho_0(\mathbf{x})$  is changed during the move. The terms affected by the moves are included in Eq. (2.88) while those not affected are not written explicitly. We have

$$\begin{aligned}
\rho_0(\mathbf{x}) \propto & \underbrace{\exp\left(-\frac{(\mathbf{r}_{j,k} - \mathbf{r}_{j,k+s})^2}{4s\lambda_m\tau}\tau\right)}_{\text{constant}} \times \\
& \underbrace{\exp\left(-\frac{(\mathbf{r}_{j,k+s/2} - \bar{\mathbf{r}}_{j,k,k+s})^2}{s\lambda_m\tau}\right)}_{\text{zeroth level}} \times \\
& \underbrace{\exp\left(-\frac{(\mathbf{r}_{j,k+s/4} - \bar{\mathbf{r}}_{j,k,k+s/2})^2}{s\lambda_m\tau/2}\right) \exp\left(-\frac{(\mathbf{r}_{j,k+3s/4} - \bar{\mathbf{r}}_{j,k+s/2,k+s})^2}{s\lambda_m\tau/2}\right)}_{\text{first level}} \times \\
& \dots, \tag{2.88}
\end{aligned}$$

where  $\bar{\mathbf{r}}_{j,\alpha',\beta'} = (\mathbf{r}_{j,\alpha'} + \mathbf{r}_{j,\beta'})/2$ . If  $s$  is equal to  $2^l$ , Eq. (2.88) contains  $l$  levels (the zeroth level is counted as one level but the constant term is not). Equation (2.88) suggests that the sampling can be done level by level. For example, for a path segment consisting of 3 time slices ( $s = 4$ ), the beginning bead is  $\mathbf{r}_{j,0}$  and the ending bead is  $\mathbf{r}_{j,4}$ . Thus, there exist two levels in total. We propose the new midpoint bead  $\mathbf{r}_{j,2}^{\text{new}}$  according to the zeroth level term in Eq. (2.88) and then the new midpoint beads  $\mathbf{r}_{j,1}^{\text{new}}$  and  $\mathbf{r}_{j,3}^{\text{new}}$  according to the first level term in Eq. (2.88).

We outline a basic version of the multi-bead move first. The “staging version” will be

discussed in a second step. The basic version of the algorithm is less efficient but can be employed in connection with the Trotter formula and the pair product approximation. The staging version can only be used in connection with the Trotter formula. For each level, we generate new position vectors using the proposal distribution given in Eq. (2.87) with the subscripts  $k-1$  and  $k+1$  adjusted accordingly. Note that the Gaussian proposal distribution for each new position vector depends only on the position vectors of the next lower level. This procedure generates a proposed new path segment  $\{\mathbf{r}_{j,k+1}^{\text{new}}, \dots, \mathbf{r}_{j,k+s-1}^{\text{new}}\}$ , which is completely independent of the old path segment  $\{\mathbf{r}_{j,k+1}, \dots, \mathbf{r}_{j,k+s-1}\}$ . We denote the time slices that are involved by  $\mathbf{R}_q^{\text{new}}$ , where  $q$  ranges from  $k+1$  to  $k+s-1$ . Using the second-order Trotter formula,  $a(\mathbf{x})$  is given by Eq. (2.82) and we accept or reject using the acceptance distribution  $A(\mathbf{x} \rightarrow \mathbf{x}')$  given in Eq. (2.77). In this case, Eq. (2.77) can be simplified to

$$A(\mathbf{x} \rightarrow \mathbf{x}') = \min \left( 1, \prod_{q=k+1}^{k+s-1} \frac{\exp[-\tau V(\mathbf{R}_q^{\text{new}})]}{\exp[-\tau V(\mathbf{R}_q)]} \right). \quad (2.89)$$

Combining the multi-bead sampling discussed in the previous paragraph with the staging algorithm, which allows one to reject the move in advance if “bad points” are drawn, a more efficient sampling scheme can be obtained [133]. The “in advance rejection” is checked for at each level  $l$ . Let us assume that we are considering level  $l$  with the new midpoint beads  $\mathbf{r}_{j,k+s(1+2q)/2^{l+1}}^{\text{new}}$ , where  $q$  ranges from 0 to  $l+1$ . Using the second-order Trotter formula, the move is accepted or rejected based on

$$A_{\text{partial}} = \min \left( 1, \prod_{q=0}^{l+1} \frac{\exp[-\tau V(\mathbf{R}_{k+s(1+2q)/2^{l+1}}^{\text{new}})]}{\exp[-\tau V(\mathbf{R}_{k+s(1+2q)/2^{l+1}})]} \right). \quad (2.90)$$

If  $A_{\text{partial}}$  is smaller than a random number drawn uniformly from the interval  $[0,1]$ , the move is rejected at the  $l$ -th level and the new configuration is set equal to the old configuration; otherwise, the move is accepted. If the move is accepted at the  $l$ -th level, we go to the  $(l+1)$ -th level and repeat the procedure. If the final level is reached and the new proposed

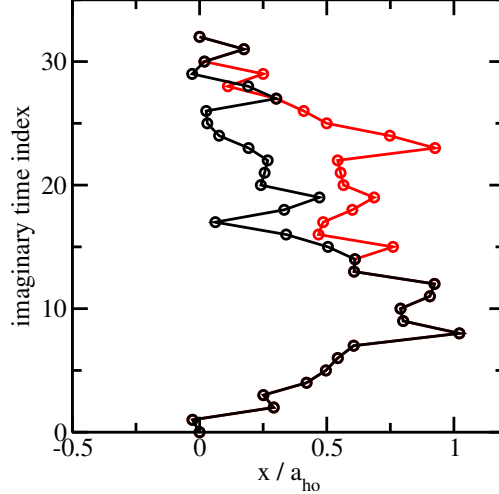


Figure 2.10: Illustration of the wobble move for a single particle in a one-dimensional harmonic trap. Black and red circles depict the old and proposed new configurations, respectively. It is assumed that the construction of the new path segment was continued after the construction of the first midpoint bead, the next two midpoint beads, and so on.

beads are accepted, then the entire path segment consisting of the proposed new beads  $\mathbf{r}_{j,k+1}^{\text{new}}, \dots, \mathbf{r}_{j,k+s-1}^{\text{new}}$  is accepted and a new configuration has been generated.

The “multi-bead sampling + staging” algorithm is equivalent to the basic multi-bead algorithm, which proposes all the beads of the path segment considered first and then accepts or rejects at the very end. The in advance rejection step (or the staged rejection) speeds up the algorithm. Importantly, the staging algorithm only works if the Trotter formula is used. If the pair product approximation is used, we need to reject at the very end because the density matrix for consecutive time slices cannot be reorganized into different levels.

Figure 2.10 illustrates the wobble move for a single particle in a one-dimensional harmonic trap ( $k = 14$  and  $s = 16$ ). The new path is constructed as follows: A new midpoint bead with index 22 is proposed and tested according to Eq. (2.90): If rejected (i.e., if the random number generated is smaller than  $A_{\text{partial}}$ ), the move is aborted in advance and the new configuration is set to the old configuration; if not rejected, the construction of the new path segment is continued (this is what is assumed in making Fig. 2.10). In the latter case, two new midpoint beads with index 18 and 26 are proposed and tested simultaneously according

to Eq. (2.90). If rejected, the move is aborted in advance and the new configuration is set to the old configuration; if not rejected, four new midpoint beads with index 16, 20, 24, and 28 are proposed and tested simultaneously according to Eq. (2.90). If rejected, the move is aborted in advance and the new configuration is set to the old configuration; if not rejected, eight new midpoint beads with index 15, 17, 19, 21, 23, 25, and 29 are tested simultaneously according to Eq. (2.90). If rejected, the move is ended with the new configuration being the old configuration; if not rejected, we accept the move in its entirety and change the path segment that involves the beads with index 15 to 29 to the new position vectors.

### 2.5.5 “Permute move”

The “permute” move is used to stochastically sample the permutations using the symmetrized density matrix given in Eq. (2.54). In this case, we need to change the sampling and the calculation of the estimators a bit since the probability distribution  $\pi(\mathbf{x})$  involves a sum over all possible permutations of products of density matrices. Accounting for permutations, the probability distribution can be written as [see Eq. (2.54)]

$$\pi(\mathbf{x}) = \sum_{P_\sigma} \text{sgn}(P_\sigma) \pi_{P_\sigma}(\mathbf{x}), \quad (2.91)$$

where  $P_\sigma$  runs through all possible permutations and  $\text{sgn}(P_\sigma)$  denotes the sign of the permutation. Specifically,  $\text{sgn}(P_\sigma)$  is equal to  $(-1)^{N_{\text{IF}}(P_\sigma)}$ , where  $N_{\text{IF}}(P_\sigma)$  denotes the number of inversions of identical fermions in  $P_\sigma$ . Equation (2.91) also applies to bosonic systems since the inversion of identical bosons does not introduce a sign flip.  $\pi_{P_\sigma}(\mathbf{x})$  represents a product over density matrices,

$$\pi_{P_\sigma}(\mathbf{R}_0, \dots, \mathbf{R}_{n-1}) = \rho(\mathbf{R}_0, \mathbf{R}_1; \tau) \dots \rho(\mathbf{R}_{n-2}, \mathbf{R}_{n-1}; \tau) \rho(\mathbf{R}_{n-1}, P_\sigma \mathbf{R}_0; \tau). \quad (2.92)$$

For a single-component  $N$  particle system, Eq. (2.91) contains  $N!$  terms and the function  $N_{\text{IF}}(P_\sigma)$  is identical to the function  $N_{\text{I}}(P_\sigma)$  used in Eq. (2.36). The function  $N_{\text{IF}}(P_\sigma)$  is more general and ensures that Eq. (2.91) applies not only to single-component systems but also to multi-component systems.

Rewriting Eq. (2.58) using Eq. (2.91), the observable reads

$$\langle \mathcal{O} \rangle = \sum_{P_\sigma} \underbrace{\frac{\text{sgn}(P_\sigma) \int_{\mathbf{x}'} \pi_{P_\sigma}(\mathbf{x}') d\mathbf{x}'}{\sum_{P_{\sigma'}} \text{sgn}(P_{\sigma'}) \int_{\mathbf{x}'} \pi_{P_{\sigma'}}(\mathbf{x}') d\mathbf{x}'}}_{\text{probability to be in permutation } P_\sigma} \underbrace{\int_{\mathbf{x}} w(\mathbf{x}) \frac{\pi_{P_\sigma}(\mathbf{x})}{\int_{\mathbf{x}'} \pi_{P_\sigma}(\mathbf{x}') d\mathbf{x}'} d\mathbf{x}}_{\text{contribution by permutation } P_\sigma}. \quad (2.93)$$

The general idea of treating the permutations is based on the following. We think of each term in Eq. (2.91) as a separate probability distribution, from which we can calculate the contribution to the observable [second part on the right hand side of Eq. (2.93)]. We then calculate the relative importance of each permutation and weigh the contribution to the observable accordingly [first part on the right hand side of Eq. (2.93)]. Note that the probability to be in permutation  $P_\sigma$  [first part on the right hand side of Eq. (2.93)] can be negative because of the  $\text{sgn}$  functions. Hence, one needs to carefully keep track of the sign. The contribution by permutation  $P_\sigma$  [second part on the right hand side of Eq. (2.93)], in contrast, is always positive. The fact that the probability to be in permutation  $P_\sigma$  can be negative leads to the well known Fermi sign problem [97, 99, 134, 135]. Readers are referred to Sec. 5.2.3 for a study that treats the signs explicitly.

The wiggle move and the naive move can be used to generate configurations according to  $\pi_{P_\sigma}$ . An additional move, the permute move, is needed to calculate the probability to be in the permutation  $P_\sigma$  [first part on the right hand side of Eq. (2.93)]. If we use Eq. (2.92) as written, we always need to permute the initial beads since  $P_\sigma$  is applied to  $\mathbf{R}_0$ . While this is formally correct, this tends to lead to low acceptance ratios in practice. To improve the efficiency of the algorithm, we use that the permutation operator commutes with the density matrix. This implies that  $P_\sigma$  can be applied to any time slice. This feature is used

in the permute move. Instead of always applying  $P_\sigma$  to  $\mathbf{R}_0$ ,  $P_\sigma$  is applied to  $\mathbf{R}_{k+s}$ , where  $k+s$  denotes the ending time slice (see the next paragraph for details).

The general idea of the permute move is that it proposes to change multiple consecutive time slices of paths of two or more particles. The proposed change consists of a permutation of the particle indices on one end. The simplest permute move is the 2-cycle permute move, which involves two particles. Let the beginning and ending time slices be  $k$  and  $k+s$ , and let the old configuration correspond to the identity permutation. We try to permute the first and second particles. As in many other moves, we use the non-interacting density matrix as our guiding function. Instead of permuting the zeroth time slice, we permute the  $(k+s)$ -th time slice, write out  $\rho_{0,P_\sigma}(\mathbf{x})$  for all particles, and reorganize the non-interacting density matrix  $\rho_{0,P_\sigma}(\mathbf{x})$  in a similar manner as in Eq. (2.88),

$$\begin{aligned}
\rho_{0,P_\sigma}(\mathbf{x}) \propto & \underbrace{\prod_{j=1}^N \exp\left(-\frac{(\mathbf{r}_{j,k} - \mathbf{r}_{P_\sigma j, k+s})^2}{4s\lambda_m\tau}\tau\right)}_{T(P_\sigma)} \times \\
& \underbrace{\prod_{j=1}^N \exp\left(-\frac{(\mathbf{r}_{j, k+s/2} - \tilde{\mathbf{r}}_{j, k, k+s})^2}{s\lambda_m\tau}\right)}_{\text{zeroth level}} \times \\
& \underbrace{\prod_{j=1}^N \exp\left(-\frac{(\mathbf{r}_{j, k+s/4} - \bar{\mathbf{r}}_{j, k, k+s/2})^2}{s\lambda_m\tau/2}\right) \exp\left(-\frac{(\mathbf{r}_{j, k+3s/4} - \tilde{\mathbf{r}}_{j, k+s/2, k+s})^2}{s\lambda_m\tau/2}\right)}_{\text{first level}} \times \\
& \dots, \tag{2.94}
\end{aligned}$$

where the average  $\tilde{\mathbf{r}}_{j, k, k+s}$  (note the “tilde”), which involves the ending time slice  $k+s$ , is defined to be  $(\mathbf{r}_{j, k} + \mathbf{r}_{P_\sigma j, k+s})/2$ . The averages  $\bar{\mathbf{r}}_{j, \alpha, \beta}$  (note the “bar”), which do not involve the ending time slice  $k+s$ , are defined below Eq. (2.88). The term  $T(P_\sigma)$  on the right hand side of Eq. (2.94) can be used to permute the particles, i.e., be used to calculate the relative probability of  $\rho_{0,P_\sigma}(\mathbf{x})$  for different  $P_\sigma$ . In practice, we construct a table of  $T(P_\sigma)$  for all

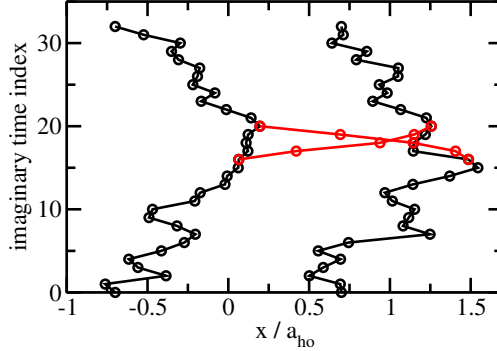


Figure 2.11: Illustration of the permute move for two particles in a one-dimensional harmonic trap. Black and red circles depict the old and proposed new configurations, respectively.

possible permutations  $P_\sigma$ . In the case of two particles, we have  $T(1)$  and  $T(P_{12})$  and the permute move is accepted with the probability  $p_{P_{12}}$ ,

$$p_{P_{12}} = \frac{T(P_{12})}{T(1) + T(P_{12})}. \quad (2.95)$$

If the move is accepted, we go to the second stage of the permute move, which samples the midpoint beads of all involved particles at time slice index  $k + s/2$  (this is similar to the wiggle move). The process is continued until the last level is reached. At any stage if the move is rejected, we abort the move. The outlined scheme can be generalized to a permutation cycle of arbitrary length and for an arbitrary number of particles [133].

Figure 2.11 illustrates the permute move for two particles in a one-dimensional harmonic trap. In the example,  $k = 16$  and  $s = 4$  and the old permutation corresponds to the identity permutation. The time slices at indices 16 and 20 are cut open. A probability to permute the path is calculated according to Eq. (2.95). If rejected (i.e., the random number generated is larger than  $p_{P_{12}}$ ), the old configuration is kept as the new configuration; otherwise, the permute move is continued by constructing two new paths that connect the beads  $\mathbf{r}_{1,16}$  and  $\mathbf{r}_{2,20}$ , and  $\mathbf{r}_{2,16}$  and  $\mathbf{r}_{1,20}$  similar to the wiggle move. We denote the time slices that are changed by  $\mathbf{R}_q^{\text{new}}$ , where  $q$  ranges from 17 to 19. We accept or reject the entire move according to

Eq. (2.89). If the second-order Trotter formula is used, this scheme can be combined—as in the wiggle move—with the staging algorithm. In this case, we construct the position vectors  $\mathbf{r}_{1,18}^{\text{new}}$  (generated from a Gaussian distribution with mean  $(\mathbf{r}_{1,16} + \mathbf{r}_{2,20})/2$  and variance  $2\lambda_m\tau$ ) and  $\mathbf{r}_{1,18}^{\text{new}}$  (generated from a Gaussian distribution with mean  $(\mathbf{r}_{2,16} + \mathbf{r}_{1,20})/2$  and variance  $2\lambda_m\tau$ ). We accept or reject at this stage according to Eq. (2.90) with  $l = 0$ . If rejected, we abort the move and set the new configuration equal to the old configuration. If accepted, we go on to the next level. In this case, we construct the position vectors  $\mathbf{r}_{1,17}^{\text{new}}$  (generated from a Gaussian distribution with mean  $(\mathbf{r}_{1,16} + \mathbf{r}_{1,18})/2$  and variance  $\lambda_m\tau$ ),  $\mathbf{r}_{1,19}^{\text{new}}$  (generated from a Gaussian distribution with mean  $(\mathbf{r}_{1,18} + \mathbf{r}_{2,20})/2$  and variance  $\lambda_m\tau$ ),  $\mathbf{r}_{2,17}^{\text{new}}$  (generated from a Gaussian distribution with mean  $(\mathbf{r}_{2,16} + \mathbf{r}_{2,18})/2$  and variance  $\lambda_m\tau$ ), and  $\mathbf{r}_{2,19}^{\text{new}}$  (generated from a Gaussian distribution with mean  $(\mathbf{r}_{2,18} + \mathbf{r}_{1,20})/2$  and variance  $\lambda_m\tau$ ). This final level is tested against Eq. (2.90) with  $l = 1$ . If rejected, we abort the move and set the new configuration equal to the old configuration; otherwise, we accept the move and update the configuration.

If the permute move is accepted at all stages, we need to change the status of the permutation of the path. Now, the beads  $\{\mathbf{r}_{1,0}, \dots, \mathbf{r}_{1,16}, \mathbf{r}_{1,17}^{\text{new}}, \mathbf{r}_{1,18}^{\text{new}}, \mathbf{r}_{1,19}^{\text{new}}, \mathbf{r}_{2,20}, \dots, \mathbf{r}_{2,31}\}$  belong to particle 1 and the beads  $\{\mathbf{r}_{2,0}, \dots, \mathbf{r}_{2,16}, \mathbf{r}_{2,17}^{\text{new}}, \mathbf{r}_{2,18}^{\text{new}}, \mathbf{r}_{2,19}^{\text{new}}, \mathbf{r}_{1,20}, \dots, \mathbf{r}_{1,31}\}$  belong to particle 2. The reason for switching the particle indices starting at time slice  $k + s$  (here  $k + s = 20$ ) is that we started the permute move with a permutation at the  $(k + s)$ -th time slice and that we need to obtain/end up with a path—according to the convention in Eq. (2.54)—that is permuted at the zeroth time slice. If one used the worm algorithm [102], this would not be needed since the worm algorithm also stores the single-particle links. Permute moves then only need to reconnect single-particle links.

Equation (2.91) contains  $N!$  terms for a single-component system. However, only  $\text{Partition}(N)$  number of distinct terms exist (for example, the probability distribution  $\pi_{P_{12}}(\mathbf{x})$  and  $\pi_{P_{13}}(\mathbf{x})$  are the same if one swaps the dummy particle indices 2 and 3), where

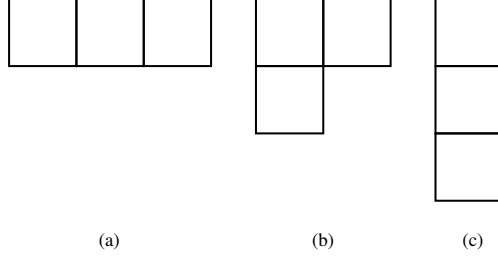


Figure 2.12: Young diagrams for (a) the 3-cycle permutation, (b) the 2-cycle permutation, and (c) the identity permutation.

Partition( $N$ ) is the number of unrestricted partitions of integer  $N$  [136]. For  $N = 1$  to 12, Partition( $N$ ) is equal to 1, 2, 3, 5, 7, 11, 15, 22, 30, 42, 56, and 77. The Partition( $N$ ) function is closely related to Young diagrams. A Young diagram is a diagram with  $n$  boxes arranged in  $n$  or fewer rows in such a way that the number of boxes in the  $i$ th row is less than that in the  $(i - 1)$ th row. For  $N$  identical particles, the number of possible Young diagrams is Partition( $N$ ). Rows that contain more than one box correspond to a permutation cycle. For example,  $P_{12}$  is a 2-cycle permutation and  $P_{123}$  is a 3-cycle permutation. The number of rows that contains  $k$  boxes is denoted as  $a_k$ . Each Young diagram represents  $n! / (\prod_{k=1}^n a_k! k^{a_k})$  permutations that contribute equally to  $\pi(\mathbf{x})$ . For example, for three particles, there are three different Young diagrams (see Fig. 2.12). The diagram shown in Fig. 2.12(a) (with  $a_3 = 1$  and  $a_1 = a_2 = 0$ ) represents the 3-cycle permutations  $P_{123}$  and  $P_{132}$ . These two permutations contribute equally, i.e.,  $\pi_{P_{123}}(\mathbf{x}) = \pi_{P_{132}}(\mathbf{x})$ . The diagram shown in Fig. 2.12(b) (with  $a_2 = 1$ ,  $a_1 = 1$ , and  $a_3 = 0$ ) represents the 2-cycle permutations  $P_{12}$ ,  $P_{13}$ , and,  $P_{23}$ . These three permutations contribute equally, since  $\pi_{P_{12}}(\mathbf{x})$ ,  $\pi_{P_{13}}(\mathbf{x})$ , and  $\pi_{P_{23}}(\mathbf{x})$  are equal. The diagram shown in Fig. 2.12(c) (with  $a_1 = 3$  and  $a_2 = a_3 = 0$ ) represents the identity permutation. In our current implementation, the reduction from  $N!$  to Partition( $N$ ) terms is not used. It seems that using the reduction could result in a more efficient algorithm. Indeed, Refs. [137, 138] do seem to employ ideas along these lines. We envision that an improved algorithm can be devised based on the following. If one monitored the probability to be in each permutation status and compared the probabilities for equivalent permutations, one

might be able to get a sense of the accuracy of the permute move and hence the algorithm. Furthermore, treating each set of equivalent permutations separately could help to reduce the sign problem (see Ref. [139] for ideas along this line).

If one uses the symmetrized density matrix, Eq. (2.55), the permute move is not needed. If fermions are involved,  $\pi(\mathbf{x})$  can be negative even though  $Z$  is positive definite. As in the permute move, the sign needs to be taken into account when calculating observables.

### 2.5.6 “Pair distance move”

The “pair distance” move is employed in systems with two-body zero-range interactions. Its use is especially important if the two-body  $s$ -wave scattering length diverges. The key motivation is that two particles can, if zero-range interactions are present, be close to each other or even on top of each other. Traditional moves such as the wiggle move and the naive move do, however, not generate configurations in which particles sit on top of each other. The reason is that the scaled pair distribution function  $4\pi r^2 P_{12}(r)$  for non-interacting particles or for uniformly distributed particles is zero at  $r = 0$ , implying that configurations with vanishing pair distance are not generated by the traditional moves. The pair distance move involves two particles with the same time slice index. The proposed move keeps the center of mass of the particle pair unchanged and modifies the relative distance. The details of the pair distance move can be found in Ch. 6.

### 2.5.7 “Whole path move”

At infinite temperature, the path of each particle shrinks to a single point because the density matrix becomes a  $\delta$ -function [see Eq. (2.9) and the discussion in the context of Figs. 2.2 and 2.3]. This means that the single-bead or multi-bead moves have a zero acceptance ratio. Moves that update the entire path, in contrast, have—in general—a finite acceptance ratio. This suggests that at high temperature, a move that updates the entire path of a particle is

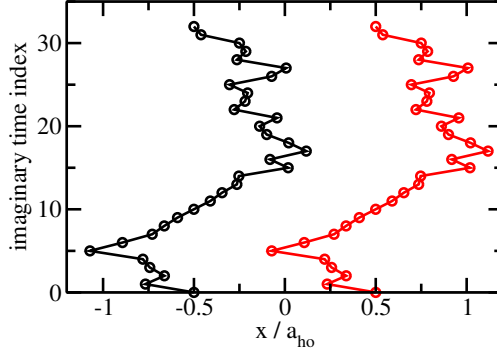


Figure 2.13: Illustration of the whole path move for a single particle in a one-dimensional harmonic trap. Black and red circles depict the old and new configurations, respectively.

necessary and efficient.

The whole path move proposes a new configuration by displacing the entire path of a single particle by  $\delta\mathbf{r}$ , where  $\delta\mathbf{r}$  is—as in the naive move—chosen uniformly from a pre-set window. Figure 2.13 illustrates the whole path move for a single particle in a one-dimensional harmonic trap. The proposed path is identical in shape to the old path but shifted by  $\delta\mathbf{r}$  (in this one-dimensional example,  $\delta\mathbf{r}$  is a scalar; in three-dimensional space,  $\delta\mathbf{r}$  has three components).

The ratio between the new probability distribution  $\pi(\mathbf{x}')$  and the old probability distribution  $\pi(\mathbf{x})$  is used to determine whether to accept or reject the move. The move is accepted if  $A(\mathbf{x} \rightarrow \mathbf{x}')$ ,

$$A(\mathbf{x} \rightarrow \mathbf{x}') = \min\left(1, \frac{\pi(\mathbf{x}')}{\pi(\mathbf{x})}\right), \quad (2.96)$$

is larger than a random number that is uniformly drawn from the interval  $[0, 1]$  and rejected otherwise. If the Trotter formula is used, one only needs to recalculate the terms involving the potential energy; the kinetic energy terms, which sit at the links and depend on  $\mathbf{r}_{k,j} - \mathbf{r}_{k,j-1}$ , are unchanged. Since the “whole path” move is typically used at high temperature, the number of time slices is comparatively small. This means that the number of operations involved in generating a new path is manageable despite the fact that the update involves the entire path.

### 2.5.8 “Center-of-mass move”

The “center-of-mass move” is motivated by the fact that the center-of-mass and relative Hamiltonian of some systems are not coupled at all or effectively decoupled. For example, for particles in a harmonic trap or in free space, the center-of-mass portion of the Hamiltonian decouples and can be treated as an effective single-particle Hamiltonian. The center-of-mass move efficiently explores the center-of-mass degrees of freedom. The center-of-mass degrees of freedom can be sampled efficiently using the multi-slice wiggle move for a single pseudoparticle with total mass  $Nm$ . The steps can be summarized as follows: i) Calculate the center-of-mass coordinates for the time slices to be updated (time slices  $k+1$  to  $k+s-1$ ). ii) Generate new center-of-mass coordinates for time slices  $k+1$  to  $k+s-1$  using the multi-bead wiggle move. iii) Shift the beads for time slices  $k+1$  to  $k+s-1$  according to the new center-of-mass coordinates. Proposing center-of-mass moves every now and then helps to reduce the correlations between configurations. In cases where the relative degrees of freedom are largely “frozen”, other moves can have a small acceptance ratio or may only change the path by a small amount while the center-of-mass move may have a large acceptance ratio, thereby helping with the exploration of the entire configuration space.

## 2.6 Estimators

In the previous two sections, we derived approximate expressions of the unsymmetrized density matrix, discussed Monte Carlo methods to generate the configurations  $\mathbf{x}$ , and introduced two different approaches to treat permutations. Looking at Eq. (2.58), having a proper form for the weight function  $w(\mathbf{x})$  is the only missing ingredient to complete the PIMC algorithm. This section derives expressions for the weight function  $w(\mathbf{x})$  for selected observables. Explicit expressions for  $w(\mathbf{x})$  can be derived for many observables using either thermodynamic relations [such as Eq. (2.6)] or the quantum estimator relation [Eq. (2.8)],

The expectation value  $\langle f(\mathbf{x}) \rangle$  of a function  $f(\mathbf{x})$  with respect to the probability density function  $p(\mathbf{x})$  is defined as

$$\langle f(\mathbf{x}) \rangle = \int_{\mathbf{x}} f(\mathbf{x})p(\mathbf{x})d\mathbf{x}. \quad (2.97)$$

In the PIMC algorithm, we generate a finite sequence  $X$  of configurations  $\mathbf{x}_j$ ,

$$X = \{\mathbf{x}_1, \mathbf{x}_2, \dots, \mathbf{x}_M\}, \quad (2.98)$$

according to the probability distribution  $\pi(\mathbf{x})$ . The expectation value  $\langle \mathcal{O} \rangle$  of the observable [Eq. (2.58)] can then be estimated by the mean value  $\bar{\mathcal{O}}$  of the series  $X$ ,

$$\bar{\mathcal{O}} = \langle \mathcal{O} \rangle_X = \sum_{j=1}^M w(\mathbf{x}_j)/M. \quad (2.99)$$

In the limit  $M \rightarrow \infty$ , the mean value  $\bar{\mathcal{O}}$  approaches the expectation value  $\langle \mathcal{O} \rangle$ .

According to the central limit theorem, the mean value  $\bar{\mathcal{O}}$  of the series  $X$  approaches the expectation value  $\langle \mathcal{O} \rangle$  in a predictive manner. The central limit theorem states that the mean of a sufficiently large number of random samples drawn from a distribution with a well-defined mean value and variance, is approximately normally distributed. A stronger version of the central limit theorem exists for Markov chains (i.e., for a series of data that is correlated for small lag and uncorrelated for large lag) [140]. To apply the central limit theorem to the PIMC samples  $w(\mathbf{x}_j)$ , we divide the series  $X$  into  $L$  groups, each with  $l = M/L$  configurations. Defining the block averages

$$S_k = \sum_{j=k \times l + 1}^{(k+1) \times l} w(\mathbf{x}_j)/l, \quad (2.100)$$

we construct the series  $\{S_1, \dots, S_L\}$ . Provided  $l$  is sufficiently large, the block averages  $S_k$  are normally distributed and the variance  $\sigma^2$  of the block averages can be estimated without

bias from the sample variance  $\langle \sigma^2 \rangle_X$ ,

$$\langle \sigma^2 \rangle_X = \sum_{j=1}^L (S_j - \bar{S}) / (L - 1), \quad (2.101)$$

where

$$\bar{S} = \sum_{j=1}^L S_j / L = \bar{\mathcal{O}}. \quad (2.102)$$

In our simulations, we use the sample standard deviation of the block averages divided by the number of block averages, i.e.,

$$\langle \sigma_{\bar{\mathcal{O}}} \rangle_X = \sqrt{\frac{\langle \sigma^2 \rangle_X}{L}}, \quad (2.103)$$

to estimate the error of the expectation value  $\langle \mathcal{O} \rangle$ . That is, we report the mean  $\bar{\mathcal{O}}$  with error  $\langle \sigma_{\bar{\mathcal{O}}} \rangle_X$ . Considering  $Q$  simulations, each yielding a series  $X_j$  and correspondingly  $\sqrt{\langle \sigma^2 \rangle_{X_j}}$  (assuming finite  $L$ ), the estimate of the standard deviation is biased because the mean value of a square root function is not equal to the square root of the mean, i.e.,

$$\frac{\sum_{j=1}^Q \sqrt{\langle \sigma^2 \rangle_{X_j}}}{Q} \neq \sqrt{\frac{\sum_{j=1}^Q \langle \sigma^2 \rangle_{X_j}}{Q}}. \quad (2.104)$$

Since the bias becomes negligible for sufficiently large  $L$ , there is no need to correct for the bias. In our simulations, we typically set  $L$  to be 80 for each processor. Because the  $\{S_1, \dots, S_L\}$  are normally distributed, the variance  $\langle \sigma^2 \rangle_X$  is approximately a constant for sufficiently large  $L$ . This implies that the error  $\langle \sigma_{\bar{\mathcal{O}}} \rangle_X$  scales as  $1/\sqrt{L}$  according to Eq. (2.103). Thus, to improve the accuracy of an observable by an order of magnitude, the computational time needs to be increased by two orders of magnitude.

To check whether the final distribution is approximately normal, one can make a histogram of the observable under study. Figure 2.14 shows the histogram for an observable

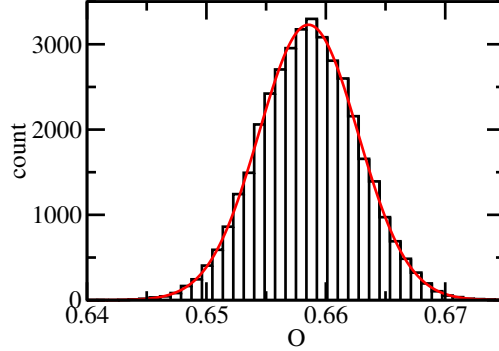


Figure 2.14: Histogram of samples of an observable  $O$  [the ratio of the partition function of the non-interacting (3,1) system and the partition function of the (3,1) system at unitarity at  $\beta\hbar\omega = 0.7$ ]. The simulation is done on 480 processors and each processor produces 80 samples. The red solid line shows the unnormalized normal distribution with mean value 0.658547 and standard deviation 0.00415146.

discussed in detail in Ch. 8, namely the ratio of the partition function of the non-interacting (3,1) system and the partition function of the (3,1) system at unitarity at  $\beta\hbar\omega = 0.7$ . The notation (3,1) refers to three spin-up fermions and one spin down fermion under external harmonic confinement. The simulation is done on 480 processors and each processor produces 80 samples. This means that the histogram in Fig. 2.14 is constructed using  $480 \times 80 = 38,400$  samples. The sample mean is 0.658547 and the sample variance is 0.0000172346 (the sample standard deviation is 0.00415146). Using the calculated mean and variance, the solid line in Fig. 2.14 shows the corresponding normal distribution. It can be seen that the solid line provides a faithful description of the histogram, indicating that the underlying samples are indeed normally distributed. The presented analysis requires a large number of block averages. In practice, it may not be feasible or advisable to obtain many block averages. In such a case, one can check if the error scales as  $\sqrt{1/L}$ . Reducing the number of block averages by a factor of two, one should observe that, if the block averages are normally distributed, the error increases roughly by a factor of  $\sqrt{2}$ . This check can be performed for as few as 5 or 10 block averages and provides, in many cases, enough information to reliably assign error bars.

To check explicitly whether the samples are independent, one needs to perform autocor-

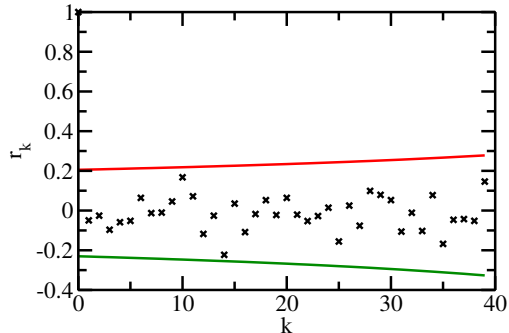


Figure 2.15: Correlation coefficient  $r_k$  as a function of the lag  $k$  for the sample and observable considered in Fig. 2.14. The results for a single processor are considered, i.e., a series of 80 data points is analyzed. The upper and lower solid lines show the 95% confidence interval.

relation tests. Figure 2.15 shows the correlation coefficient  $r_k$  [Eq. (2.62) for  $M = 80$ ] for a single processor (i.e., a series of 80 data points) as a function of the lag  $k$  for the system and observable considered in Fig. 2.14. Since the correlation coefficients lie all within the confidence band, we say that the data pass the autocorrelation test. Similar results are obtained for the data generated by the other 479 processors. This verifies that the samples are truly independent.

### 2.6.1 Energy estimator

The energy, which can be calculated in PIMC simulations, is a key quantity in understanding the thermodynamics of a system. The literature discusses a number of different energy estimators [19]. In the following, we discuss a few of these. Using the thermodynamic relation, Eq. (2.6), and plugging in one of the approximate expressions for the density matrix, an explicit expression for the weight function  $w(\mathbf{x})$  can be derived.

As an example, we derive the thermodynamic energy estimator for the second-order Trotter formula, Eq. (2.23), for particles without permutations. Using Eq. (2.22), the partition

function  $Z$  reads

$$Z = \int_{\mathbf{R}_0} \dots \int_{\mathbf{R}_{n-1}} \rho(\mathbf{R}_0, \mathbf{R}_1; \tau) \dots \rho(\mathbf{R}_{n-1}, \mathbf{R}_n; \tau) d\mathbf{R}_0 \dots d\mathbf{R}_{n-1} \quad (2.105)$$

$$\begin{aligned} &= \int_{\mathbf{R}_0} \dots \int_{\mathbf{R}_{n-1}} \rho_0(\mathbf{R}_0, \mathbf{R}_1; \tau) \dots \rho_0(\mathbf{R}_{n-1}, \mathbf{R}_n; \tau) \times \\ &\quad \exp\left(-\tau \sum_{j=0}^{n-1} V(\mathbf{R}_j)\right) d\mathbf{R}_0 \dots d\mathbf{R}_{n-1}, \end{aligned} \quad (2.106)$$

where  $\mathbf{R}_n = \mathbf{R}_0$  and  $\rho_0$  is defined in Eq. (2.11). Note that the second-order Trotter formula gives the same result for  $Z$  as the first-order Trotter formula since  $Z$  can be written in terms of the diagonal part of the density matrix. If the off-diagonal parts of the density matrix are needed, such as in PIGS simulations or simulations involving open paths, special care needs to be taken in evaluating terms that depend on the two open ends. Taking the derivative with respect to  $\beta$  on both sides of Eq. (2.106), dividing by  $-Z$ , and using the relation  $\beta = n\tau$ , we arrive at

$$\begin{aligned} \langle E_T \rangle &= -\frac{1}{Z} \frac{\partial Z}{\partial \beta} \quad (2.107) \\ &= -\frac{1}{Z} \int_{\mathbf{R}_0} \dots \int_{\mathbf{R}_{n-1}} \frac{1}{n} \times \\ &\quad \frac{\partial}{\partial \tau} \left( \rho_0(\mathbf{R}_0, \mathbf{R}_1; \tau) \dots \rho_0(\mathbf{R}_{n-1}, \mathbf{R}_n; \tau) \exp\left(-\tau \sum_{j=0}^{n-1} V(\mathbf{R}_j)\right) \right) d\mathbf{R}_0 \dots d\mathbf{R}_{n-1}. \end{aligned} \quad (2.108)$$

Combining Eqs. (2.57) and (2.23), we recognize that Eq. (2.108) can be rewritten in terms of  $\pi(\mathbf{x})$ ,

$$\langle E_T \rangle = -\frac{1}{Z} \int_{\mathbf{x}} \frac{1}{n} \frac{\partial}{\partial \tau} \pi(\mathbf{x}) d\mathbf{x}. \quad (2.109)$$

Applying the chain rule to evaluate  $\partial\pi(\mathbf{x})/\partial\tau$ , we obtain

$$\langle E_T \rangle = \frac{1}{Z} \int_{\mathbf{x}} \frac{1}{n} \sum_{j=0}^{n-1} \left( \frac{3N}{2\tau} - \frac{(\mathbf{R}_j - \mathbf{R}_{j+1})^2}{4\lambda_m\tau^2} + V(\mathbf{R}_j) \right) \pi(\mathbf{x}) d\mathbf{x}. \quad (2.110)$$

Comparing Eqs. (2.110) and (2.58), we obtain

$$w(\mathbf{x}) = \frac{1}{n} \sum_{j=0}^{n-1} \left( \frac{3N}{2\tau} - \frac{(\mathbf{R}_j - \mathbf{R}_{j+1})^2}{4\lambda_m\tau^2} + V(\mathbf{R}_j) \right). \quad (2.111)$$

Equation (2.111) can be evaluated straightforwardly for any configuration  $\mathbf{x}$ .

Using the quantum estimator relation, Eq. (2.8), an alternative energy estimator can be derived. Here, we derive the quantum energy estimator for particles without permutations using the second-order Trotter formula as an example. The position representation of the Hamiltonian  $\hat{H}$  reads [35]

$$\langle \mathbf{R} | \hat{H} | \mathbf{R}' \rangle = H_{\mathbf{R}} \delta(\mathbf{R} - \mathbf{R}') = [-\lambda_m \nabla_{\mathbf{R}}^2 + V(\mathbf{R})] \delta(\mathbf{R} - \mathbf{R}'). \quad (2.112)$$

Using Eq. (2.112) and inserting a closure relation [Eq. (2.13) with  $\mathbf{R} = \mathbf{R}''$ ],  $\langle \mathbf{R} | \exp(-\tau \hat{H}) \hat{H} | \mathbf{R}' \rangle$  can be written as

$$\langle \mathbf{R} | \exp(-\tau \hat{H}) \hat{H} | \mathbf{R}' \rangle = \int_{\mathbf{R}''} \langle \mathbf{R} | \exp(-\tau H) | \mathbf{R}'' \rangle \langle \mathbf{R}'' | \exp(-\tau H) | \mathbf{R}' \rangle d\mathbf{R}'' \quad (2.113)$$

$$= \int_{\mathbf{R}''} \rho(\mathbf{R}, \mathbf{R}''; \tau) [-\lambda_m \nabla_{\mathbf{R}''}^2 + V(\mathbf{R}'')] \delta(\mathbf{R}'' - \mathbf{R}') d\mathbf{R}'' . \quad (2.114)$$

Applying integration by parts twice to Eq. (2.114), we obtain

$$\langle \mathbf{R} | \exp(-\tau \hat{H}) \hat{H} | \mathbf{R}' \rangle = \int_{\mathbf{R}''} \delta(\mathbf{R}'' - \mathbf{R}') [-\lambda_m \nabla_{\mathbf{R}''}^2 + V(\mathbf{R}'')] \rho(\mathbf{R}, \mathbf{R}''; \tau) d\mathbf{R}'' \quad (2.115)$$

$$= [-\lambda_m \nabla_{\mathbf{R}'}^2 + V(\mathbf{R}')] \rho(\mathbf{R}, \mathbf{R}'; \tau). \quad (2.116)$$

Inserting the closure relation [Eq. (2.13)]  $n - 1$  times into Eq. (2.8) with  $\hat{\mathcal{O}} = \hat{H}$ , we obtain

$$\langle E_H \rangle = \frac{\text{Tr} \left[ \left( \prod_{j=1}^n e^{-\tau \hat{H}} \right) \hat{H} \right]}{Z} \quad (2.117)$$

$$= -\frac{1}{Z} \int_{\mathbf{R}_0} \cdots \int_{\mathbf{R}_{n-1}} \rho(\mathbf{R}_0, \mathbf{R}_1; \tau) \rho(\mathbf{R}_1, \mathbf{R}_2; \tau) \cdots \rho(\mathbf{R}_{n-2}, \mathbf{R}_{n-1}; \tau) \times \\ \{ [-\lambda_m \nabla_{\mathbf{R}_0}^2 + V(\mathbf{R}_0)] \rho(\mathbf{R}_{n-1}, \mathbf{R}_0; \tau) \} d\mathbf{R}_0 \cdots d\mathbf{R}_{n-1}. \quad (2.118)$$

Applying the second-order Trotter formula [Eq. (2.23)] to Eq. (2.118), we obtain

$$\langle E_H \rangle = \int_{\mathbf{x}} \left( \frac{3N}{2\tau} - \frac{(\mathbf{R}_0 - \mathbf{R}_{n-1})^2}{4\lambda_m \tau^2} + V(\mathbf{R}_0) - (\mathbf{R}_0 - \mathbf{R}_{n-1}) \cdot \nabla_{\mathbf{R}_0} V(\mathbf{R}_0) \right. \\ \left. + \lambda_m \tau \nabla_{\mathbf{R}_0}^2 V(\mathbf{R}_0) - \lambda_m \tau^2 (\nabla_{\mathbf{R}_0} V(\mathbf{R}_0))^2 \right) \pi(\mathbf{x}) d\mathbf{x}. \quad (2.119)$$

Because  $\hat{H}$  commutes with the density matrix,  $\hat{H}$  can be applied to any time slice. Averaging over all time slices to improve the accuracy (i.e., to take more measurements for each configuration), we obtain

$$\langle E_H \rangle = \int_{\mathbf{x}} \frac{1}{n} \sum_{j=0}^{n-1} \left( \frac{3N}{2\tau} - \frac{(\mathbf{R}_j - \mathbf{R}_{j+1})^2}{4\lambda_m \tau^2} + V(\mathbf{R}_j) - (\mathbf{R}_j - \mathbf{R}_{j+1}) \cdot \nabla_{\mathbf{R}_j} V(\mathbf{R}_j) \right. \\ \left. + \lambda_m \tau \nabla_{\mathbf{R}_j}^2 V(\mathbf{R}_j) - \lambda_m \tau^2 (\nabla_{\mathbf{R}_j} V(\mathbf{R}_j))^2 \right) \pi(\mathbf{x}) d\mathbf{x}, \quad (2.120)$$

where  $\mathbf{R}_n = \mathbf{R}_0$ . Comparing Eqs. (2.120) and (2.58), we obtain

$$w(\mathbf{x}) = \frac{1}{n} \sum_{j=0}^{n-1} \left( \frac{3N}{2\tau} - \frac{(\mathbf{R}_j - \mathbf{R}_{j+1})^2}{4\lambda_m \tau^2} + V(\mathbf{R}_j) - (\mathbf{R}_j - \mathbf{R}_{j+1}) \cdot \nabla_{\mathbf{R}_j} V(\mathbf{R}_j) \right. \\ \left. + \lambda_m \tau \nabla_{\mathbf{R}_j}^2 V(\mathbf{R}_j) - \lambda_m \tau^2 (\nabla_{\mathbf{R}_j} V(\mathbf{R}_j))^2 \right). \quad (2.121)$$

Compared to Eq. (2.111), Eq. (2.121) contains three extra terms in the sum. In the  $n \rightarrow \infty$  limit, both estimators approach the true expectation value. However, for finite  $n$ , the two

generally give different estimates of the energy. For example, Fig. 6.5 shows the thermodynamic energy estimator as a function of the time step  $\tau$ . To obtain accurate results, one needs to extrapolate the finite  $\tau$  calculations to the zero time step limit. If accuracy is not crucial, the difference between the two estimators for a single  $\tau$  may be used as an estimate of the systematic error [19].

Other energy estimators such as the virial estimator, which originates from the virial theorem [19], exist.

## 2.6.2 Structural properties

Structural properties such as the single, pair, and triple distribution functions can be obtained from the diagonal term of the density matrix in position space. Compared to the energy estimator, the determination of  $w(\mathbf{x})$  for structural properties is much more straightforward. For example, the operator  $\hat{D}_2(r)$  for obtaining the scaled pair distribution function  $4\pi r^2 P_{12}(r)$ , which is normalized according to  $\int_0^\infty 4\pi P_{12}(r)r^2 dr = 1$ , between particle 1 and 2 can be expressed as  $\hat{D}_2(r) = \delta(|\mathbf{r}_1 - \mathbf{r}_2| - r)$ . This expression can be inserted into the quantum estimator and  $w(\mathbf{x})$  can be derived. In PIMC simulations, the diagonal term of the density matrix corresponds to the information carried by the time slices. Since all time slices are equivalent, we can treat the information of all time slices on equal footing and accumulate the weight of the structural properties according to all time slices  $\mathbf{R}_j$ . Similar to the stochastic evaluation of structural properties for zero-temperature wave function, the  $\delta$ -function in the operator  $\hat{D}_2(r)$  amounts to sorting the distribution into finite spaced windows and counting the number of configurations that fall into each of the windows.

For example, to obtain the scaled pair distribution function  $4\pi r^2 P_{12}(r)$  for two particles in a harmonic trap, we discretize the pair distance  $r_{12}$ ,  $r_{12} = |\mathbf{r}_1 - \mathbf{r}_2|$ , into a series of  $k_{\max}$  bins,  $[k\delta r, (k+1)\delta r]$ , where  $k$  range from 0 to  $k_{\max} - 1$ . During the simulation, the pair distance is calculated for several configurations and sorted into the bins, i.e., a histogram

of the pair distances is collected. For each configuration considered (note, we may skip configurations to ensure that the samples collected have small correlations), the pair distance  $r_{12}$  is calculated for each time slice  $\mathbf{R}_j$  ( $j = 0, \dots, n - 1$ ). The bin number  $l$  of the histogram is calculated by evaluating  $l = \text{Floor}(r_{12}/\delta r)$ , where  $\text{Floor}(x)$  gives the largest integer smaller or equal to  $x$ , and the histogram value  $v_l$  of the  $l$ -th bin is increased by one. At the end, the histogram defined by the  $v_l$  is normalized by dividing by the total number  $B_t$  of pair distances considered and the bin size  $\delta r$ . The histogram created is a discretized version of the scaled pair distribution function  $4\pi r^2 P_{12}(r)$ . Importantly, the approach outlined yields the correct normalization even if some pair distances generated during the simulation are larger than  $j_{\max}\delta r$ . We typically monitor how many distances cannot be sorted into the histogram by comparing  $\sum_l v_l$  with  $B_t$ . If the fraction is too large, then the “cutoff”  $j_{\max}\delta r$  needs to be increased.

Because the process involved in calculating different structural properties such as the pair distribution function and triple distribution function is the same, the data structure used to accumulate different distribution functions and the accumulating process can be described by a single class in object oriented programming languages. This avoids duplication of the code. In the code, we construct the desired estimator (the “object”) such as the pair distribution estimator and the triple distribution estimator according to the same class but initialize with observable specific parameters such as the bin size, the bin number, and the number of particles. To accumulate the weight and finalize the results, we call the same virtual methods for different estimators. The actual implementation for these virtual methods may or may not be the same for different estimators. For example, in my code, the scaled pair and scaled triple distribution functions share the same implementation since both are described by an operator of the form  $\delta(r_{\text{ref}} - r)$ , where  $r_{\text{ref}}$  is either the pair distance or the tree-body hyperradius. The (unscaled) pair distribution function, in contrast, is described by an operator of the form  $\frac{1}{4\pi r^2}\delta(r_{\text{ref}} - r)$  and implemented separately.

## 2.7 Brief summary

All ingredients needed to perform a PIMC simulation have now been discussed. In this section, we combine the ingredients and sketch the PIMC algorithm.

1. Initialization.
  - (a) Read in parameters such as the temperature, the number of time slices, the number of particles, ... and initialize everything including the random number seeds. The seeds should be different and uncorrelated for different processors if the program is run in parallel.
  - (b) Read in or generate an initial configuration  $\mathbf{x}$ . The generation of an initial configuration could be done semi-randomly (coordinates are chosen randomly from a pre-defined window). An initial configuration is “good” if the corresponding probability distribution  $\pi(\mathbf{x})$  is large.
2. Equilibration (if the initial configuration was obtained from a previous, equilibrated simulation, the equilibration step is not needed). Update the initial configuration until the new configuration has no memory of the initial configuration. The new configurations are generated using the moves discussed in Secs. 2.5.3-2.5.8. It is not always clear *a priori* which moves are efficient and which ones are not; while some intuition can be developed based on physical arguments, in general, the simulator has to explore the efficiency of the various moves by “trial and error”. In practice, the length of the equilibration process can be estimated by analyzing the autocorrelation of selected estimators. During the equilibration process, estimators typically “curve” toward the true expectation value with increasing simulation time. It is important to be aware that the convergence rate toward the true expectation value can be very different for different estimators.
3. Accumulation of expectation values (“measurement”).

- (a) Update the configuration using the moves discussed in Secs. 2.5.3-2.5.8. Each type of move is used multiple times and the number of moves is adjusted to ensure that the configurations used for calculating the estimators have small correlations.
  - (b) Apply the estimators and accumulate expectation values.
  - (c) Repeat steps (a) and (b) for  $L$  times to get a list of block averages  $\{S_1 \dots S_L\}$  of the expectation values for each estimator.
4. Finalization. Determine the mean and error for each observable using Eqs. (2.99) and (2.103). Save the final configuration for use in future simulations.

The algorithm outlined is for a fixed time step  $\tau$  (or a fixed number of time slices  $n$ ). For observables like the energy, we need to perform PIMC simulations for different  $\tau$  and extrapolate to the zero  $\tau$  limit. For observables like the structural properties, we usually simulate at a sufficiently small time step and check the error due to the finite time step by comparing the structural properties for different time steps. The reason for bypassing the extrapolation process is that the convergence for different bins is different and, in general, needs to be performed separately for each bin.

# Chapter 3

## Harmonically trapped Fermi gas: Temperature dependence of the Tan contact

by Yangqian Yan<sup>1</sup> and D. Blume<sup>1,2</sup>

<sup>1</sup>Department of Physics and Astronomy, Washington State University, Pullman,  
Washington 99164-2814, USA

<sup>2</sup>ITAMP, Harvard-Smithsonian Center for Astrophysics, 60 Garden Street, Cambridge,  
Massachusetts 02138, USA

Copyright (2013) by the American Physical Society

Ultracold atomic gases with short-range interactions are characterized by a number of universal species-independent relations. Many of these relations involve the two-body Tan contact. Employing the canonical ensemble, we determine the Tan contact for small harmonically trapped two-component Fermi gases at unitarity over a wide range of temperatures, including the zero and high temperature regimes. A cluster expansion that describes the properties of the  $N$ -particle system in terms of those of smaller subsystems is introduced

and shown to provide an accurate description of the contact in the high temperature regime. Finite-range corrections are quantified and the role of the Fermi statistics is elucidated by comparing results for Fermi, Bose and Boltzmann statistics.

### 3.1 Harmonically trapped Fermi gas: Temperature dependence of the Tan contact

Systems with short-range interactions are characterized by universal relations that are independent of the details of the underlying interactions. The Tan contact [49–51, 141, 142], e.g., enters into a large number of universal relations and connects physically distinct quantities such as the large momentum tail, the inelastic loss rate, the number of pairs with small interparticle distances, and certain characteristics of radio frequency (rf) spectra. A striking feature of many of the universal relations is that they apply to homogeneous *and* inhomogeneous systems at zero *and* finite temperature. Yet, although many universal relations that evolve around the Tan contact are known, only a few explicit measurements [52–56] and calculations [57–67] of the Tan contact exist. For example, the dependence of the Tan contact of the spin-balanced homogeneous two-component Fermi gas at unitarity on the temperature is highly debated. While some studies predict a monotonic decrease of the contact with increasing temperature, others predict a non-monotonic dependence.

Recently, small trapped atomic Fermi gases have been prepared experimentally [91, 93], motivating theoretical studies of few-fermion systems as a function of the temperature. While the contact of large harmonically-trapped spin-balanced two-component Fermi gases is predicted to decrease monotonically with increasing temperature, the behavior of few-atom systems is largely unexplored. As we will show in this work, such studies provide a detailed qualitative understanding of the temperature dependence of the contact, while at the time establishing accurate benchmarks.

This paper considers small Fermi gases consisting of  $N_1$  spin-up and  $N_2$  spin-down fermions under external spherically symmetric harmonic confinement. Working in the canonical ensemble, we determine the Tan contact at unitarity with an accuracy at the few percent level as a function of the temperature, including the low (near zero) temperature regime and the high temperature regime. Our main findings are: *(i)* We devise a cluster expansion in the canonical ensemble that describes the high temperature tail of the Tan contact accurately. This expansion assumes a fixed number of particles and is thus, unlike the virial expansion [88, 89, 143, 144], applicable to small and large systems. The cluster expansion can be applied to any thermodynamic observable calculated in the canonical ensemble. *(ii)* While the contact of the trapped  $(N_1, N_2) = (1, 1)$  and  $(2, 2)$  systems is maximal at  $T = 0$ , that of the  $(2, 1)$ ,  $(3, 1)$  and  $(4, 1)$  systems shows a maximum at finite temperature. A microscopic interpretation of this behavior is offered. *(iii)* For the cases studied, the contact shows a non-negligible dependence on the range  $r_0$  of the underlying two-body potential at low temperature; in the high temperature regime, in contrast, the range dependence is negligible. *(iv)* Fermi statistics plays a role at temperatures where three-body physics is non-negligible. The role of the Fermi statistics is elucidated by turning the exchange symmetry off and by switching to Bose statistics.

The two-component Fermi gas consisting of  $N$  atoms with mass  $m$  and position vectors  $\mathbf{r}_j$  ( $j = 1, \dots, N$ ) is described by the model Hamiltonian  $H$ ,

$$H = \sum_{j=1}^N \left( \frac{-\hbar^2}{2m} \nabla_j^2 + \frac{1}{2} m \omega^2 \mathbf{r}_j^2 \right) + \sum_{j=1}^{N_1} \sum_{k=N_1+1}^N V_{\text{tb}}(\mathbf{r}_{jk}), \quad (3.1)$$

where  $\omega$  denotes the angular trapping frequency. We consider two different interspecies two-body potentials  $V_{\text{tb}}$ , a regularized zero-range pseudopotential  $V_{\text{F}}$  [3] and a short-range Gaussian potential  $V_{\text{G}}$  with depth  $U_0$  ( $U_0 < 0$ ) and range  $r_0$ ,  $V_{\text{G}}(\mathbf{r}_{jk}) = U_0 \exp[-\mathbf{r}_{jk}^2/(2r_0^2)]$ . For a given  $r_0$ , we adjust  $U_0$  such that  $V_{\text{G}}$  supports a single zero-energy  $s$ -wave bound state in free space, i.e., such that the  $s$ -wave scattering length  $a_s$  diverges. Our calculations use

$r_0 \ll a_{\text{ho}}$ , where  $a_{\text{ho}}$  is the harmonic oscillator length,  $a_{\text{ho}} = \sqrt{\hbar/(m\omega)}$ . This paper considers temperatures ranging from  $T = 0$  to  $k_B T \gg E_{\text{ho}}$ , where  $E_{\text{ho}} = \hbar\omega$ . The largest temperatures considered are chosen such that the two-body interactions can be reliably parametrized by the  $s$ -wave scattering length and corresponding effective range correction, i.e., so that higher partial wave contributions in the two-body sector can be neglected.

To determine the Tan contact  $C_{N_1, N_2}$ , we employ the adiabatic and pair relations,

$$C_{N_1, N_2} = \frac{4\pi m}{\hbar^2} \left\langle \frac{\partial E(a_s)}{\partial(-a_s^{-1})} \right\rangle_{\text{th}} \quad (3.2)$$

and

$$C_{N_1, N_2} = 4\pi \lim_{s \rightarrow 0} \frac{\langle N_{\text{pair}}^{r < s} \rangle_{\text{th}}}{s}; \quad (3.3)$$

here, the  $\langle \cdot \rangle_{\text{th}}$  notation indicates a thermal average and  $E(a_s)$  denotes the energy of the system. The quantity  $N_{\text{pair}}^{r < s}$  is the number of pairs with interspecies distances smaller than  $s$ . For zero-range interactions,  $s$  is taken to zero. For finite-range interactions, in contrast,  $s$  goes to a small value such that  $s$  is larger than the range  $r_0$  of the underlying two-body potential. The pair relation can be written in terms of the short distance behavior of the pair distribution function  $P_{12}(r)$  for the spin-up—spin-down pairs [49–51, 57]. Throughout, we employ the normalization  $4\pi \int_0^\infty P_{12}(r)r^2 dr = N_1 N_2$ . The thermally averaged expectation values are obtained by employing two complementary approaches, a “microscopic approach” and a “direct approach”.

In the microscopic approach, the thermal expectation value of an observable  $A$  is obtained using  $\langle A \rangle_{\text{th}} = \sum_j \exp[-E_j/(k_B T)] A_j / \sum_j \exp[-E_j/(k_B T)]$ , where the sum runs over all eigen energies  $E_j$  (with associated eigen states  $\psi_j$ ) of the Hamiltonian  $H$  and  $A_j = \langle \psi_j | A | \psi_j \rangle / \langle \psi_j | \psi_j \rangle$ . The solutions to the time-independent Schrödinger equation are obtained semi-analytically for the interaction model  $V_F$  [145, 146] and using a basis set expansion approach for the interaction model  $V_G$  [2, 147, 148]. The basis set expansion approach is

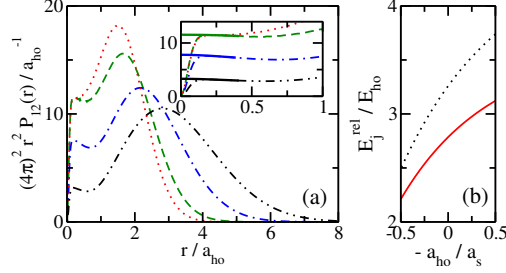


Figure 3.1: (a) The dotted, dashed, dash-dotted and dash-dot-dotted lines show the scaled pair distribution function  $r^2 P_{12}(r)$  for  $k_B T / (\hbar\omega) = 0, 0.6, 1.2$  and  $2$ , respectively, for the  $(3, 1)$  system interacting through  $V_G$  with  $r_0 = 0.06 a_{\text{ho}}$ . The  $T = 0$  curve is determined using the basis set expansion approach while the finite  $T$  curves are determined using the PIMC approach. The thick solid lines in the inset of panel (a), which is a blow-up of the small  $r$  region, show the extrapolation to  $r = 0$ . (b) The solid and dotted lines show the relative energy of the ground state with  $L^\Pi = 1^-$  and first excited state with  $L^\Pi = 0^+$  of the  $(2, 1)$  system interacting through  $V_G$  with  $r_0 = 0.06 a_{\text{ho}}$  as a function of  $-1/a_s$ .

summarized in Appendix 3.2.1. The direct approach is based on calculating  $\langle A \rangle$  from the density matrix  $\rho$ ,  $\langle A \rangle = \text{Tr}(A\rho) / \text{Tr}(\rho)$ . To sample  $\rho$ , we employ the path integral Monte Carlo (PIMC) approach [19]. Because of the Fermi sign problem [135], the applicability of this approach is expected to be limited to the high temperature regime. The PIMC approach is summarized in Appendix 3.2.2.

Figure 3.1(a) shows the scaled pair distribution function  $r^2 P_{12}(r)$  for the  $(3, 1)$  system for four temperatures,  $k_B T / E_{\text{ho}} = 0, 0.6, 1.2$  and  $2$ . At  $T = 0$  [dotted line in Fig. 3.1(a)],  $P_{12}$  is governed by the lowest eigenstate, which has  $L^\Pi = 1^+$  symmetry [2] ( $L$  and  $\Pi$  denote the orbital angular momentum and parity, respectively). As the temperature increases, excited states contribute. The second lowest state has  $1^-$  symmetry. Compared to the ground state, its  $P_{12}$  has an increased amplitude in the small but finite  $r$  region. The scaled pair distribution function  $r^2 P_{12}$  for  $k_B T = 0.6 E_{\text{ho}}$  (dashed line) has a comparable amplitude to that for  $T = 0$ ; however, clear differences are visible at larger interspecies distances  $r$ . For yet larger  $T$ , the small  $r$  amplitude decreases drastically [see dash-dotted and dash-dot-dotted lines in Fig. 3.1(a)] while the maximum of  $r^2 P_{12}$  moves to larger  $r$ . To extract the contact from  $r^2 P_{12}$ , we fit the small  $r$  region ( $r$  larger than  $r_0$ ) and extrapolate the fit to  $r = 0$  [see

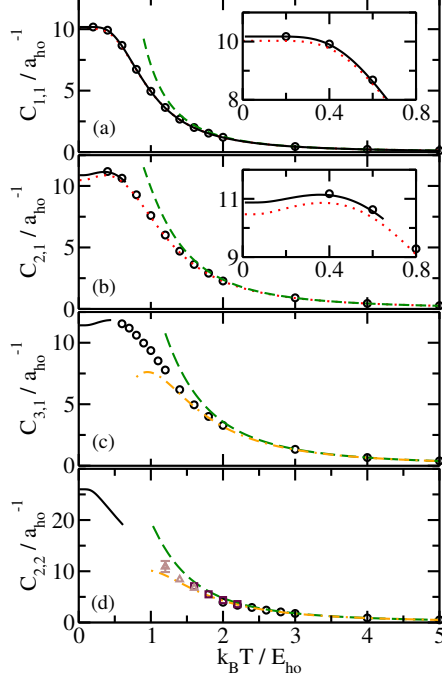


Figure 3.2: Contact  $C_{N_1, N_2}$  as a function of  $k_B T / E_{ho}$  for the (a) (1, 1), (b) (2, 1), (c) (3, 1), and (d) (2, 2) systems. The circles, squares and triangles show  $C_{N_1, N_2}$  for  $V_G$  with  $r_0/a_{ho} = 0.06, 0.08$  and  $0.1$  obtained using the PIMC approach. The solid lines show  $C_{N_1, N_2}$  for  $V_G$  with  $r_0 = 0.06a_{ho}$  obtained using the basis set expansion approach. For comparison, the dotted lines in panels (a) and (b) show  $C_{N_1, N_2}$  obtained using  $V_F$ . (a) The dashed line shows the first-order Taylor expansion at high temperature. (b) The dashed line shows the cluster expansion, i.e., the quantity  $2C_{1,1}$ . (c)/(d) The dashed and dash-dotted lines show the leading order term of the cluster expansion and the full cluster expansion, respectively. The insets of panels (a) and (b) show blow-ups of the low temperature regions.

thick solid lines in the inset of Fig. 3.1(a)].

Figure 3.2 shows the contact  $C_{N_1, N_2}$  at unitarity for  $N = 2 - 4$  as a function of the temperature. The symbols show the PIMC results, obtained by analyzing the scaled pair distribution functions  $r^2 P_{12}(r)$  for  $V_G$  with  $r_0 \ll a_{ho}$ . The solid lines in Fig. 3.2 show the contact for  $r_0 = 0.06a_{ho}$  obtained by evaluating the adiabatic relation via the microscopic approach. It can be seen that the contact calculated by evaluating the adiabatic relation via the microscopic approach and the pair relation via the direct approach agree or connect smoothly for the three system sizes considered.

To estimate the dependence of the contact on the range  $r_0$  of the underlying two-body

potential, we determine the contact of the (1, 1) and (2, 1) systems with zero-range interactions (see Appendix 3.2.3 and 3.2.4). The dotted lines in Figs. 3.2(a) and 3.2(b) show the result. In the low temperature regime, the contact for  $r_0 = 0$  lies below that for  $r_0 > 0$  for the (1, 1) and (2, 1) systems. At  $k_B T = 0.4E_{\text{ho}}$ , e.g., the (1, 1) and (2, 1) contacts for  $r_0 = 0.06a_{\text{ho}}$  lie 1.5% and 3%, respectively, above the contact for  $r_0 = 0$ . At large  $T$ , the dependence of the contact on the range is negligibly small. Our PIMC simulations suggest a similar range dependence for the (3, 1), (4, 1) and (2, 2) systems.

Figures 3.2(a)-3.2(d) show an intriguing dependence of the contact on the temperature.  $C_{1,1}$  and  $C_{2,2}$  decrease monotonically with increasing temperature while  $C_{2,1}$  and  $C_{3,1}$  exhibit a maximum at  $k_B T \approx 0.36E_{\text{ho}}$  and between  $0.4E_{\text{ho}}$  and  $0.5E_{\text{ho}}$ , respectively. To explain this behavior, it is instructive to evaluate the adiabatic relation via the microscopic approach.

For the (1, 1) system with zero-range interactions, one finds

$$\frac{\partial E_j}{\partial(-a_s^{-1})} = \frac{\Gamma(j + 1/2)2^{3/2}}{\pi(2j)!} E_{\text{ho}} a_{\text{ho}} \quad (3.4)$$

for the  $s$ -wave states and  $\partial E_j / (\partial(-a_s^{-1})) = 0$  for all higher partial wave states [145, 149]. The fact that  $C_{1,1}$  decreases monotonically with decreasing temperature is thus a direct consequence of the fact that  $\partial E_j / (\partial(-a_s^{-1}))$  (for  $s$ -wave states) decreases with increasing  $j$ . The inclusion of effective range corrections does not, if applied to the Gaussian model interaction with sufficiently small  $r_0$ , change this picture (see Appendix 3.2.3). A similar analysis, based on the numerically determined energies, holds for the (2, 2) system. Figure 3.1(b) shows the lowest two relative eigen energies, which correspond to states with  $L^{\text{II}} = 1^-$  and  $0^+$  symmetry, respectively, of the (2, 1) system as a function of  $-a_{\text{ho}}/a_s$  for  $r_0 = 0.06a_{\text{ho}}$ . The slope of the  $1^-$  state is smaller than that of the  $0^+$  state. This can be understood as follows. In the  $a_s \rightarrow 0^-$  limit, the lowest state has  $L^{\text{II}} = 1^-$  symmetry. In the  $a_s \rightarrow 0^+$  limit, in contrast, the lowest state has  $L^{\text{II}} = 0^+$  symmetry. The two states cross at  $a_{\text{ho}}/a_s \approx 1$  [150–152]. Correspondingly, in the unitary regime the energy of the lowest  $L = 0$  state changes more

rapidly with  $-1/a_s$  than that of the lowest  $L = 1$  state, implying that the contact at unitarity increases in the low temperature regime where the inclusion of only two states yields converged results. A more comprehensive analysis that accounts for all states is presented in Appendix 3.2.4. For the  $(3, 1)$  system, a similar argument can be made in the low temperature regime where the inclusion of just a few states suffices. The calculations presented here suggest that  $C_{N_1, N_2}$  decreases monotonically with  $T$  if  $N_1 - N_2 = 0$  and exhibits a maximum at finite  $T$  if  $N_1 - N_2 \neq 0$ . While it is tempting to generalize these results to larger systems, it should be noted that the density of states increases dramatically with increasing  $N$  and that application of a few-state model will be limited to smaller temperatures as  $N$  increases.

We now introduce a high temperature cluster expansion of the contact at unitarity. A formal discussion of the cluster expansion in the canonical ensemble applied to classical systems is provided in Ref. [153]. The  $(N_1, N_2)$  system contains  $N_1 N_2$  interacting pairs and one might expect that, using the argument that two-component Fermi gases behave universally [32, 76], the high temperature tail of  $C_{N_1, N_2}$  is governed by  $N_1 N_2 C_{1,1}$  for  $k_B T \gg E_{\text{ho}}$  [see dashed lines in Figs. 3.2(b)-3.2(d)]. The next term in the cluster expansion, applicable to systems with  $N > 3$ , depends on the “three-body term”  $C_{2,1} - 2C_{1,1}$ ,

$$\frac{C_{N_1, N_2}}{N_1 N_2} = C_{1,1} + \frac{N_1 + N_2 - 2}{2} (C_{2,1} - 2C_{1,1}) + \dots \quad (3.5)$$

The dashed and dash-dotted lines in Figs. 3.2(c) and 3.2(d) show the leading term and the sum of the leading and sub-leading terms for the  $(3, 1)$  and  $(2, 2)$  systems. The inclusion of the three-body term improves the validity regime of the cluster expansion notably. Assuming zero-range interactions, the leading order terms of the Taylor expansions of  $C_{1,1}$  and  $C_{2,1} - 2C_{1,1}$  around  $\tilde{\omega} \ll 1$ , where  $\tilde{\omega} = E_{\text{ho}}/(k_B T)$ , are  $4\pi^{1/2}\tilde{\omega}^{5/2}a_{\text{ho}}^{-1}$  and  $-7.012(12)\tilde{\omega}^{11/2}a_{\text{ho}}^{-1}$ , indicating that the three-body term is suppressed by  $\tilde{\omega}^3$  compared to the leading order two-body term. Figures 3.2(c) and 3.2(d) show that the numerically obtained  $C_{3,1}$  and  $C_{2,2}$  contacts (symbols) lie above the cluster prediction (dash-dotted line), suggesting that

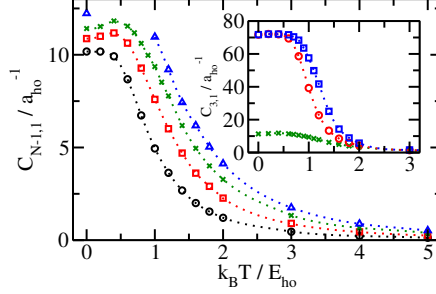


Figure 3.3: Circles, squares, crosses and triangles show  $C_{N_1, N_2}$  for the (1, 1), (2, 1), (3, 1) and (4, 1) systems, respectively, interacting through  $V_G$  with  $r_0 = 0.06a_{ho}$  as a function of  $T$  [6]. Dotted lines serve as a guide to the eye. Inset: Crosses, squares and circles show the contact of the (3, 1) system for Fermi, Boltzmann and Bose statistics, respectively.

the corresponding leading order four-body expansion coefficients are positive. The above expansions can be viewed as canonical analogs of the virial equation of state description of the contact within the grand canonical ensemble [67, 89] (see Appendix 3.2.5 for details).

Equation (3.5) shows that the contact  $C_{N-1,1}$  with  $N > 2$  is  $N - 1$  times larger than  $C_{1,1}$  in the high temperature limit. In the low temperature limit (see Fig. 3.3), in contrast,  $C_{N-1,1}$  with  $N > 2$  is only slightly larger than  $C_{1,1}$ , reflecting the fact that, to leading order, the system can form one and not  $N - 1$  bound pairs. It is also interesting to compare the limiting behaviors of  $C_{3,1}$  and  $C_{2,2}$ .  $C_{2,2}$  is  $4/3$  times larger than  $C_{3,1}$  at large  $T$  [see Eq. (3.5)] but roughly two times larger at low  $T$ . The latter reflects the fact that the (2, 2) and (3, 1) systems can form two dimers and one dimer, respectively.

To elucidate the role of the Fermi statistics, we focus on the (3, 1) system at unitarity with  $r_0 = 0.06a_{ho}$ . The inset of Fig. 3.3 shows the contact obtained by treating the majority particles as identical fermions (crosses; these are the same data as discussed above), as identical bosons (circles) and as distinguishable “Boltzmann particles” (squares). In the high temperature regime, the Fermi and Bose statistics can be treated as a correction to the Boltzmann statistics. In the low temperature regime, in contrast, appreciable differences are revealed. The (3, 1) systems with Bose and Boltzmann statistics share the same ground

state and thus the same contact in the zero temperature limit. Compared to the contact of the Bose and Boltzmann systems, that of the Fermi system is strongly suppressed as a consequence of the Pauli exclusion principle. Specifically, the  $(3, 1)$  Fermi system at unitarity does not support a bound state in free space while the  $(3, 1)$  Bose and Boltzmann systems do. The existence of self-bound states leads to an increased amplitude of the pair distribution function at small interspecies distances. Moreover, the Bose and Boltzmann systems are—unlike the Fermi system—not fully universal, i.e., their properties are, in addition to the  $s$ -wave scattering length, governed by a three-body parameter. This implies that the Bose and Boltzmann systems are characterized by a non-zero three-body contact in addition to the two-body contact considered throughout this paper [154, 155].

Finite-temperature effects play an important role in many finite-sized systems, including atomic clusters, and quantum dots. Our work demonstrates that small harmonically trapped two-component Fermi gases with infinitely strong interspecies  $s$ -wave interactions, which can be realized and probed experimentally, also exhibit intriguing dependencies on the temperature. In particular, we proposed a high-temperature cluster expansion in the canonical ensemble, quantified the range dependence of the contact, observed and interpreted the distinctly different behavior of the contact of spin-balanced and spin-imbalanced Fermi gases in the low temperature regime, and elucidated the role of the Fermi statistics. The ability to change the particle statistics is unique to the PIMC technique and has contributed notably to the understanding of microscopic superfluidity and condensation of bosonic helium droplets [156, 157]. Future studies aim at determining the critical temperature, and the superfluid fraction and superfluid density of small trapped Fermi gases.

Acknowledgement: Support by the National Science Foundation (NSF) through Grant No. PHY-1205443 is gratefully acknowledged. This work used the Extreme Science and Engineering Discovery Environment (XSEDE), which is supported by NSF grant number OCI-1053575, and the WSU HPC. This work was additionally supported by the NSF through

a grant for the Institute for Theoretical Atomic, Molecular and Optical Physics at Harvard University and Smithsonian Astrophysical Observatory.

## 3.2 Appendix

### 3.2.1 Basis set expansion approach

The explicitly correlated Gaussian basis set expansion approach with semi-stochastic parameter optimization has been used extensively in the literature to describe the behavior of small harmonically trapped two-component Fermi gases with short-range interactions (see, e.g., Ref. [2] for details). The energies of the three- and four-body systems can be calculated with an accuracy of better than 1% (and often better than 0.1%). To determine the solid lines in Figs. 3.2(b)-3.2(d), we used energy cutoffs  $E^{\text{rel}}$  around  $11E_{\text{ho}}$ ,  $9E_{\text{ho}}$ , and  $9.5E_{\text{ho}}$ , respectively. Including the degeneracies arising from the projection quantum number as well as the relative energies of states that are only very weakly affected by the short-range interactions, this amounts to around 1250, 230 and 700 energy levels for the (2, 1), (3, 1) and (2, 2) systems, respectively. The use of a finite energy cutoff implies that the determination of the finite-range contact within the microscopic approach is limited to the low temperature regime. Convergence of the contact with respect to the energy cutoff was tested by including successively fewer energy levels.

### 3.2.2 Path integral Monte Carlo approach

Our PIMC implementation largely follows that described in Refs. [19, 133]. In the low temperature regime, we find that we have to adjust the simulation parameters that control the sampling of the unpermuted configurations as well as those that control the sampling of the permutations carefully. We employ the second- and fourth-order Trotter formula [112, 158]; higher-order propagation schemes did not seem to lead to further improvements.

It is well known that the standard PIMC algorithm, as employed here, suffers from the Fermi sign problem [135]. Simply put, the signal to noise ratio decreases exponentially with decreasing temperature and increasing number of particles. As demonstrated by our simulation results, the Fermi sign problem is sufficiently small for the parameter region considered in this paper. In particular, the PIMC algorithm allows us to investigate a region of the physical parameter space (strong short-range interactions and relatively low temperature) that is inaccessible by other numerical approaches.

### 3.2.3 (1,1) system with zero-range interactions

The relative energies of the (1, 1) system with  $s$ -wave zero-range interactions can be determined by solving the transcendental equation [145]

$$\frac{\sqrt{2}\Gamma(3/4 - E^{\text{rel}}/(2E_{\text{ho}}))}{\Gamma(1/4 - E^{\text{rel}}/(2E_{\text{ho}}))} = \frac{a_{\text{ho}}}{a_s}. \quad (3.6)$$

At unitarity, the relative  $s$ -wave energies read  $E_j^{\text{rel}} = (2j + 1/2)E_{\text{ho}}$ , where  $j = 0, 1, \dots$ . States with relative orbital angular momentum  $L$  greater than zero are not affected by the interactions. Using these energies and the expressions for the change of the relative energies with  $-1/a_s$ , Eq. (3.4), one finds

$$C_{1,1}(\tilde{\omega}) = 8\sqrt{\pi} \frac{e^{\tilde{\omega}} (e^{\tilde{\omega}} - 1)^2 \sqrt{e^{-\tilde{\omega}} \sinh(\tilde{\omega})}}{e^{\tilde{\omega}} [e^{\tilde{\omega}} (e^{\tilde{\omega}} - 2) + 4] - 1} a_{\text{ho}}^{-1} \quad (3.7)$$

[see dotted line in Fig. 3.2(a)].

To quantify the corrections that arise from the finite range of the interspecies interaction potential, we consider three approaches:

(i) Using a B-spline approach, we calculate the relative energies of the (1, 1) system as a function of  $-1/a_s$  up to  $500E_{\text{ho}}$  for the first 50 angular momentum channels. Using these energies and the corresponding slopes, we calculate the contact numerically. The solid line

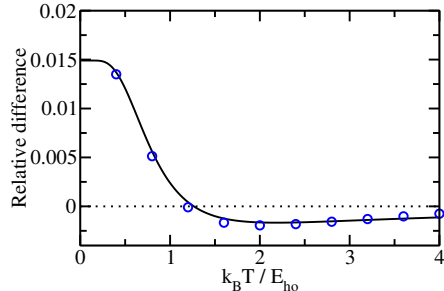


Figure 3.4: Range dependence of the contact  $C_{1,1}$  for  $r_0 = 0.06a_{\text{ho}}$  as a function of  $k_B T / E_{\text{ho}}$ . The circles show the difference between the finite-range contact calculated using approach (i) and the zero-range contact, normalized by the zero-range contact. The solid line shows the difference between the finite-range contact calculated using approach (ii) and the zero-range contact, normalized by the zero-range contact. In the large  $T$  limit, the difference approaches zero from below. In approach (ii),  $r_{\text{eff}} = 0.12178a_{\text{ho}}$ —corresponding to  $V_G$  with  $r_0 = 0.06a_{\text{ho}}$ —has been used.

in Fig. 2(a) shows the result for the Gaussian potential with  $r_0 = 0.06a_{\text{ho}}$ .

(ii) We replace  $-1/a_s$  in Eq. (3.6) by  $-1/a_s + r_{\text{eff}}k^2/2$ , where  $r_{\text{eff}}$  denotes the effective range and  $k$  is related to the relative energy via  $\hbar^2 k^2 / m = E^{\text{rel}}$ . The leading order effective range corrections to the energy and to the change of the energy at unitarity can then be derived analytically [149]. Using these expressions, the contact can be readily determined numerically within the microscopic approach. On the scale of Fig. 3.2(a), the resulting contact would be indistinguishable from the solid line.

(iii) To account for the fact that higher partial wave channels are affected by the inter-species interactions if the range of the underlying two-body potential is finite, we generalize the above effective range treatment to finite angular momenta. Specifically, we replace the generalized scattering lengths in the transcendental equations for the higher partial waves [159] by the corresponding effective range expansions and determine the corrections to the energy and to the slope of the energy for vanishing generalized scattering lengths due to the effective range. Calculating the effective ranges for the Gaussian potential with  $r_0 = 0.06a_{\text{ho}}$  for the lowest few partial wave channels, we find that the effective range correction of the contact due to the  $L = 1$  channel is about 0.0003% and 0.015% for  $k_B T / E_{\text{ho}} = 1/2$

and 2, respectively. For fixed  $T$ , the corrections decrease with increasing  $L$ . Although the  $L = 1$  channel leads to a larger percentage correction at large  $T$  than at small  $T$ , its overall role is negligible since the contact itself is small in the large  $T$  regime.

Overall, the agreement between the contacts calculated using approaches (i)-(iii) is excellent. To bring out the size of the finite-range corrections, Fig. 3.4 shows the difference between the finite-range and zero-range contacts, normalized by the zero-range contact. The circles show the relative difference for the case where the finite-range contact is calculated using approach (i) while the solid line shows the relative difference for the case where the finite-range contact is calculated using approach (ii). The difference is largest at low  $T$  and decreases rapidly. The difference changes sign at  $k_B T \approx 1.25 E_{\text{ho}}$  and then approaches zero from the negative side. For  $k_B T \gtrsim E_{\text{ho}}$ , the percentage deviation is smaller than 0.5% and thus, for all practical purposes, negligible.

A key result of the above analysis is that the two-body contact is nearly fully determined by the  $s$ -wave channel and that higher partial wave contributions play a negligible role if the interspecies interactions are modeled by the Gaussian potential  $V_G$  with  $r_0 = 0.06 a_{\text{ho}}$ . This is crucial for our analysis of the (2, 1) system discussed in Appendix 3.2.4, which assumes interspecies  $s$ -wave zero-range interactions. It also suggests that our high temperature results for larger systems, obtained by using  $V_G$  with  $r_0 = 0.06 a_{\text{ho}}$ , are very close to the universal zero-range results.

### 3.2.4 (2,1) system with zero-range interactions

To determine the contact of the (2, 1) system with zero-range interactions at unitarity, we resort to the hyperspherical coordinate approach [146, 160]. In this approach, the solutions of the relative Schrödinger equation are obtained in a two step process. First, the hyperangular Schrödinger equation is solved for fixed hyperradius  $R$ . Second, a set of coupled hyperradial Schrödinger equations is solved. For zero-range interactions with infinitely large  $s$ -wave

scattering length, the coupling between the hyperangular and hyperradial degrees of freedom vanishes and the relative eigen energies at unitarity can be written as  $E^{\text{rel}} = (2q + s_{L,\nu} + 1)E_{\text{ho}}$ , where the hyperradial quantum number  $q$  takes the values  $0, 1, \dots$ . The  $s_{L,\nu}$  are solutions of the transcendental equation [146, 160]

$$\begin{aligned} & \frac{(-1)^L {}_2F_1\left(\frac{1}{2}(L - s_{L,\nu} + 2), \frac{1}{2}(L + s_{L,\nu} + 2); L + \frac{3}{2}; \frac{1}{4}\right)}{\pi(2L + 1)!!} + \\ & \frac{1}{\Gamma\left(\frac{1}{2}(L - s_{L,\nu} + 1)\right)\Gamma\left(\frac{1}{2}(L + s_{L,\nu} + 1)\right)} \\ & = \frac{1}{\sqrt{2}\Gamma\left(\frac{1}{2}(L - s_{L,\nu} + 2)\right)\Gamma\left(\frac{1}{2}(L + s_{L,\nu} + 2)\right)} \frac{R}{a_s} \end{aligned} \quad (3.8)$$

for  $1/a_s = 0$ . In Eq. (3.8), the hyperradius  $R$  is defined through  $R^2 = 2(r_{12}^2 + r_{23}^2 + r_{13}^2)/3$  and  ${}_2F_1$  denotes the hypergeometric function.

To determine the change of the relative energies at unitarity with  $-1/a_s$ , we replace  $s_{L,\nu}$  in Eq. (3.8) by  $s_{L,\nu} + \Delta s_{L,\nu}$ , where  $|\Delta s_{L,\nu}|$  is assumed to be small. Taylor expanding Eq. (3.8) around the known  $s_{L,\nu}$  value, we find  $\Delta s_{L,\nu} = c_{L,\nu}R/a_s$ . We insert this into the effective hyperradial potential  $\hbar^2[(s_{L,\nu} + \Delta s_{L,\nu})^2 - 1/4]/(2mR^2)$  and treat the leading order correction as a perturbation, i.e., we define  $V_{\text{pert}}(R) = \hbar^2 c_{L,\nu} s_{L,\nu} / (mR a_s)$ . For each  $s_{L,\nu}$ , we calculate the exact proportionality constant  $c_{L,\nu}$  and determine the change of the relative energy by treating  $V_{\text{pert}}(R)$  in first-order perturbation theory in the hyperradial Schrödinger equation, i.e., by evaluating the integral  $\int_0^\infty |F_{q,s_{L,\nu}}(R)|^2 V_{\text{pert}}(R) dR$ . The unperturbed radial wave functions  $F_{q,s_{L,\nu}}(R)$  are obtained by solving the hyperradial Schrödinger equation for the unitary problem. Using the known expressions for  $F_{q,s_{L,\nu}}(R)$  [146], the integral can be evaluated analytically, yielding the leading-order variation of  $E^{\text{rel}}$  with  $-1/a_s$  for each  $s_{L,\nu}$  and  $q = 0, 1, \dots$ . The approach outlined here reproduces the recurrence relations of Refs. [141, 161]. Using Mathematica, the energies and slopes of the energies of the (2, 1) system at unitarity can be calculated with essentially arbitrary accuracy, thereby allowing us to calculate the temperature-dependent contact with high accuracy. In calculating the

Table 3.1: Contact  $C_{2,1}$  as a function of temperature for  $s$ -wave zero-range interactions at unitarity.

$k_B T/E_{\text{ho}}$	$C_{2,1}/a_{\text{ho}}^{-1}$	$k_B T/E_{\text{ho}}$	$C_{2,1}/a_{\text{ho}}^{-1}$
0.1	10.4986	2.6	1.23893
0.2	10.6717	2.7	1.13335
0.3	10.8225	2.8	1.03959
0.4	10.8529	2.9	0.956067
0.5	10.7047	3.0	0.881422
0.6	10.3479	3.1	0.814516
0.7	9.79272	3.2	0.754375
0.8	9.08421	3.3	0.700163
0.9	8.28504	3.4	0.651166
1.0	7.45680	3.5	0.606768
1.1	6.64831	3.6	0.566439
1.2	5.89176	3.7	0.529719
1.3	5.20435	3.8	0.496209
1.4	4.59212	3.9	0.465562
1.5	4.05395	4.0	0.437476
1.6	3.58469	4.1	0.411684
1.7	3.17735	4.2	0.387954
1.8	2.82444	4.3	0.366081
1.9	2.51872	4.4	0.345884
2.0	2.25359	4.5	0.327202
2.1	2.02320	4.6	0.309894
2.2	1.82248	4.7	0.293834
2.3	1.64710	4.8	0.278908
2.4	1.49338	4.9	0.265017
2.5	1.35820	5.0	0.252072

partition function, care has to be exercised as the above formalism excludes a large number of “trivial energy levels” that are not affected by the  $s$ -wave interactions [146]. We account for these “trivial states” using the ideas discussed in Ref. [148].

Table 3.1 tabulates the contact  $C_{2,1}$  [see also dotted line in Fig. 3.2(b)]. These zero-range results serve as a benchmark for our PIMC simulations. Moreover, the semi-analytic expressions for the energy and its variation with  $-1/a_s$  can also be used to calculate the third-order contact coefficient [67]. We find 0.0269223(3), which notably improves upon the accuracy of the value of 0.02692(2) of Ref. [67]; a more detailed discussion of the connection

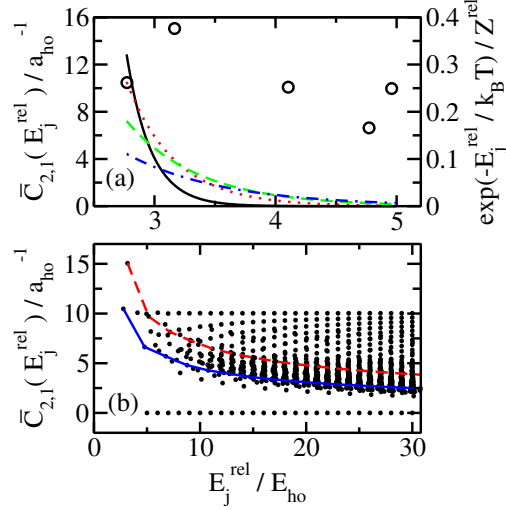


Figure 3.5: (a) The solid, dotted, dashed and dash-dotted lines show the weight factor  $\exp[-E_j^{\text{rel}}/(k_B T)]/Z^{\text{rel}}$  (see right axis) as a function of the relative energy for  $k_B T/E_{\text{ho}} = 0.2, 0.4, 0.6$  and  $0.8$ , respectively. The circles show the zero-temperature contact  $\bar{C}_{2,1}$  (see left axis) for states with  $E_j^{\text{rel}} < 5E_{\text{ho}}$ . (b) The dots show the zero-temperature contact  $\bar{C}_{2,1}$  as a function of the relative energy for  $E_j^{\text{rel}} \lesssim 30E_{\text{ho}}$ . The solid (dashed) line connects the contacts of  $L = 1$  ( $L = 0$ ) states, which are characterized by the same  $s_{L,\nu}$  value but different  $q$  values; the  $s_{L,\nu}$  values chosen are the smallest ones for both  $L = 1$  and  $0$ .

between the second- and third-order contact coefficients [67] and our cluster expansion is given in Appendix 3.2.5.

We now refine the two-state model, which was used in the main text to explain why the maximum of  $C_{2,1}$  occurs at finite  $T$ . Circles in Fig. 3.5 show the zero-temperature contacts  $\bar{C}_{2,1}(E_j^{\text{rel}})$ ,  $\bar{C}_{2,1}(E_j^{\text{rel}}) = (4\pi m/\hbar^2)\partial E_j^{\text{rel}}/(\partial(-a_s^{-1}))$ , associated with the  $j$ th eigenstate of the  $(2, 1)$  system at unitarity as a function of  $E^{\text{rel}}$ . Panel (a) focuses on the small  $E^{\text{rel}}$  region while panel (b) extends up to  $E^{\text{rel}} = 30E_{\text{ho}}$ . Figure 3.5 shows that the zero-temperature contacts are non-negative. Moreover, all  $\bar{C}_{2,1}(E_j^{\text{rel}})$  but one are smaller than  $11a_{\text{ho}}^{-1}$ . The ‘‘outlier’’ corresponds to the lowest  $L = 0$  state, i.e., the state with the second lowest eigen energy. To calculate the temperature-dependent contact  $C_{2,1}$  within the microscopic approach, the zero-temperature contacts  $\bar{C}_{2,1}(E_j^{\text{rel}})$  need to be weighted by the temperature-dependent Boltzmann factors  $\exp[-E_j^{\text{rel}}/(k_B T)]/Z^{\text{rel}}(T)$ , where  $Z^{\text{rel}}(T)$  denotes the partition function

Table 3.2: High-temperature expansion coefficients  $c_{1,1}^{(i)}$  and  $c_{2,1}^{(i)}$  for the cluster expansion in the canonical ensemble.

$i$	0	1	2	3	4
$c_{1,1}^{(i)}$	$4\sqrt{\pi}$	0	$\sqrt{\pi}/6$	$-2\sqrt{\pi}$	$\sqrt{\pi}/96$
$c_{2,1}^{(i)}$				$-7.012(12)$	$0.0(1)$

that accounts for the relative degrees of freedom. Lines in Fig. 3.5(a) show these “weight factors” for four different  $T$ ,  $k_B T/E_{\text{ho}} = 0.2, 0.4, 0.6$  and  $0.8$ . It can be seen that the weight factor drops off quickly for  $k_B T/E_{\text{ho}} = 0.2$ , indicating that the “outlier” as well as the zero-temperature contacts of the other excited states contribute negligibly to  $C_{2,1}$ . At  $k_B T/E_{\text{ho}} = 0.4$ , in contrast, the “outlier” carries appreciable weight compared to the zero-temperature contact of the lowest eigen state. At yet higher  $T$ , the weight factor falls off slower, thereby reducing the relative importance of the “outlier”.

### 3.2.5 Cluster expansion in canonical ensemble and connection to virial equation of state in grandcanonical ensemble

This section elaborates on the cluster expansion introduced in the main part of the text. To further explore the high temperature behavior, we Taylor expand  $C_{1,1}$  and  $C_{2,1} - 2C_{1,1}$  around  $\tilde{\omega} \ll 1$ . We find

$$C_{1,1} = \tilde{\omega}^{5/2} \sum_{i=0}^{\infty} c_{1,1}^{(i)} \tilde{\omega}^i a_{\text{ho}}^{-1} \quad (3.9)$$

and

$$C_{2,1} - 2C_{1,1} = \tilde{\omega}^{5/2} \sum_{i=3}^{\infty} c_{2,1}^{(i)} \tilde{\omega}^i a_{\text{ho}}^{-1}. \quad (3.10)$$

Table 3.2 lists the dimensionless coefficients  $c_{1,1}^{(i)}$  and  $c_{2,1}^{(i)}$  for  $i \leq 4$ .

We now connect the high temperature cluster expansion in the canonical ensemble to

the more frequently used high-temperature virial expansion in the grand canonical ensemble [87], which assumes large number of particles. For simplicity, we consider spin-balanced harmonically trapped systems, i.e., systems with  $N_1 = N_2 = N/2$ . The contact  $C_{gc}$  in the grand canonical virial expansion reads [67]

$$C_{gc} = 2^{7/2} \pi^{3/2} \tilde{\omega}^{-1/2} Z_1(\tilde{\omega}) [c_2(\tilde{\omega})z^2 + c_3(\tilde{\omega})z^3 + \dots] a_{ho}^{-1}, \quad (3.11)$$

where  $Z_1(\tilde{\omega})$  denotes the partition function of a single particle in a spherically symmetric harmonic trap and  $z$  the fugacity,  $z = \exp(\mu/k_B T)$ ; here,  $\mu$  is the chemical potential. The contact coefficients  $c_2(\tilde{\omega})$  and  $c_3(\tilde{\omega})$  for the trapped system depend on the temperature and can be derived from the second- and third-order virial coefficients of the trapped system [67]. In the following, we use the high temperature expansions

$$c_2(\tilde{\omega}) = \frac{1}{2\sqrt{2}\pi} \left( 1 - \frac{\tilde{\omega}^2}{12} + \dots \right) \quad (3.12)$$

and

$$c_3(\tilde{\omega}) = 0.0269223(3) + \dots \quad (3.13)$$

The high-temperature expansion of the partition function reads

$$Z_1(\tilde{\omega}) = \tilde{\omega}^{-3} \left( 1 - \frac{\tilde{\omega}^2}{8} + \dots \right). \quad (3.14)$$

The fugacity  $z$  can be determined from the number equation [67]. Expanding the number equation for small  $z$ , we find

$$z = \frac{N}{2} \left( \tilde{\omega}^3 + \frac{\tilde{\omega}^5}{8} - \frac{3}{8} \frac{N}{2} \tilde{\omega}^6 + \dots \right). \quad (3.15)$$

Table 3.3: High-temperature expansion coefficients  $c_{\text{gc};1,1}^{(i)}$  and  $c_{\text{gc};2,1}^{(i)}$  extracted from the contact determined in the grand canonical ensemble.

$i$	0	1	2	3
$c_{\text{gc};1,1}^{(i)}$	$4\sqrt{\pi}$	0	$\sqrt{\pi}/6$	$-7.01342(2)$
$c_{\text{gc};2,1}^{(i)}$				$-7.01342(2)$

Inserting the expansions given in Eqs. (3.12)-(3.15) into Eq. (3.11), we find

$$C_{\text{gc}} = \left( 4\sqrt{\pi} \frac{N^2}{4} \tilde{\omega}^{5/2} + \frac{\sqrt{\pi}}{6} \frac{N^2}{4} \tilde{\omega}^{9/2} - 3\sqrt{\pi} \frac{N^3}{8} \tilde{\omega}^{11/2} - 1.69606(2) \frac{N^3}{8} \tilde{\omega}^{11/2} + \dots \right) a_{\text{ho}}^{-1}. \quad (3.16)$$

To relate Eq. (3.16) to Eqs. (3.9) and (3.10), we write, in analogy with Eq. (4) of the main text,

$$\frac{C_{\text{gc}}}{N^2/4} = C_{\text{gc};1,1} + \frac{N-2}{2} (C_{\text{gc};2,1} - 2C_{\text{gc};1,1}) + \dots, \quad (3.17)$$

where

$$C_{\text{gc};1,1} = \tilde{\omega}^{5/2} \sum_{i=0}^{\infty} c_{\text{gc};1,1}^{(i)} \tilde{\omega}^i a_{\text{ho}}^{-1} \quad (3.18)$$

and

$$C_{\text{gc};2,1} - 2C_{\text{gc};1,1} = \tilde{\omega}^{5/2} \sum_{i=3}^{\infty} c_{\text{gc};2,1}^{(i)} \tilde{\omega}^i a_{\text{ho}}^{-1}. \quad (3.19)$$

The coefficients  $c_{\text{gc};1,1}^{(i)}$  and  $c_{\text{gc};2,1}^{(i)}$  are listed in Table 3.3. Comparison of Tables 3.2 and 3.3 shows that the coefficients with  $i = 0 - 2$  agree but that discrepancies exist for  $i = 3$ . Specifically, our analysis shows that the leading order three-body coefficients agree, i.e.,  $c_{\text{gc};2,1}^{(3)} = c_{2,1}^{(3)}$ , but that the two-body term at the same order in  $\tilde{\omega}$  does not agree, i.e.,

$c_{\text{gc};1,1}^{(3)} \neq c_{1,1}^{(3)}$ . Disagreement is expected since the canonical and grand canonical ensembles are known to yield different results. The fact that the disagreement appears in the term proportional to  $N^2$  and not the term proportional to  $N^3$  makes sense, since our analysis in the grand canonical ensemble assumes large  $N$ , rendering the term proportional to  $N^2$  less important than the term proportional to  $N^3$ .

### 3.2.6 Note on the temperature scales

Throughout, we reported the temperature in terms of the natural energy scale of the harmonic oscillator. Other relevant temperature scales are the Fermi temperature  $T_F$  and the critical temperature  $T_c$ . The Fermi temperature of small harmonically trapped two-component Fermi gases is defined through the energy of the highest single-particle state of the non-interacting system, yielding  $T_F = 2.5E_{\text{ho}}/k_B$  for  $N = 3 - 5$ . The critical temperature for the trapped spin-balanced system is  $T_c \approx 0.2T_F$  [162]. Our calculations cover temperatures much smaller and much larger than these characteristic temperature scales.

# Chapter 4

## Abnormal superfluid fraction of harmonically trapped few-fermion systems

by Yangqian Yan<sup>1</sup> and D. Blume<sup>1</sup>

<sup>1</sup>Department of Physics and Astronomy, Washington State University, Pullman,  
Washington 99164-2814, USA

Copyright (2014) by the American Physical Society

Superfluidity is a fascinating phenomenon that, at the macroscopic scale, leads to dissipationless flow and the emergence of vortices. While these macroscopic manifestations of superfluidity are well described by theories that have their origin in Landau's two-fluid model, our microscopic understanding of superfluidity is far from complete. Using analytical and numerical *ab initio* approaches, this paper determines the superfluid fraction and local superfluid density of small harmonically trapped two-component Fermi gases as a function of the interaction strength and temperature. At low temperature, we find that the superfluid fraction is, in certain regions of the parameter space, negative. This counterintuitive finding

is traced back to the symmetry of the system's ground state wave function, which gives rise to a diverging quantum moment of inertia  $I_q$ . Analogous abnormal behavior of  $I_q$  has been observed in even-odd nuclei at low temperature. Our predictions can be tested in modern cold atom experiments.

## 4.1 Abnormal superfluid fraction of harmonically trapped few-fermion systems

Superfluidity plays a crucial role in various areas of physics. The core of neutron stars is thought to be superfluid, giving rise to modifications of the specific heat and rapid cooling [163, 164]. In laboratory settings, superfluidity of bosonic liquid helium-4 below 2.17K and fermionic liquid helium-3 below 3mK leads to dissipationless flow and the formation of vortices [12]. More recently, superfluidity has been demonstrated in dilute atomic Bose and Fermi gas experiments [165–168]. The superfluid fraction shows a strong dependence on the dimensionality and the size of the system. In particular, transitions that are sharp in homogeneous systems are smeared out in finite-sized systems [169–171].

Over the past 20 years or so, non-classical rotations in small doped bosonic helium-4 and molecular para-hydrogen clusters have been interpreted within the framework of microscopic superfluidity [172–177]. Elements of this framework date back to the 50s when nuclear physicists introduced a moment of inertia based method for the study of superfluidity in finite-sized nuclei [178–180]. In nuclei, superfluidity is tied to the pairing of nucleons [169, 181, 182]. As a consequence of pairing, the quantum moment of inertia of even-even nuclei, i.e., nuclei with an even number of protons and an even number of neutrons, tends to go to zero in the zero temperature limit while that of even-odd nuclei tends to increase sharply as the temperature approaches zero [169, 182, 183].

We investigate the superfluid fraction and local superfluid density of small harmonically

trapped dilute atomic Fermi gases over a wide range of interaction strengths. In the low temperature region, we identify parameter combinations where the quantum moment of inertia is abnormally large, i.e., larger than the classical moment of inertia, implying a negative superfluid fraction. The negative superfluid fraction is linked to the topology of the density matrix. Specifically, the superfluid fraction takes on negative values in the low temperature regime when one of the energetically low-lying eigenstates supports a Pauli vortex with finite circulation [184–186] at the center of the trap. Intuitively, this can be understood as follows: In the absence of a low-energy eigenstate with finite circulation, the superfluid few-fermion gas “does not respond” to an infinitesimal rotation. This situation closely resembles that for a superfluid few-boson gas. In the presence of a low-energy eigenstate with finite circulation, however, the superfluid few-fermion gas “responds strongly” to an infinitesimal rotation, i.e., the infinitesimal rotation leads to a dynamical instability. We find that the radial superfluid density is negative near the trap center and positive near the edge of the cloud, indicating that the dynamical instability develops at the vortex core. A related instability also exists for bosonic few-atom systems. However, since the instability for bosons does not occur for an infinitesimal rotation but when the rotating frequency is comparable to the angular trapping frequency [187], the superfluid fraction, which is defined in the limit of infinitesimal rotation [188–191], is not affected by the instability. We note that a negative superfluid fraction has also been predicted to exist for the Fulde-Ferrell-Larkin-Ovchinnikov state of fermions loaded into an optical lattice [192].

We consider  $N$  atoms of mass  $m$  described by the Hamiltonian  $H$  in a spherically symmetric harmonic trap. The system Hamiltonian under a small rotation about the  $z$ -axis can, in the rotating frame, be expressed as  $H_{\text{rot}} = H - \Omega L_z$  [12], where  $\Omega$  denotes the angular rotating frequency and  $L_z$  the  $z$ -component of the angular momentum operator  $\mathbf{L}$ . The superfluid fraction  $n_s$  is defined as  $n_s = 1 - I_q/I_c$  [188–191], where the quantum moment of

inertia  $I_q$  is defined in terms of the response to an infinitesimal rotation,

$$I_q = \left. \frac{\partial \langle L_z \rangle_{\text{th}}}{\partial \Omega} \right|_{\Omega=0}, \quad (4.1)$$

and  $\langle \cdot \rangle_{\text{th}}$  indicates the thermal average. The classical moment of inertia  $I_c$  is defined through  $I_c = \langle m \sum_n r_{n,\perp}^2 \rangle_{\text{th}}$ , where  $r_{n,\perp}$  is the distance of the  $n$ th particle to the rotating axis [193].

We work in the canonical ensemble and determine the superfluid fraction of small trapped systems as a function of the temperature  $T$  using two different approaches. (i) We use the path integral Monte Carlo (PIMC) approach to sample the density matrix at temperature  $T$  [19, 133, 194]. The superfluid fraction  $n_s$  and local superfluid density  $\rho_s$  are then obtained using the area estimator [94, 191, 195]. (ii) We employ a microscopic approach [194]: For the systems considered,  $\mathbf{L}^2$  and  $L_z$  commute with the Hamiltonian  $H$ , implying that the total orbital angular momentum quantum number  $L$  and corresponding projection quantum number  $M$  are good quantum numbers. One finds  $I_q = \hbar^2 \langle M^2 \rangle_{\text{th}} / (k_B T)$ , where the thermal average runs over the system at rest [196]. To evaluate  $I_q$ , we calculate a large portion of the quantum mechanical energy spectrum and thermally average the quantity  $M^2$ . From the same set of calculations, we determine  $r_{n,\perp}^2$  (and correspondingly  $I_c$ ) via the generalized virial theorem [49–51], which applies to systems with short-range interactions with  $s$ -wave scattering length  $a_s$  under spherically symmetric harmonic confinement with angular trapping frequency  $\omega$ ,  $3\omega^2 \sum_n \langle m r_{n,\perp}^2 \rangle_{\text{th}} = 2 \langle E + a_s (\partial E / \partial a_s) / 2 \rangle_{\text{th}}$ . Here,  $E$  denotes the total energy.

We first consider  $N$  identical non-interacting harmonically trapped bosons or fermions described by the Hamiltonian  $H = H_{\text{ni}}$ ,

$$H_{\text{ni}} = \sum_{j=1}^N \left( \frac{-\hbar^2}{2m} \nabla_j^2 + \frac{1}{2} m \omega^2 \mathbf{r}_j^2 \right), \quad (4.2)$$

where  $\mathbf{r}_j$  denotes the position vector of the  $j$ th atom. Using the  $N$ -body partition function,

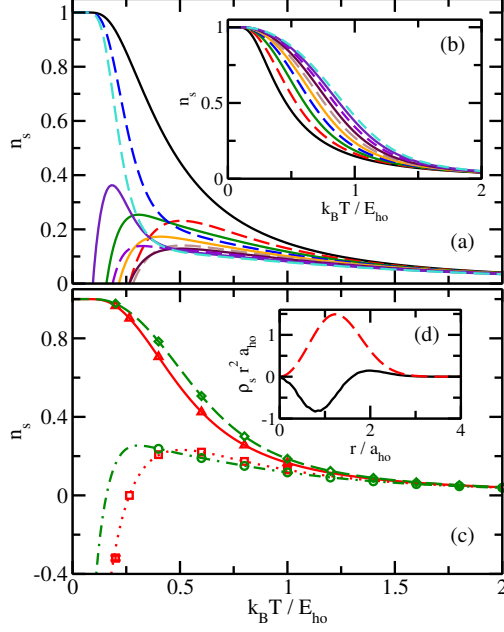


Figure 4.1: Superfluid properties of the non-interacting trapped single-component gas as a function of  $k_B T / E_{ho}$ . (a) From top to bottom at  $k_B T = E_{ho}$ , the alternating solid and dashed lines show  $n_s$  for the Fermi gas with  $N = 1 - 10$ . (b) From bottom to top, alternating solid and dashed lines show  $n_s$  for the Bose gas with  $N = 1 - 10$ . (c) The dashed and solid lines replot  $n_s$  for  $N = 2$  and  $3$ , respectively. For comparison, symbols show  $n_s$  obtained using the PIMC approach. The errorbars are smaller than the symbol size. (d) The dashed and solid lines show the scaled radial total and superfluid density for  $N = 2$ .

we calculate the thermal averages for  $I_c$  and  $I_q$  [197]. Figure 4.1(b) shows  $n_s$  for  $N = 1 - 10$  non-interacting bosons. For all  $N$ ,  $n_s$  goes to 1 as the temperature approaches zero. This is a direct consequence of the fact that the ground state has  $L = 0$ . As the particle number increases, the superfluid region broadens. Figure 4.1(a) shows  $n_s$  for  $N = 1 - 10$  non-interacting fermions. The curves have similar asymptotic behavior at high temperature, yet differ dramatically at low temperature. The  $N = 1, 4$  and  $10$  curves increase monotonically with decreasing temperature and approach one at  $T = 0$ . Due to the closed shell nature, the ground state of these Fermi systems is, as that of the Bose systems, non-degenerate and has vanishing angular momentum. The curves for the other  $N$  values dive down to negative infinity at zero temperature. The ground state of these open-shell systems is degenerate and contains finite angular momentum states. Figure 4.1(c) compares the analytical results

(lines) for  $N = 2$  and 3 with those obtained by the PIMC approach (symbols). The excellent agreement confirms the correctness of our analytical results and demonstrates that our PIMC simulations yield highly accurate results. Given that BCS theory predicts a vanishing superfluid fraction for the homogeneous Fermi gas in the absence of an effective attraction, one might wonder where the non-vanishing  $n_s$  values for the non-interacting trapped Fermi gas come from. Our analysis shows that the non-vanishing  $n_s$  is due to the trap energy scale  $E_{\text{ho}}$ , where  $E_{\text{ho}} = \hbar\omega$ . An analogous energy scale does not exist in the non-interacting homogeneous system, for which the moment of inertia based method predicts, in agreement with BCS theory, that  $n_s$  vanishes. Lastly, we note that although Stringari [198] determined  $n_s$  for trapped non-interacting single-component Fermi gases, no negative superfluid fraction was observed because the semi-classical treatment employed assumed  $k_B T \gg E_{\text{ho}}$ .

To get a sense of the spatial distribution of the superfluid fraction, we calculate the radial superfluid density  $\rho_s(r)$  [195, 199]. As an example, the solid line in Fig. 4.1(d) shows the scaled radial superfluid density  $\rho_s(r)r^2$  for the two-fermion system at  $T = 0.265E_{\text{ho}}/k_B$ . For this temperature, we have  $n_s = 0$ . The radial superfluid density is negative for small  $r$  and positive for large  $r$ . For comparison, the dashed line shows the scaled radial total density. For the non-interacting trapped Fermi systems investigated, we find that the negative part of the radial superfluid density develops in the small  $r$  region and then, with decreasing temperature, grows outward.

To interpret this behavior, we consider the  $N = 2$  case at  $T = 0$ . In the absence of rotation, the ground state has  $L = 1$  and the expectation value of  $L_z$  averages to zero. The three-fold degenerate state splits under a small rotation, with the  $M = 1$  state having the lowest energy; correspondingly, the expectation value of  $L_z$  is  $\hbar$ . Using these results to express  $I_q$ , see Eq. (4.1), as a finite difference, we find that  $I_q$  scales as  $\lim_{\Omega \rightarrow 0} \hbar\Omega^{-1}$  at  $T = 0$ . This shows that the divergence of  $I_q$  (and hence the negative value of  $n_s$ ) is due to the  $M = 1$  state, which contains a vortex at the center of the trap with circulation 1.

Figure 4.1(d) shows that this is where the radial superfluid density is negative, i.e., this is the region where the dynamical instability develops.

Next, we consider two-component Fermi gases consisting of  $N_1$  spin-up and  $N - N_1$  spin-down particles with short-range interspecies interactions. As the  $s$ -wave scattering length is tuned from small negative values to infinity to small positive values, the system changes from forming Cooper pairs to composite bosonic molecules [32]. In what follows we investigate how the change from “fermionic” (Cooper pairs) to “bosonic” (composite molecules) is reflected in the superfluid properties of the trapped system. We consider the Hamiltonian  $H = H_{\text{int}}$ ,

$$H_{\text{int}} = H_{\text{ni}} + \sum_{j=1}^{N_1} \sum_{k=N_1+1}^N V_{\text{tb}}(\mathbf{r}_{jk}), \quad (4.3)$$

for two different interspecies two-body potentials  $V_{\text{tb}}$ , a regularized zero-range pseudopotential  $V_{\text{F}}$  [3] and a short-range Gaussian potential  $V_{\text{G}}$  with depth  $U_0$  ( $U_0 < 0$ ) and range  $r_0$ ,  $V_{\text{G}}(\mathbf{r}_{jk}) = U_0 \exp[-\mathbf{r}_{jk}^2/(2r_0^2)]$ . The depth and range are adjusted so that  $V_{\text{G}}$  yields the desired  $a_s$ ; throughout, we consider potentials with  $r_0 \ll a_{\text{ho}}$  [ $a_{\text{ho}} = \sqrt{\hbar/(m\omega)}$ ] that support at most one free-space  $s$ -wave bound state.

For the trapped (2, 1) system with zero-range interactions, we determine a large portion of the energy spectrum by solving the Lippman Schwinger equation for arbitrary scattering length [150]. This means that  $n_s$  can be determined within the microscopic approach over a wide temperature regime. Figure 4.2(b) shows the classical moment of inertia  $I_c$  of the (2, 1) system as a function of the temperature for different  $1/a_s$  ( $a_s$  positive).  $I_c$  decreases for fixed  $T$  with increasing  $1/a_s$  and increases for fixed  $a_s$  with increasing  $T$ . Figure 4.2(c) shows the quantum moment of inertia  $I_q$ . In the high temperature regime,  $I_q$  and  $I_c$  are nearly identical. However, in the low temperature regime, notable differences exist. For  $1/a_s = 0$ ,  $I_q$  diverges to positive infinity as  $T \rightarrow 0$ . For  $a_{\text{ho}}/a_s \approx 1$ , in contrast,  $I_q$  is zero at  $T = 0$ , increases sharply for  $k_B T \lesssim 0.1E_{\text{ho}}$ , and then decreases for  $k_B T \approx 0.1 - 0.5E_{\text{ho}}$ . As  $a_{\text{ho}}/a_s$  increases, the local maximum moves to larger temperatures and eventually disappears for

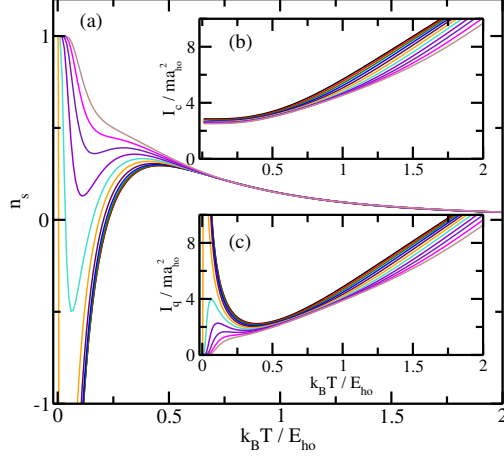


Figure 4.2: Properties of the interacting trapped  $(2, 1)$  system as a function of  $k_B T / E_{ho}$ . (a) The lines from bottom to top show  $n_s$  for  $a_{ho}/a_s = 0, 0.2, \dots, 2$ . (b)/(c) The lines from top to bottom show  $I_c$  and  $I_q$ , respectively, for  $a_{ho}/a_s = 0, 0.2, \dots, 2$ .

$a_{ho}/a_s \approx 2$ . The dramatic change of  $I_q$  at low  $T$  on the positive  $a_s$  side can be traced back to the symmetry change of the ground state wave function. The lowest eigenstate of the  $(2, 1)$  system has  $L = 1$  for  $a_{ho}/a_s \lesssim 1$  and  $L = 0$  for  $a_{ho}/a_s \gtrsim 1$ . Correspondingly,  $I_q$  goes, in the zero  $T$  limit, to  $+\infty$  for  $a_{ho}/a_s \lesssim 1$  and to 0 for  $a_{ho}/a_s \gtrsim 1$ . The strong variation of  $I_q$  near  $a_{ho}/a_s \approx 1$  in the low  $T$  regime reflects the “competing” contributions of the  $L = 0$  and  $L = 1$  states to the thermal average.

Combining  $I_c$  and  $I_q$  yields  $n_s$  [see Fig. 4.2(a)]. The  $(2, 1)$  systems with  $a_{ho}/a_s \lesssim 1$  and  $a_{ho}/a_s \gtrsim 1$  have a superfluid fraction that goes to negative infinity and one, respectively, at zero temperature. This can be viewed as a “quantum phase transition like” feature [150, 200]. At  $k_B T = 0.2 E_{ho}$ —a temperature that might be achievable with current experimental setups [90, 92]— $n_s$  varies between  $-0.14(1)$  and  $0.54(1)$  for  $a_{ho}/a_s = 0$  to 2. For a given  $a_s$ ,  $n_s$  varies notably over a small temperature regime. The fact that  $n_s$  is essentially independent of  $a_s$  for  $k_B T \gtrsim 0.75 E_{ho}$  and strongly dependent on  $a_s$  for  $k_B T \lesssim 0.4 E_{ho}$  might prove advantageous for qualitatively verifying the predicted behavior experimentally.

We now investigate a trapped spin-balanced system. Figure 4.3(a) shows  $n_s$  for the  $(2, 2)$  system with  $a_s/a_{ho} = 0, -0.2, -1$ , and  $\infty$ . The ground state of the non-interacting  $(2, 2)$

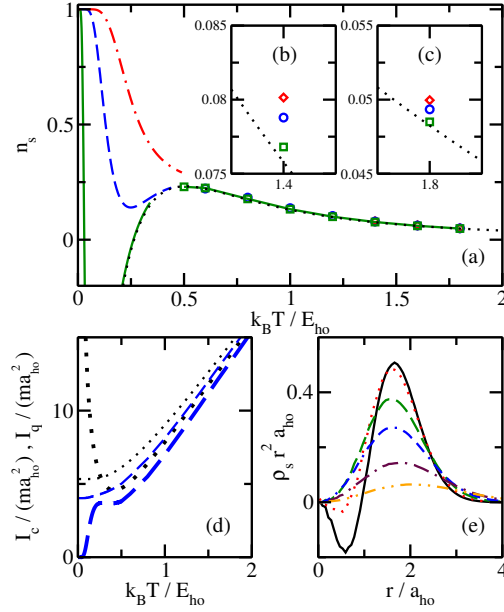


Figure 4.3: Properties of the trapped (2, 2) system. (a) The dotted, solid, dashed, and dash-dotted lines show  $n_s$  as a function of  $k_B T / E_{ho}$  for  $a_s/a_{ho} = 0, -0.2, -1$ , and  $\infty$ , respectively. The squares, circles, and diamonds show  $n_s$  obtained by the PIMC approach for  $a_s/a_{ho} = -0.2, -1$ , and  $\infty$ , respectively. (b) and (c) show blowups of the high-temperature region. (d) The thin dotted and dashed lines show  $I_c$  for  $a_s = 0$  and  $-a_{ho}$ , respectively; the thick dotted and dashed lines show  $I_q$  for  $a_s = 0$  and  $-a_{ho}$ , respectively. The dashed curves are obtained by the microscopic approach (using  $r_0 = 0.06a_{ho}$ ) for  $k_B T / E_{ho} \leq 0.5$  and by the PIMC approach (using  $r_0 = 0.1a_{ho}$ ) for  $k_B T / E_{ho} \geq 0.6$ . (e) The solid, dotted, dashed, dash-dash-dotted, dash-dotted, and dash-dot-dotted lines show  $\rho_s r^2$  for  $a_s = -0.2a_{ho}$  and  $k_B T / E_{ho} = 0.5, 0.6, 0.8, 1, 1.4$ , and  $2$ , respectively.

system is nine-fold degenerate (one state has  $L = 0$ , three states have  $L = 1$ , and five states have  $L = 2$ ). The degeneracy of the ground state makes  $I_q$  [see thick dotted line in Fig. 4.3(d)] diverge to plus infinity at  $T = 0$ . The superfluid fraction, in turn, goes to minus infinity as  $T \rightarrow 0$ . As the interactions are turned on, the degeneracy of the states with different  $L$  is lifted, with the energy of the  $L = 0$  state lying below that of the  $L = 1$  and 2 states. This implies that  $I_q$  goes to zero at  $T = 0$  for  $a_s \neq 0$  [for  $a_s/a_{\text{ho}} = -1$ , see the thick dashed line in Fig. 4.3(d)]. The behavior of the (2, 2) system is similar to that of the (2, 1) system in that the zero temperature limit of  $n_s$  changes from minus infinity to one as the scattering length is tuned. The transition, however, occurs at different scattering lengths [ $a_s = 0$  for the (2, 2) system and  $a_{\text{ho}}/a_s \approx 1$  for the (2, 1) system].

Figure 4.3(e) shows the radial superfluid density for the (2, 2) system with  $a_s = -0.2a_{\text{ho}}$  for various temperatures. For the lowest temperature considered ( $k_B T = 0.5E_{\text{ho}}$ ),  $n_s$  is equal to 0.230(3). Although  $n_s$  is positive, the radial superfluid density is negative in the small  $r$  region, reflecting the admixture of finite  $L$  states to the density matrix. As the temperature increases, the amplitude of the negative part of the radial superfluid density decreases and moves to smaller  $r$ . When the radial superfluid density is positive everywhere, it roughly has the same shape as the total radial density (not shown) but with significantly decreased amplitude. This shows that the superfluid density is, in this regime, distributed roughly uniformly throughout the cloud and not localized primarily near the center or edge of the cloud. We find similar behavior for other  $a_s$ .

In practice, thermal equilibrium can not be reached if the confinement is spherically symmetric. We have checked that our results hold qualitatively for anisotropic traps provided that  $|\omega_x - \omega_y| \ll \omega_x + \omega_y$ . Moreover, the abnormal behavior of  $n_s$  and  $I_q$  is also found for finite rotating frequencies, provided that  $\hbar\Omega \ll E_{\text{ho}}$ . Instead of probing the response to a rotation of the trap, it might be possible to simulate the rotation (and the resulting effective magnetic field) by applying an effective gauge field [201].

To summarize, we determined the superfluid properties of small harmonically trapped Fermi gases as functions of the  $s$ -wave scattering length and temperature. At low temperature, the quantum moment of inertia behaves, in certain regimes, abnormal, i.e., it is larger than the classical moment of inertia, yielding a negative superfluid fraction. The abnormal behavior arises if one or more of the low-lying eigenstates have a finite circulation, i.e., support a vortex. The relevant temperature is roughly  $\lesssim 0.5E_{\text{ho}}/k_B$ . Our predictions are unique to small systems, since such low temperatures can only be reached in few-fermion systems [90, 92] and not in large Fermi gases.

*Acknowledgement:* Support by the National Science Foundation (NSF) through Grant No. PHY-1205443 is gratefully acknowledged. This work used the Extreme Science and Engineering Discovery Environment (XSEDE), which is supported by NSF Grant No. OCI-1053575, and the WSU HPC.

# Chapter 5

## Temperature-dependence of small harmonically trapped atom systems with Bose, Fermi and Boltzmann statistics

by Yangqian Yan<sup>1</sup> and D. Blume<sup>1</sup>

<sup>1</sup>Department of Physics and Astronomy, Washington State University, Pullman,  
Washington 99164-2814, USA

Copyright (2014) by the American Physical Society

While the zero-temperature properties of harmonically trapped cold few-atom systems have been discussed fairly extensively over the past decade, much less is known about the finite-temperature properties. Working in the canonical ensemble, we characterize small harmonically trapped atomic systems as a function of the temperature using analytical and numerical techniques. We present results for the energetics, structural properties, condensate fraction, superfluid fraction, and superfluid density. Our calculations for the two-body sys-

tem underline that the condensate and superfluid fractions are distinctly different quantities. Our work demonstrates that the path integral Monte Carlo method yields reliable results for bosonic and fermionic systems over a wide temperature range, including the regime where the de Broglie wave length is large, i.e., where the statistics plays an important role. The regime where the Fermi sign problem leads to reasonably large signal to noise ratios is mapped out for selected parameter combinations. Our calculations for bosons focus on the unitary regime, where the physics is expected to be governed by the three-body parameter. If the three-body parameter is large compared to the inverse of the harmonic oscillator length, we find that the bosons form a droplet at low temperature and behave approximately like a non-interacting Bose and eventually Boltzmann gas at high temperature. The change of the behavior occurs over a fairly narrow temperature range. A simple model that reproduces the key aspects of the phase transition like feature, which can potentially be observed in cold atom Bose gas experiments, is presented.

## 5.1 Introduction

Ultracold atomic gases provide a flexible platform for studying a myriad of phenomena that are driven by quantum mechanics [32, 76, 170, 171, 202, 203]. Generally speaking, quantum statistical effects dominate when the de Broglie wave length is comparable to or larger than the average interparticle spacing. When the de Broglie wave length is small, the particle statistics plays a negligible role and the system dynamics is governed by Boltzmann statistics. Since the de Broglie wave length scales as  $1/\sqrt{T}$  [170, 171], where  $T$  is the temperature, changing the temperature allows one to turn the particle statistics “on” and “off”. Atomic gases, which can be cooled to below the quantum degeneracy temperature, thus provide an ideal platform for investigating the importance of particle statistics.

For macroscopic samples, a prominent example for a thermal phase transition is the transition from the normal to the superfluid phase as observed in bosonic liquid  $^4\text{He}$  and

fermionic liquid  $^3\text{He}$  [12]. Bose-Einstein condensation, the macroscopic occupation of a single particle state, is another important example. While Bose-Einstein condensation occurs for ultracold bosonic atomic gases [202], it does not occur, at least not directly, for ultracold fermionic atomic gases [30, 32]. Condensation for fermions occurs only when two fermions form composite bosons (diatomic molecules or Cooper pairs) [30, 32, 204, 205]. If the number of particles is finite (as opposed to infinite), phase transitions get smeared out and the usual concept, which considers statistical properties in the thermodynamic limit, has to be revised [206, 207].

The main objective of this paper is to study the temperature dependence of small harmonically trapped atomic Bose and Fermi systems. To describe these systems, we adopt the canonical ensemble, i.e., we assume that the system under study is in thermal contact with a heat bath or thermostat, which has a large number of particles and a well defined temperature  $T$  [208]. We monitor various system properties as a function of the temperature, the number of particles, the particle statistics, and the interaction strength. Particular emphasis is placed on the strongly-interacting unitary regime, where the  $s$ -wave scattering length diverges. At zero temperature, it is well established that the particle statistics has a paramount effect on the system properties. Two-component Fermi gases with infinitely large interspecies scattering length are fully described by the  $s$ -wave scattering length alone [32, 71, 203, 209, 210], while the properties of Bose gases additionally depend on a three-body parameter [41, 211]. These fundamental differences, which are due to the particle statistics, continue to play an important role at low temperature but die out at sufficiently high temperature. An interesting question, which we attempt to answer in this paper, is thus what happens at intermediate temperatures. As expected, we find that the low and intermediate temperature behavior of Bose and Fermi gases is vastly different. For certain parameter combinations, we find a thermal phase transition like feature for Bose systems that is governed by the three-body Efimov parameter. Specifically, we find a transition from a droplet like state to a gas-like

state. No such transition exists for two-component Fermi gases.

The remainder of this paper is organized as follows. Section 5.2 introduces the system Hamiltonian and reviews the connections between the free-space Efimov spectrum and the zero temperature spectrum of the harmonically trapped three-boson system. Moreover, the path integral Monte Carlo (PIMC) approach is introduced and some numerical details are discussed. Section 5.3 presents finite temperature characteristics of the trapped two-atom system. Emphasis is placed on the condensate and superfluid fractions. The radial superfluid density is calculated and analyzed. Section 5.4 discusses our finite temperature results for systems with three and more particles. Section 5.4.1 focuses on systems consisting of  $N$  identical bosons while Sec. 5.4.2 considers a trapped gas with Bose, Fermi or Boltzmann statistics with an impurity. Lastly, Sec. 5.5 concludes.

## 5.2 Theoretical background

### 5.2.1 System Hamiltonian and observables

This section introduces the system Hamiltonian and reviews two frameworks for determining thermally averaged observables. We fix the number of particles and work in the canonical ensemble. We consider  $N$  particles with position vectors  $\mathbf{r}_j$  and mass  $m_a$  in a spherically symmetric harmonic trap with angular trapping frequency  $\omega$ . The model Hamiltonian  $\hat{H}$  reads

$$\hat{H} = \hat{H}_0 + \hat{V}, \quad (5.1)$$

where  $\hat{H}_0$ ,

$$\hat{H}_0 = \sum_{j=1}^N \left( \frac{-\hbar^2}{2m_a} \nabla_j^2 + \frac{1}{2} m_a \omega^2 \mathbf{r}_j^2 \right), \quad (5.2)$$

denotes the non-interacting Hamiltonian. The interaction potential  $\hat{V}$  reads

$$\hat{V} = \sum_{j=1}^N \sum_{k>j}^N V_{\text{tb}}^{(jk)}(r_{jk}), \quad (5.3)$$

where  $r_{jk}$  ( $r_{jk} = |\mathbf{r}_j - \mathbf{r}_k| = |\mathbf{r}_{jk}|$ ) denotes the relative distance between the  $j$ th and  $k$ th particles and  $V_{\text{tb}}^{(jk)}$  the interaction potential for the  $j$ th and  $k$ th particles. We employ two different interaction models. Our calculations presented in Sec. 5.3 employ the regularized zero-range Fermi-Huang pseudopotential  $V_{\text{F}}^{(jk)}$  [3] with  $s$ -wave scattering length  $a_s^{(jk)}$ . Our PIMC calculations presented in Sec. 5.4 employ a finite-range Gaussian potential  $V_{\text{G}}^{(jk)}$ , where  $V_{\text{G}}^{(jk)}(r_{jk}) = U_0^{(jk)} \exp[-r_{jk}^2/(2r_0^2)]$  with depth  $U_0^{(jk)}$  ( $U_0^{(jk)} < 0$ ) and range  $r_0$ . The depth and range are adjusted so that  $V_{\text{G}}^{(jk)}$  yields the desired  $s$ -wave scattering length  $a_s^{(jk)}$ . Throughout, we consider potentials that support at most one free-space  $s$ -wave bound state and whose range  $r_0$  is much smaller than the characteristic harmonic trap length  $a_{\text{ho}}$ , where  $a_{\text{ho}} = \sqrt{\hbar/(m_a\omega)}$ .

To calculate thermally averaged quantities, we introduce the density operator  $\hat{\rho}$  [19, 207],

$$\hat{\rho} = e^{-\beta\hat{H}}, \quad (5.4)$$

where  $\beta$  is the inverse temperature,  $\beta = 1/(k_B T)$ . The expectation value for an operator  $\hat{\mathcal{O}}$  is  $\text{Tr}(\hat{\rho}\hat{\mathcal{O}})/Z$ , where ‘‘Tr’’ stands for the trace of the matrix that is created by projecting the operator onto a complete basis set, and  $Z = \text{Tr}(\hat{\rho})$  is the partition function.

A convenient basis set consists of the energy eigen states  $\psi_j$  of the Hamiltonian  $\hat{H}$ . In this case, the density operator is diagonal and can be written as [207]

$$\hat{\rho} = \sum_j e^{-\beta E_j} |\psi_j\rangle \langle\psi_j|, \quad (5.5)$$

where  $E_j$  denotes the eigen energy of state  $\psi_j$ , and the partition function reads

$$Z = \sum_j e^{-\beta E_j}. \quad (5.6)$$

The sums in Eqs. (5.5) and (5.6) are limited to the energy eigen states  $\psi_j$  that have the proper particle statistics. For  $N = 2$ , e.g., the eigen states can be grouped into states that are symmetric and those that are anti-symmetric under the exchange of the two particles. If we treat two identical bosons (fermions), only the symmetric (anti-symmetric) states are included in the sums in Eqs. (5.5) and (5.6). Importantly, if the complete set is known, the thermal average  $\langle \hat{\mathcal{O}} \rangle$  of the operator  $\hat{\mathcal{O}}$  can be calculated,

$$\langle \hat{\mathcal{O}} \rangle = Z^{-1} \sum_j e^{-\beta E_j} \langle \psi_j | \hat{\mathcal{O}} | \psi_j \rangle. \quad (5.7)$$

While the determination of a large number of energy eigen states  $\psi_j$  is feasible for small systems, say  $N \lesssim 4$ , it becomes unfeasible for larger systems.

An alternative formulation, which forms the starting point of the PIMC approach [19] (see Sec. 5.2.3 for details), projects the density operator onto the position basis,

$$\rho_{\text{non-symm}}(\mathbf{R}, \mathbf{R}', \beta) = \langle \mathbf{R} | \hat{\rho} | \mathbf{R}' \rangle. \quad (5.8)$$

Here,  $\mathbf{R}$  and  $\mathbf{R}'$  collectively denote the position vectors  $\mathbf{r}_1, \dots, \mathbf{r}_N$  and  $\mathbf{r}'_1, \dots, \mathbf{r}'_N$ , respectively. The thermal average of the operator  $\hat{\mathcal{O}}$  then reads

$$\langle \hat{\mathcal{O}} \rangle_{\text{non-symm}} = (Z_{\text{non-symm}})^{-1} \times \int d\mathbf{R} d\mathbf{R}' \rho_{\text{non-symm}}(\mathbf{R}, \mathbf{R}', \beta) \langle \mathbf{R}' | \hat{\mathcal{O}} | \mathbf{R} \rangle, \quad (5.9)$$

where the partition function  $Z_{\text{non-symm}}$ ,

$$Z_{\text{non-symm}} = \int d\mathbf{R} \rho_{\text{non-symm}}(\mathbf{R}, \mathbf{R}, \beta), \quad (5.10)$$

is again the trace over the diagonal elements. To properly symmetrize or anti-symmetrize the density operator, we introduce the symmetrizer  $\hat{\mathcal{P}}$  [19]. For the single-component Bose and Fermi gases,  $\hat{\mathcal{P}}$  can be written as [121]

$$\hat{\mathcal{P}} = \frac{1}{N!} \sum_{\sigma} (\pm 1)^{N_I(\sigma)} \hat{P}_{\sigma}, \quad (5.11)$$

where  $\sigma$  denotes the permutation of particle indices,  $N_I(\sigma)$  the number of inversions in  $\sigma$  [122], and  $\hat{P}_{\sigma}$  the corresponding permutation operator. For two identical fermions, e.g.,  $\hat{\mathcal{P}}$  reads  $(1 - \hat{P}_{12})/2$ , where  $\hat{P}_{12}$  exchanges the particle labels 1 and 2. For mixtures, the symmetrizer  $\hat{\mathcal{P}}$  has to be generalized appropriately. The partition function and thermally averaged observables then read [19]

$$Z = \int d\mathbf{R} \rho(\hat{\mathcal{P}}\mathbf{R}, \mathbf{R}, \beta) \quad (5.12)$$

and

$$\langle \hat{\mathcal{O}} \rangle = Z^{-1} \int d\mathbf{R} d\mathbf{R}' \rho(\hat{\mathcal{P}}\mathbf{R}, \mathbf{R}', \beta) \langle \mathbf{R}' | \hat{\mathcal{O}} | \mathbf{R} \rangle. \quad (5.13)$$

In addition to the thermally averaged energy  $E$ , this work considers a number of thermally averaged structural properties. The scaled radial density  $4\pi r_j^2 \rho_{\text{rad}}(r_j)$  with normalization  $4\pi \int dr_j \rho_{\text{rad}}(r_j) r_j^2 = N$  [212] tells one the likelihood of finding the  $j$ th particle at distance  $r_j$  from the trap center. The scaled pair distribution function  $4\pi r_{jk}^2 P_{\text{pair}}(r_{jk})$  with normalization  $4\pi \int dr_{jk} P_{\text{pair}}(r_{jk}) r_{jk}^2 = 1$  tells one the likelihood of finding particles  $j$  and  $k$  at distance  $r_{jk}$ . The hyperradial distribution function  $P_{\text{hyper}}(R)$  with normalization  $\int dR P_{\text{hyper}}(R) = 1$

tells one the likelihood of finding particles  $j$ ,  $k$  and  $l$  in a configuration of size  $R$ ; here,  $R^2 = (r_{jk}^2 + r_{kl}^2 + r_{jl}^2)/3$ . For  $N = 3$ ,  $R$  is the hyperradius (see Sec. 5.2.2 for details).

We also consider the condensate fraction, superfluid fraction, and superfluid density. For homogeneous systems, the condensate fraction  $n_c$  is typically defined through the large distance behavior of the one-body density matrix for bosons and the two-body density matrix for two-component fermions [30, 32]. It indicates the off-diagonal long-range order of the system. For inhomogeneous systems, the condensate fraction is defined as the largest eigenvalue of the one- and two-body density matrices for bosons and fermions, respectively [29–31]. Intuitively, it is clear that the long-range behavior is “cut off” by the confinement or the finite extend of the system, implying that the asymptotic behavior of the density matrix contains no information about non-trivial correlations. Section 5.3 reports the dependence of the condensate fraction  $n_c$  on the temperature for two identical bosons and two distinguishable particles. These studies extend the zero temperature calculations of  $n_c$  presented in Ref. [149] to finite temperature. The finite temperature behavior of  $n_c$  has previously been reported for two harmonically trapped particles in one dimension [213] but not, to the best of our knowledge, for two harmonically trapped particles in three dimensions.

The superfluid fraction  $n_s$  can be defined in various ways (see, e.g., Refs. [30, 214–216] for a discussion). In this work, we utilize the moment of inertia based definition, which has its origin in the two-fluid model [188–191],

$$n_s = 1 - \frac{I_q}{I_c}. \quad (5.14)$$

The quantum moment of inertia  $I_q$  is defined in terms of the response to an infinitesimal rotation about the  $z$ -axis,

$$I_q = \beta(\langle \hat{L}_{\text{tot},z}^2 \rangle - \langle \hat{L}_{\text{tot},z} \rangle^2), \quad (5.15)$$

where  $\hat{L}_{\text{tot},z}$  denotes the  $z$ -component of the total angular momentum operator  $\hat{\mathbf{L}}_{\text{tot}}$ . The classical moment of inertia  $I_c$  is defined through

$$I_c = \langle m_a \sum_j r_{j,\perp}^2 \rangle, \quad (5.16)$$

where  $r_{j,\perp}$  denotes the distance of the  $j$ th particle to the  $z$ -axis,  $r_{j,\perp} = |\mathbf{r}_j \times \hat{z}|$ . The superfluid density is defined such that  $m_a \int d\mathbf{r} \rho_s(\mathbf{r}) r_\perp^2 = I_c - I_q$ , where  $r_\perp$  denotes the distance to the  $z$ -axis [195]. The moment of inertia based definitions of the superfluid fraction and superfluid density have previously been applied to a variety of finite-sized quantum liquids [173–177, 217, 218]. Knowing the complete set of energy eigen states and eigen energies and using Eq. (5.7), the thermally averaged expectation values  $\langle \hat{L}_{\text{tot},z} \rangle$  and  $\langle \hat{L}_{\text{tot},z}^2 \rangle$  can be calculated, thereby yielding  $I_q$ . Within the PIMC approach, the superfluid fraction and superfluid radial density are evaluated using the area estimator [94, 191, 195, 219] (see Sec. 5.2.3 for details on the PIMC approach).

## 5.2.2 Efimovian states of three identical bosons in a trap

This section reviews the zero-temperature properties of three identical harmonically-trapped bosons. As discussed in the literature [76], harmonically trapped unitary Bose and Fermi gases with short-range interactions exhibit universal properties, provided the range of the interaction is smaller than all other length scales in the problem. The properties of the two-component Fermi gas near a broad  $s$ -wave resonance (and away from  $p$ - and higher-partial wave resonances) are governed by the interspecies  $s$ -wave scattering length  $a_s$  and the harmonic oscillator length  $a_{\text{ho}}$ . In the unitarity limit, i.e., for  $|a_s| = \infty$ , the  $s$ -wave scattering length does not define a meaningful length scale and the only remaining length scale is  $a_{\text{ho}}$  [32, 76, 146, 203, 220]. The corresponding energy scale is  $E_{\text{ho}} = \hbar\omega$ . For three or more identical bosons, an additional parameter, namely, the three-body parameter  $\kappa_*$ , is

necessary to describe the ground state properties of the Bose gas [41, 146, 211, 220].

The role of  $\kappa_*$  can be made transparent using the hyperspherical coordinate approach [41, 76]. To this end, we separate off the center of mass motion and divide the remaining six coordinates into the hyperradius  $R$  and five hyperangles collectively denoted by  $\mathbf{\Omega}$ . In the limit of pairwise additive zero-range interactions with  $1/a_s = 0$ , the hyperradial and hyperangular degrees of freedom are separable [41, 146, 211]. The lowest eigen value of the hyperangular Schrödinger equation for the channel with vanishing relative angular momentum angular  $l$  is typically denoted by  $s_0$ , where  $s_0 \approx 1.006i$  [41, 211]. The hyperradial Hamiltonian  $\hat{H}_R$  can then be written as

$$\hat{H}_R = \frac{-\hbar^2}{2m_a} \frac{\partial^2}{\partial R^2} + \frac{1}{2} m_a \omega^2 R^2 + \frac{\hbar^2 (s_0^2 - 1/4)}{2m_a R^2}. \quad (5.17)$$

The last term can be interpreted as an effective attractive potential, which diverges in the  $R = 0$  limit. Without a three-body parameter, the system exhibits the Thomas collapse [43]. The scaled radial solution in the small  $R$  limit is proportional to  $\sqrt{R} \sin(\theta_b + \text{Im}(s_0) \ln R)$  [221], where  $\theta_b$ ,

$$\theta_b = \arg \left( \frac{\Gamma(\frac{1}{2} - \frac{E_{\text{rel}}}{2E_{\text{ho}}} + \frac{s_0}{2})}{\Gamma(1 + s_0)} \right), \quad (5.18)$$

is the three-body phase that determines the short-range behavior of the hyperradial wave function and  $E_{\text{rel}}$  denotes the relative three-body energy. The three-body phase can be related to the three-body parameter  $\kappa_*$ .

Solving Eq. (5.18), the solid lines in Fig. 5.1 show the relative three-body zero-range eigen energies as a function of the three-body phase  $\theta_b$  for infinitely large  $s$ -wave scattering length. For a fixed  $\theta_b$ , the energies of the negative part of the energy spectrum are spaced roughly by the factor 515 [221, 222]. These geometrically spaced energy levels are the signature of the three-body Efimov effect. In free space, the spacing is exactly  $\exp(2\pi/|s_0|) \approx (22.7)^2 \approx 515$  and the three-body parameter  $\kappa_*$  is defined as the binding momentum of one of the Efimov

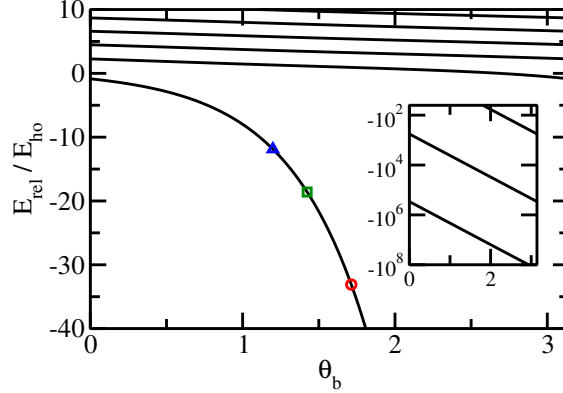


Figure 5.1: Relative energy spectrum as a function of the three-body phase  $\theta_b$  for three identical bosons in a harmonic trap interacting through zero-range potentials with infinite  $s$ -wave scattering lengths. The circle, square, and triangle show the ground state energy for the Gaussian two-body interaction with range  $r_0/a_{\text{ho}} = 0.06, 0.08,$  and  $0.1,$  respectively. The inset shows the negative energy regime on a log scale. The spacing between the energy levels for fixed  $\theta_b$  is very close to 515, i.e., very close to the free-space scaling factor.

trimers,  $E_{\text{rel}} = \hbar^2 \kappa_*^2 / m$  [41]. Knowing  $\kappa_*$ , the ratio between consecutive energy levels of the free-space system is fixed. For the trapped system, corrections arise when the trimer size approaches the harmonic oscillator length. For the states with positive energy, the spacing between consecutive states is approximately  $2E_{\text{ho}}$  [221–223].

We now connect the energy spectrum for the Gaussian interaction model  $V_G$  with that for the zero-range model. In free-space, the three-body system with pairwise Gaussian interaction supports infinitely many states. The spacing between the ground state and the first excited state at unitarity is  $(22.98)^2$  and between the energies of the first excited state and the second excited state is  $(22.7)^2$ . These values are close to the universal scaling factor. Indeed, the Gaussian interaction model has been used extensively in the literature to describe Efimov physics [7, 78, 224]. For the trapped system, the ratio between the range  $r_0$  of the two-body interaction and the harmonic oscillator length comes into play. The circle, square and triangle in Fig. 5.1 show the relative energy of the lowest state of the trapped system for  $r_0/a_{\text{ho}} = 0.06, 0.08$  and  $0.1,$  respectively. Assuming that the zero-range energy spectrum provides a reasonable description, Fig. 5.1 allows us to estimate the three-body phase.

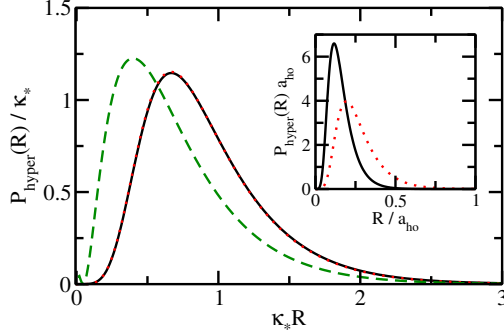


Figure 5.2: Hyperradial density  $P_{\text{hyper}}(R)$  for three identical bosons at unitarity. Solid and dotted lines show the PIMC results at  $k_B T/E_{\text{ho}} = 0.4$  for the Gaussian model potential with  $r_0/a_{\text{ho}} = 0.06$  and  $0.1$ , respectively (in the main panel, the curves are indistinguishable on the scale shown). The main panel and the inset show the same data but use a different scaling: The main panel uses units derived from the energy of the three-boson system at  $T = 0$  while the inset employs harmonic oscillator units. For comparison, the dashed line shows the hyperradial density obtained using the zero-range pseudopotential with  $\kappa_*$  determined by the relative energy of the finite-range potential.

For our purposes, the size of the trimer compared to the range of the interaction is relevant. For the three  $r_0$  considered, the size of the lowest trimer, as measured by the expectation value of the hyperradius  $R$ , is roughly  $0.160a_{\text{ho}}$ ,  $0.212a_{\text{ho}}$  and  $0.266a_{\text{ho}}$ , i.e., the trimers are much smaller than  $a_{\text{ho}}$ , and thus very close to the free space trimers. The lowest Efimov trimer is only a bit larger than  $r_0$  (the size is about  $2.66r_0$  for all cases), implying that we expect finite-range effects to be non-negligible. Indeed, Fig. 5.2 shows that the hyperradial densities of the lowest state of the finite-range three-body system (solid and dotted lines) differ notably from the hyperradial density of the zero-range system (dashed line). This difference cannot be attributed to the fact that the hyperradial densities are calculated at finite temperature (the finite-range  $T = 0$  hyperradial densities are, on the scale chosen, indistinguishable from those shown in Fig. 5.2) but is due to finite-range effects. Despite these finite-range corrections, the Gaussian interaction model allows us to gain insights into finite-temperature effects that are governed by the lowest Efimov state of the three-body system (see Sec. 5.4 for details).

### 5.2.3 PIMC approach

This section reviews the finite-temperature continuous-space PIMC approach [19]. The key idea behind the PIMC approach is to convert the calculations at low temperature (large  $\beta$ ) into a series of calculations at high temperature. Specifically, the PIMC approach rewrites  $\exp(-\beta\hat{H})$  in terms of the product  $\prod_{j=1}^M \exp(-\tau\hat{H})$ , where  $\tau = \beta/M$ . The idea is to use a sufficiently small  $\tau$  (sufficiently large integer  $M$ ) so that the integrals involving  $\tau$  can be factorized with controllable error. In the calculations reported in Sec. 5.4, we use  $M \approx 400 - 7000$  (the actual number used depends on the temperature  $T$  and the two-body range  $r_0$ ). Inserting  $\int_j |\mathbf{R}_j\rangle \langle \mathbf{R}_j|$  repeatedly, Eq. (5.13) becomes [19]

$$\begin{aligned} \langle \hat{\mathcal{O}} \rangle = Z^{-1} \int d\mathbf{R}_0 \dots d\mathbf{R}_M & \rho(\hat{\mathcal{P}}\mathbf{R}_0, \mathbf{R}_1; \tau) \times \\ & \rho(\mathbf{R}_1, \mathbf{R}_2; \tau) \times \dots \\ & \times \rho(\mathbf{R}_{M-1}, \mathbf{R}_M; \tau) \langle \mathbf{R}_M | \mathcal{O} | \mathbf{R}_0 \rangle. \end{aligned} \quad (5.19)$$

To evaluate expectation values of operators that probe the diagonal but not the off-diagonal elements of the real-space density matrix, only closed paths with  $\hat{\mathcal{P}}\mathbf{R}_0 = \mathbf{R}_M$  are needed. The density matrix  $\rho(\mathbf{R}_{j-1}, \mathbf{R}_j; \tau)$  is, in general, unknown. Using the second- or fourth-order factorization [19, 112, 158], the high-temperature density operator can be divided into the non-interacting and interacting parts,

$$\begin{aligned} \exp \left[ -\tau(\hat{H}_0 + \hat{V}) \right] = \exp \left( -\tau \frac{\hat{V}}{2} \right) \exp \left( -\tau \hat{H}_0 \right) \times \\ \exp \left( -\tau \frac{\hat{V}}{2} \right) + \dots \end{aligned} \quad (5.20)$$

and

$$\begin{aligned} \exp \left[ -\tau(\hat{H}_0 + \hat{V}) \right] &= \exp \left( -\tau \frac{\hat{V}}{6} \right) \exp \left( -\tau \frac{\hat{H}_0}{2} \right) \times \\ &\exp \left( -\tau \frac{2\tilde{V}}{3} \right) \exp \left( -\tau \frac{\hat{H}_0}{2} \right) \exp \left( -\tau \frac{\hat{V}}{6} \right) \\ &\quad + \dots, \end{aligned} \tag{5.21}$$

where  $\tilde{V}$  is given by  $\hat{V} + \tau^2[\hat{V}, [\hat{H}_0, \hat{V}]]/48$ . For observables that are determined by the diagonal elements of the density matrix, these factorizations yield errors that scale as  $\tau^3$  and  $\tau^5$ , respectively [112]. The non-interacting part of the density matrix in the position basis can be written compactly [20, 207],

$$\begin{aligned} \langle \mathbf{R} | e^{-\tau \hat{H}_0} | \mathbf{R}' \rangle &= a_{\text{ho}}^{-3N} \left[ 2\pi \sinh(\tilde{\beta}) \right]^{-3N/2} \times \\ &\exp \left[ -\frac{(\mathbf{R}^2 + \mathbf{R}'^2) \cosh(\tilde{\beta}) - 2\mathbf{R} \cdot \mathbf{R}'}{2 \sinh(\tilde{\beta}) a_{\text{ho}}^2} \right]. \end{aligned} \tag{5.22}$$

Here,  $\tilde{\beta}$  denotes the dimensionless inverse temperature,  $\tilde{\beta} = \beta E_{\text{ho}}$ . The potential dependent part of the density matrix reduces to evaluating the potential at the given configuration.

The energy and structural expectation values are calculated following standard procedures [19]. The superfluid fraction is calculated using the area estimator [19, 94, 191]. The superfluid density is calculated following Ref. [195]. The condensate fraction requires off-diagonal elements of the density matrix, i.e., open paths [225]. We have not yet implemented this.

In the high temperature limit, the particle statistics becomes negligible and the system behaves, to leading order, as a non-interacting gas of Boltzmann particles. To analyze the effects of the particle statistics for systems with two or more identical particles in the low temperature regime, we find it useful to divide the partition function  $Z$  into “even” and

“odd” contributions (a closely related definition can be found in Ref. [97]),

$$Z = Z_{\text{even}} \pm Z_{\text{odd}}, \quad (5.23)$$

where

$$Z_{\text{even}} = \sum_{P_{\text{even}}} \int d\mathbf{R} \rho(\hat{\mathcal{P}}\mathbf{R}, \mathbf{R}, \beta) \quad (5.24)$$

and

$$Z_{\text{odd}} = \sum_{P_{\text{odd}}} \int d\mathbf{R} \rho(\hat{\mathcal{P}}\mathbf{R}, \mathbf{R}, \beta); \quad (5.25)$$

the plus and minus sign apply if the system contains identical bosons and fermions, respectively (here and in the remainder of this section we assume that the system contains only one type of identical particles). The sum over  $P_{\text{even}}$  includes the permutations that are characterized by even  $N_I(\sigma)$  and the sum over  $P_{\text{odd}}$  includes the permutations that are characterized by odd  $N_I(\sigma)$ . The sum over  $P_{\text{odd}}$  is only non-zero if the system under study contains two or more identical particles. When the temperature is high, only the identity permutation (and thus only the first term) contributes, i.e., the statistics is suppressed and the system behaves like a Boltzmann gas. As the temperature decreases, the relative importance of the second term increases. In the zero temperature limit, the two terms contribute equally. We define the statistical factor  $S$  as the normalized ratio of the “even” and “odd” partition functions [97] [226],

$$S = \frac{Z_{\text{even}} - Z_{\text{odd}}}{Z_{\text{even}} + Z_{\text{odd}}}. \quad (5.26)$$

The statistical factor  $S$  approaches 1 in the high-temperature limit and 0 in the zero-temperature limit. Since the partition function enters into the denominator of the thermal expectation values, the statistical factor characterizes the numerical demands on the simulation for systems with identical fermions. The smaller  $S$  is, the harder the simulation is. As a

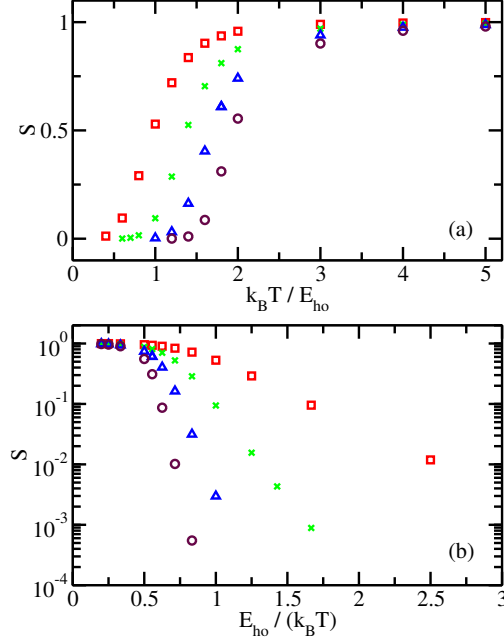


Figure 5.3: Statistical factor  $S$  for the  $(N - 1, 1)$  system with interspecies potential  $V_G$  with  $r_0 = 0.06a_{ho}$  and  $1/a_s = 0$ . Squares, crosses, triangles, and circles show the statistical factor  $S$  as a function of (a) the temperature  $T$  and (b) the inverse temperature  $T^{-1}$  for  $N = 3, 4, 5,$  and  $6$ , respectively.

rule of thumb, if we compare the  $S$  value for the same system at two different temperatures, then the simulation time required to obtain comparable accuracy for the observables at the two temperatures is  $(S_{high}/S_{low})^2$  times larger at the lower temperature than at the higher temperature (here,  $S_{high}$  and  $S_{low}$  are the  $S$  values at the higher and lower temperature, respectively). This phenomenon is known as the Fermi sign problem [97, 99, 134, 135]. A related interpretation of  $S$  is in terms of the “quantum statistics” of the system under study. For both bosons and fermions, a value of  $S$  around 1 indicates that the particles approximately follow Boltzmann statistics while a value of  $S$  close to 0 indicates that exchange effects play an important role.

Figure 5.3(a) shows the statistical factors as a function of the temperature for the  $N$  particle system consisting of  $N - 1$  identical particles and one impurity. The identical particles do not interact while the unlike particles interact through a Gaussian potential with  $r_0 = 0.06a_{ho}$  and infinite  $s$ -wave scattering length. The statistical factor deviates notably

from one when the temperature is of the order of the “Fermi temperature” or lower. The Fermi temperature is equal to  $5E_{\text{ho}}/2$  to  $7E_{\text{ho}}/2$  for the  $(N - 1, 1)$  systems with  $N = 3 - 6$ . At low temperature, the statistical factor depends exponentially on the inverse temperature, i.e.,  $S \propto \exp(-\beta\alpha_N)$  [97], where  $\alpha_N$  increases faster than linear with increasing  $N$ . We have performed reliable calculations for the symbols shown in Fig. 5.3. The lowest temperature that can be reached depends, of course, on the available computational resources. However, since the Fermi sign problem increases exponentially with decreasing temperature, the lower  $T$  limit shown in Fig. 5.3 is somewhat generic. The physics of the  $(N - 1, 1)$  systems with Bose, Fermi and Boltzmann statistics is discussed in more detail in Sec. 5.4.2.

### 5.3 Condensate and superfluid fractions of the two-body system

The condensate and superfluid fractions are distinct physical quantities that vanish when the de Broglie wave length is small but differ from zero when the de Broglie wave length is large. This section compares the condensate and superfluid fractions for the simplest interacting system, namely for two particles in a harmonic trap with zero-range  $s$ -wave interactions. For this system, the eigen spectrum and eigen functions are known in compact analytical form [145], which facilitates the calculation of  $n_c$  and  $n_s$  over a wide temperature range. The superfluid fraction is calculated using the energy eigen states in the moment of inertia based definition [see Eq. (5.14)].

An important point of this section is that the superfluid and condensate fractions are meaningful quantities not just for large systems but also for small systems. We will show in Sec. 5.4.1 that the superfluid fraction of the  $N$  boson system is, for certain parameter combinations, approximated well by that of a single particle. The superfluid fraction reflects symmetry properties of the system [216, 227, 228]. The connection between superfluidity

and angular momentum decoupling mechanisms, e.g., has been discussed in some detail in the context of small doped bosonic helium droplets [229, 230]. The condensate fraction is given by the largest eigen value of the one-body reduced density matrix  $\rho_{\text{red}}$  or, equivalently, the largest occupation number of the natural orbitals [29–31]. Since the natural orbitals are defined by decomposing the reduced density matrix in a specific way, the occupation numbers, and hence the condensate fraction, can be interpreted as a particular measure of the particle-particle correlations of the system. Our approach for determining the finite temperature reduced density matrix of the two-body system (which is discussed in the following paragraphs) also allows one to determine entanglement measures such as the concurrence [231] and negativity [232] of the two-particle system over a wide temperature range. Such calculations appear to have been challenging in the past [233].

The reduced density matrix  $\rho_{\text{red}}$  for the two-particle system reads

$$\rho_{\text{red}}(\mathbf{r}'_1, \mathbf{r}_1, \beta) = Z^{-1} \int d\mathbf{r}_2 \rho(\mathbf{r}'_1, \mathbf{r}_2, \mathbf{r}_1, \mathbf{r}_2, \beta). \quad (5.27)$$

Using the separation of the center of mass and relative coordinates, Eq. (5.27) becomes

$$\begin{aligned} \rho_{\text{red}}(\mathbf{r}'_1, \mathbf{r}_1, \beta) = \\ Z^{-1} \int d\mathbf{r}_2 \rho_{\text{rel}}(\mathbf{r}'_{\text{rel}}, \mathbf{r}_{\text{rel}}, \beta) \rho_{\text{cm}}(\mathbf{r}'_{\text{cm}}, \mathbf{r}_{\text{cm}}, \beta), \end{aligned} \quad (5.28)$$

where  $\mathbf{r}_{\text{rel}} = \mathbf{r}_1 - \mathbf{r}_2$ ,  $\mathbf{r}'_{\text{rel}} = \mathbf{r}'_1 - \mathbf{r}_2$ ,  $2\mathbf{r}_{\text{cm}} = \mathbf{r}_1 + \mathbf{r}_2$ ,  $2\mathbf{r}'_{\text{cm}} = \mathbf{r}'_1 + \mathbf{r}_2$ ,

$$\begin{aligned} \rho_{\text{rel}}(\mathbf{r}'_{\text{rel}}, \mathbf{r}_{\text{rel}}, \beta) = \\ \sum_{ilm} e^{-\beta E_{i,l}} \psi_{ilm}^*(\mathbf{r}'_{\text{rel}}) \psi_{ilm}(\mathbf{r}_{\text{rel}}), \end{aligned} \quad (5.29)$$

and

$$\rho_{\text{cm}}(\mathbf{r}'_{\text{cm}}, \mathbf{r}_{\text{cm}}, \beta) = \sum_{QLM} e^{-\beta E_{Q,L}} \psi_{QLM}^*(\mathbf{r}'_{\text{cm}}) \psi_{QLM}(\mathbf{r}_{\text{cm}}). \quad (5.30)$$

In Eq. (5.30),  $E_{Q,L}$  denotes the center-of-mass eigen energy, which can be conveniently written in terms of the principal quantum number  $Q$  ( $Q = 0, 1, \dots$ ) and the center of mass angular momentum quantum number  $L$  ( $L = 0, 1, \dots$ ),  $E_{Q,L} = (2Q + L + 3/2)E_{\text{ho}}$ . The energies are independent of the projection quantum number  $M$  ( $M = -L, -L + 1, \dots, L$ ). In Eq. (5.29),  $E_{i,l}$  denotes the relative eigen energy. For two Boltzmann particles, all  $l$  values are allowed. For two identical bosons, in contrast, only even  $l$  values are allowed. For finite relative angular momentum  $l$ , the relative energy reads  $E_{i,l} = (2i + l + 3/2)E_{\text{ho}}$ , where  $i = 0, 1, \dots$ . For  $l = 0$ ,  $i$  denotes a non-integer quantum number whose values are determined semi-analytically by solving a transcendental equation [145]. As in the center of mass case, the relative energies are independent of the projection quantum number  $m$  ( $m = -l, -l + 1, \dots, l$ ).

To evaluate  $\rho_{\text{rel}}$ , we use the fact that the  $l > 0$  states are not affected by the zero-range interactions and write  $\rho_{\text{rel}} = \rho_{\text{rel}}^{l>0,\text{NI}} + \rho_{\text{rel}}^{l=0,\text{int}}$ , where  $\rho_{\text{rel}}^{l>0,\text{NI}}$  denotes the  $l > 0$  contributions to the density matrix (these contributions are independent of the  $s$ -wave scattering length) and  $\rho_{\text{rel}}^{l=0,\text{int}}$  the  $l = 0$  contribution that depends on  $a_s$ . To evaluate the latter, it is convenient to project the interacting  $l = 0$  energy eigen states onto the non-interacting harmonic oscillator states,  $\psi_{i00}(\mathbf{r}_{\text{rel}}) = \sum_{q=0}^{\infty} C_q^{(i)} \psi_{q00}(\mathbf{r}_{\text{rel}})$ , where  $q = 0, 1, \dots$ . The expansion coefficients  $C_q^{(i)}$  are known analytically [145, 149]. Now that  $\rho_{\text{cm}}$  and  $\rho_{\text{rel}}$  are expressed in terms of the non-interacting wave functions in the relative and center of mass coordinates, the integral over  $d\mathbf{r}_2$  can be performed by reexpressing, using the Talmi-Moshinsky brackets [234, 235], the harmonic oscillator eigen states in the relative and center of mass coordinates in terms of the harmonic oscillator eigen states in the single particle coordinates. After integrating over  $d\mathbf{r}_2$ ,

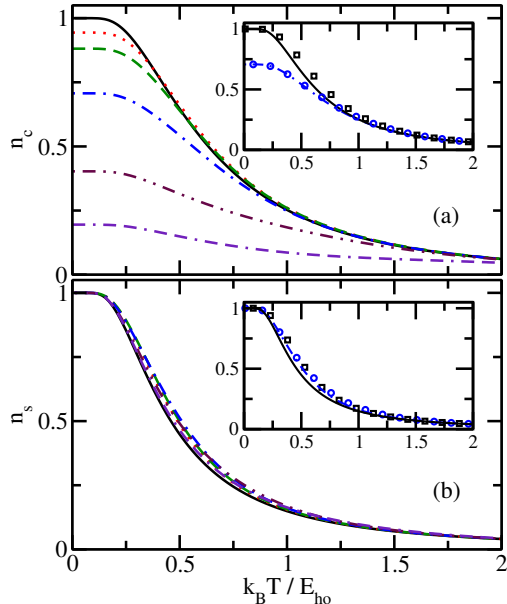


Figure 5.4: The lines show (a) the condensate fraction  $n_c$  and (b) the superfluid fraction  $n_s$  as a function of the temperature  $T$  for two Boltzmann particles with zero-range interaction for various  $a_s$ . The solid, dotted, dashed, dash-dotted, dash-dot-dotted, and dash-dash-dotted lines are for  $a_{\text{ho}}/a_s = -\infty, -2, 1, 0, 1,$  and  $2$ , respectively. In panel (b), the dependence on  $a_s$  is small. The insets compare (a) the condensate fraction  $n_c$  and (b) the superfluid fraction  $n_s$  for two Boltzmann particles (lines; these are the same data as shown in the main parts of the figure) and two identical bosons (squares and circles correspond to  $a_{\text{ho}}/a_s = -\infty$  and  $0$ , respectively) as a function of the temperature.

we project the reduced density matrix onto single-particle states in the  $\mathbf{r}_1$  coordinate. Using the orthogonality of the Clebsch-Gordon coefficients as well as other standard identities from angular momentum algebra, the calculation of the matrix elements simplifies dramatically. The resulting one-body density matrix is found to be block diagonal in the  $l$  and  $m$  quantum numbers. Furthermore, since the lowest  $l = 0$  state always minimizes the energy, the largest occupation number comes from the  $(l, m) = (0, 0)$  submatrix. The results discussed in the following are obtained by diagonalizing a  $20 \times 20$  submatrix. Increasing the matrix size to  $50 \times 50$  changes the results by less than 1%.

The main panel of Fig. 5.4(a) shows the condensate fraction  $n_c$  for two Boltzmann particles as a function of the temperature for various  $s$ -wave scattering lengths  $a_s$ . Solid, dotted, dashed, dash-dotted, dash-dot-dotted and dash-dash-dotted lines are for  $a_{\text{ho}}/a_s =$

$-\infty, -2, -1, 0, 1,$  and  $2,$  respectively. As the temperature increases, the condensate fraction  $n_c$  decreases for all interaction strengths. At zero temperature,  $n_c$  decreases as the inverse scattering length increases. At finite temperature, however, we observe in some cases [see the  $k_B T \approx E_{\text{ho}}/2$  to  $E_{\text{ho}}$  regime in Fig. 5.4(a)] that the condensate fraction increases slightly as  $|a_s|$  ( $a_s < 0$ ) increases. This is caused by the interplay of the interaction energy and the temperature dependent Boltzmann weight.

The condensate fraction for two identical bosons is very similar to that for two Boltzmann particles. The inset of Fig. 5.4(a) compares the condensate fraction for two identical bosons (symbols) with those for two Boltzmann particles (lines) for  $a_{\text{ho}}/a_s = -\infty$  and  $0,$  respectively. It can be seen that the condensate fraction for two identical bosons falls off slightly slower with increasing temperature than that for two Boltzmann particles. This is because the Bose statistics excludes the states with odd relative angular momentum  $l,$  implying that the  $l = 0$  states (which are responsible for the non-zero condensate fraction) are relatively more important for two identical bosons than for two Boltzmann particles.

For comparison, Fig. 5.4(b) shows the superfluid fraction  $n_s$  for two Boltzmann particles for the same scattering lengths. The superfluid fraction  $n_s$  depends weakly on the  $s$ -wave scattering length. Specifically, the superfluid fraction approaches 1 in the low temperature regime for all  $s$ -wave scattering lengths. This is a consequence of the fact that the lowest energy eigen state has vanishing total orbital angular momentum for all  $s$ -wave scattering lengths. The inset of Fig. 5.4(b) compares the superfluid fraction for two Boltzmann particles (lines) with those for two identical bosons (symbols). As in the case of the condensate fraction, the switch from Boltzmann to Bose statistics changes the superfluid fraction only by a small amount.

A comparison of Figs. 5.4(a) and 5.4(b) shows that the condensate and superfluid fractions are distinctly different quantities. When the two-body system forms a molecule (for positive  $a_s$ ), the condensate fraction is small. The superfluid fraction, in contrast, remains

approximately 1 in the low temperature regime, indicating that the response to an infinitesimal rotation is largely independent of the size of the system (the density decreases with increasing  $1/a_s$ ) and instead largely determined by its spherical shape.

Next, we consider two identical fermions. Naively, this system might be thought to be “uninteresting” since the Pauli exclusion principle prohibits scattering in the  $s$ -wave channel. As we show now, two non-interacting identical fermions display intriguing temperature-dependent behaviors. For two identical non-interacting fermions, the condensate fraction equals  $1/2$  at  $T = 0$  and decreases monotonically. The superfluid fraction displays [see Fig. 5.5(c)] a non-monotonic dependence on the temperature. As expected,  $n_s$  is zero in the high  $T$  limit, increases to around 0.2 at  $k_B T = E_{\text{ho}}/2$ , and then diverges to  $-\infty$  in the zero temperature limit. As discussed in Ref. [228], this behavior can be understood by analyzing the classical moment of inertia  $I_c$  and the quantum moment of inertia  $I_q$  [see the Figs. 5.5(d) and 5.5(e), respectively]. Specifically, the fact that the lowest energy eigen state has  $L_{\text{tot}} = 1$  is responsible for the increase of  $I_q$  at low temperature. Motivated by the nuclear physics literature [180, 183], we refer to this behavior as “abnormal”.

The fact that the superfluid fraction for two identical fermions becomes negative in the low-temperature regime can be understood as follows [228]. Two identical bosons at low temperature do not respond to an infinitesimal external rotation ( $n_s \rightarrow 1$  as  $T \rightarrow 0$ ) since the lowest energy eigen state has  $L_{\text{tot}} = 0$ . Two identical fermions at low temperature, however, do respond to an infinitesimal external rotation ( $n_s \rightarrow -\infty$  as  $T \rightarrow 0$ ) since the lowest energy eigen state has  $L_{\text{tot}} = 1$ . The physical picture is that the system “speeds up” faster than we would expect for a normal fluid with the same classical moment of inertia [228].

To gain further insight into the superfluid properties of the fermionic system, we analyze the radial and superfluid densities. The radial densities for particles 1 and 2 are identical and the subscript  $j$  of  $r_j$  will be dropped in what follows. Solid, dotted and dashed lines in Fig. 5.5(a) show the scaled radial density  $4\pi\rho_{\text{rad}}(r)r^2$  for  $k_B T/E_{\text{ho}} = 0.5, 0.26459,$  and

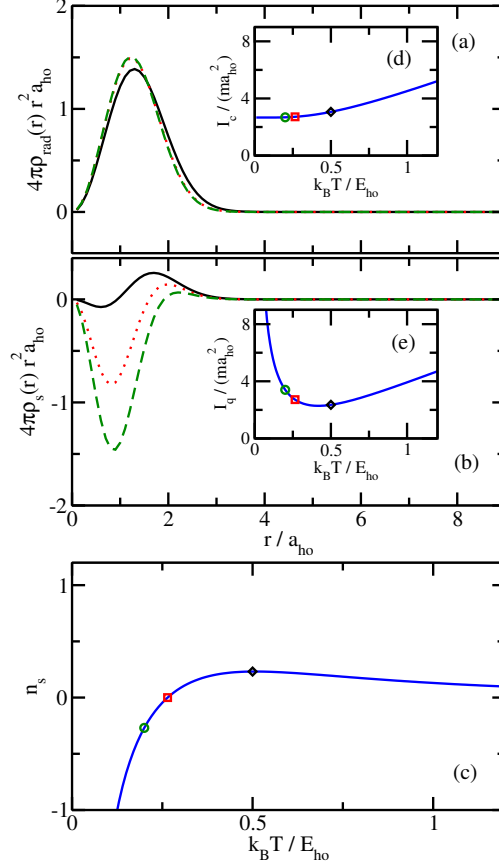


Figure 5.5: Panels (a) and (b) show radial densities for two identical non-interacting fermions. Solid, dotted, and dashed lines show (a) the scaled radial total density and (b) the scaled radial superfluid density, for  $k_B T / E_{\text{ho}} = 0.5, 0.26459, \text{ and } 0.2$ , respectively. In panel (a), the dotted line is hardly distinguishable from the dashed line. The solid lines in panels (c), (d), and (e) show (c) the superfluid fraction  $n_s$ , (d) the classical moment of inertia  $I_c$ , and (e) the quantum mechanical moment of inertia  $I_q$  as a function of the temperature  $T$ . The diamond, square and circle mark the temperatures considered in panels (a) and (b).

0.2, respectively. The radial density is fairly insensitive to the temperature. The radial superfluid density [see Fig. 5.5(b)], in contrast, changes notably with the temperature. This is not unexpected since the superfluid fraction varies strongly in the low temperature regime. The radial superfluid density takes negative values near the trap center and positive values near the edge of the cloud. The oscillation of the radial superfluid density reflects the fact that the lowest energy eigen state has total angular momentum quantum number  $L_{\text{tot}} = 1$ . For large  $r$ , the probability of finding two particles close to each other is extremely low. This translates into the Fermi statistics playing a negligible role. On the other hand, we expect that the Fermi statistics is much more important near the trap center. In the language of path integrals, the “permuted paths” (i.e., the paths that come from exchanging particles 1 and 2 and thus contribute with a negative sign to the partition function) are largely concentrated near the center. These “permuted paths” contribute negatively to the area estimator and span larger areas compared to the “unpermuted paths”. As a consequence, the superfluid density is negative near the trap center.

The analysis presented here for two non-interacting identical fermions can be extended to two-component Fermi gases with interspecies  $s$ -wave interactions consisting of  $N = 3$  or more particles. Selected results were presented in our earlier work [228]. We anticipate that the analysis of the superfluid properties presented in the previous paragraphs for two non-interacting fermions will inspire other studies, for bosons or fermions, that are concerned with understanding the distribution of the superfluid properties in finite sized systems or systems with interfaces [176, 177, 195, 217, 218, 229, 236–238].

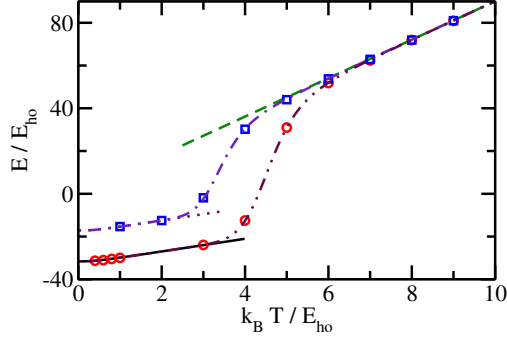


Figure 5.6: Energies as a function of the temperature  $T$  for three identical bosons at unitarity interacting through  $V_G$  with different  $r_0$ . Circles and squares show the PIMC results for  $r_0/a_{\text{ho}} = 0.06$  and  $0.08$ , respectively. For comparison, the solid and dotted lines show the result obtained using the droplet state plus center of mass excitations. The dashed line shows the thermally averaged energy for three identical non-interacting bosons. Dash-dot-dotted and dash-dotted lines show results obtained using the simple combined model for  $r_0/a_{\text{ho}} = 0.06$  and  $0.08$  (see the text for discussion).

## 5.4 $N$ -body systems

### 5.4.1 $N$ identical bosons

This section discusses the temperature dependent properties of  $N$  identical bosons under external spherically symmetric harmonic confinement interacting through the Gaussian model potential  $V_G$  with infinite  $s$ -wave scattering length. Circles and squares in Fig. 5.6 show the energy of the three-boson system, obtained from the PIMC simulations, as a function of the temperature for  $r_0/a_{\text{ho}} = 0.06$  and  $0.08$ , respectively. For both ranges, the energy shows three distinct regions. The energy increases approximately linearly at small  $T$ , turns up relatively sharply around  $k_B T = 4E_{\text{ho}}$  or  $3E_{\text{ho}}$ , and then changes again linearly. The energy at low temperature—if expressed in harmonic oscillator units—shows a strong range dependence. The energy at high temperature, in contrast, is to leading order independent of  $r_0$ . We refer to the rapid change of the energy from one approximately linear regime to the other approximately linear regime as a phase transition like feature.

We now introduce a simple parameter-free model that reproduces the energy curves semi-

quantitatively (see the dash-dot-dotted and dash-dotted lines in Fig. 5.6). The assumptions going into the model are that the low-temperature behavior is governed by the properties of the lowest Efimov trimer and that the high-temperature behavior is governed by the properties of the non-interacting three-boson gas. Treating only the lowest Efimov trimer state and its center of mass excitations, we obtain the solid and dotted lines in Fig. 5.6 for  $r_0/a_{\text{ho}} = 0.06$  and  $0.08$ , respectively. These thermally averaged energies are obtained using the lowest eigen energy of the trapped three-boson system, i.e., using the eigen energy of the state that shows Efimov characteristics, and summing over the center of mass excitations. The dashed line shows the thermally averaged energy of three non-interacting identical bosons. If we combine these two limiting behaviors, the model partition function  $Z_{\text{model}}$  reads

$$Z_{\text{model}}(\beta) = Z_{\text{droplet}}(\beta) + Z_{\text{gas}}(\beta), \quad (5.31)$$

where  $Z_{\text{droplet}}(\beta) = z(\beta) \exp(-\beta E_{\text{droplet}})$  and  $Z_{\text{gas}}(\beta) = [z^3(\beta) + 3z(2\beta)z(\beta) + 2z(3\beta)]/6$ . Here,  $E_{\text{droplet}}$  denotes the lowest relative eigen energy of the three-boson system and  $z(\beta)$  the partition function of a single harmonically trapped particle. The second and third terms in  $Z_{\text{gas}}$  originate from the symmetrization of  $Z_{\text{gas}}$ . The resulting energies are shown in Fig. 5.6 by the dash-dot-dotted and dash-dotted lines for  $r_0/a_{\text{ho}} = 0.06$  and  $0.08$ , respectively. The agreement between this simple combined model and the PIMC calculations is very good.

One may ask why the simple combined model works so well. We attribute this to primarily two things. First, for the examples shown in Fig. 5.6 the energy separation between the lowest Efimov trimer state and the gas-like states is large (the case where  $|E_{\text{droplet}}|$  is not much larger than  $E_{\text{ho}}$  is briefly discussed at the end of this section). Second, although the system is strongly-interacting, the non-interacting Bose gas model describes the density of states approximately correctly. The reason is that a significant fraction of the states is not affected by the  $s$ -wave interactions [146]. In fact, if we replace the partition function  $Z_{\text{gas}}$

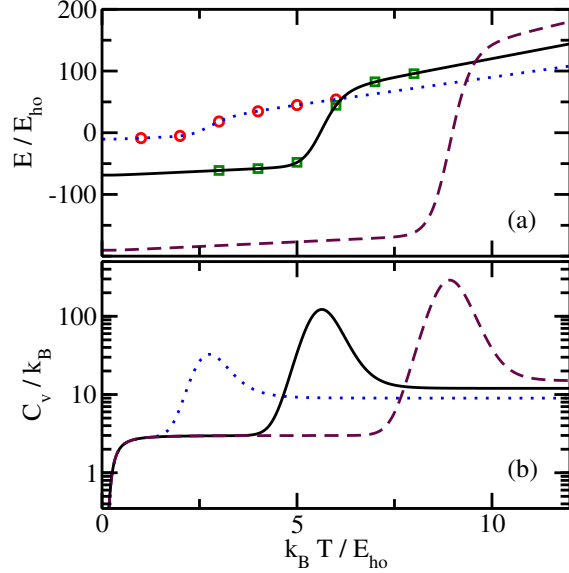


Figure 5.7: Phase transition like feature for  $N$  identical harmonically trapped bosons interacting through  $V_G$  with  $1/a_s = 0$ . (a) Circles and squares show the energy obtained by the PIMC approach for  $r_0 = 0.1a_{ho}$  and  $N = 3$  and 4, respectively, as a function of the temperature  $T$ . The dotted, solid, and dashed lines show the energies for  $N = 3, 4$ , and 5 obtained using the simple combined model. (b) The dotted, solid and dashed lines show the heat capacity  $C_v$  for  $N = 3, 4$ , and 5, respectively, as a function of  $T$ .

for the non-interacting Bose gas by the partition function for the non-interacting Boltzmann gas, then the model predicts that the energy changes rapidly at a lower temperature than predicted by the PIMC results. If, on the other hand, we replace the partition function  $Z_{gas}$  for the non-interacting Bose gas by a partition function for three identical bosons that accounts for the  $s$ -wave interactions in an approximate manner (we reduce the energy of all states that are affected by the  $s$ -wave interactions by  $E_{ho}$ ), the resulting energy curves are, on the scale of Fig. 5.6, indistinguishable from the dash-dot-dotted and dash-dotted curves.

Circles and squares in Fig. 5.7(a) show the thermally averaged PIMC energies for the Gaussian model interaction with  $r_0/a_{ho} = 0.1$  and  $1/a_s = 0$  for  $N = 3$  and 4, respectively. As the three-boson system, the four-boson system displays a “phase transition like” feature. To model four- and higher-body boson systems, we generalize the combined model introduced above as follows. In Eq. (5.31),  $Z_{droplet}(\beta)$  now denotes the partition function determined by

the lowest  $N$ -boson energy state plus center of mass excitations and  $Z_{\text{gas}}(\beta)$  denotes the partition function of the non-interacting  $N$ -boson gas. As above,  $Z_{\text{gas}}$  is properly symmetrized. The solid line in Fig. 5.7(a) shows the resulting energy for the four-boson system. The agreement with the PIMC results is good. It should be noted that the combined model neglects, for systems with  $N > 3$ , a large number of states. For example, for the four-boson system, it neglects the excited four-boson Efimov state whose energy is, in the universal regime, 1.002 times the trimer energy [239] as well as “atom-trimer states” that can be approximately described as consisting of an Efimov trimer with the fourth particle occupying one of the harmonic oscillator states. These states contribute relatively little to the partition function for two reasons. First, the separation between the four-body ground state energy and the energy of the excited tetramer and the separation between the four-body ground state energy and the atom-trimer states is large (the factor for the former is 4.61 in the universal regime [239]). Second, the density of states of the atom-trimer states is negligible compared to the density of states of the gas-like boson-boson-boson-boson states. We conjecture that the combined model also provides a good description for larger Bose systems. We stress that the combined model is fully analytical, provided that the eigen energy of the lowest  $N$ -body state, which can be considered as being tied to the lowest trimer eigen state, is known. The dashed line in Fig. 5.7(a) shows the energy for  $N = 5$  bosons interacting through  $V_G$  with  $r_0/a_{\text{ho}} = 0.1$  and  $1/a_s = 0$  as a function of the temperature. This curve is obtained using the combined model with the eigen energy of the lowest  $N = 5$  energy eigen state as input (see Table 5.1 for the energy).

Figure 5.7(a) shows that the phase transition like feature for fixed  $r_0$  moves to higher temperature with increasing  $N$ . To estimate the transition temperature  $T_{\text{tr}}$ , we calculate the heat capacity  $C_v$ ,  $C_v = \partial E / \partial T$ . The dotted, solid and dashed lines in Fig. 5.7(b) show  $C_v$ , obtained using the combined model for the thermally averaged energy [see lines in Fig. 5.7(a)], as a function of the temperature for  $N = 3, 4$ , and  $5$ , respectively. The

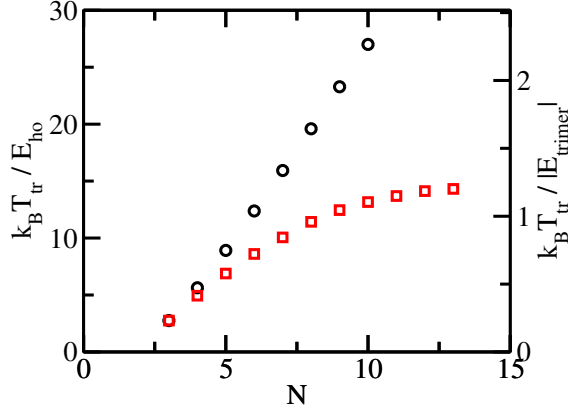


Figure 5.8: Transition temperature  $T_{\text{tr}}$  for  $N$  identical bosons in a harmonic trap at unitarity as a function of  $N$ . The transition temperature is calculated using the simple combined model. The circles show  $T_{\text{tr}}$  using the droplet energies for the Gaussian two-body interaction model employed in this work. For comparison, the squares show  $T_{\text{tr}}$  using the droplet energies for a model Hamiltonian with attractive two-body and repulsive three-body interactions [7] (to obtain the squares, the three-body eigen energy  $E_{\text{droplet}} = E_{\text{trimer}}$  is chosen such that it agrees with that for the Gaussian two-body interaction model, i.e., the circle and the square agree for  $N = 3$ ).

heat capacity curves show distinct maxima. We define the transition temperature  $T_{\text{tr}}$  as the temperature at which the heat capacity takes on its maximum.

The circles in Fig. 5.8 show the transition temperature for  $N$  bosons interacting through  $V_G$  with  $r_0/a_{\text{ho}} = 0.1$  and  $1/a_s = 0$  as a function of  $N$ . To obtain the transition temperature, we extrapolate the PIMC energies at low temperature to the zero temperature limit. The resulting zero-temperature energies  $E_{\text{droplet}}$  are reported in Table 5.1. We find that the energy  $E_{\text{droplet}}$  scales with the number of pairs, i.e., as  $N(N-1)/2$ . This implies that the transition temperature increases linearly with increasing  $N$ .

Since the  $N$ -body droplet states are only somewhat larger than  $r_0$ , the Gaussian interaction model employed in our work suffers from finite-range effects and provides only an approximate description of the  $N$ -body Efimov scenario. Note that the recent work by Gattobigio and Kievsky [1] suggests a means to correct for these finite-range effects. Here, we pursue a different approach. To see how the transition temperature changes when the droplet energies scale to leading order linearly with  $N$ —which is one of the scalings that

Table 5.1: Relative zero-temperature energy  $E_{\text{droplet}}$  for  $N$  bosons interacting through the Gaussian potential  $V_G$  with diverging  $s$ -wave scattering length. The energies in columns 2 and 5 are obtained by extrapolating the PIMC results to  $T = 0$ . The energies are expressed in units of the short-range energy scale  $E_{\text{sr}}$ ,  $E_{\text{sr}} = \hbar^2/(mr_0^2)$ . Column 3 reports the energies from Ref. [1]; no errorbars are reported in that reference. For comparison, our basis set expansion approach (see Ref. [2] for a discussion of the approach) yields  $E_{\text{droplet}}/E_{\text{sr}} = -0.11923(1)$  and  $-0.70173(5)$  for  $N = 3$  and 4, respectively.

$N$	$E_{\text{droplet}}/E_{\text{sr}}$	$E_a/E_{\text{sr}}$	$N$	$E_{\text{droplet}}/E_{\text{sr}}$
3		-0.1191	7	-6.544(11)
4	-0.700(4)	-0.70	8	-10.075(16)
5	-1.9127(5)	-1.92	9	-14.48(2)
6	-3.839(6)	-3.84	10	-19.76(4)

has been proposed to hold in the fully universal Efimov scenario [7] [240]—, we apply our combined model to the data of Ref. [7]. In that work, the  $N$ -boson system was assumed to interact through a combination of two- and three-body potentials. The resulting transition temperature  $T_{\text{tr}}$  is shown by squares in Fig. 5.8. The two cases display different large  $N$  behavior: The transition temperature increases roughly linearly with  $N$  for the Gaussian two-body model interaction but increases much slower for the system with two- and three-body interactions. We note that the finite temperature behavior of the trapped  $N = 100$  Bose system was investigated by Piatecki and Krauth using the PIMC approach [241]. In the regime where  $|E_{\text{trimer}}|$  is much larger than  $E_{\text{ho}}$ , Ref. [241] finds, in agreement with our work, a transition from a droplet state to a gas-like state. Reference [241] refers to the phase that is governed by the droplet state as Efimov liquid phase. We emphasize that our calculations neglect decay to non-universal states. Such states would need to be accounted for if one wanted to analyze the stability of the droplet phase.

We now discuss the system characteristics below and above  $T_{\text{tr}}$  in more detail. As already mentioned in Sec. 5.2.2, the hyperradial distribution functions  $P_{\text{hyper}}(R)$  for the three-boson system interacting through  $V_G$  with ranges  $r_0 = 0.06a_{\text{ho}}$  and  $0.1a_{\text{ho}}$  at low temperature (see Fig. 5.2 for  $k_B T = 0.4E_{\text{ho}}$ ) are essentially identical to the free-space three-boson systems with the same  $r_0$  at zero temperature. Figure 5.9 shows the temperature dependence of  $P_{\text{hyper}}(R)$

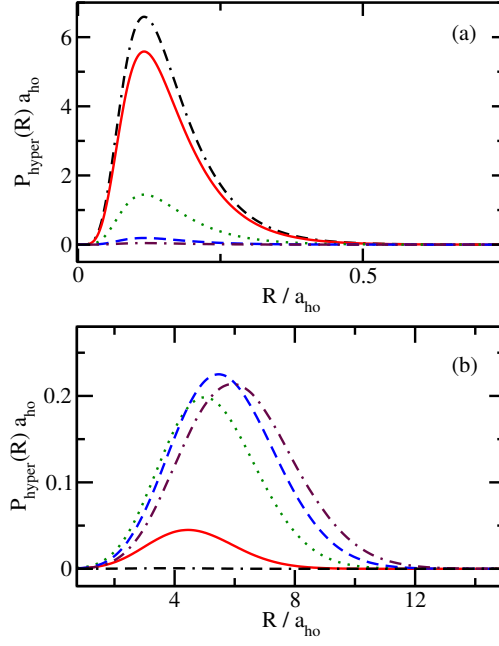


Figure 5.9: Hyperradial density  $P_{\text{hyper}}(R)$  for three identical bosons at unitarity interacting through  $V_G$  with  $r_0 = 0.06a_{\text{ho}}$  for various temperatures  $T$ . Dash-dash-dotted, solid, dotted, dashed, and dash-dotted lines are for  $k_B T / E_{\text{ho}} = 3, 4, 5, 6$ , and  $7$ , respectively. Panel (a) shows the small  $R$  region while panel (b) shows the large  $R$  region. Note that panels (a) and (b) have different scales for the  $x$ -axis and the  $y$ -axis.

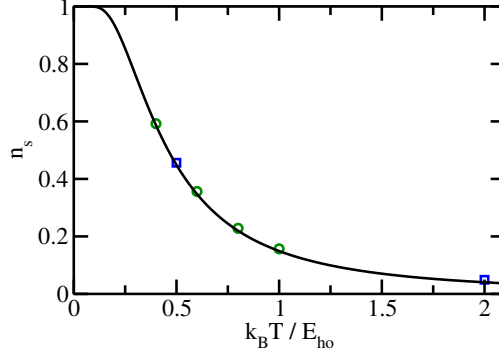


Figure 5.10: Superfluid fraction  $n_s$  as a function of the temperature  $T$  for  $N$  identical bosons at unitarity. The circles and squares show the PIMC results for the Gaussian potential  $V_G$  with  $r_0 = 0.1a_{\text{ho}}$  for  $N = 3$  and 4, respectively. The errorbars are smaller than the symbol size. For comparison, the solid line shows the result obtained using a single-particle model (see text for discussion).

for  $N = 3$  and  $r_0 = 0.06a_{\text{ho}}$ . The dash-dash-dotted line shows the hyperradial distribution function for  $k_B T = 3E_{\text{ho}}$ , i.e., for a temperature below  $T_{\text{tr}}$ . For this temperature,  $P_{\text{hyper}}(R)$  exhibits a maximum at  $R \approx 0.15a_{\text{ho}}$  and falls off monotonically at larger  $R$ . For slightly larger  $T$ , i.e.,  $k_B T = 4E_{\text{ho}}$  (solid line), the maximum at  $R \approx 0.15a_{\text{ho}}$  is smaller and a second peak at  $R \approx 4 - 5a_{\text{ho}}$  appears. At yet higher  $T$  (above the transition temperature), the amplitude of the large  $R$  peak is more pronounced and the hyperradial distribution function resembles that of a gaseous system. The temperature dependence of the hyperradial distribution function for the  $N = 3$  system supports our interpretation introduced above, namely, the notion that the system undergoes a transition from an Efimov trimer to a gas state as the temperature changes from below to above  $T_{\text{tr}}$ . The hyperradial distribution functions for larger systems show analogous behavior, i.e., they support the notion that the system undergoes a transition from an  $N$ -body droplet state to a gas state with increasing temperature.

To further characterize the properties of the  $N$ -boson system, symbols in Fig. 5.10 show the superfluid fraction  $n_s$  as a function of the temperature for  $N = 3$  and 4 obtained using the PIMC approach (here,  $r_0 = 0.1a_{\text{ho}}$  and  $1/a_s = 0$ ). The superfluid fractions for these two system sizes seem to fall on one curve. The solid line, which is obtained analytically

(see below for the model that produces the solid line), provides a good description of the numerical data. Figure 5.10 suggests that the superfluid fraction approaches one in the zero temperature limit and is smaller than 0.05 for  $k_B T \gtrsim 2E_{\text{ho}}$ . From Figs. 5.6 and 5.7 and the surrounding discussion, we know that the temperature regime  $k_B T \lesssim 2E_{\text{ho}}$  is—for the parameters considered—well described by the partition function  $Z_{\text{droplet}}$ , i.e., the system behavior is dominated by the lowest  $N$ -droplet energy eigen state and its center of mass excitations. In particular, this means that the droplet itself can be considered as “frozen”. Correspondingly, we expect that the behavior of the superfluid fraction displayed in Fig. 5.10 is approximately described by that of a single harmonically trapped particle of mass  $Nm_a$  (see the solid line in Fig. 5.10). We observe that the PIMC points lie slightly above the solid line. This could be due to the fact that the classical moment of inertia calculated using the single-particle framework is slightly smaller than the classical moment of inertia calculated using the full Hamiltonian.

We now relate the fall off of the superfluid fraction to the transition temperature. As discussed above, the fall off of  $n_s$  is governed by center of mass excitations, i.e., the relevant temperature scale is set by the harmonic oscillator frequency. To make some estimates, we say that the superfluid fraction, defined through the moment of inertia, is “undetectably small” for  $k_B T$  around  $2E_{\text{ho}}$ , independent of the number of particles and interaction model. This estimate assumes that the absolute value of the eigen energy of the lowest droplet state is large enough for  $Z_{\text{droplet}}$  to provide a reasonably accurate description of the low temperature dynamics. For the three- and four-body systems, this implies that  $|E_{\text{droplet}}|$  has to be larger than a few times  $E_{\text{ho}}$ . For cold atom systems, the three-body parameter is found to be approximately universal [77, 78, 242], i.e.,  $a_- \approx -9.7R_{\text{vdW}}$ , where  $R_{\text{vdW}}$  denotes the van der Waals length and  $a_-$  the scattering length at which the Efimov trimer merges with the three-atom continuum. Using this approximate universality together with the known relation between  $a_-$  and  $\kappa_*$  [41], we estimate that  $E_{\text{trimer}}$  is roughly equal to  $-0.024E_{\text{vdW}}$  at

unitarity. Here,  $E_{\text{vdW}}$  is defined as  $E_{\text{vdW}} = \hbar^2 / (m_a R_{\text{vdW}}^2)$ . For Cs in a spherically symmetric harmonic trap with a frequency  $\nu \approx 2\text{kHz}$  (a value that can be reached easily), the Efimov trimer would have an energy of about  $-33E_{\text{ho}}$  (the system is approximately described by the circles in Fig. 5.6). For these experimental conditions, the superfluid fraction is vanishingly small for  $T \gtrsim T_{\text{tr}}$ .

A key ingredient of the above analysis is that the fall off of the superfluid fraction is due to the center of mass excitations. This suggests an alternative viewpoint that defines the superfluid fraction with respect to the relative degrees of freedom only. If we replace the  $z$ -component  $\hat{L}_{\text{tot},z}$  of the total orbital angular momentum operator in Eq. (5.15) by the  $z$ -component of the relative orbital angular momentum operator and modify the definition of the classical moment of inertia accordingly, then we find that the fall off of the superfluid fraction is correlated with the transition temperature. The spirit of the latter approach underlies the arguments of Ref. [241], which considers a Bose gas with  $N = 100$  and refers to the phase governed by the  $N$ -droplet state as superfluid phase. We emphasize, however, that Ref. [241] did not perform any quantitative calculations of the superfluid fraction or superfluid properties of the system. Instead, Ref. [241] put forward qualitative arguments based on the exchange paths.

We reiterate that the combined model breaks down when  $|E_{\text{droplet}}|$  is not much larger than  $E_{\text{ho}}$ , i.e., when the size of the trimer approaches the harmonic oscillator length. In this case, the lowest Efimov trimer does not define a separate energy scale and the phase transition like feature discussed in this work disappears. Qualitatively, we expect that the Bose gas with  $N = 3, 4, \dots$  changes from having a significant superfluid fraction to a small superfluid fraction as the temperature increases from zero to a few times  $E_{\text{ho}}$ . The  $N = 100$  case has been considered in Ref. [241].

### 5.4.2 Single-component gas with a single impurity

This section considers a single-component gas consisting of  $N - 1$  particles with an impurity. We assume that the impurity interacts with the  $N - 1$  “background” atoms through the Gaussian potential  $V_G$  with diverging  $s$ -wave scattering length  $a_s$ . The background atoms do not interact with each other. Our goal is to investigate the temperature-dependence of the system properties as the statistics of the  $N - 1$  background atoms changes from Bose to Boltzmann to Fermi statistics. As before, we consider equal mass systems. Efimov trimers do not exist for two identical fermions and a third distinguishable particle (in our case, the impurity) [41, 243]. For two identical bosons and a third particle or two Boltzmann particles (i.e., two distinguishable particles) and a third particle, however, Efimov trimers can exist [244]. An interesting question is thus how the finite temperature properties of the  $(N - 1, 1)$  system with  $N \geq 3$  depend on the statistics.

From the discussion in the previous subsection it is clear that the properties of the trimer at low temperature determine the characteristics of larger Bose systems provided  $|E_{\text{trimer}}|$  is much larger than  $E_{\text{ho}}$ . Throughout this section, we consider the situation where the lowest energy eigen state of the  $(2, 1)$  system with Bose statistics has an energy comparable to  $E_{\text{ho}}$ , i.e.,  $|E_{\text{trimer}}| \approx E_{\text{ho}}$  [note, the lowest energy eigen state of the  $(2, 1)$  system with Boltzmann statistics has the same energy]. For the same model interactions, the lowest energy eigen state of the  $(2, 1)$  system with Fermi statistics also has an energy comparable to  $E_{\text{ho}}$ ; the energy for the system with Fermi statistics is, however, larger than that for the system with Bose statistics. We will show that the low temperature properties of the  $(N - 1, 1)$  systems display, as might be expected naively, statistics dependent characteristics for temperatures around or below  $E_{\text{ho}}$ . Concretely, we focus on systems with interspecies Gaussian interactions with  $r_0 = 0.06a_{\text{ho}}$  and  $1/a_s = 0$ . The relative ground state energy of the harmonically trapped  $(2, 1)$  system with Bose statistics is  $0.508E_{\text{ho}}$  [or  $141\hbar^2/(mr_0^2)$ ]. For comparison, the relative ground state energy of the corresponding free-space system is  $-18.1\hbar^2/(mr_0^2)$ , indicating

that the trap modifies the lowest energy eigen state of the free-space system with Efimov characteristics. The relative ground state energy of the harmonically trapped  $(2, 1)$  system with Fermi statistics is  $2.785E_{\text{ho}}$ . The corresponding free-space system is not bound [76].

Figure 5.11 shows the scaled pair distribution functions  $r_{j4}^2 P_{\text{pair}}(r_{j4})$ ,  $j < 4$ , for the  $(3, 1)$  system with  $r_0/a_{\text{ho}} = 0.06$  and  $1/a_s = 0$  for different statistics and temperatures. The dotted, dashed, and solid lines are for Bose, Fermi, and Boltzmann statistics, respectively. Figures 5.11(a)-5.11(d) are for  $k_B T/E_{\text{ho}} = 0.6, 1.2, 2$  and  $3$ , respectively. At high temperature [see Fig. 5.11(d)], the pair distribution functions are to a very good approximation independent of the particle statistics. As the temperature decreases [see Fig. 5.11(c)], the particle statistics has a visible effect on the pair distribution functions. In the PIMC language, the temperature in Fig. 5.11(c) is such that the “permuted paths” contribute only a small fraction to the partition function. This implies that the particle statistics can be treated perturbatively, i.e., the partition functions  $Z_{\text{Bose}}(\beta)$  and  $Z_{\text{Fermi}}(\beta)$  of the systems with Bose and Fermi statistics can be written approximately as  $[Z_{\text{Boltz}}(\beta) \pm \Delta Z(\beta)]/3!$ , where  $Z_{\text{Boltz}}(\beta)$  denotes the partition function of the system with Boltzmann statistics and  $\Delta Z(\beta)$  a small correction. The factor of  $1/3!$  arises due to the presence of the three identical particles (bosons or fermions). Correspondingly, the sum of the energies of the systems with Bose and Fermi statistics equal, to a good approximation, twice the energy of the system with Boltzmann statistics. Indeed, for the temperature considered in Fig. 5.11(c), we find  $E/E_{\text{ho}} = 23.86(2)$ ,  $23.33(2)$ , and  $22.76(1)$  for Fermi, Boltzmann and Bose statistics, respectively. The energy differences are  $0.53(4)$  and  $0.57(3)$ , in agreement with the expectation based on the perturbative argument.

For yet lower temperatures, the particle statistics becomes non-perturbative. In Fig. 5.11(b), e.g., the pair distribution functions for the three different statistics differ notably. In Fig. 5.11(a), the pair distribution functions for the systems with Boltzmann and Bose statistics are nearly indistinguishable and notably different from the pair distribution

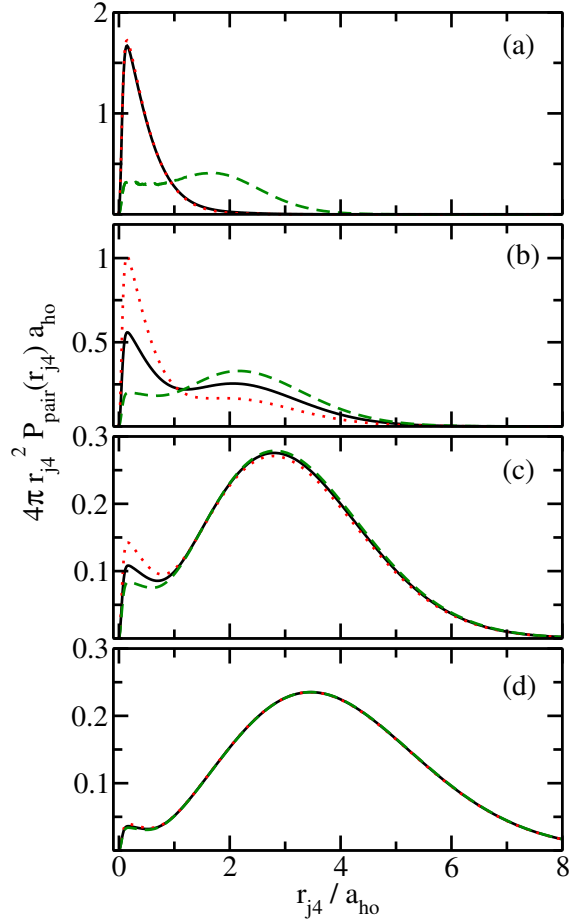


Figure 5.11: Scaled pair distribution functions  $r_{j4}^2 P_{\text{pair}}(r_{j4})$  ( $j < 4$ ) for the (3, 1) system with interspecies interaction  $V_G$  with  $r_0 = 0.06a_{\text{ho}}$  and diverging interspecies scattering length  $a_s$  at temperature (a)  $k_B T / E_{\text{ho}} = 0.6$ , (b)  $k_B T / E_{\text{ho}} = 1.2$ , (c)  $k_B T / E_{\text{ho}} = 2$ , and (d)  $k_B T / E_{\text{ho}} = 3$ . Dashed, solid, and dotted lines are for systems with Fermi, Boltzmann, and Bose statistics, respectively. The error bars are comparable to or smaller than the line widths. In panel (a), the solid and dotted lines are hardly distinguishable. In panel (d), all three lines nearly coincide.

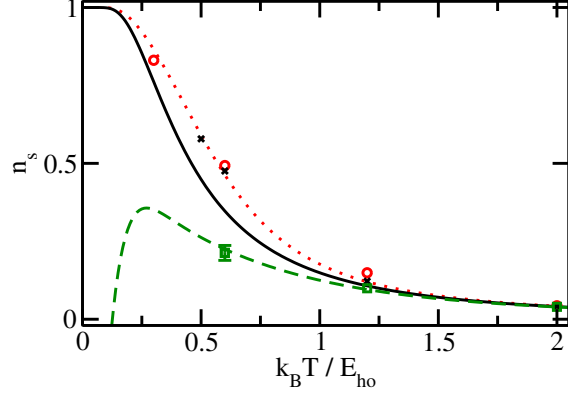


Figure 5.12: Superfluid fraction  $n_s$  as a function of the temperature  $T$  for the  $(3, 1)$  system with interspecies potential  $V_G$  with  $r_0 = 0.06a_{ho}$  and  $1/a_s = 0$ . The circles, crosses, and squares are obtained from the PIMC simulations with Bose, Boltzmann, and Fermi statistics, respectively. The error bars are only shown when they are larger than the symbol size. For comparison, dotted, solid, and dashed lines show the superfluid fraction for the non-interacting  $(3, 1)$  systems with Bose, Boltzmann, and Fermi statistics, respectively.

function for the system with Fermi statistics. This can be explained as follows. The systems with Bose and Boltzmann statistics have the same ground state energy while the system with Fermi statistics has a notably larger ground state energy. Due to the absence of bound trimer states for the system with Fermi statistics for vanishing confinement (i.e., for  $w = 0$ ), the pair distribution function is fully determined by the trap length and the temperature [32, 76, 203]. For the systems with Bose and Boltzmann statistics, the pair distribution function takes on large values at small  $r$ , reflecting the fact that these systems form a droplet like state for vanishing confinement. An important consequence is that the two-body contacts for the systems with Bose and Boltzmann statistics are, in the low temperature regime, much larger than the two-body contact for the system with Fermi statistics.

Symbols in Fig. 5.12 show the superfluid fraction  $n_s$  as a function of the temperature for the  $(3, 1)$  system with interspecies potential  $V_G$  with  $r_0 = 0.06a_{ho}$  and infinitely large  $s$ -wave scattering length. Circles, crosses, and squares are for Bose, Boltzmann, and Fermi statistics, respectively. As the temperature decreases, the superfluid fraction increases for the systems with Boltzmann and Bose statistics and reaches 1 at zero temperature. The superfluid frac-

tion of the (3, 1) system with Fermi statistics lies below that for the (3, 1) system with Bose and Boltzmann statistics at high temperature. Our calculations go down to  $k_B T = 0.6 E_{\text{ho}}$ . Based on our earlier work [228], we expect that the superfluid fraction for the system with Fermi statistics will take on negative values as the temperature approaches zero. At high temperature, the perturbative analysis, introduced earlier for the energy, can be applied to the superfluid fraction. The “permuted paths” contribute perturbatively to the quantum moment of inertia and the classical moment of inertia. The combination of the two gives rise to a correction of the superfluid fraction calculated from the “unpermuted paths”, i.e., a correction to the superfluid fraction for the (3, 1) systems with Boltzmann statistics due to the exchanges of identical particles. At  $k_B T = 2 E_{\text{ho}}$ , we find  $n_s = 0.03976(5)$ ,  $0.04132(1)$ , and  $0.04294(3)$  for the (3, 1) systems with Fermi, Boltzmann, and Bose statistics, respectively. The differences are  $0.00156(6)$  and  $0.00162(4)$ , in agreement with the expectation based on the perturbative argument. For comparison, dotted, solid, and dashed lines show the superfluid fraction for the non-interacting (3,1) systems with Bose, Boltzmann and Fermi statistics, respectively. For the system with Bose statistics, the unitary interactions change the superfluid fraction only slightly. For the system with Boltzmann statistics, the interactions have a notably larger effect on the superfluid fraction. The non trivial shift comes from the interplay between the temperature and the interactions.

Finally, we comment that the single-particle model, where the droplet is described as a single particle of mass  $N m_a$ , is not applicable. The superfluid fraction for this model coincides with the solid line in Fig. 5.12. If  $|E_{\text{trimer}}|$  was much larger than  $E_{\text{ho}}$ , we would expect that the superfluid fraction for the systems with Bose and Boltzmann statistics would follow the solid line. The fact that the symbols deviate from the solid line indicates that the single particle model is not applicable. Interestingly though, the superfluid fraction seems to only change weakly as  $E_{\text{trimer}}/E_{\text{ho}}$  changes, suggesting that  $n_s$  is not a sensitive probe of the phase transition like feature or absence thereof.

## 5.5 Conclusions

This paper considered the finite temperature properties of small  $s$ -wave interacting systems under spherically symmetric harmonic confinement. For two particles in the harmonic trap, we compared the condensate and superfluid fractions as a function of the temperature. The role of the particle statistics on these quantities was discussed. For two Boltzmann particles, the condensate fraction exhibits a strong dependence on the interaction strength while the superfluid fraction is only weakly dependent on the interaction strength. Changing from Boltzmann to Bose statistics changes the observables by a relatively small amount while changing from Boltzmann to Fermi statistics introduces significant quantitative changes.

We further considered  $N$  bosons with finite-range two-body Gaussian interactions at unitarity in the regime where the absolute value of the  $N$ -boson droplet energy  $|E_{\text{droplet}}|$  is much larger than the harmonic oscillator energy. We observed a sharp transition as the temperature increases from a liquid droplet like state to a gas-like state. The energy, heat capacity, hyperradial distribution function, and superfluid fraction were monitored as a function of the temperature. A simple model that semi-quantitatively captures the entire temperature regime was proposed. The model was not only applied to systems with Gaussian interactions but also to systems with two- and three-body interactions. No evidence for “intermediate phases” such as a gas consisting of trimers or tetramers was found. Finally, we considered the  $(3, 1)$  system with infinitely large interspecies scattering length. We compared the pair distribution function for systems with Bose, Boltzmann, and Fermi statistics. We established that the statistics can be treated perturbatively at high temperature.

In the future, it will be interesting to extend the few-body studies presented here to larger number of particles. For bosons, this should be fairly straightforward. For fermions, however, the sign problem will place constraints on the temperature regime that can be covered. Large weakly-interacting trapped  $N$ -boson systems at finite temperature have been studied using classical field theory and other approaches [245, 246]. These approaches assume

that the system is in a gas-like state and capture the shift of the transition temperature from a thermal gas to a Bose-Einstein condensate with the number of particles. These techniques are, however, not applicable when the  $s$ -wave scattering length becomes infinitely large. In this regime, beyond mean-field approaches are needed. Earlier work based on the  $\epsilon$ - or  $1/N$ - expansion [247, 248], renormalized interactions [249], and the diffusion Monte Carlo approach [250] treated unitary interactions but were restricted to zero temperature. The PIMC approach employed here and in Ref. [241] provides, in our view, a powerful means to study the finite temperature behavior of the strongly correlated  $N$ -boson system over a wide range of system sizes.

An important question is if the  $N$ -boson droplet state discussed here can be probed experimentally. Our calculations excluded non-universal energetically lower lying states, which could lead to atom losses. Moreover, we assumed that the system is in thermal equilibrium. In practice, experimental investigations will have to work in a parameter regime where the equilibration time is faster than the atom loss time. It remains an open question if quench experiments such as those recently conducted at JILA [251] could, if applied to small systems, probe the phase transition like feature discussed in this work. A possible scheme would be to start with a weakly interacting system with known but variable temperature, to jump the magnetic field to unitarity, and last to probe the system after a variable hold time.

Our calculations for few-fermion systems showed that a temperature of less than  $E_{\text{ho}}/k_B$  leads to notable changes in the structural properties. This suggests that the analysis of few-fermion experiments has to account for finite-temperature effects. A similar conclusion was reached in Refs. [252, 253], which considered—motivated by the Heidelberg experiments [90–92]—the temperature dependence of one-dimensional few-fermion systems.

*Acknowledgement:* Support by the National Science Foundation (NSF) through Grant No. PHY-1205443 is gratefully acknowledged. This work used the Extreme Science and

Engineering Discovery Environment (XSEDE), which is supported by NSF Grant No. OCI-1053575, and the WSU HPC. YY and DB acknowledge support from the Institute for Nuclear Theory during the program INT-14-1, “Universality in Few-Body Systems: Theoretical Challenges and New Directions”.

# Chapter 6

## Incorporating exact two-body propagators for zero-range interactions into $N$ -body Monte Carlo simulations

by Yangqian Yan<sup>1</sup> and D. Blume<sup>1</sup>

<sup>1</sup>Department of Physics and Astronomy, Washington State University, Pullman,  
Washington 99164-2814, USA

Copyright (2015) by the American Physical Society

Ultracold atomic gases are, to a very good approximation, described by pairwise zero-range interactions. This paper demonstrates that  $N$ -body systems with two-body zero-range interactions can be treated reliably and efficiently by the finite temperature and ground state path integral Monte Carlo approaches, using the exact two-body propagator for zero-range interactions in the pair product approximation. Harmonically trapped one- and three-dimensional systems are considered. A new propagator for the harmonically trapped two-

body system with infinitely strong zero-range interaction, which may also have applications in real time evolution schemes, is presented.

## 6.1 Introduction

Systems with two-body zero-range interactions constitute important models in physics. Although realistic two-body interactions do typically have a finite range, results for systems with zero-range interactions provide a starting point for understanding complicated few- and many-body dynamics. In 1934 [254], Fermi used the zero-range model in quantum mechanical calculations to explain the scattering of slow neutrons off bound hydrogen atoms. Nowadays, the two-body contact interaction is discussed in elementary quantum texts [42]. It has, e.g., been used to gain insights into the correlations of molecules, such as  $\text{H}_2^+$  and  $\text{H}_2$ , and to model atom-laser interactions [46–48].

In the 60s [31, 255–258], zero-range interactions were used extensively to model strongly-interacting one-dimensional systems at zero and finite temperature. Many of these models are relevant to electronic systems where the screening of the long-range Coulomb interactions leads to effectively short-range interactions [259]. More recently, ultracold atomic gases interacting through two-body van der Waals potentials have been, in the low temperature regime, modeled successfully using zero-range interactions [32, 202, 203]. One-, two-, and three-dimensional systems have been considered.

While zero-range interactions have been at the heart of a great number of discoveries, including the Efimov effect [41, 211, 260], their incorporation into numerical schemes is not always straightforward. Loosely speaking, the challenge in using zero-range interactions in numerical schemes that work with continuous spatial coordinates stems from the fact that we, in general, do not know how to incorporate the boundary conditions implied by the zero-range potential into numerical approaches at the four- and higher-body level.

This paper discusses an approach that allows for the use of zero-range potentials in many-

body simulations. We work in position space and consider a system with fixed number of particles. We develop a scheme to incorporate pairwise zero-range interactions into  $e^{-\tau H}$  directly, where  $H$  is the system Hamiltonian. The quantity  $e^{-\tau H}$  is of fundamental importance. If  $\tau$  is identified with  $1/(k_B T)$ , where  $k_B$  and  $T$  denote the Boltzmann constant and temperature, respectively, then  $e^{-\tau H}$  is the density matrix for the system at finite temperature. Knowing the density matrix, the thermodynamic properties can be calculated. If, on the other hand,  $\tau$  is identified with  $it/\hbar$ , where  $t$  denotes the real time, then  $e^{-\tau H}$  can be interpreted as the real time propagator and be used to calculate dynamic properties. Throughout this paper, we refer to  $\tau$  as imaginary time, keeping in mind that  $\tau$  carries units of 1/energy and that  $\tau$  can be associated with inverse temperature or real time.

The remainder of this paper is organized as follows. Section II reviews the pair product approximation, which relates the many-body propagator to the two-body propagator. Section III derives the two-body propagator for various systems with zero-range interactions. Sections IV and V demonstrate that the two-body zero-range propagators yield reliable results if used in one- and three-dimensional path integral Monte Carlo (PIMC) [19, 20, 133] and path integral ground state (PIGS) [19, 100, 101, 261, 262] simulations of trapped  $N$ -atom systems. The performance and implementation details will be discussed. While the free-space zero-range propagators have been reported in the literature [113–116], the zero-range propagators for the harmonically trapped system with infinite coupling constant are, to the best of our knowledge, new. Finally, Sec. VI concludes.

## 6.2 $N$ -body density matrix

We consider  $N$  particles with mass  $m_j$  and position vector  $\mathbf{r}_j$  ( $j = 1, \dots, N$ ) interacting via a sum of zero-range potentials with interaction strength  $g$ . The Hamiltonian  $H$  of the system

can be written as

$$H = \sum_{j=1}^N H_j^{\text{sp}} + \sum_{j<k}^N V_{jk}, \quad (6.1)$$

where  $H_j^{\text{sp}}$  denotes the non-interacting single-particle Hamiltonian of the  $j$ th particle and  $V_{jk}$  the two-body potential between the  $j$ th and  $k$ th particle. In the following, it will be convenient to separate the Hamiltonian  $H_{jk}$ , where  $H_{jk} = H_j^{\text{sp}} + H_k^{\text{sp}} + V_{jk}$ , of atoms  $j$  and  $k$  into relative and center of mass pieces,  $H_{jk} = H_{jk}^{\text{rel}} + H_{jk}^{\text{c.m.}}$ , where  $H_{jk}^{\text{rel}}$  depends on the relative vector  $\mathbf{r}_{jk}$ , and  $H_{jk}^{\text{c.m.}}$  on the center of mass vector  $\mathbf{r}_{jk}^{\text{c.m.}}$ ,  $\mathbf{r}_{jk} = \mathbf{r}_j - \mathbf{r}_k$  and  $\mathbf{r}_{jk}^{\text{c.m.}} = (m_j \mathbf{r}_j + m_k \mathbf{r}_k)/(m_j + m_k)$ . Below, the non-interacting two-particle system will serve as a reference system and we define  $H_{jk}^0 = H_j^{\text{sp}} + H_k^{\text{sp}}$  and  $H_{jk}^0 = H_{jk}^{\text{rel},0} + H_{jk}^{\text{c.m.}}$ .

The  $N$ -particle density matrix  $\rho_{\text{tot}}(\mathbf{R}, \mathbf{R}'; \tau)$  in position space can be written as

$$\rho_{\text{tot}}(\mathbf{R}, \mathbf{R}'; \tau) = \langle \mathbf{R} | e^{-\tau H} | \mathbf{R}' \rangle, \quad (6.2)$$

where  $\mathbf{R} = (\mathbf{r}_1, \dots, \mathbf{r}_N)$  and  $\mathbf{R}' = (\mathbf{r}'_1, \dots, \mathbf{r}'_N)$  collectively denote the coordinates of the  $N$ -particle system. For sufficiently small  $\tau$ ,  $\rho_{\text{tot}}(\mathbf{R}, \mathbf{R}'; \tau)$  can be constructed using the pair-product approximation [19],

$$\rho_{\text{tot}}(\mathbf{R}, \mathbf{R}'; \tau) \approx \left( \prod_{j=1}^N \rho^{\text{sp}}(\mathbf{r}_j, \mathbf{r}'_j; \tau) \right) \times \left( \prod_{j<k}^N \bar{\rho}^{\text{rel}}(\mathbf{r}_{jk}, \mathbf{r}'_{jk}; \tau) \right), \quad (6.3)$$

where  $\bar{\rho}^{\text{rel}}(\mathbf{r}_{jk}, \mathbf{r}'_{jk}; \tau)$  denotes the normalized pair density matrix,

$$\bar{\rho}^{\text{rel}}(\mathbf{r}_{jk}, \mathbf{r}'_{jk}; \tau) = \frac{\rho^{\text{rel}}(\mathbf{r}_{jk}, \mathbf{r}'_{jk}; \tau)}{\rho^{\text{rel},0}(\mathbf{r}_{jk}, \mathbf{r}'_{jk}; \tau)}, \quad (6.4)$$

and  $\rho^{\text{rel}}(\mathbf{r}_{jk}, \mathbf{r}'_{jk}; \tau)$  and  $\rho^{\text{rel},0}(\mathbf{r}_{jk}, \mathbf{r}'_{jk}; \tau)$  the relative density matrices of the interacting and

non-interacting two-body systems,

$$\rho^{\text{rel}}(\mathbf{r}_{jk}, \mathbf{r}'_{jk}; \tau) = \langle \mathbf{r}_{jk} | e^{-\tau H_{jk}^{\text{rel}}} | \mathbf{r}'_{jk} \rangle \quad (6.5)$$

and

$$\rho^{\text{rel},0}(\mathbf{r}_{jk}, \mathbf{r}'_{jk}; \tau) = \langle \mathbf{r}_{jk} | e^{-\tau H_{jk}^{\text{rel},0}} | \mathbf{r}'_{jk} \rangle. \quad (6.6)$$

In Eq. (6.3),  $\rho^{\text{sp}}(\mathbf{r}_j, \mathbf{r}'_j; \tau)$  denotes the single-particle density matrix,

$$\rho^{\text{sp}}(\mathbf{r}_j, \mathbf{r}'_j; \tau) = \langle \mathbf{r}_j | e^{-\tau H_j^{\text{sp}}} | \mathbf{r}'_j \rangle. \quad (6.7)$$

The key idea behind Eq. (6.3) is that the one- and two-body density matrices can, often times, be calculated analytically. Indeed, the non-interacting propagator is known in the literature both for the free-space and harmonically trapped systems [19, 207]. Moreover, the eigen energies and eigen states of the Hamiltonian  $H_{jk}^{\text{rel}}$  have, for a class of two-body interactions, compact expressions, which enables the analytical evaluation of the relative two-body density matrix in certain cases (see Sec. 6.3).

It should be noted that the pair product approximation is only valid in the small  $\tau$  limit since it does not account for three- and higher-body correlations. For the real time dynamics, this means that the time step is limited by the importance of  $N$ -body ( $N > 2$ ) correlations. If  $\tau$  is identified with  $1/(k_B T)$ , the pair product approximation is limited to high temperature. In this case, the pair product approximation is analogous to a virial expansion that includes the second-order but not the third-order virial coefficient [87].

### 6.3 Two-body relative density matrix

In the following, we consider one- and three-dimensional systems, without and with external harmonic confinement, and discuss the evaluation of the relative density matrix for zero-

range interactions. For notational simplicity, we leave off the subscripts  $j$  and  $k$  throughout this section, i.e., we denote the relative distance vector by  $\mathbf{r}$  for the three-dimensional system and  $x$  for the one-dimensional system, respectively, and the relative part of the two-body Hamiltonian by  $H^{\text{rel}}$ .

### 6.3.1 One-dimensional system

The complete set of bound and continuum states of  $H^{\text{rel}}$  is spanned by  $\psi_n$  with eigen energies  $E_n$  and  $\psi_k$  with energies  $\hbar^2 k^2 / (2\mu)$ , where  $\mu$  denotes the reduced two-body mass and  $k$  the relative scattering wave vector. If the  $\psi_n$  and  $\psi_k$  are normalized according to

$$\int \psi_n^*(x) \psi_{n'}(x) dx = \delta_{nn'} \quad (6.8)$$

and

$$\int \psi_k^*(x) \psi_{k'}(x) dx = \delta(k - k'), \quad (6.9)$$

then the relative density matrix  $\rho^{\text{rel}}(x, x'; \tau)$  can be written as [207]

$$\begin{aligned} \rho^{\text{rel}}(x, x'; \tau) = & \sum_n \psi_n^*(x) e^{-\tau E_n} \psi_n(x') + \\ & \int_0^\infty \psi_k^*(x) e^{-\tau \hbar^2 k^2 / (2\mu)} \psi_k(x') dk. \end{aligned} \quad (6.10)$$

*Free-space system:* The relative Hamiltonian for the free-space system with zero-range interaction can be written as

$$H^{\text{rel}} = -\frac{\hbar^2}{2\mu} \frac{\partial^2}{\partial x^2} + g\delta(x), \quad (6.11)$$

where  $g$  denotes the coupling constant of the  $\delta$ -function potential. For positive  $g$ , the Hamiltonian given in Eq. (6.11) does not support a bound state and the corresponding energy

spectrum is continuous. The symmetric and anti-symmetric scattering states with energy  $\hbar^2 k^2 / (2\mu)$  read [263]

$$\psi_k^s(x) = \frac{1}{\sqrt{\pi}} \sin(k|x| + \delta(k)) \quad (6.12)$$

and

$$\psi_k^a(x) = \frac{1}{\sqrt{\pi}} \sin(kx), \quad (6.13)$$

respectively;  $\delta(k) = \arctan[\hbar^2 k / (g\mu)]$  is the phase shift. For negative  $g$ , the Hamiltonian additionally supports a bound state with symmetric wave function

$$\psi_0^s(x) = \sqrt{\frac{\mu|g|}{\hbar^2}} e^{-\mu|gx|/\hbar^2} \quad (6.14)$$

and energy  $-g^2\mu/(2\hbar^2)$ . Integrating over the symmetric and anti-symmetric scattering states, and adding, for negative  $g$ , the additional bound state, one finds the normalized relative density matrix  $\bar{\rho}_{1D,free}^{rel}$  [113–116],

$$\begin{aligned} \bar{\rho}_{1D,free}^{rel}(x, x'; \tau) = 1 - \exp\left(-\frac{\mu(xx' + |xx'|)}{\tau\hbar^2}\right) \times \\ \sqrt{\frac{\pi\mu\tau}{2}} \frac{g}{\hbar} \operatorname{erfc}(u) \exp(u^2), \end{aligned} \quad (6.15)$$

where  $u = \mu(|x'| + |x| + g\tau) / \sqrt{2\mu\tau\hbar^2}$  and  $\operatorname{erfc}$  is the complementary error function. We emphasize that Eq. (6.15) holds for positive and negative  $g$ . The corresponding relative non-interacting density matrix reads

$$\rho_{1D,free}^{rel,0}(x, x'; \tau) = \left(\frac{\mu}{2\pi\tau\hbar^2}\right)^{1/2} \exp\left(-\frac{\mu(x-x')^2}{2\tau\hbar^2}\right). \quad (6.16)$$

The free-space propagator given in Eq. (6.15) was employed in a PIMC study of the harmonically trapped spin-polarized two-component Fermi gas with negative  $g$  [264].

For large  $|g|$ ,  $u$  approaches  $\sqrt{\mu\tau/2g/\hbar}$  and, using  $\lim_{u\rightarrow\infty} \sqrt{\pi}u \operatorname{erfc}(u) \exp(u^2) = 1$ , Eq. (6.15) reduces to

$$\bar{\rho}_{1\text{D},\text{free}}^{\text{rel}}(x, x'; \tau) = \begin{cases} 1 - \exp\left(-\frac{2\mu xx'}{\tau\hbar^2}\right) & \text{for } xx' > 0 \\ 0 & \text{for } xx' \leq 0. \end{cases} \quad (6.17)$$

Equation (6.17) suggests that the relative coordinate does not change sign during the imaginary time evolution. Since the interaction strength is infinitely strong, the two particles fully reflect during any scattering process, i.e., the transmission coefficient is zero. This means that the initial particle ordering remains unchanged during the time evolution. This is a direct consequence of the Bose-Fermi duality of one-dimensional systems [31, 265, 266]. Specifically, the phase shift of the symmetric wave function given in Eq. (6.12) goes to zero when  $|g| \rightarrow \infty$ , implying that the symmetric wave functions coincide, except for an overall  $\operatorname{sgn}(x)$  factor, with the anti-symmetric scattering wave functions of non-interacting fermions. The implications of the Bose-Fermi duality for Monte Carlo simulations of  $N$ -body systems with infinite  $g$  is discussed in Sec. 6.4.

*Trapped system:* For two particles in a harmonic trap, the system Hamiltonian reads

$$H^{\text{rel}} = -\frac{\hbar^2}{2\mu} \frac{\partial^2}{\partial x^2} + g\delta(x) + \frac{1}{2}\mu\omega^2 x^2, \quad (6.18)$$

where  $\omega$  denotes the angular trapping frequency. The energy spectrum of  $H^{\text{rel}}$  is discrete and the eigen energies and eigen functions are known analytically in compact form [145]. These solutions can be used to evaluate Eq. (6.10) numerically. The corresponding relative

non-interacting density matrix reads

$$\rho_{\text{1D,trap}}^{\text{rel},0}(x, x'; \tau) = [2\pi \sinh(\tau\hbar\omega) a_{\text{ho}}^2]^{-1/2} \times \exp\left(-\frac{(x^2 + x'^2) \cosh(\tau\hbar\omega) - 2xx'}{2 \sinh(\tau\hbar\omega) a_{\text{ho}}^2}\right), \quad (6.19)$$

where  $a_{\text{ho}}$  denotes the harmonic oscillator length,  $a_{\text{ho}} = \sqrt{\hbar/(\mu\omega)}$ . For fixed  $\tau$  and finite  $g$ , one can then tabulate  $\bar{\rho}_{\text{1d,trap}}^{\text{rel}}(x, x'; \tau)$  for discrete  $x$  and  $x'$  using Eq. (6.10) and use a two-dimensional interpolation during the  $N$ -body simulation. The infinite sum in Eq. (6.10) can be truncated by omitting terms with  $n > n_{\text{max}}$ , where  $n_{\text{max}}$  is chosen such that the Boltzmann factor fulfills the inequality  $e^{-\tau E_n} \ll e^{-\tau E_0}$ . The value of  $n_{\text{max}}$  depends on the time step: smaller  $\tau$  require larger  $n_{\text{max}}$ .

For infinite  $g$ , we were able to derive a compact analytical expression for  $\bar{\rho}_{\text{1D,trap}}^{\text{rel}}(x, x'; \tau)$ . As  $g$  goes to infinity, the probability distribution of each even state coincides with that of an odd state, i.e., the system is fermionized. The complete set of even and odd eigen states for  $g = \infty$  can be written as

$$\psi_n^s(x) = \phi_n(|x|) \quad (6.20)$$

and

$$\psi_n^a(x) = \phi_n(x), \quad (6.21)$$

where  $\phi_n(x)$  is the non-interacting harmonic oscillator wave function,

$$\phi_n(x) = (\sqrt{\pi} 2^n n! a_{\text{ho}})^{-1/2} e^{-x^2/(2a_{\text{ho}}^2)} H_n(x/a_{\text{ho}}), \quad (6.22)$$

$H_n(x)$  denotes the Hermite polynomial of order  $n$ , and  $n$  takes the values  $1, 3, 5, 7, \dots$ . The

corresponding energies are  $E_n = (n + 1/2)\hbar\omega$  for both the symmetric and anti-symmetric states, i.e., each energy level is two-fold degenerate. Using Eqs. (6.20) and (6.21) in Eq. (6.10) and evaluating the infinite sum analytically, we find

$$\bar{\rho}_{1\text{D},\text{trap}}^{\text{rel}}(x, x'; \tau) = \begin{cases} 1 - \exp\left(-\frac{2xx'}{\sinh(\tau\hbar\omega)a_{\text{ho}}^2}\right) & \text{for } xx' > 0 \\ 0 & \text{for } xx' \leq 0. \end{cases} \quad (6.23)$$

For  $\tau\hbar\omega \ll 1$ , i.e., when the trap energy scale is much smaller than  $1/\tau$ , the trap propagator [Eq. (6.23)] equals the free-space propagator [Eq. (6.17)].

To test the one-dimensional propagators for infinite  $g$ , we consider the Hamiltonian given in Eq. (6.18) and prepare an initial state using a linearly discretized spatial grid. Our aim is to determine the ground state wave function and energy by imaginary time propagation. Two approaches are used. First, the initial state is propagated using the exact trap propagators [see Eqs. (6.23) and (6.19)]. In this case, the error originates solely from the discretization of the spatial degree of freedom; indeed, we find that the energy approaches the exact ground state energy quadratically with decreasing grid spacing  $\delta x$ . Second, the initial state is propagated using the free-space propagator [see Eqs. (6.17) and (6.16)]. We apply the Trotter formula [110] and move half of the trap potential to the left and half to the right of the free-space Hamiltonian. This is known as the primitive approximation [19], which is expected to yield a quadratic time step error since the trap potential does not commute with the free-space Hamiltonian. The error is found to scale quadratically with both the time step and the grid spacing. For  $\tau = (50\hbar\omega)^{-1}$ ,  $\delta x = \sqrt{2}a_{\text{ho}}/40$ , and  $x_{\text{max}} = -x_{\text{min}} = 4\sqrt{2}a_{\text{ho}}$ , where  $x_{\text{min}} \leq x \leq x_{\text{max}}$ , we obtain energies that deviate by  $2.4 \times 10^{-5}\hbar\omega$  and  $2 \times 10^{-12}\hbar\omega$  for the free-space propagator and the trap propagator, respectively, from the exact ground state energy of  $3\hbar\omega/2$ .

### 6.3.2 Three-dimensional system

Because the  $s$ -wave zero-range potential is spherically symmetric, the relative orbital angular momentum operator commutes with the relative Hamiltonian. Correspondingly, we label the bound states  $\psi_{nlm}$  with eigen energies  $E_{nl}$  and the continuum states  $\psi_{klm}$  with energies  $\hbar^2 k^2 / (2\mu)$  by the relative orbital angular momentum quantum number  $l$  and the projection quantum number  $m$ . If the  $\psi_{nlm}$  and  $\psi_{klm}$  are normalized according to

$$\int \psi_{nlm}^*(\mathbf{r}) \psi_{n'l'm'}(\mathbf{r}) \, d\mathbf{r} = \delta_{nn'} \delta_{ll'} \delta_{mm'} \quad (6.24)$$

and

$$\int \psi_{klm}^*(\mathbf{r}) \psi_{k'l'm'}(\mathbf{r}) \, d\mathbf{r} = \delta(k - k') \delta_{ll'} \delta_{mm'}, \quad (6.25)$$

the relative density matrix  $\rho^{\text{rel}}(\mathbf{r}, \mathbf{r}'; \tau)$  can be written as [207]

$$\begin{aligned} \rho^{\text{rel}}(\mathbf{r}, \mathbf{r}'; \tau) &= \sum_{nlm} \psi_{nlm}^*(\mathbf{r}) e^{-\tau E_{nl}} \psi_{nlm}(\mathbf{r}') + \\ &\sum_{lm} \int_0^\infty \psi_{klm}^*(\mathbf{r}) e^{-\tau \hbar^2 k^2 / (2\mu)} \psi_{klm}(\mathbf{r}') \, dk. \end{aligned} \quad (6.26)$$

*Free-space system:* The Hamiltonian of the three-dimensional system in free space reads

$$H^{\text{rel}} = -\frac{\hbar^2}{2\mu} \nabla_{\mathbf{r}}^2 + \frac{2\pi \hbar^2 a_s}{\mu} \delta^{(3)}(\mathbf{r}) \frac{\partial}{\partial r}, \quad (6.27)$$

where  $a_s$  is the  $s$ -wave scattering length. The second term on the right hand side of Eq. (6.27) is the regularized two-body zero-range pseudopotential [3]. The  $l > 0$  continuum states read

$$\psi_{klm}(\mathbf{r}) = i^l \sqrt{\frac{2}{\pi}} k j_l(kr) Y_{lm}(\hat{\mathbf{r}}), \quad (6.28)$$

where the  $j_l$  and  $Y_{lm}$  denote spherical Bessel functions of the first kind and spherical harmonics, respectively. The continuum states for the  $s$ -wave channel read

$$\psi_{k00}(\mathbf{r}) = \frac{1}{\sqrt{2\pi r}} \sin(kr + \delta_s(k)), \quad (6.29)$$

where  $\delta_s(k) = \arctan(-a_s k)$  is the  $s$ -wave phase shift. For positive  $a_s$ , there exists an  $s$ -wave bound state with eigen function  $\psi_{000}(\mathbf{r}) = 1/\sqrt{2\pi a_s r^2} \exp(-r/a_s)$  and eigen energy  $-\hbar^2/(2\mu a_s^2)$ . As is evident from the above eigen states, only the  $s$ -wave states are affected by the interactions. Thus, we construct the relative interacting density matrix  $\rho_{3D,\text{free}}^{\text{rel}}$  by writing the non-interacting relative density matrix  $\rho_{3D,\text{free}}^{\text{rel},0}$  and subtracting from it the non-interacting  $s$ -wave contribution and adding to it the  $s$ -wave contribution for finite  $a_s$ .

For negative  $a_s$ , there exist only continuum states and the density matrix can be expressed as

$$\begin{aligned} \rho_{3D,\text{free}}^{\text{rel}}(\mathbf{r}, \mathbf{r}'; \tau) = & \rho_{3D,\text{free}}^{\text{rel},0}(\mathbf{r}, \mathbf{r}'; \tau) + \\ & \int_0^\infty e^{-\frac{\tau \hbar^2 k^2}{2\mu}} \frac{1}{2\pi^2 r r'} [\sin(kr + \delta_s(k)) \sin(kr' + \delta_s(k)) - \\ & \sin(kr) \sin(kr')] dk, \end{aligned} \quad (6.30)$$

where the non-interacting relative density matrix reads

$$\rho_{3D,\text{free}}^{\text{rel},0}(\mathbf{r}, \mathbf{r}'; \tau) = (2\pi \hbar^2 \tau / \mu)^{-3/2} e^{-\mu(\mathbf{r}-\mathbf{r}')^2 / (2\hbar^2 \tau)}. \quad (6.31)$$

The integral in Eq. (6.30) can be done analytically [267] and the normalized relative density

matrix reads [115, 116]

$$\bar{\rho}_{3\text{D},\text{free}}^{\text{rel}}(\mathbf{r}, \mathbf{r}'; \tau) = 1 + \frac{\hbar^2 \tau}{\mu r r'} \exp\left(-\frac{\mu r r' (1 + \cos \theta)}{\hbar^2 \tau}\right) \times \left(1 + \frac{\hbar}{a_s} \sqrt{\frac{\pi \tau}{2\mu}} \operatorname{erfc}(v) \exp(v^2)\right), \quad (6.32)$$

where  $\cos \theta = \mathbf{r} \cdot \mathbf{r}' / (r r')$  and  $v = [r + r' - \tau \hbar^2 / (\mu a_s)] / \sqrt{2\tau \hbar^2 / \mu}$ . Adding the bound state contribution to Eq. (6.30) [see the first term on the right hand side of Eq. (6.26)] for positive  $a_s$ , one finds Eq. (6.32), i.e., the same propagator as for negative  $a_s$  [116].

For  $|a_s| = \infty$ , Eq. (6.32) simplifies to

$$\bar{\rho}_{3\text{D},\text{free}}^{\text{rel}}(\mathbf{r}, \mathbf{r}'; \tau) = 1 + \frac{\hbar^2 \tau}{\mu r r'} \exp\left(-\frac{\mu r r' (1 + \cos \theta)}{\hbar^2 \tau}\right). \quad (6.33)$$

This propagator was recently used in a proof-of-principle diffusion Monte Carlo study of the homogeneous two-component Fermi gas at unitarity with zero-range interactions [268].

*Trapped system:* The Hamiltonian for two particles in a spherically symmetric harmonic trap with  $s$ -wave scattering length  $a_s$  reads

$$H^{\text{rel}} = -\frac{\hbar^2}{2\mu} \nabla_{\mathbf{r}}^2 + \frac{1}{2} \mu \omega^2 \mathbf{r}^2 + \frac{2\pi \hbar^2 a_s}{\mu} \delta^{(3)}(\mathbf{r}) \frac{\partial}{\partial r} r. \quad (6.34)$$

The non-interacting relative density matrix reads

$$\rho_{3\text{D},\text{trap}}^{\text{rel},0}(\mathbf{r}, \mathbf{r}'; \tau) = a_{\text{ho}}^{-3} [2\pi \sinh(\tau \hbar \omega)]^{-3/2} \times \exp\left(-\frac{(\mathbf{r}^2 + \mathbf{r}'^2) \cosh(\tau \hbar \omega) - 2\mathbf{r} \cdot \mathbf{r}'}{2 \sinh(\tau \hbar \omega) a_{\text{ho}}^2}\right). \quad (6.35)$$

Similar to the free-space case, the relative interacting density matrix is obtained from the non-interacting density matrix with the difference of the  $s$ -wave eigen states and energies of the interacting and non-interacting systems added. For finite  $a_s$ , we were not able to

evaluate the infinite sum analytically. Because of the rotational invariance, the infinite sum depends only on  $r$  and  $r'$  (and not the direction of the vectors  $\mathbf{r}$  and  $\mathbf{r}'$ ), allowing for an efficient tabulation of the reduced relative density matrix. For infinitely large  $a_s$ , we find an analytical expression. In this case, the bound state wave functions that are affected by the  $\delta$ -function interaction can be written as  $\sqrt{2}\phi_n(r)/\sqrt{4\pi r^2}$ , where the  $\phi_n(r)$  are defined in Eq. (6.22) with  $x$  replaced by  $r$  and  $n = 0, 2, 4, \dots$ . The relative two-body density matrix reads

$$\begin{aligned} \rho_{3\text{D},\text{trap}}^{\text{rel}}(\mathbf{r}, \mathbf{r}'; \tau) &= \rho_{3\text{D},\text{trap}}^{\text{rel},0}(\mathbf{r}, \mathbf{r}'; \tau) + \\ &\sum_{n=0}^{\infty} e^{-\tau(n+\frac{1}{2})\hbar\omega} \frac{(-1)^n}{2\pi r r'} \phi_n^*(r) \phi_n(r'), \end{aligned} \quad (6.36)$$

where the even  $n$  terms in the sum over  $n$  come from the  $s$ -wave states that are affected by the interactions and the odd  $n$  terms come from the  $s$ -wave states of the non-interacting system. Performing the infinite sum, we find for the normalized relative density matrix

$$\begin{aligned} \bar{\rho}_{3\text{D},\text{trap}}^{\text{rel}}(\mathbf{r}, \mathbf{r}'; \tau) &= 1 + \\ &\frac{a_{\text{ho}}^2}{r r'} \sinh(\tau\hbar\omega) \exp\left(-\frac{r r' (1 + \cos\theta)}{a_{\text{ho}}^2 \sinh(\tau\hbar\omega)}\right). \end{aligned} \quad (6.37)$$

Setting  $\tau\hbar\omega = 0$ , Eq. (6.37) reduces to Eq. (6.33), i.e., to the corresponding free-space expression.

Equations (6.17) and (6.33) show that the one- and three-dimensional free-space propagators for systems with infinitely large  $\delta$ -function strength are characterized by the length  $\sqrt{\tau\hbar^2/\mu}$ , which is proportional to the de Broglie wave length. The trap propagators for infinitely large coupling constant [see Eqs. (6.23) and (6.37)], in contrast, are characterized additionally by the harmonic oscillator length. For finite interaction strength, the coupling constant defines a second length scale for the free-space system and a third length scale for the trapped system.

## 6.4 One-dimensional tests

This section incorporates the trapped two-body propagator into PIMC calculations for one-dimensional  $N$ -particle systems with pairwise zero-range interactions. We find that the conventional PIMC sampling approaches [19, 133] yield an efficient and robust description of one-dimensional systems with two-body zero-range interactions.

As a first example, we consider  $N$  distinguishable harmonically trapped particles with mass  $m$  in one spatial dimension with pairwise zero-range interactions of infinite strength. The  $N$ -particle system with infinitely large interaction strength is unique in that the particle statistics becomes irrelevant for local observables. For example, the energy is the same for  $N$  identical bosons,  $N$  identical fermions and  $N$  distinguishable particles at any temperature provided all particles interact via two-body zero-range interactions. We employ the zero-range trap propagator together with the single-particle trap propagator. Symbols in Fig. 6.1(a) show the PIMC energy for  $N$  distinguishable particles at temperature  $k_B T = \hbar\omega$ . Circles and squares are for simulations with imaginary time step  $\tau\hbar\omega = 1/8$  and  $1/128$ , respectively. For comparison, the dotted line is calculated directly from the partition function of  $N$  non-interacting fermions. Figure 6.1(b) shows the energy difference  $\Delta E$  between the simulation and the analytical results. It can be seen that the calculations for the larger time step (circles in Fig. 6.1) exhibit a systematic time step error, which is found to scale quadratically with the time step  $\tau$  for fixed  $N$  and to originate from the pair product approximation. Since we include the two-body correlations exactly, the leading order error is expected to come from three-body correlations. Indeed, for relatively small fixed  $\tau$  ( $\tau^{-1}$  around  $16\hbar\omega$ ) and varying  $N$ , we find that the error  $\Delta E$  scales approximately linearly with the number of triples, suggesting that the error is dominated by three-body correlations with sub-leading contributions arising from four-body correlations. As the number of particles  $N$  or the time step  $\tau$  increase, four- and higher-body correlations become more important. This error analysis suggests that an improved propagator could be obtained if the three-body

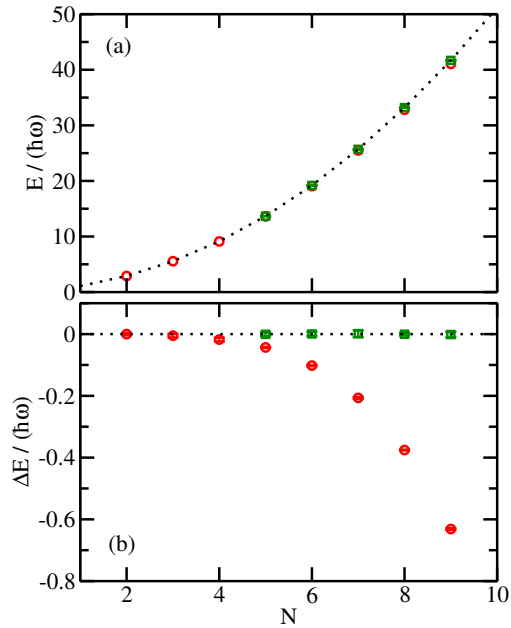


Figure 6.1: PIMC results for  $N$  harmonically trapped distinguishable one-dimensional particles with two-body zero-range interactions of infinite strength at temperature  $T = \hbar\omega/k_B$ . (a) The symbols show the energy obtained by the PIMC approach as a function of the number of particles  $N$ . For comparison, the dotted line shows the exact thermally averaged energy. (b) Symbols show the energy difference  $\Delta E$  between the PIMC energies and the exact results. As a reference, the dotted line shows the  $\Delta E = 0$  curve. In (a) and (b), the circles and squares are calculated using 8 and 128 time slices, respectively.

problem could be solved analytically. We note that the performance of the zero-range trap propagator for the system with infinite  $g$  is quite similar to that of the free-space propagator using the second- or fourth-order Trotter decomposition. The reason is that the error is dominated by three- and higher-body correlations.

We now discuss that the simulations need to be modified to treat  $N$  identical bosons or fermions with pairwise zero-range interactions of infinite strength. Equations (6.17) and (6.23) indicate that the paths for any two particles cannot cross. This implies that the permute move, implemented following the approach discussed in Ref. [261], yields a zero acceptance probability. This is consistent with our finite  $g$  simulations for  $N$  identical bosons. As we change  $g$  for otherwise fixed simulation parameters from small positive to large positive values, the probability of sampling the identity permutation approaches 1. The fact that particle permutations are always rejected, causes two problems for the infinite  $g$  simulations. First, since the particle ordering does not change, the one-body density for the first particle differs from that of the second particle, and so on. To calculate the one-body density  $\rho(x)$  of, e.g., the  $N$  identical boson system, one can average the one-body density  $\rho_j(x)$  of the  $j$ th particle over all  $j$ ,  $\rho(x) = N^{-1} \sum_{j=1}^N \rho_j(x)$ . An analogous average can be performed for other local (closed paths) structural properties. Second, the simulation of open paths, which allow for the calculation of off-diagonal long-range order, requires that the sampling scheme be modified since open paths do allow for permutations. The two-particle density matrix  $\rho(\{x_1, x_2\}, \{x_2, x'_1\}; \tau)$ , e.g., is finite if  $x_1 < x_2 < x'_1$ . The calculation of non-local observables is beyond the scope of the present paper.

As a next example, we apply the zero-range trap propagator to  $N = 2$  and 3 identical bosons in a harmonic trap with  $g = \hbar^2/(\sqrt{2}\mu a_{\text{ho}})$ . For the PIMC calculations, we tabulate the density matrix for the time step of interest and interpolate during the simulation. For small number of particles, we expect the zero-range trap propagator to work well even for a large time step and we use  $\tau\hbar\omega = 1/2$ . For  $k_B T = \hbar\omega/32$ , we obtain an energy of  $1.3067(1)\hbar\omega$

and  $2.3880(1)\hbar\omega$  for  $N = 2$  and  $3$ , respectively. The temperature is so low that the system is essentially in the ground state. For comparison, we determined the ground state energy using the transcendental equation from Ref. [145] and by solving the Lippmann-Schwinger equation [269]. The resulting ground state energies [ $1.306746\hbar\omega$  and  $2.3880(1)\hbar\omega$  for  $N = 2$  and  $3$ , respectively] agree within error bars with the PIMC results.

To demonstrate that the PIMC simulations describe the short-distance behavior of systems with zero-range interactions correctly, we analyze the pair distribution function  $P_{12}(x)$ , which is normalized to  $\int_{-\infty}^{\infty} P_{12}(x) dx = 1$ , for  $N = 2$  and  $3$  identical bosons with finite  $g$ . To start with, we derive the short-distance properties of the pair distribution function  $P_{12}$  for  $N$  identical bosons with zero-range interactions. Using the Hellmann-Feynman theorem, the partial derivative of the energy with respect to  $g$  can be related to the pair distribution function at  $x = 0$  [64],

$$P_{12}(0) = \frac{2}{N(N-1)} \frac{\partial E}{\partial g}. \quad (6.38)$$

Note that Eq. (6.38) is the one-dimensional analog of equating the three-dimensional adiabatic and pair relations [49]. Second, from the Bethe-Peierls boundary condition of the  $N$ -body wave function  $\Psi$  (the derivatives are taken while all other coordinates are kept fixed),

$$\left. \frac{\partial \Psi}{\partial x_{jk}} \right|_{x_{jk} \rightarrow 0^+} - \left. \frac{\partial \Psi}{\partial x_{jk}} \right|_{x_{jk} \rightarrow 0^-} = \frac{2\mu g}{\hbar^2} \Psi \Big|_{x_{jk} \rightarrow 0}, \quad (6.39)$$

one can derive that the slope of the pair distribution function at any temperature satisfies

$$\frac{\partial}{\partial x} P_{12}(x) \Big|_{x \rightarrow 0^+} - \frac{\partial}{\partial x} P_{12}(x) \Big|_{x \rightarrow 0^-} = \frac{4\mu g}{\hbar^2} P_{12}(x) \Big|_{x \rightarrow 0}. \quad (6.40)$$

For identical bosons,  $\partial P_{12}(x)/\partial x \Big|_{x \rightarrow 0^+}$  and  $\partial P_{12}(x)/\partial x \Big|_{x \rightarrow 0^-}$  have the same magnitude but opposite signs.

The dashed and dotted lines in Fig. 6.2 show  $P_{12}(x)$  obtained from our PIMC simulation for  $N = 2$  and  $3$ , respectively. For comparison, the solid lines are obtained using Eqs. (6.38)

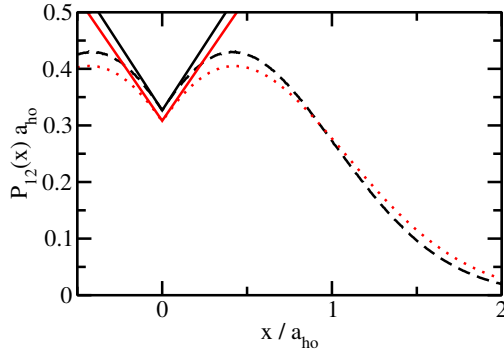


Figure 6.2: PIMC results for harmonically trapped one-dimensional bosons interacting through two-body zero-range interactions with coupling constant  $g = \hbar^2/(\sqrt{2}\mu a_{\text{ho}})$  at temperature  $T = \hbar\omega/(32k_B)$ . The dashed and dotted lines show the pair distribution function obtained by the PIMC approach for  $N = 2$  and  $3$  bosons, respectively. For comparison, the solid lines show the asymptotic short-range behavior obtained by alternative means (see text).

and (6.40). The values of  $\partial E/\partial g$  are obtained through independent energy calculations using the techniques of Refs. [145, 269]. We find  $P_{12}(0) = 0.3266002/a_{\text{ho}}$  and  $0.308245(2)/a_{\text{ho}}$  for  $N = 2$  and  $3$ , respectively. Our PIMC results agree well with the solid lines in the small  $|x|$  regime, demonstrating that the PIMC approach describes the short-range behavior accurately.

## 6.5 Three-dimensional tests

The pair distribution function of the non-interacting three-dimensional system is, unlike that of the non-interacting one-dimensional system, zero at vanishing interparticle distance. This fact leads, as we discuss now, to non-ergodic behavior unless the traditional path integral sampling methods are complemented by an additional move. To motivate the introduction of this new “pair distance move”, we consider the two-particle system.

Solid and dashed lines in Fig. 6.3 show the scaled pair distribution functions for two distinguishable particles with infinitely large  $s$ -wave scattering length in a three-dimensional harmonic trap at  $k_B T/(\hbar\omega) = 1$  interacting through a zero-range potential and a finite-range

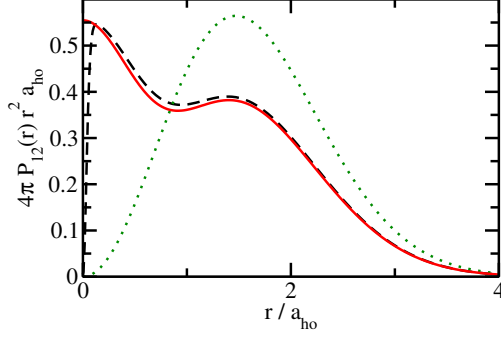


Figure 6.3: Scaled pair distribution functions  $4\pi P_{12}(r)r^2$  for two distinguishable particles of mass  $m$  in a harmonic trap at  $k_B T/(\hbar\omega) = 1$ . The solid and dashed lines are for two particles with infinitely large  $s$ -wave scattering length interacting through the zero-range potential and a Gaussian potential with effective range  $r_e \approx 0.0861a_{\text{ho}}$ , respectively. For comparison, the dotted line is for the non-interacting system.

Gaussian potential with effective range  $r_e \approx 0.0861a_{\text{ho}}$ , respectively. The pair distribution function  $P_{12}(r)$  is normalized according to  $4\pi \int_0^\infty P_{12}(r)r^2 dr = 1$ . The pair distribution functions for the finite-range and zero-range potentials nearly coincide for large  $r$ , but differ for small  $r$ . The pair distribution function for the Gaussian potential drops to 0 as  $r$  approaches 0 while that for the zero-range potential approaches a non-zero value.

PIMC and PIGS simulations typically use the first term on the right hand side of Eq. (6.3) as the “prior distribution” and the second term as the “correction”. This is suitable for  $N$ -body systems with two-body finite-range potentials for which the scaled pair distribution function is, as that of the non-interacting system (see the dotted line in Fig. 6.3 for a two-body example), zero at  $r = 0$ . Since the prior distribution has zero probability at  $r = 0$ , the pair distribution function of the system with zero-range interactions is not properly sampled if standard sampling schemes are used. Ergodicity is violated at  $r = 0$  and the probability to sample the region near  $r = 0$  is small. Moreover, the correction term [see Eqs. (6.37) and (6.33)] diverges as  $r$  or  $r'$  go to 0. This means that the probability to sample configurations with  $r \approx 0$  is small. However, if such a configuration is chosen, there is a small probability to accept a new configuration with much larger  $r$ , i.e., the correlation length is large. Similarly, if one uses the naive uniform distribution for the prior distribution, i.e., if one proposes a

move for which all Cartesian coordinates differ by  $\delta x$  from the current configuration, where  $\delta x$  is a random value between  $-\Delta x$  and  $\Delta x$ , the problems discussed above still exist.

To remedy the problems that arise if the standard sampling approaches are used, we introduce a “pair distance move” for which the prior distribution scales as  $1/r^2$  in the pair distances. First, particles  $j$  and  $k$  and a bead  $l$  are chosen (the coordinates for the  $l$ th bead are collectively denoted by  $\mathbf{R}_l$ ) and the distance  $r_{jk} = |\mathbf{r}_{jk}|$  and the direction  $\hat{\mathbf{r}}_{jk}$  are calculated. A new vector  $\mathbf{r}_{jk,\text{new}}$  that lies along  $\hat{\mathbf{r}}_{jk}$  or  $-\hat{\mathbf{r}}_{jk}$  is proposed,  $\mathbf{r}_{jk,\text{new}} = \epsilon \hat{\mathbf{r}}_{jk}$ . The quantity  $\epsilon$  is written as  $\epsilon = r_{jk} + \delta r$ , where  $\delta r$  is obtained by choosing uniformly from  $-\Delta r$  to  $\Delta r$ . If the weight  $w$ ,

$$w = \min\left[1, \frac{\rho_{\text{tot}}(\mathbf{R}_{l-1}, \mathbf{R}_{l,\text{new}}; \tau) \rho_{\text{tot}}(\mathbf{R}_{l+1}, \mathbf{R}_{l,\text{new}}; \tau) \epsilon^2}{\rho_{\text{tot}}(\mathbf{R}_{l-1}, \mathbf{R}_l; \tau) \rho_{\text{tot}}(\mathbf{R}_{l+1}, \mathbf{R}_l; \tau) r_{jk}^2}\right], \quad (6.41)$$

is larger than a uniform random number between 0 and 1, then the proposed move is accepted. Otherwise, it is rejected and the old configuration is kept. The value of  $\Delta r$  is adjusted such that about 50% of the proposed moves are accepted. It can be easily proven that detailed balance is fulfilled. Our PIMC calculations for the two-body system with zero-range interactions show that the “pair distance move” significantly improves the sampling. Without this move, the short-range behavior of the pair distribution function has a long correlation length, which increases with decreasing  $\tau$ . With this move, the small  $r$  behavior is described accurately. The move described here is related to the compression-dilation move introduced in Ref. [241]. Few details were given in Ref. [241] and no comparison with that approach is made in this paper.

We now demonstrate that the outlined sampling scheme provides a reliable description of Bose systems at unitarity, which have attracted a great deal of attention recently experimentally and theoretically [241, 247, 250, 251, 270–273]. While the properties of unitary Fermi systems with zero-range interactions are fully determined by the  $s$ -wave scattering length [32, 76, 203, 209, 210, 220] those of Bose systems additionally depend on a three-body

parameter [41, 211]. Specifically, if the two-body interactions are modeled by zero-range potentials, then a three-body regulator is needed to prevent the Thomas collapse of the  $N$ -boson ( $N \geq 3$ ) system [41, 43]. Here, we utilize a purely repulsive three-body potential of the form

$$V_{3b}(R_{jkl}) = \frac{C_6}{R_{jkl}^6}, \quad (6.42)$$

where  $R_{jkl}$  denotes the three-body hyperradius,  $R_{jkl} = \sqrt{(r_{jk} + r_{jl} + r_{kl})/3}$ . In the  $N$ -boson system, each of the  $N(N-1)(N-2)/6$  triples feels the regulator, i.e., the term  $\sum_{j < k < l} V_{3b}(R_{jkl})$  is added to the Hamiltonian with pairwise zero-range interactions. In the absence of an external trap, the zero temperature three-body ground state energy  $E_{\text{trimer}}$  of the unitary system is set by the  $C_6$  coefficient. The corresponding length scale is  $1/\kappa$ , where  $\kappa = \sqrt{m|E_{\text{trimer}}|}/\hbar$  is the binding momentum.

Our goal is to determine the ground state properties of self-bound  $N$ -boson droplets at unitarity in the absence of an external confinement. In the context of the present paper, it would seem that our goal could be readily achieved using the PIGS approach. It turns out, however, that without a good initial trial wave function, the number of time slices needed to converge the calculations is rather large, making the simulations computationally quite expensive. Instead, one might consider performing PIMC calculations at various temperatures and extrapolating to the zero temperature limit. This approach also turns out to be computationally extensive. Our simulations pursue an alternative approach, in which the scattering states of the system are discretized in such a way that the relative ground state energy  $E_{\text{cluster}}$  of the  $N$ -body cluster is much larger than the energy scale introduced by the discretization. We utilize a spherically symmetric harmonic trap and adjust the trapping frequency such that  $|E_{\text{cluster}}| \gg \hbar\omega$ . Simulations are then performed at a temperature where the Bose droplet is in the ground-state dominated liquid-phase [10, 241], where the finite temperature introduces center-of-mass excitations but not excitations of the relative degrees of freedom. The temperature  $T_{\text{tr}}$  at which excitations of the relative degrees of freedom be-

come relevant can be estimated using the “combined model” introduced in Ref. [10]. As we show now, this approach allows for a fairly robust determination of the  $N$ -boson properties at zero temperature.

We set the trap energy  $\hbar\omega$  to  $0.27|E_{\text{trimer}}|$  ( $E_{\text{trimer}}$  is the ground state energy of the three-boson system in free space) and the temperature to  $\hbar\omega/k_B$ . These parameters provide a good compromise: First, the temperature is sufficiently low that finite temperature effects are negligible (i.e.,  $T < T_{\text{tr}}$  for the  $N$  considered below,  $N = 3 - 9$ ) and high enough that convergence can be reached with the computational resources available to us. Second, the size of the  $N$ -boson system is smaller than the harmonic oscillator length such that structural properties such as the pair distribution function are largely unaffected by the external confinement for  $N \gtrsim 5$ .

Our path integral simulations use the two-body zero-range trap propagator. The repulsive three-body potentials are treated using the Trotter formula. In the second-order scheme, half of the sum of the three-body potentials is moved to the left and half to the right of the Hamiltonian  $H$  that accounts for the two-body interactions and the external confinement. In the fourth-order scheme, a more involved decomposition is used [112, 158]. In addition to the standard moves and the “pair distance move”, we implement a move that updates the center-of-mass coordinates. The introduction of this center-of-mass move is motivated by the fact that the relative degrees of freedom are expected to be, to a good approximation, “frozen” in the ground state while low-energy center-of-mass excitations are allowed. Indeed, the center-of-mass energy is given by  $E_{\text{c.m.}} = 3\hbar\omega \coth(\hbar\omega/(2k_B T))/2$ , which evaluates to  $3.24593\hbar\omega$  for  $T = \hbar\omega/k_B$ , indicating that center-of-mass excitations cannot be neglected.

The squares in Fig. 6.4 show the pair distribution function calculated by the PIMC approach for three identical bosons at  $T = \hbar\omega/k_B$ . For comparison, the solid line and the circles show zero-temperature results. The solid line is calculated using the PIGS approach with a trial wave function that coincides with the exact ground state wave function [274]

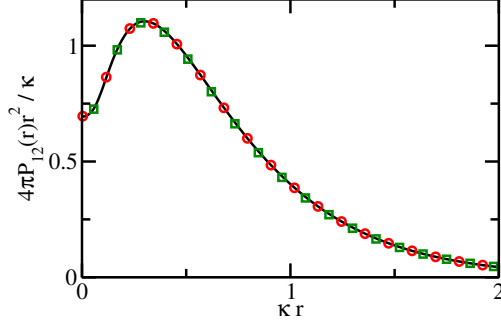


Figure 6.4: Scaled pair distribution function  $4\pi P_{12}(r)r^2$  for three identical harmonically trapped three-dimensional bosons with two-body zero-range interactions with infinitely large  $s$ -wave scattering length and repulsive  $1/R^6$  three-body potential. The solid line and squares are calculated by the zero-temperature PIGS approach and the PIMC approach at  $T = \hbar\omega/k_B$ . For comparison, the circles show the scaled pair distribution function obtained by sampling the exact ground state density using the Metropolis algorithm.

while the circles are calculated by sampling the exact zero-temperature ground state density using the Metropolis algorithm. The agreement between the three sets of calculations is very good, demonstrating (i) that excitations of the relative degrees of freedom are negligible at the temperature considered and (ii) that the path integral approaches accurately resolve the short-range behavior of the pair distribution function. The pair distribution functions shown in Fig. 6.4 are affected by the trap, i.e., they move to larger  $r$  as the trap frequency  $\omega$  is reduced. The reason is that  $\hbar\omega$  is only about four times smaller than  $|E_{\text{trimer}}|$ . The magnitude of the  $N$ -boson energy  $E_{\text{cluster}}$  increases rapidly with  $N$  [1, 7, 9], implying that the trap effects decrease quickly with increasing  $N$ , thus allowing us to extract the free-space energy  $E_{\text{cluster}}$  from the finite-temperature trap energies  $E_{\text{sim}}$ .

Symbols in Fig. 6.5 exemplarily show our PIMC energies  $E_{\text{sim}}$  for the five-boson system at  $T = \hbar\omega/k_B$  as a function of the time step  $\tau$ . Circles and squares are obtained using the second- and fourth-order schemes (see earlier discussion), respectively, to treat the term  $\exp(-\sum_{j<k<l}\tau V_{3b}(R_{jkl}))$ . The statistical errors are smaller than the symbol size. The fourth-order results display, as expected, a smaller time step dependence than the second-order results and are well described by a function of the form  $c_0 + c_2\tau^2 + c_4\tau^4$ , whereas the

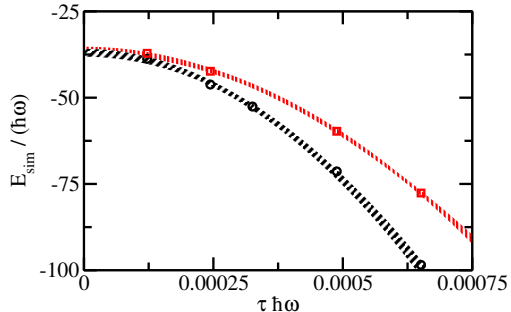


Figure 6.5: PIMC energies for  $N = 5$  harmonically trapped three-dimensional bosons with two-body zero-range interactions with infinite scattering length and repulsive  $1/R^6$  three-body interaction at temperature  $T = \hbar\omega/k_B$  as a function of the time step  $\tau$ . The circles (lower-lying data set) and squares (higher-lying data set) show the energy obtained using the second- and fourth-order scheme, respectively. The error bands are obtained by fitting the data for different  $\tau$  intervals.

second-order results are described by a function of the form  $c_0 + c_2\tau^2$ . The presence of the  $\tau^2$  term for the fourth-order results is due to the fact that the pair product approximation neglects three- and higher-body correlations (see also Sec. 6.4). The shaded regions in Fig. 6.5 show errorbands obtained by fitting the two sets of PIMC energies for different  $\tau$  intervals. The errorbars of the extrapolated zero time step energies are found to overlap. We find  $E_{\text{sim}} = -37.0(1.2)\hbar\omega$  and  $-36.2(1.0)\hbar\omega$  for the second- and fourth-order scheme, respectively. The free-space energy  $E_{\text{cluster}}$  is then obtained by subtracting the center-of-mass energy,  $E_{\text{cluster}} = E_{\text{sim}} - E_{\text{c.m.}}$ .

The squares in Fig. 6.6 show  $E_{\text{cluster}}$  for  $N = 5 - 9$ . The corresponding energies  $E_{\text{sim}}$  are obtained using the fourth-order scheme with  $\tau\hbar\omega \approx 0.000122$ . As can be seen from Fig. 6.5, this energy lies within the extrapolated  $\tau = 0$  errorbands for  $N = 5$ . Figure 6.6 scales the energy  $E_{\text{cluster}}$  by the corresponding zero-temperature free-space trimer energy  $E_{\text{trimer}}$  calculated by the hyperspherical coordinate approach. For comparison, the dotted line shows the  $N$ -boson ground state energies from Ref. [7] for a finite-range two-body Gaussian potential with infinitely large  $s$ -wave scattering length and a hardcore three-body regulator. While the model interactions differ, the agreement between the two sets of calculations is good, providing further support for the (approximate) universality of  $N$ -boson droplets.

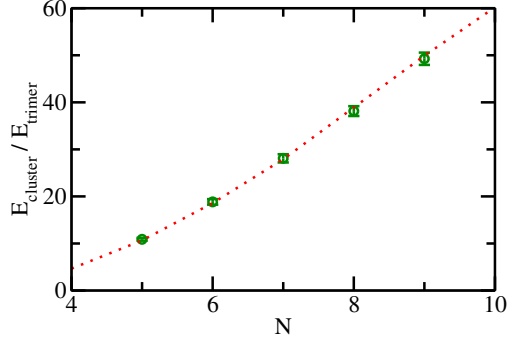


Figure 6.6: Free-space  $N$ -boson ground state energy  $E_{\text{cluster}}$  as a function of  $N$  for infinitely large two-body  $s$ -wave scattering length. The circles with errorbars are extracted from our PIMC simulations. The dotted line shows the energies reported in Ref. [7].

More detailed comparisons will be presented elsewhere [275].

## 6.6 Conclusion

This paper discussed how to treat zero-range two-body interactions in  $N$ -body Monte Carlo simulations. We showed that the incorporation of the exact two-body zero-range propagator via the pair product approximation allows for an accurate description of paradigmatic strongly-interacting one- and three-dimensional model Hamiltonian.

An important aspect of the studies presented is that the strength of the contact interaction requires no renormalization since the simulations are performed using the regularized two-body zero-range pseudopotential and continuous spatial coordinates in an unrestricted Hilbert space. The fact that the interaction strength does not need to be renormalized distinguishes the simulations presented in this paper from lattice approaches [276–278] and from configuration interaction approaches [279–281].

The developments presented in this paper open a number of possibilities. The use of two-body zero-range interactions, e.g., provides direct access to the two-body Tan contact [49], without extrapolation to the zero-range limit. The two-body Tan contact is defined for systems with two-body zero-range interactions. It relates distinct physical observables such

as the large momentum tail and aspects of the radio frequency spectrum, and has attracted a great deal of theoretical [59, 61, 64, 66, 141, 142, 194] and experimental [52–55, 251] interest. From the computational perspective, the adiabatic relation, which involves the change of the energy with the scattering length, and the pair relation [49, 57], which gives the probability of finding two particles at the same position, are most convenient. Earlier work applied these relations to systems with finite-range interactions and extrapolated to the zero-range limit. Using our zero-range propagators, these relations can be used directly for the determination of the Tan contact, eliminating the extrapolation step.

*Acknowledgement:* We thank Ebrahim Gharashi for providing the energies of three identical bosons calculated using the approach of Ref. [269] and Maurizio Rossi for very useful comments on an earlier version of the manuscript. Support by the National Science Foundation (NSF) through Grant No. PHY-1415112 is gratefully acknowledged. This work used the Extreme Science and Engineering Discovery Environment (XSEDE), which is supported by NSF Grant No. OCI-1053575, and the WSU HPC.

# Chapter 7

## Energy and structural properties of $N$ -boson clusters attached to three-body Efimov states: Two-body zero-range interactions and the role of the three-body regulator

by Yangqian Yan<sup>1</sup> and D. Blume<sup>1</sup>

<sup>1</sup>Department of Physics and Astronomy, Washington State University, Pullman,

Washington 99164-2814, USA

Copyright (2015) by the American Physical Society

The low-energy spectrum of  $N$ -boson clusters with pairwise zero-range interactions is believed to be governed by a three-body parameter. We study the ground state of  $N$ -boson clusters with infinite two-body  $s$ -wave scattering length by performing *ab initio* Monte Carlo simulations. To prevent Thomas collapse, different finite-range three-body regulators are

used. The energy and structural properties for the three-body Hamiltonian with two-body zero-range interactions and three-body regulator are in much better agreement with the “ideal zero-range Efimov theory” results than those for Hamiltonian with two-body finite-range interactions. For larger clusters we find that the ground state energy and structural properties of the Hamiltonian with two-body zero-range interactions and finite-range three-body regulators are not universally determined by the three-body parameter, i.e., dependences on the specific form of the three-body regulator are observed. For comparison, we consider Hamiltonian with two-body van der Waals interactions and no three-body regulator. For the interactions considered, the ground state energy of the  $N$ -body clusters is—if scaled by the three-body ground state energy—fairly universal, i.e., the dependence on the short-range details of the two-body van der Waals potentials is small. Our results are compared with the literature.

## 7.1 Introduction

The unitary regime, where the two-body  $s$ -wave scattering length is infinitely large, can be reached in ultra cold dilute atomic gases using Feshbach resonance techniques [4]. Two-component Fermi gases were realized experimentally and found to be stable and universal even in the large  $s$ -wave scattering length regime [34, 282, 283], i.e., the properties of the system were found to be governed, to a very good approximation, by the  $s$ -wave scattering length  $a_s$  alone and independent of the details of the interaction potential [32, 76, 203]. Unitary Bose gases, in contrast, are short-lived [251, 270, 271]. Their properties depend on the details of the interaction potential. Typically, this dependence is encapsulated by a three-body parameter [41].

Efimov predicted that three identical bosons interacting through two-body potentials with infinitely large  $s$ -wave scattering length  $a_s$  and vanishing effective range support an infinite number of three-body bound states [211]. The binding momenta  $\kappa_3^{(n)}$  of the trimers

( $n$  labels the states) display a geometric scaling, i.e.,  $\kappa_3^{(n)}/\kappa_3^{(n+1)} \approx 22.6944$  [41, 211]. If the binding momentum of one trimer is known, that of the other trimers is also known. Importantly, the binding momenta themselves cannot be determined solely from a theory that is based on two-body zero-range potentials. Rather, a three-body parameter is needed to regularize the problem (i.e., to set the absolute scale of the three-body spectrum). The three-body regulator can be introduced in many ways. In this work, we consider three different regularization approaches: (i) a Hamiltonian with two-body zero-range potentials and a zero-range three-body potential, (ii) a Hamiltonian with two-body zero-range potentials and a purely repulsive three-body potential, and (iii) a Hamiltonian with finite-range two-body potentials and no three-body potential.

Much less is known about four- and higher-body systems at unitarity [1, 82, 83, 85, 284–288].  $N$ -body cluster states are believed to be attached to each trimer, i.e., for a trimer with binding momentum  $\kappa_3^{(n)}$ , two  $N$ -body states are believed to exist with binding momenta  $C_N^{(1)}\kappa_3^{(n)}$  and  $C_N^{(2)}\kappa_3^{(n)}$ , where  $C_N^{(1)}$  and  $C_N^{(2)}$  are dimensionless parameters that do not depend on  $n$ . Whether four- and higher-body parameters exist has been under debate in the literature.

The study of  $N$ -body states attached to Efimov trimers is challenging for several reasons. To date, no analytical solutions for  $N \geq 4$  exist. Numerical treatments have to be capable of describing vastly different length scales. For finite-range two-body interactions, the lowest trimer state is typically not a “pure” Efimov state. Thus, one would ideally like to investigate  $N$ -body droplets that are tied to the first- or second-excited trimer states. The corresponding  $N$ -body states ( $N \geq 4$ ; see Fig. 7.1 for an illustration of the four-body spectrum as a function of  $1/a_s$ ) are not bound states but resonance states, which are not stable with respect to break-up into smaller sub-units. Thus, the numerical approach of choice would ideally be capable of treating  $N$ -body resonance states whose size is many orders of magnitude larger than the range of the underlying two-body potential.

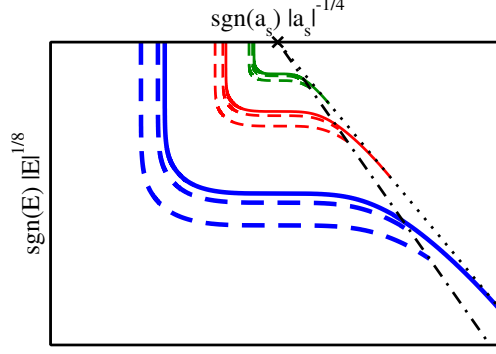


Figure 7.1: Schematic illustration of the energy spectrum for four identical bosons. The x marks the  $(1/a_s, E) = (0, 0)$  point. The dotted line shows the energy of the weakly-bound dimer. The solid lines show different Efimov trimer states, which become unbound on the positive scattering length side at the atom-dimer threshold. The dashed lines show “ground state” and “excited state” tetramers that are attached to each Efimov trimer. These tetramer states hit the dimer-dimer threshold on the positive scattering length side (the energy of the two dimers is shown by the dash-dotted line). It should be noted that the excited tetramer state turns into a virtual state for a certain region of positive scattering lengths [8]; this detail is not reflected in the plot.

To bypass these numerical challenges, this work pursues, as have other works before [1, 7], an approach that considers  $N$ -body droplets (the thick dashed lines in Fig. 7.1 show the two four-body states) tied to the energetically lowest-lying trimer state (thick solid line in Fig. 7.1). To ensure that the trimer ground state has the key characteristics of a true Efimov trimer state, we employ two-body zero-range interactions together with a purely repulsive three-body potential that serves as a regulator; we refer to this model as 2bZR+3bRp (2b, ZR, 3b, and R stand for two-body, zero-range, three-body, and repulsive, respectively, and  $p$  denotes the power of the repulsive three-body potential; see below). The forms of  $V_{2b}$  and  $V_{3b}$  for the model 2bZR+3bRp are given in Table 7.1 and the Hamiltonian  $H$  for  $N$  particles with mass  $m$  and position vector  $\mathbf{r}_j$  reads

$$H = - \sum_{j=1}^N \frac{\hbar^2}{2m} \nabla_j^2 + \sum_{j<k}^N V_{2b}(\mathbf{r}_{jk}) + \sum_{j<k<l}^N V_{3b}(R_{jkl}), \quad (7.1)$$

where the two-body potential  $V_{2b}$  depends on the interparticle distance vector  $\mathbf{r}_{jk}$  ( $\mathbf{r}_{jk} =$

Table 7.1: Summary of potential models considered in this work. For each model, the two-body potential  $V_{2b}$  and the three-body potential  $V_{3b}$  are listed.  $V_{2b}$  for 2bZR+3bZR, 2bZR+3bHC, and 2bZR+3bRp is the Fermi-Huang pseudopotential [3];  $a_s$  is set to infinity.  $V_{ZR}(R)$  for 2bZR+3bZR is treated as a zero-range boundary condition.  $V_{HC,R_0}(R)$  is the hardcore repulsive potential;  $V_{HC,R_0}(R) = 0$  for  $R > R_0$  and  $V_{HC,R_0}(R) = \infty$  for  $R < R_0$ .  $V_0$  and  $r_0$  for 2bG,  $c_{12}$  and  $c_6$  for 2bLJ,  $c_{10}$  and  $c_6$  for 2b10-6, and  $c_8$  and  $c_6$  for 2b8-6 are chosen such that the  $s$ -wave scattering length is infinitely large and the two-body system supports one zero-energy  $s$ -wave bound state.

model	$V_{2b}$	$V_{3b}$
2bZR+3bZR	$\frac{4\pi\hbar^2}{m} a_s \delta^{(3)}(\mathbf{r}) \frac{\partial}{\partial r} r$	$V_{ZR}(R)$
2bZR+3bHC	$\frac{4\pi\hbar^2}{m} a_s \delta^{(3)}(\mathbf{r}) \frac{\partial}{\partial r} r$	$V_{HC,R_0}(R)$
2bZR+3bRp	$\frac{4\pi\hbar^2}{m} a_s \delta^{(3)}(\mathbf{r}) \frac{\partial}{\partial r} r$	$\frac{C_p}{R^p}$
2bG	$V_0 \exp[-r^2/(2r_0^2)]$	—
2bLJ	$\frac{c_{12}}{r^{12}} - \frac{c_6}{r^6}$	—
2b10-6	$\frac{c_{10}}{r^{10}} - \frac{c_6}{r^6}$	—
2b8-6	$\frac{c_8}{r^8} - \frac{c_6}{r^6}$	—

$\mathbf{r}_j - \mathbf{r}_k$ ) and the three-body potential  $V_{3b}$  depends on the three-body hyperradius  $R_{jkl}$ ,

$$R_{jkl} = \sqrt{(\mathbf{r}_{jk}^2 + \mathbf{r}_{jl}^2 + \mathbf{r}_{kl}^2)/3}. \quad (7.2)$$

Importantly, the  $N$ -body Hamiltonian  $H$  is well behaved, i.e., the ground state is well defined thanks to the three-body regulator. As we show in Sec. 7.2, the three-body regulator produces three-body states that share many characteristics with the pure three-body Efimov state. Pure three-body Efimov states are obtained if the two-body interactions are of zero range and the hyperradial boundary condition at  $R_{123} = 0$  is specified [41]. Since the hyperradial boundary condition or logarithmic derivative can be imposed via a delta-function in the hyperradius, we refer to this model as 2bZR+3bZR.

Our work considers the  $N$ -body ground state using a novel Monte Carlo approach [289] that allows for the treatment of two-body zero-range interactions. The Monte Carlo approach can unfortunately not treat three-body zero-range interactions, i.e., it is not capable of treating the Hamiltonian 2bZR+3bZR. A key objective of the present work is then to investigate how the properties of  $N$ -body droplets in the ground state, supported by the model

Hamiltonian 2bZR+3bRp, change with the number of particles and with the power  $p$  of the three-body regulator. An important question is to which degree the  $N$ -body properties are determined by the three-body parameter.

For comparison, we also consider Hamiltonian with finite-range two-body Gaussian or van der Waals interactions and no three-body interaction. The ground state manifolds of these models, referred to as 2bG, 2bLJ, 2b10-6, and 2b8-6 (see Table 7.1), lack—as we show—a number of key Efimov characteristics. Two-body Gaussian interactions have been employed extensively in the literature [1, 10, 78, 287, 290], sometimes also in combination with a repulsive three-body regulator [7, 291].

Although the structural properties of the ground state trimers for the Hamiltonian with two-body van der Waals interactions differ notably from those for the pure Efimov trimer [292, 293], these systems exhibit universal features [77, 78, 294–300]. Specifically, the trimer ground state binding momentum  $\kappa_3^{(1)}$  at unitarity is, to a good approximation, determined by the van der Waals length  $L_{\text{vdW}}$  [77, 78] and independent of the short-range details. For the two-body Lenard-Jones potential, one finds  $\kappa_3^{(1)} \approx 0.230/L_{\text{vdW}}$  [301], where  $L_{\text{vdW}} = (\sqrt{mc_6}/\hbar)^{1/2}/2$ . This relationship is nowadays being attributed to van der Waals universality. Moreover, the binding momentum spacing of 23.4 between the ground state and the first excited state is quite close to the spacing of 22.6944 exhibited by consecutive pure Efimov trimers [301]. It is thus interesting to investigate if van der Waals universality exists for  $N > 3$ , i.e., to answer the question whether or not the  $N$ -body ground state energy depends on the short-range details of the two-body van der Waals potential.

The remainder of this paper is organized as follows. Section 7.2 compares the properties of the three-boson system with infinitely large  $s$ -wave scattering length interacting through 2bZR+3bZR, 2bZR+3bHC, and 2bZR+3bRp and illustrates the benefits and limitations of these models. Section 7.3 reviews several literature results for  $N$ -body droplets. Section 7.4 extends the calculations for the 2bZR+3bRp interaction model to clusters with  $N \leq 15$ .

In addition to the energy, various structural properties are discussed in detail. Section 7.5 compares the results for the model 2bZR+3bRp with those for systems with two-body finite-range interactions (i.e., for the models 2bG, 2bLJ, 2b10-6, and 2b8-6). Finally, Sec. 7.6 concludes.

## 7.2 Three-body system at unitarity

To understand the three-body system, it is instructive to rewrite the Hamiltonian  $H$ , Eq. (7.1), for  $N = 3$  in hyperspherical coordinates [75]. To this end, we first separate off the center of mass degrees of freedom and restrict ourselves to states with vanishing relative orbital angular momentum. For the 2bZR+3bZR, 2bZR+3bHC, and 2bZR+3bRp models with infinitely large two-body  $s$ -wave scattering length  $a_s$ , the hyperradial and hyperangular degrees of freedom separate [41, 221]. The lowest eigen value of the hyperangular Schrödinger equation is typically denoted by  $s_0$ , where  $s_0 \approx 1.006\iota$  [41, 211]. This eigen value enters into the hyperradial Schrödinger equation with hyperradial Hamiltonian  $H_R$ ,

$$H_R = -\frac{\hbar^2}{2m} \frac{\partial^2}{\partial R^2} + \frac{\hbar^2(s_0^2 - 1/4)}{2mR^2} + V_{3b}(R) \quad (7.3)$$

(for notational simplicity, the three-body hyperradius is denoted by  $R$  throughout this section). If  $V_{3b}(R)$  is equal to zero, the eigen energies of the Hamiltonian  $H_R$  are not well defined. To make the problem well-defined without explicitly introducing a length scale, a boundary condition at  $R = 0$ , which serves as a regulator and defines a scale, can be specified. This is the model 2bZR+3bZR. The energy spectrum of the 2bZR+3bZR model Hamiltonian displays a perfect geometric series [41]. For an eigen state with binding momentum  $\kappa_3^{(n)}$  [the corresponding energy is  $(\hbar\kappa_3^{(n)})^2/m$ ], there exists a tighter and a looser bound state with binding momentum  $\kappa_3^{(n-1)} = \exp(\pi/|s_0|)\kappa_3^{(n)}$  and  $\kappa_3^{(n+1)} = \exp(-\pi/|s_0|)\kappa_3^{(n)}$ , respectively. Here,  $\exp(\pi/|s_0|)$  is approximately equal to 22.6944. The three-body spectrum

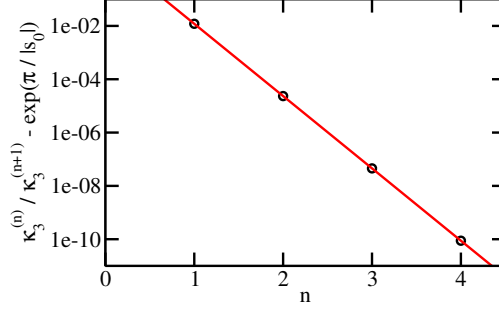


Figure 7.2: Breaking of the scale invariance for the three-boson system at unitarity with three-body hardcore regulator. The circles show the difference between the binding momentum ratio  $\kappa_3^{(n)}/\kappa_3^{(n+1)}$  of the  $n$ th and  $(n+1)$ th states for the model 2bZR+3bHC and the ratio  $\exp(\pi/|s_0|) = 22.6944$  for the model 2bZR+3bZR as a function of  $n$ . The solid line shows a fit to the data points. The breaking of the scale invariance becomes weaker with increasing  $n$ .

for the 2bZR+3bZR model is not bounded from below; in our notation, this means that  $n$  can take non-positive values, i.e.,  $n = \dots, -2, -1, 0, 1, 2, \dots$ . There exists an infinity of three-body bound states and each hyperradial wavefunction  $\psi_n(R)$  has infinitely many nodes. The hyperradial wavefunctions of these states collapse if scaled by the binding momentum  $\kappa_3^{(n)}$ , i.e.,  $(\kappa_3^{(n)})^{1/2}\psi_n(\kappa_3^{(n)}R)$  is the same for all states.

We now consider finite-range three-body regulators. As a first toy model, we consider a hardcore repulsive three-body potential, i.e., we consider the model 2bZR+3bHC (see Table 7.1). In this case, the hyperangular and hyperradial parts separate as before and the Hamiltonian  $H_R$  supports a well defined ground state with energy  $E_3^{(1)}$  or binding momentum  $\kappa_3^{(1)}$  (in our notation,  $n = 1, 2, \dots$ ). For the  $n$ th state with binding momentum  $\kappa_3^{(n)}$ , the hyperradial wavefunction has  $n-1$  nodes. The circles in Fig. 7.2 show the difference between the binding momentum ratios for the model 2bZR+3bHC and the model 2bZR+3bZR. The binding momentum ratio for the ground and first excited states of the model 2bZR+3bHC is approximately 22.7064. The deviation from the model 2bZR+3bZR is 0.0120 or 0.053%. As we go to excited states, the deviations decrease exponentially. A log-linear fit of the deviations yields  $\kappa_3^{(n)}/\kappa_3^{(n+1)} - \exp(\pi/|s_0|) \approx \exp(1.823 - 6.244n)$  (see the solid line in Fig. 7.2). The overlap between the wavefunction of the ground state of the model 2bZR+3bHC and

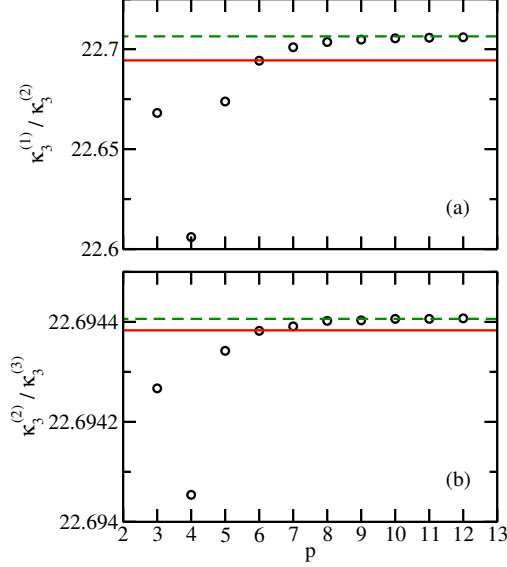


Figure 7.3: Binding momentum characteristics for the three-boson system with three-body power law regulator at unitarity. The circles show the ratio of the binding momentum of two consecutive states for the model 2bZR+3bRp as a function of  $p$ . Panel (a) shows the binding momentum ratio for the ground and the first excited states while panel (b) shows the ratio for the first and the second excited states. The solid and dashed lines show the binding momentum ratio for the models 2bZR+3bZR and 2bZR+3bHC, respectively.

the wavefunction of the model 2bZR+3bZR with the same binding momentum is 0.99947, i.e., the inner region where the wavefunction for the model 2bZR+3bHC deviates from the true Efimov wavefunction is insignificant. The three-body hardcore potential breaks the scale-invariance and introduces  $n$ -dependent energy spacings.

The discontinuity of the derivative of the wavefunction at  $R = R_0$  makes the three-body hardcore regulator challenging to treat numerically, at least by the path integral Monte Carlo (PIMC) technique employed in Sec. 7.4. Thus, we consider three-body power law potentials, which approach the hardcore potential for  $p \rightarrow \infty$ . The circles in Fig. 7.3 show the binding momentum ratios for the model 2bZR+3bRp as a function of  $p$ . Figures 3(a) and 3(b) show the binding momentum ratios for the ground and first excited states, and the first and second excited states, respectively. As expected, the binding momentum ratios approach the value for the model 2bZR+3bHC (dashed lines) in the large  $p$  limit. For comparison, the solid lines show the binding momentum ratio for the model 2bZR+3bZR. The deviations between

the binding momentum ratios for the 2bZR+3bRp and the 2bZR+3bHC models are largest for  $p = 4$ . Similar to the model 2bZR+3bHC, the binding momentum ratios for the model 2bZR+3bRp approach the value  $\exp(\pi/|s_0|)$  exponentially with increasing  $n$ .

The spacing of the momenta is not the only way to characterize how universal the system is, i.e., how close a given system is to the true Efimov scenario described by the model 2bZR+3bZR. The structural properties provide additional insights. Indeed, the structures of weakly-bound three-body systems with positive  $a_s$  have recently been measured [292, 293]. We first look at the distribution of the angles  $\theta_{jkl}$  between each pair of position vectors,  $\theta_{jkl} = \arccos(\hat{\mathbf{r}}_{jk} \cdot \hat{\mathbf{r}}_{kl})$ . The distribution  $P_{\text{tot}}(\theta)$  considers all three angles of each triangle, while the distribution  $P_{\text{min}}(\theta)$  [ $P_{\text{max}}(\theta)$ ] considers only the smallest [largest] of the three angles of each triangle. The normalizations are chosen such that  $\int_0^\pi P_{\text{tot}}(\theta)d\theta = 3$  and  $\int_0^\pi P_{\text{min}}(\theta)d\theta = \int_0^\pi P_{\text{max}}(\theta)d\theta = 1$ . For infinitely large  $a_s$  (as considered throughout this section), these angular distributions only depend on the hyperangles and not on the hyperradius. Thus, they are the same for the models 2bZR+3bZR, 2bZR+3bHC, and 2bZR+3bRp. The circles, triangles, and squares in Fig. 7.4 show  $P_{\text{tot}}(\theta)$ ,  $P_{\text{min}}(\theta)$ , and  $P_{\text{max}}(\theta)$ , respectively, for these models.  $P_{\text{tot}}(\theta)$  is approximately linear and approaches a finite value for  $\theta \rightarrow 0$ . We are interested in the angular distributions for two reasons. (i) For the models 2bG, 2bLJ, 2b10-6, and 2b8-6, the hyperangular and hyperradial degrees of freedom do not separate and the difference between their angular distributions and those for the two-body zero-range models provides valuable insights (see Ref. [301]). (ii) For the  $N$ -body clusters, the angular distributions, which depend on both the hyperangles and the  $N$ -particle hyperradius, can serve to monitor the three-body correlations.

Solid, dotted, and dashed lines in Fig. 7.4 show the angular distributions  $P_{\text{tot}}(\theta)$ ,  $P_{\text{min}}(\theta)$ , and  $P_{\text{max}}(\theta)$ , respectively, of the three-body ground state for the model 2bG. Compared to that for the two-body zero-range models, the angular distribution near  $\theta = 0$  for the finite-range model displays distinctly different behavior. For the Gaussian model, the probability

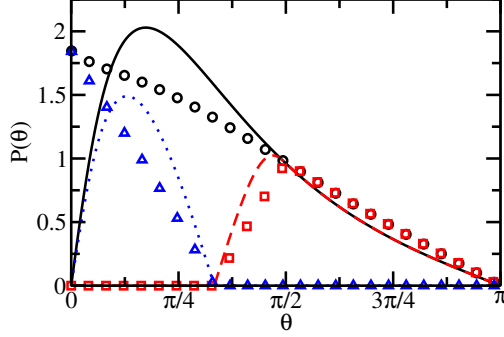


Figure 7.4: Angular distributions for three identical bosons at unitarity. The circles, triangles and squares show the angular distributions  $P_{\text{tot}}(\theta)$ ,  $P_{\text{min}}(\theta)$ , and  $P_{\text{max}}(\theta)$  for the model 2bZR; these distributions are identical to those for the models 2bZR+3bHC and 2bZR+3bRp. The solid, dotted, and dashed lines show the angular distributions  $P_{\text{tot}}(\theta)$ ,  $P_{\text{min}}(\theta)$ , and  $P_{\text{max}}(\theta)$  for the model 2bG.

of finding an angle of zero is zero and the angular distribution peaks at around  $0.17\pi$  or  $31^\circ$ . For the zero-range model, the angular distribution peaks at 0 and  $P_{\text{tot}}(0)$  is finite. This is because the zero-range boundary condition makes the probability to find two particles at the same position finite. A vanishing interparticle distance corresponds to a triangle in which one of the three angles  $\theta_{jkl}$  is zero. Since the angular distributions for the models 2bZR+3bZR and 2bG show distinctly different features, one might expect that the binding momentum ratios  $\kappa^{(1)}/\kappa^{(2)}$  for these two models also differ. The value of  $\kappa_3^{(1)}/\kappa_3^{(2)}$  for the model 2bG is 22.983, which differs by only 1.27% from that for the model 2bZR+3bZR. This indicates that it is insufficient to only evaluate the binding momentum ratios to judge how universal the system is. We note that the distribution  $P(\theta)$  for the ground state of the  $N = 3$  system with two-body Lenard-Jones interactions is quite similar to that for the ground state of the  $N = 3$  system with two-body Gaussian interactions [301].

We now consider the radial density  $\rho(r)$  ( $r$  is measured relative to the center of mass of the three-body system) for the models 2bZR+3bZR and 2bZR+3bRp with  $p = 6$ . The radial density  $\rho(r)$  is normalized such that  $4\pi \int_0^\infty \rho(r)r^2 dr = N$  and depends on the hyperradius and the hyperangles. The dashed and solid lines in Fig. 7.5 show the radial density  $\rho(r)$  for the models 2bZR+3bZR and 2bZR+3bRp with  $p = 6$ , respectively. For the latter, the

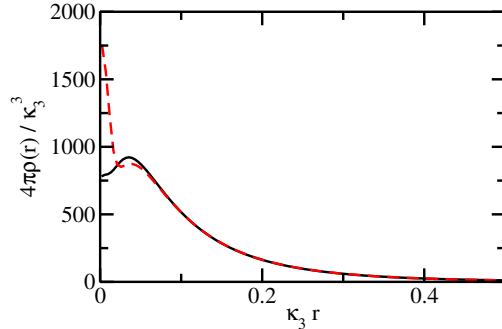


Figure 7.5: Radial density  $\rho(r)$  for three identical bosons at unitarity ( $r$  is measured relative to the center of mass of the three-body system). The dashed and solid lines show  $\rho(r)$  for the models 2bZR+3bZR and 2bZR+3bRp with  $p = 6$ , respectively.

ground state density is shown. The radial densities are scaled by their respective binding momentum  $\kappa_3$ . The solid and dashed lines agree well in the large  $r$  region and differ notably in the small  $r$  region. The deviation in the small  $r$  region comes from the fact that the hyperradial density for the model 2bZR+3bZR decays much slower for small  $R$  than that for the model 2bZR+3bRp. Note that even though the radial densities for the two models differ by about a factor of two in the small  $r$  region, the difference between the integrated contributions is small because the volume element contains an  $r^2$  factor.

### 7.3 $N$ -body clusters at unitarity: Overview of literature results

This section discusses various literature results for the energy of weakly-bound  $N$ -body droplets ( $N > 3$ ) at unitarity. The diamonds in Fig. 7.6(a) show the  $N$ -boson energy per particle  $E_N/N$  for the model 2bG as a function of  $N$  [1, 10, 290]. The energy per particle increases approximately linearly with  $N$  for  $N > 6$  (for smaller  $N$ , some deviations from the linear behavior exist). Based on the fact that the energy per particle, and correspondingly the binding momentum, scale linearly with  $N$  for the model 2bG, Gattobigio *et al.* [1] proposed an analytical form for the  $N$ -boson system with two-body zero-range interactions and fixed

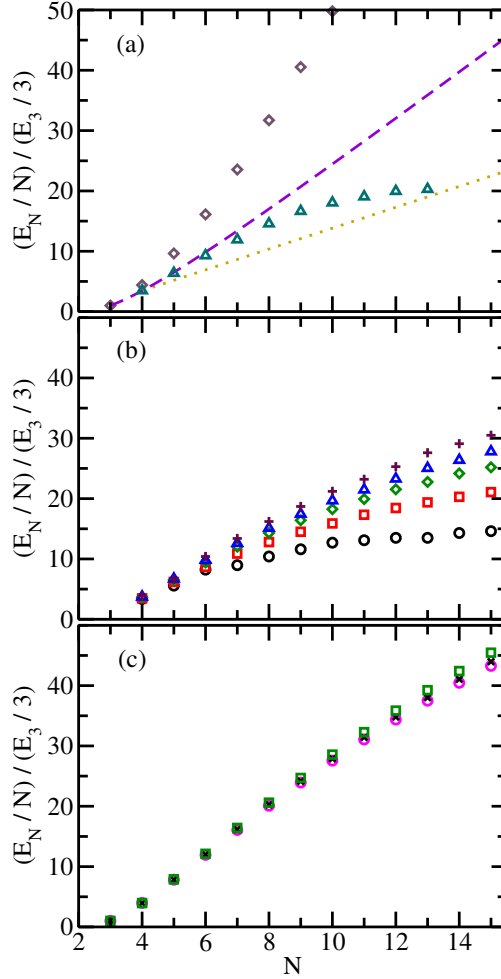


Figure 7.6: Energy per particle of  $N$ -boson clusters at unitarity. (a) Summary of literature results. The dashed and dotted lines show the analytical prediction by Gattobigio and Kievsky [1] and Nicholson [9], respectively. The triangles show the diffusion Monte Carlo (DMC) energies for a Hamiltonian with two-body square well interaction and repulsive three-body hardcore regulator [7]. The diamonds show the energy for the model 2bG [10]. (b) Summary of our PIMC calculations. The circles and pluses are for the model 2bZR+3bRp with  $p = 4$  and 8, respectively; the error bars (not shown) are of the order of the symbol sizes. The squares, diamonds, and triangles are for the model 2bZR+3bRp with  $p = 5, 6,$  and 7, respectively; the error bars (not shown) are smaller than the symbol sizes. (c) Summary of our calculations for two-body van der Waals models. The circles, crosses, and squares show our DMC results for the models 2bLJ, 2b10-6, and 2b8-6, respectively.

three-body parameter,

$$\frac{\kappa_N}{\kappa_3} = 1 + \left( \frac{\kappa_4}{\kappa_3} - 1 \right) (N - 3) \quad (7.4)$$

[see the dashed line in Fig. 7.6(a)]. The ratio  $\kappa_4/\kappa_3$  is not taken from the ground state calculations for the Gaussian two-body interaction model, for which  $\kappa_4/\kappa_3 = \sqrt{5.86}$ , but from Deltuva's calculations for highly excited four-body resonance states. Deltuva finds the universal ratio  $\kappa_4/\kappa_3 = \sqrt{4.61}$  [285]. Gattobigio *et al.*'s expression, converted to the energy, exhibits a leading order  $N^2$  and sub-leading order  $N$  dependence.

It should be noted that the ground state energy of the Hamiltonian with pairwise Gaussian interactions scales differently with  $N$  for  $N \gtrsim 10$  than that of Hamiltonian with pairwise interactions with short-range repulsion. For interactions with repulsive core, it is well-established that the energy per particle increases weaker than linear for  $N \gtrsim 10$  (see, e.g., the literature on helium and tritium droplets [302, 303]). Gattobigio *et al.* [290] noted that Eq. (7.4) applies not only to systems with zero-range interactions but also to systems with finite-range interactions in the regime where  $E/N$  is approximately proportional to  $N$  (e.g., to helium droplets with  $N \lesssim 10$ ). In this case, the ratio  $\kappa_4/\kappa_3$  for the finite-range potential is taken as input and the binding momentum for  $N > 4$  is predicted. We return to this discussion in Sec. 7.5.

Independent evidence for the leading-order  $N$  dependence of the energy per particle for the Hamiltonian with two-body zero-range interactions comes from lattice calculations for even  $N$  [9]. Assuming that the distribution of the two-body correlator is exactly log normal, Nicholson deduced an analytical expression for the energy per particle,  $E_N/N = (N/2 - 1)E_4/4$  [see the dotted line in Fig. 7.6(a)] [9]. To plot this expression, we used Deltuva's value of  $E_4/E_3 = 4.61$ . It should be noted that the coefficients predicted by Gattobigio *et al.* and Nicholson for the leading order  $N$  dependence differ by about a factor of 2.

A somewhat different  $N$ -dependence of the energy per particle was observed in the numerical calculations by von Stecher [see triangles in Fig. 7.6(a)] [7]. In fact, the idea to use a three-body regulator, as in our model 2bZR+3bRp, to make the ground state trimer large and Efimov-like was introduced in Ref. [7]. Von Stecher employed a model Hamiltonian with two-body square well potential with infinitely large two-body  $s$ -wave scattering length and three-body hardcore potential. For  $N \lesssim 10$ , the energy per particle increases approximately linearly with increasing  $N$ . For larger  $N$ , the triangles in Fig. 7.6(a) flatten. Reference [241] interpreted this as a turnover to a  $N^0$  dependence of the energy per particle. Such a behavior suggests a saturation of the density for large  $N$ . This saturation would be a consequence of the balance of the two-body attractive and three-body repulsive interactions.

The discussion above shows that the dependence of the energies tied to Efimov trimers is not well understood. Specifically, neither the functional form of the energy per particle nor the coefficients are agreed upon. In the following sections, we attempt to understand where the discrepancies of the literature results come from.

## 7.4 $N$ -body results at unitarity for the model 2bZR+3bRp

To calculate the  $N$ -boson energy for the Hamiltonian with interaction model 2bZR+3bRp, we apply the PIMC technique [19, 289]. The PIMC technique is an, in principle, exact finite-temperature method; the errors, which originate from the discretization of the imaginary time and the stochastic evaluation of integrals, can be reduced systematically. To obtain the ground state energy of the  $N$ -boson Hamiltonian, the PIMC approach has to be extended to the zero-temperature limit. Typically, this is achieved by the path integral ground state approach [19, 100]. Here, we pursue an alternative strategy. Namely, we work in the finite temperature regime where the thermal contribution to the energy is known and where the

Table 7.2: PIMC energies for the model 2bZR+3bRp for  $N = 4 - 15$ . Columns 2-4 show the scaled energy  $E_N/N/(E_3/3)$  for  $p = 5, 6$ , and  $7$ , respectively. The error bars (not explicitly reported) are around 3%.

$N$	2bZR+3bR5	2bZR+3bR6	2bZR+3bR7
4	3.46	3.64	3.73
5	6.19	6.53	6.70
6	8.69	9.42	9.81
7	10.9	12.0	12.6
8	12.8	14.3	15.1
9	14.5	16.4	17.5
10	15.9	18.3	19.7
11	17.3	20.0	21.5
12	18.4	21.5	23.3
13	19.4	22.8	25.0
14	20.3	24.2	26.4
15	21.1	25.2	27.8

structural properties of interest are not affected by the temperature. This approach was introduced and benchmarked in Ref. [10]. The basic idea is to place the droplet in a weak external harmonic confinement, whose angular frequency  $\omega$  is chosen such that the center of mass energy spectrum becomes discretized and the relative motion is unaffected by the trap. This requirement corresponds to  $|E_N| \gg \hbar\omega$ . Since the density of states of the harmonically trapped center of mass pseudoparticle is known analytically, the ground state energy  $E_N$  of the  $N$ -boson droplet in free space can be extracted from the finite-temperature energy [10, 289].

The circles, squares, diamonds, triangles, and pluses in Fig. 7.6(b) show the energy per particle for the model 2bZR+3bRp with  $p = 4, 5, 6, 7$ , and  $8$ , respectively, as a function of  $N$  (see also Table 7.2 and the Supplemental Material [304]). For each  $p$ , the energy per particle is scaled by the respective trimer energy per particle. For a fixed  $p$ , the energy per particle increases monotonically and smoothly as a function of  $N$ , i.e, even-odd effects, which have been observed in trapped and homogeneous two-component Fermi gases [209, 305, 306], are—if existent—smaller than our statistical error bars. For fixed  $N$ , the scaled energy per

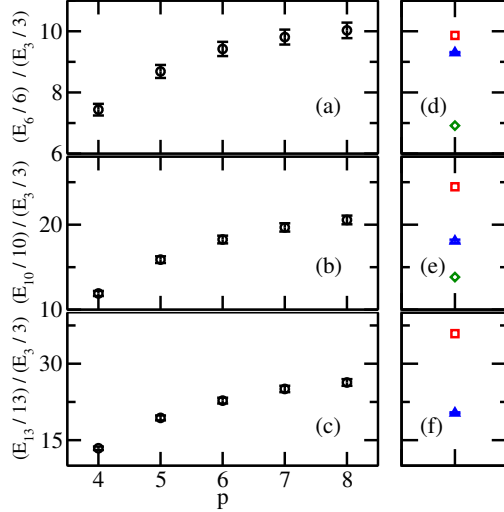


Figure 7.7: Comparison of our PIMC energies (left) and literature results (right) for selected  $N$ . Panels (a), (b), and (c) show our PIMC energy per particle for  $N$ -boson clusters interacting through the model 2bZR+3bRp as a function of  $p$  for  $N = 6, 10$ , and  $13$ , respectively. For comparison, panels (d), (e), and (f) show the energy per particle from the literature for the same  $N$ . The triangles, diamonds, and squares are from von Stecher [7], Nicholson [9], and Gattobigio *et al.* [1]. Since the work by Nicholson is restricted to even  $N$ , comparison for  $N = 13$  cannot be made.

particle increases with increasing  $p$  ( $p \geq 4$ ); this increase becomes smaller with increasing  $p$ . Similarly to von Stecher’s energy per particle [7] [triangles in Fig. 7.6(a)], the scaled energy per particle increases roughly linearly for smallish  $N$  and then flattens out for larger  $N$ . This effect is most pronounced for  $p = 4$  and  $5$ , where the flattening sets in around  $N = 8 - 10$ , and least pronounced for  $p = 8$ . The reason for the flattening is that the clusters develop, for sufficiently large  $N$ , more than one pair distance scale (see below for more details).

The circles in Fig. 7.7 replot the PIMC energy per particle for selected  $N$ . As the power  $p$  increases, the scaled energy approaches a constant. Based on our discussion in Sec. 7.2, the  $p \rightarrow \infty$  energy should coincide with the energy for the model 2bZR+3bHC. It is thus instructive to compare our scaled energies, extrapolated by eye to the  $p \rightarrow \infty$  limit, with those obtained by von Stecher [7], who employed a two-body square well potential and a three-body hardcore regulator [see triangles in Figs. 7.7(d)-7.7(f)]. We find that our  $p \rightarrow \infty$  energy per particle lies above von Stecher’s energy per particle by something like 10 – 20%,

20 – 30%, and 30 – 50% for  $N = 6, 10$ , and  $13$ , respectively. Since the three-body sectors are treated on consistent footing (3bRp $\rightarrow$ 3bHC as  $p \rightarrow \infty$ ), we speculate that the difference arises from the different two-body interactions. However, we did not perform calculations to confirm this and can thus not rule out other reasons. As can be seen from Fig. 7.7, Nicholson’s energy prediction lies notably below our large  $p$  energies while Gattobigio *et al.*’s prediction lies above our large  $p$  energies for  $N \gtrsim 8$ .

If the  $N$ -body energies were determined solely by a three-body parameter  $\kappa_3$ , the model 2bZR+3bRp for different  $p$  would yield the same scaled energies, i.e., the symbols in Fig. 7.6(b) would collapse to a single curve. The fact that they do not collapse indicates that the three-body parameter is not sufficient to predict the energy of the  $N$ -boson clusters, at least not for the models considered. To gain more insight into this, it is instructive to analyze the length scales of the model 2bZR+3bRp. Four length scales can be identified (see rows 3–6 of Table 7.3). (i) The characteristic length scale  $L_p$  of the three-body repulsive potential. (ii) The length scale  $\bar{L}_3$  defined by the three-body binding energy. (iii) The length scale  $\bar{L}_N$  defined by the energy of the cluster. And, (iv) the length scale  $\bar{l}_N$  associated with the energy per particle of the cluster. Inspection of the definitions given in Table 7.3 shows that  $\bar{L}_N$  and  $\bar{l}_N$  are not independent.

For  $p = 4$ –8, we find  $\bar{L}_3/L_p \approx 29.3, 28.8, 27.6, 26.6$ , and  $25.9$ , i.e., the trimer is significantly larger than the scale of the underlying repulsive three-body potential. This ensures, as discussed in Sec. 7.2, that the trimer ground state described by the model 2bZR+3bRp with  $p \geq 4$  exhibits the key characteristics of an Efimov state. It is instructive to alternatively think about the trimer size in terms of the average interparticle spacing  $\bar{r}$ . For trimers with  $p = 4$ –8, we find  $\bar{r}/L_p \approx 18.7, 18.5, 17.7, 17.1$ , and  $16.6$ .

For  $p = 6$ , we find that  $\bar{L}_N/L_p$  changes from 11.2 for  $N = 4$  to 8.37 for  $N = 5$  to 2.46 for  $N = 15$ . This suggests that the  $N$ -boson droplet “sees” increasingly more of the three-body regulator as  $N$  increases, i.e., that the dependence of  $E_N/N$  on  $p$  increases with increasing

Table 7.3: Summary of the definitions of length scales. The van der Waals length  $L_{\text{vdW}}$  is defined in Ref. [4].  $L_p$  for  $p = 6$  agrees with  $L_{\text{vdW}}$  if  $m$  is replaced by the reduced two-body mass  $m/2$ .

length scale	definition	description
$L_g$	$r_0$	characteristic length scale of the two-body Gaussian potential
$L_{\text{vdW}}$	$(\sqrt{mc_6}/\hbar)^{1/2}/2$	characteristic length scale of the two-body van der Waals potential
$L_p$	$[1/(p-2)\sqrt{2mC_p/\hbar}]^{2/(p-2)}$	characteristic length scale of the three-body repulsive potential
$\bar{L}_3$	$1/\kappa_3 = \hbar/\sqrt{m E_3 }$	length scale set by the three-body binding energy
$\bar{L}_N$	$1/\kappa_N = \hbar/\sqrt{m E_N }$	length scale set by the $N$ -body binding energy
$\bar{l}_N$	$\hbar/\sqrt{m E_N }/N = \sqrt{N}\bar{L}_N$	length scale set by the $N$ -body binding energy per particle
$\bar{r}$		average interparticle spacing
$\bar{R}$		average sub-three-body hyperradius

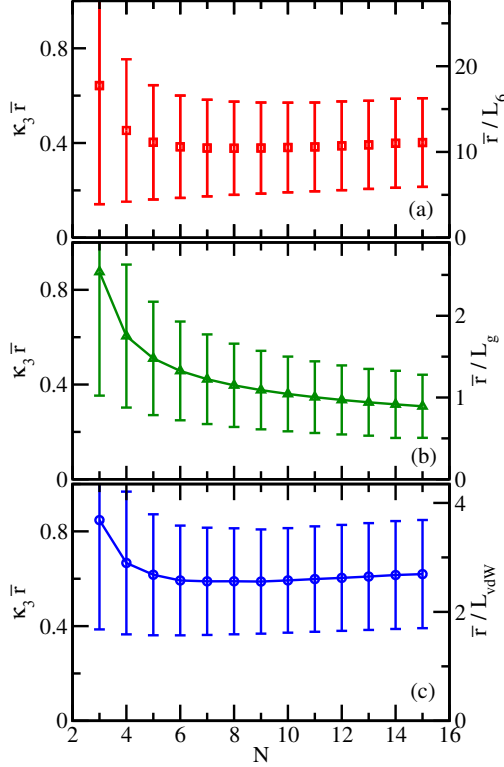


Figure 7.8: Expectation value  $\bar{r}$  of the pair distance as a function of  $N$  for  $N$ -boson systems interacting through various models. (a) The squares are for the model 2bZR+3bRp with  $p = 6$ . (b) The triangles are for the model 2bG. (c) The circles are for the model 2bLJ. The error bars show the variance of the pair distance. The pair distances are plotted using two different units: (i) the inverse three-body binding momentum (left axis) and (ii) the characteristic length scale of the model Hamiltonian (right axis).

$N$ . The length scale  $\bar{l}_N$ , in contrast, suggests a larger separation of scales; for  $N = 13$ , e.g., we have  $\bar{l}_N/L_p = 7.69$  for  $p = 4$  and  $\bar{l}_N/L_p = 6.85$  for  $p = 8$ . In fact, if  $E_N/N$  scales as  $N$ , then  $\bar{L}_N$  and  $\bar{l}_N$  scale as  $1/N$  and  $1/\sqrt{N}$ , respectively. If  $E_N/N$  scales as  $N^0$ , then  $\bar{L}_N$  and  $\bar{l}_N$  scale as  $1/\sqrt{N}$  and  $N^0$ , respectively. This implies that—unless the energy scales linearly (or even weaker) with  $N$  for large  $N$ —the properties of the  $N$ -boson droplets are expected to be notably affected by the choice of the three-body regulator.

Alternatively, one can consider the average interparticle distance  $\bar{r}$  and the average sub-three-body hyperradius  $\bar{R}$ . The squares in Fig. 7.8(a) show the average interparticle spacing  $\bar{r}$ , i.e., the expectation value of the pair distance, as a function of  $N$  in units of  $1/\kappa_3$  (left

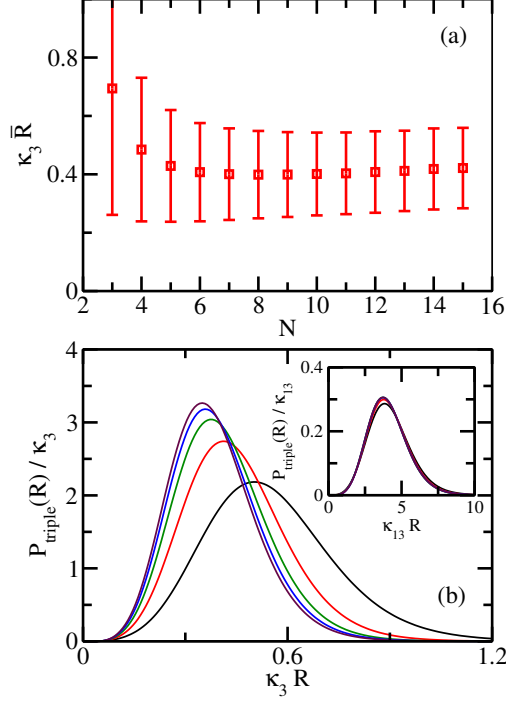


Figure 7.9: (a) Expectation value  $\bar{R}$  of the sub-three-body hyperradius (triple size) as a function of  $N$  for  $N$ -boson systems interacting through the model 2bZR+3bR6. The error bars show the variance of the triple size. (b) Triple distribution function  $P_{\text{triplet}}(R)$  for the  $N = 13$  cluster scaled using the three-body binding momentum  $\kappa_3$ . The solid lines from top to bottom at  $\kappa_3 R = 0.6$  are for the model 2bZR+3bRp with  $p = 4, 5, 6, 7,$  and  $8$ . The inset replots the triple distribution functions using the binding momentum  $\kappa_{13}$  of the  $N = 13$  droplet. In these units, the triple distribution functions for different  $p$  collapse.

axis) and in units of  $L_6$  (right axis) for the model 2bZR+3bRp with  $p = 6$ . The error bars indicate the variance  $\Delta r$  of the pair distance,  $\Delta r = \sqrt{\langle r^2 \rangle - \langle r \rangle^2}$ , where  $\langle \rangle$  indicates the quantum mechanical expectation value [307]. As the number of particles  $N$  increases, both the mean and variance of the pair distance are nearly constant. The mean and variance of the pair distance are about one order of magnitude larger than the internal length scale  $L_p$ . The relatively large variance of the Hamiltonian with model interaction 2bZR+3bRp implies that the clusters are diffuse and liquid-like. The squares in Fig. 7.9(a) show the average sub-three-body hyperradius  $\bar{R}$ , i.e., the expectation value of the triple size, as a function of  $N$  for the model 2bZR+3bRp with  $p = 6$ . The error bars indicate the variance. The mean and variance of the sub-three-body hyperradius behave similar to the mean and variance of

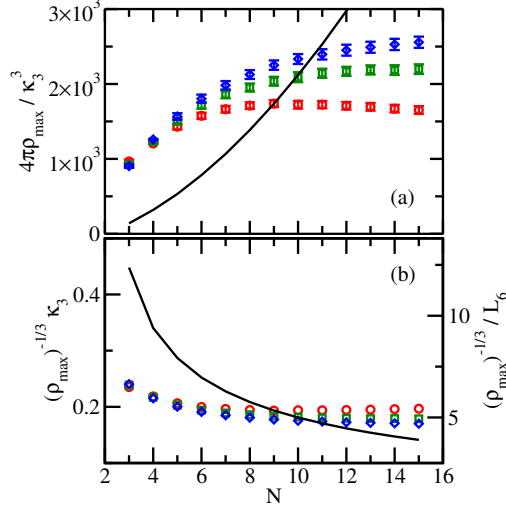


Figure 7.10: (a) Maximum density  $\rho_{\max}$  as a function of  $N$  for  $N$ -boson systems interacting through various models. The circles, squares, and diamonds are for the model 2bZR+3bRp with  $p = 5$  (lowest data set), 6, and 7 (highest data set), respectively. For comparison, the line is for the model 2bG. (b) Same data as in (a) but replotted as the minimum average interparticle distance  $(\rho_{\max})^{-1/3}$ . The right axis shows the data for the model 2bZR+3bR6 in units of  $L_6$ .

the pair distance.

The average pair distance and sub-three-body hyperradius are obtained by averaging over all possible pairs and triples regardless of whether or not the particles are close to each other. To get more “local” information, we calculate the maximum density and subsequently the closest pair distance. The circles, squares, and diamonds in Fig. 7.10(a) show the maximum  $\rho_{\max}$  of the radial density for the model 2bZR+3bRp with  $p = 5, 6$ , and 7, respectively, as a function of  $N$ . We find that unlike for  $N = 3$  (see Fig. 7.5), the radial density peaks at  $r = 0$  for  $N \geq 4$ . For all  $p$ , the maximum of the radial density is roughly a constant for the largest  $N$  considered. This constant depends—as the energy per particle—on the three-body regulator. The circles, squares, and diamonds in Fig. 7.10(b) show the smallest average pair distance for the model 2bZR+3bRp with  $p = 5, 6$ , and 7, respectively, as a function of  $N$ . The smallest average pair distance decreases with increasing  $N$  and approximately saturates for the largest  $N$  considered. The smallest average pair distance is only about five times

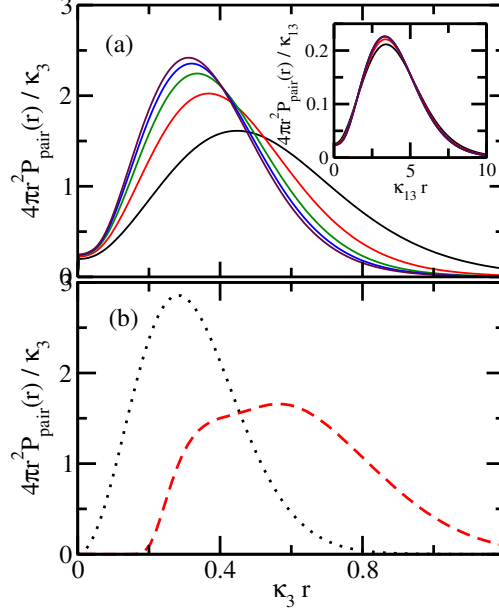


Figure 7.11: Scaled pair distribution function  $4\pi r^2 P_{\text{pair}}(r)$  for  $N = 13$  bosons interacting through various models. (a) The solid lines from top to bottom at  $\kappa_3 r = 0.8$  are for the model 2bZR+3bRp with  $p = 4-8$ , scaled using the three-body binding momentum  $\kappa_3$ . The inset replots the pair distribution functions scaled using the binding momentum  $\kappa_{13}$  of the  $N = 13$  droplet. In these units, the pair distribution functions for different  $p$  collapse. (b) The dashed and dotted lines show the scaled distribution functions for the models 2bLJ and 2bG, respectively, using the three-body binding momentum  $\kappa_3$ .

larger than the characteristic length scale  $L_p$  of the three-body regulator.

The above length scale discussion can be expanded by considering distribution functions. The scaled pair distribution function  $4\pi r^2 P_{\text{pair}}(r)$ , normalized according to  $4\pi \int_0^\infty r^2 P_{\text{pair}}(r) dr = 1$ , tells one the probability to find two particles at a distance  $r$  from each other. The lines from top to bottom at  $\kappa_3 r = 0.8$  in Fig. 7.11(a) show the scaled pair distribution function  $4\pi r^2 P_{\text{pair}}(r)$  for  $N = 13$  interacting through 2bZR+3bRp with  $p = 4-8$ . The amplitude at  $r = 0$  is finite and roughly independent of  $p$ . This makes sense as it is a signature of the two-body zero-range interactions, which enforce a finite amplitude at  $r = 0$ .

The triple distribution function  $P_{\text{triple}}(R)$ , normalized according to  $\int_0^\infty P_{\text{triple}}(R) dR = 1$ , tells one the probability to find three particles with sub-three-body hyperradius  $R$ . The solid lines from top to bottom at  $\kappa_3 R = 0.6$  in Fig. 7.9(b) show the triple distribution function

$P_{\text{triple}}(R)$  for  $N = 13$  interacting through 2bZR+3bRp with  $p = 4-8$ . The triple distribution functions are broad and structureless, indicating that the clusters are diffuse and liquid-like and that no small three-body sub-systems are formed.

Figures 7.9(b) and 7.11(a) show that the distribution functions  $P_{\text{pair}}(r)$  and  $P_{\text{triple}}(R)$  do not collapse if scaled by the three-body binding momentum  $\kappa_3$ . The distribution functions for  $p = 4$  are notably broader than those for  $p > 4$ . Figures 7.9(a) and 7.11(a) suggest that the distribution functions converge in the large  $p$  limit (i.e., in the three-body hardcore regulator limit). Similar behavior is observed for other  $N$ . As shown in the insets of Figs. 7.9(b) and 7.11(a), the distribution functions collapse to a very good approximation to a single curve if scaled by the binding momentum  $\kappa_N$  of the  $N$ -body droplet. This can be understood as a new type of universality, which is weaker than the ‘‘Efimov universality’’: The binding momentum  $\kappa_N$  allows one to collapse the distribution functions for the models 2bZR+3bRp for sufficiently large  $p$  but  $\kappa_N$  is not determined by  $\kappa_3$  (the latter would constitute ‘‘Efimov universality’’). The dominance of  $\kappa_N$  arises because the vast majority of the wave function amplitude is located in the classically forbidden region [308] (for pure zero-range interactions, the classically allowed region is reduced to a single point).

At the three-body level, the angular distribution functions for the models 2bZR+3bRp and 2bZR+3bZR coincide since the hyperradial and hyperangular degrees of freedom separate. This is not the case for  $N > 3$ , since the three-body regulator depends on the  $N$ -body hyperradius and a subset of the  $3N - 4$  hyperangles. For fixed  $N$ , we find that the dependence of the angular distribution functions  $P_{\text{tot}}(\theta)$  on the power  $p$  of the three-body regulator is small [much smaller than the dependence of  $P_{\text{pair}}(r)$  and  $P_{\text{triple}}(R)$  on  $p$ ]. Figure 7.12 shows the angular distribution function  $P_{\text{tot}}(\theta)$  for  $N$ -boson clusters interacting through 2bZR+3bR6 for various  $N$ . The lines from top to bottom at  $\theta = 0$  are for  $N = 5, 6, 7, 9$ , and 13. As the number of particles increases, the probability of finding triangles with small angles decreases but remains finite. Intuitively, this is because  $P_{\text{tot}}(\theta)$

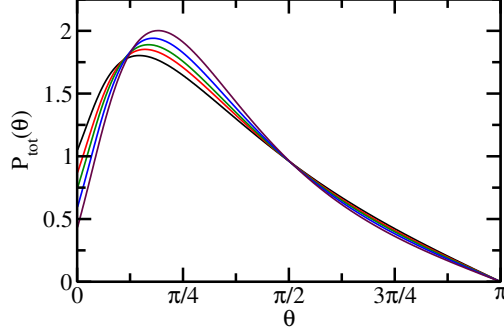


Figure 7.12: Angular distribution  $P_{\text{tot}}(\theta)$  for  $N$ -boson clusters interacting through the model 2bZR+3bRp with  $p = 6$ . The lines from top to bottom at  $\theta = 0$  are for  $N = 5, 6, 7, 9$ , and 13.

accounts for all the trimer configurations and not just the “closest trimers”.

Combining the information displayed in Figs. 7.6–7.12, the key characteristics of the ground state of  $N$ -boson droplets interacting through the model 2bZR+3bRp with  $p \geq 4$  can be summarized as follows: (i) The dependence of the energy and the structural properties on the three-body regulator decreases with increasing  $p$ ; (ii) the dependence of the energy and the structural properties on the three-body regulator cannot be explained by simple length scale arguments (the separation of scales is largest for the  $p = 4$  regulator and smallest for the  $p = 8$  regulator); (iii) the pair and triple distribution functions collapse to a very good approximation to a single curve if scaled by the binding momentum of the  $N$ -body system, suggesting that  $1/\kappa_N$  and not  $1/\kappa_3$  is the governing length scale for  $N > 3$ .

## 7.5 Results for other interaction models

We now compare the findings for  $N$ -boson systems interacting through the model 2bZR+3bRp with  $p = 4 - 8$  (see the previous section) with those for  $N$ -boson systems interacting through the models 2bG, 2bLJ, 2b10-6 and 2b8-6.

We start our discussion with the model 2bG, for which the energy per particle scales, to a very good approximation, linearly with  $N$  for  $N \gtrsim 6$  [see diamonds in Fig. 7.6(a)]. The

model 2bG has no repulsive core and is characterized by a single length scale, the width  $r_0$ . Using a simple variational Gaussian product wave function in the single-particle coordinates, one can readily show that the ground state energy scales as  $N^2$  and that the peak density increases quadratically with  $N$ . Indeed, our calculations shown in Figs. 7.8(b) and 7.10 for up to  $N = 15$  clearly support that the droplet shrinks with increasing  $N$ . As can be seen in Fig. 7.8(b), the average interparticle distance quickly decreases to a value smaller than  $r_0$ . We conclude that the  $N^2$  scaling of the energy for the model 2bG predominantly reflects the absence of a repulsive core in the potential energy and less so Efimov characteristics.

Next, we discuss the properties of the Hamiltonian interacting through the van der Waals models 2bLJ, 2b10-6, and 2b8-6. Our calculations at unitarity are performed using the same atomic mass and the same  $c_6$  coefficient for the three models while the short-range coefficients are tuned such that the dimer supports a single  $s$ -wave bound state with zero energy. For the three-body system, we find  $\kappa_3 L_{\text{vdW}} = 0.230$  for the model 2bLJ,  $\kappa_3 L_{\text{vdW}} = 0.233$  for the model 2b10-6, and  $\kappa_3 L_{\text{vdW}} = 0.245$  for the model 2b8-6, i.e., the three-body binding momentum depends weakly on the short-range scale of the two-body potential. The  $N$ -body energies per particle, in units of the three-body energy per particle, are summarized in Table 7.4. These energies are obtained by the DMC approach [124]. Dividing the  $N$ -body energies by the corresponding three-body energy, the energy per particle curves for the three van der Waals interaction models nearly collapse [see Fig. 7.6(c)]. This can be interpreted as van der Waals universality in the  $N$ -body sector. Due to the repulsive core, the energy per particle flattens around  $N = 10$ , indicating that the system starts to grow outward, i.e., starts to form a “second layer” (of course, the system is liquid-like and individual layers cannot be identified). Consistent with this, Fig. 7.8(c) shows that the average interparticle distance first decreases with increasing  $N$  and then slowly increases for  $N \gtrsim 8$ .

The dashed line in Fig. 7.11(b) shows the pair distribution function of the  $N = 13$  system interacting through the model 2bLJ. The amplitude in the small  $r$  region is suppressed

Table 7.4: DMC energies for the Hamiltonian with two-body van der Waals interactions for  $N = 4 - 15$ . Columns 2-4 show the scaled energy  $E_N/N/(E_3/3)$  for the models 2bLJ, 2b10-6, and 2b8-6, respectively. The error bars (not explicitly reported) are around 1%.

$N$	2bLJ	2b10-6	2b8-6
4	3.978	3.953	3.960
5	7.827	7.841	7.887
6	11.95	11.99	12.12
7	16.07	16.15	16.40
8	20.09	20.24	20.59
9	23.94	24.15	24.69
10	27.57	27.89	28.57
11	31.07	31.44	32.29
12	34.37	34.81	35.86
13	37.50	38.02	39.25
14	40.46	41.06	42.41
15	43.27	43.97	45.46

compared to the other interaction models considered due to the repulsive two-body core. Scaling  $r^2 P_{\text{pair}}(r)$  using  $\kappa_{13}$  (not shown) does not bring the pair distribution function for the model 2bLJ in agreement with the scaled pair distribution functions shown in the inset of Fig. 7.11(a) for the model 2bZR+3bRp with  $p = 4 - 8$ . This reflects the fact that a notably smaller fraction of the wave function amplitude resides in the classically forbidden region for the model 2bLJ than for the model 2bZR+3bRp with  $p = 4 - 8$ .

As already mentioned in Sec. 7.3, Eq. (7.4) applies, according to Ref. [290], not only to systems with zero-range interactions but also to systems with finite-range two-body interactions. To assess the applicability of Eq. (7.4), we denote the left hand side of Eq. (7.4) by  $\kappa_N^{\text{appr}}/\kappa_3$  and plot the normalized difference between  $\kappa_N^{\text{appr}}/\kappa_3$  and the exact  $\kappa_N/\kappa_3$ , as determined by our calculations. Circles and triangles in Fig. 7.13 shows the quantity  $(\kappa_N^{\text{appr}} - \kappa_N)/\kappa_N$  for the models 2bG and 2bLJ, respectively. For  $N = 3$  and  $N = 4$ , the normalized difference is zero by construction. For  $N > 4$ , the normalized difference is negative for the model 2bG and positive for the model 2bLJ. The deviations from the functional form proposed by Gattobigio *et al.* increase roughly linearly with  $N$  for the model 2bLJ, reaching 13% for

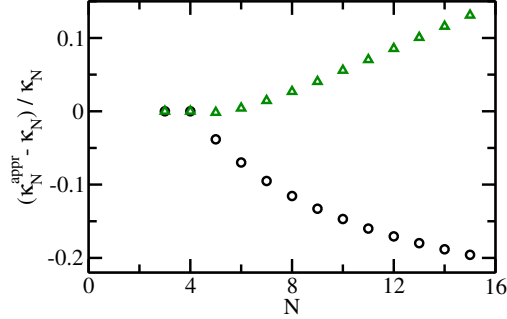


Figure 7.13: Assessing the applicability of Eq. (7.4) for  $N$ -boson systems with two-body finite-range interactions at unitarity. Circles and triangles show the normalized difference  $(\kappa_N^{appr} - \kappa_N)/\kappa_N$  for the models 2bG and 2bLJ, respectively, as a function of the number of particles  $N$ .

$N = 15$ , and non-linearly for the model 2bG, reaching  $-20\%$  for  $N = 15$ . Thus if high accuracy predictions are sought, then Eq. (7.4) should be used with caution.

## 7.6 Conclusions

This paper studied weakly-bound Bose droplets at unitarity. These systems are obtained by adding one atom at a time to an Efimov trimer or a weakly-bound trimer with Efimov characteristics. We carefully analyzed the three-body system and then studied larger systems.

The three-body ground state of the Hamiltonian with two-body zero-range interactions and repulsive three-body potential (model 2bZR+3bRp) is a nearly ideal Efimov state. The premise was (see also Ref. [7]) that this would allow us to determine the universal properties of droplets tied to a three-body Efimov state by studying  $N$ -body ground states. Somewhat surprisingly, we found dependences of the ground state cluster properties on the three-body regulator, suggesting that the ground states become less universal with increasing  $N$ . This is a somewhat disappointing finding as the treatment of  $N$ -body excited and resonance states, which are expected to exhibit universal characteristics, is a computationally much more demanding task. Yet, our study revealed a different type of universality for these model

Hamiltonian. We found that if the lengths are scaled by the  $N$ -body binding momentum, then the dependence on the three-body regulator diminishes notably. This suggests that the ground states of these systems are halo states [308], i.e., states whose amplitude is predominantly located in the classically forbidden region. The  $N$ -body binding momentum itself is, however, not—as it would be in the case of  $N$ -body Efimov universality—determined by the three-body binding momentum, especially not as  $N$  increases.

Hamiltonian with two-body van der Waals interaction at unitarity were also investigated. It was found that the energy per particle, if scaled by the three-body energy, collapses to a very good approximation to a single curve, suggesting that the short-range details of the van der Waals interaction impact the three- and higher-body sectors in a similar manner (i.e., the short-range details are to a very good approximation “taken out” by scaling by the three-body energy). The calculations presented were for Lenard-Jones and modified Lenard-Jones potentials; the latter potentials have a  $-c_6/r^6$  tail but a softer repulsive core at small distances than typical van der Waals interactions. We also performed calculations for (i) the true helium-helium potential scaled by an overall factor such that the  $s$ -wave scattering length is infinitely large and (ii) the true helium-helium potential with modified short-range potential such that the  $s$ -wave scattering length is infinitely large (these models were labeled He-He(scale) and He-He(arctan) in Ref. [301]). The energy per particle curves for these systems, which have a more complicated long-range tail, also collapse, to a very good approximation, to the same curves as those for 2bLJ, 2b10-6, and 2b8-6 if scaled by the three-body energy. The structural properties, specifically the pair and triple distribution functions, for the van der Waals systems do not collapse to the same curves as those for the 2bZR+3bRp model with  $p = 4 - 8$  if scaled using the  $N$ -body binding momentum  $\kappa_N$ , suggesting that a good portion of the wave function amplitude of the van der Waals systems is located in the classically allowed region.

In the future, it would be interesting to extend the calculations presented here to excited

and resonance states. We expect that the  $N$ -body properties become universal if sufficiently high excitations are being considered. In the four-body sector, e.g., Deltuva [285] extracted the universal numbers for  $\kappa_4/\kappa_3$  by going to high-lying resonance states (in this case, “high-lying” means third or higher resonance states). Extending calculations such as those conducted by Deltuva to  $N > 4$  is, however, challenging. It would also be interesting to extend the studies presented in this paper to finite  $s$ -wave scattering lengths and to Bose droplets with an impurity.

*Acknowledgement:* We thank Aksel Jensen for suggesting that we think about weakly-interacting systems in the context of classically allowed and classically forbidden regions. Support by the National Science Foundation (NSF) through Grant No. PHY-1415112 is gratefully acknowledged. This work used the Extreme Science and Engineering Discovery Environment (XSEDE), which is supported by NSF Grant No. OCI-1053575, and the WSU HPC.

## 7.7 Supplemental material

The PIMC energies reported in Table II of the main text were obtained using the “fourth-order propagator” described in Ref. [289] using a fixed time step of  $0.00045/E_3$ . Table 7.5 summarizes the energies obtained by extrapolating the energies obtained using the second-order propagator for 3-4 different time steps to the zero time step limit. Comparison of Table II of the main text and Table 7.5 shows that the energies for the model 2bZR+3bRp with  $p = 5 - 7$  obtained by the two different approaches agree within error bars (for  $p = 4$  and 8, we did not perform calculations using the fourth-order propagator).

Table 7.6 reports our DMC energies, obtained by extrapolating energies for 4-5 finite time steps to the zero time step limit, for the models He-He(scale) and He-He(arctan) [301].

Table 7.5: PIMC energies for the model 2bZR+3bRp for  $N = 5 - 15$ . Columns 2-6 show the scaled energy  $E_N/N/(E_3/3)$  for  $p = 4-8$ , respectively. The error bars (not explicitly reported) are around 6%.

$N$	2bZR+3bR4	2bZR+3bR5	2bZR+3bR6	2bZR+3bR7	2bZR+3bR8
5	5.58	6.36	6.67	6.70	6.63
6	8.22	8.90	9.53	10.2	10.4
7	8.96	11.1	12.1	12.3	13.4
8	10.4	12.9	14.8	15.6	16.2
9	11.6	14.8	16.8	18.1	18.7
10	12.7	16.5	17.9	20.0	21.2
11	13.1	18.0	20.5	22.0	23.2
12	13.5	18.7	22.0	23.8	25.3
13	13.5	20.0	23.5	25.7	27.6
14	14.3	20.9	24.8	27.6	29.1
15	14.6	21.5	25.9	28.9	30.5

Table 7.6: DMC energies for the Hamiltonian with two-body van der Waals interactions for  $N = 4 - 15$ . Columns 2-3 show the scaled energy  $E_N/N/(E_3/3)$  for the models He-He(scale) and He-He(arctan), respectively. The error bars (not explicitly reported) are around 1%.

$N$	He-He(scale)	He-He(arctan)
4	3.952	3.936
5	7.761	7.737
6	11.81	11.78
7	15.86	15.80
8	19.76	19.67
9	23.50	23.38
10	27.06	26.87
11	30.40	30.11
12	33.60	33.26
13	36.60	36.18
14	39.45	38.81
15	42.16	41.66

# Chapter 8

## Path integral Monte Carlo determination of the fourth-order virial coefficient for unitary two-component Fermi gas with zero-range interactions

by Yangqian Yan<sup>1</sup> and D. Blume<sup>1</sup>

<sup>1</sup>Department of Physics and Astronomy, Washington State University, Pullman,

Washington 99164-2814, USA

This work has been posted on the arXiv (arXiv:1602.02328)

and been submitted for publication

The unitary equal-mass Fermi gas with zero-range interactions constitutes a paradigmatic model system that is relevant to atomic, condensed matter, nuclear, particle, and astro physics. This work determines the fourth-order virial coefficient  $b_4$  of such a strongly-

interacting Fermi gas using a customized *ab initio* path integral Monte Carlo (PIMC) algorithm. In contrast to earlier theoretical results, which disagreed on the sign and magnitude of  $b_4$ , our  $b_4$  agrees within error bars with the experimentally determined value, thereby resolving an ongoing literature debate. Utilizing a trap regulator, our PIMC approach determines the fourth-order virial coefficient by directly sampling the partition function. An on-the-fly anti-symmetrization avoids the Thomas collapse and, combined with the use of the exact two-body zero-range propagator, establishes an efficient general means to treat small Fermi systems with zero-range interactions.

## 8.1 Introduction

Strongly-interacting Fermi gases manifest themselves in nature in different forms, from neutrons in neutron stars [309] to electrons in solids [310]. These systems are generally deemed difficult to treat theoretically because of the lack of a small interaction parameter. Superconductivity [311] and exotic states such as fractional quantum hall [312] or Fulde-Ferrell-Larkin-Ovchinnikov [313–315] states have been observed or predicted to exist in these systems. Ultracold Fermi gases [32, 203], which can nowadays be produced routinely in table-top experiments, are ideal for studying strongly-interacting systems since (i) the van der Waals interaction is short-ranged, which means that it can be approximated by a contact potential that introduces a single length scale, i.e., the  $s$ -wave scattering length  $a_s$ ; and (ii)  $a_s$  can be tuned at will utilizing Feshbach resonance techniques [4]. When  $a_s$  diverges, i.e., becomes infinitely large, the two-body contact potential does not define a length scale [316]. Just like the non-interacting Fermi gas, the properties of the unitary Fermi gas (Fermi gas with infinite  $a_s$ ) are determined by two length scales, the de Broglie wavelength  $\lambda$  and interparticle spacing  $\bar{r}$  [317].

At high temperature,  $\lambda$  is much smaller than  $\bar{r}$  and the grand canonical thermodynamic potential  $\Omega$  can be expanded in terms of the fugacity [87, 143]. The  $n^{\text{th}}$ -order expansion

or virial coefficient  $b_n$  is determined by the partition functions of clusters containing  $n$  or fewer fermions. Since all thermodynamic properties at high temperature can be derived from the virial coefficients  $b_n$  [89], the  $b_n$ 's are essential to understanding the normal state of strongly-interacting Fermi gases.

While the second- and third-order virial coefficients are well understood [87–89, 318–320], none of the theoretical calculations for  $b_4$  [2, 321–323] agree with the experimental data [11, 320]. This letter rectifies this situation: our theoretically determined  $b_4$  agrees with the experimentally determined value. Our approach uses a trap regulator and employs the path integral Monte Carlo (PIMC) technique [19, 133], with the contact interactions incorporated exactly via the two-body zero-range propagator [289]. The “post-antisymmetrization” [19, 133], traditionally employed in PIMC calculations, does not work for the system with zero-range interactions, since the sampled paths shrink due to the Thomas collapse, a well known phenomenon for bosons [41, 43], to a single point. For bosons, the three-body Thomas collapse is cured by introducing an additional scale or three-body parameter [41]. For fermions, such a three-body parameter is not needed since the Pauli exclusion principle acts as an effective three-body repulsion [71, 324]. Thus, rather than the standard “post-antisymmetrization”, we use an “on-the-fly scheme” [134, 325], which antisymmetrizes at each imaginary time step. While the anti-symmetrization is, within Monte Carlo frameworks, usually associated with the infamous Fermi sign problem [97–99], in our case it stabilizes the simulation and affords the use of significantly smaller number of time slices than the use of finite-range interactions would. Our approach reproduces the trap regulated  $b_3$  over a wide temperature range. We determine the trap regulated  $b_4$  as a function of the temperature  $T$ . In the low-temperature regime, we find agreement with Ref. [2]. We separate the spin-balanced ( $b_{2,2}/2$ ) and spin-imbalanced ( $b_{3,1}$ ) sub-cluster contributions to  $b_4$ ,  $b_4 = b_{3,1} + b_{2,2}/2$ , and find  $b_{2,2} < 0$  and  $b_{3,1} > 0$  at all considered temperatures.  $b_{2,2}$  dominates at low  $T$  and  $b_{3,1}$  at high  $T$ . Converting the trap regulated virial coefficient  $b_4$  to

that of the homogeneous system using the local density approximation (LDA) [88], we find agreement with the experimentally determined values [11, 320].

## 8.2 Virial expansion framework

The  $n^{\text{th}}$ -order virial coefficient  $b_n^{\text{hom}}$  of the homogeneous system at unitarity is related to the high-temperature limit  $b_n^0$  of the harmonically trapped unitary system via  $b_n^{\text{hom}} = n^{3/2}b_n^0$  [88]. To determine  $b_n^0$ , we calculate the virial coefficient  $b_n$  of the harmonically trapped system for various temperatures and then take the  $T \rightarrow \infty$  limit. The trap Hamiltonian  $H(n_1, n_2)$  for  $n_1$  particles of species 1 and  $n_2$  particles of species 2 with interspecies  $s$ -wave interactions reads

$$H(n_1, n_2) = \sum_{j=1}^{n_1+n_2} \left( \frac{-\hbar^2}{2m} \nabla_{\mathbf{r}_j}^2 + \frac{1}{2} m \omega^2 \mathbf{r}_j^2 \right) + \sum_{i=1}^{n_1} \sum_{j=n_1+1}^{n_1+n_2} V_{2b}(\mathbf{r}_i - \mathbf{r}_j), \quad (8.1)$$

where  $m$  denotes the mass of the particles,  $\mathbf{r}_j$  the position vector of the  $j^{\text{th}}$  particle,  $\omega$  the angular trapping frequency, and  $V_{2b}$  the regularized Fermi-Huang pseudopotential with infinite  $a_s$  [3]. The grand canonical thermodynamic potential  $\Omega$  can be written in terms of the fugacities  $z_i$  of species  $i$ ,

$$\Omega = -k_B T \ln \left( \sum_{n_1=0}^{\infty} \sum_{n_2=0}^{\infty} Q_{n_1, n_2} z_1^{n_1} z_2^{n_2} \right), \quad (8.2)$$

where  $z_i$  is equal to  $\exp[\mu_i/(k_B T)]$ ,  $\mu_i$  is the chemical potential of species  $i$ , and  $Q_{n_1, n_2}$  is the canonical partition function for  $H(n_1, n_2)$ ,

$$Q_{n_1, n_2} = \text{Tr} \exp [-H(n_1, n_2)/(k_B T)]. \quad (8.3)$$

Here,  $\text{Tr}$  is the trace operator. Defining  $\Delta\Omega = \Omega - \Omega^{\text{ni}}$ , where  $\Omega^{\text{ni}}$  is the grand canonical potential of the non-interacting system, and Taylor expanding around  $z_1 = z_2 = 0$  [326, 327], one finds

$$\Delta\Omega = -k_B T Q_{1,0} \left( \sum_{n_1=1}^{\infty} \sum_{n_2=1}^{\infty} b_{n_1, n_2} z_1^{n_1} z_2^{n_2} \right). \quad (8.4)$$

For spin-balanced systems,  $z_1$  and  $z_2$  are equal and Eq. (8.4) reduces to

$$\Delta\Omega = -2k_B T Q_{1,0} \left( \sum_{n=2}^{\infty} b_n z^n \right), \quad (8.5)$$

where  $b_2 = b_{1,1}/2$ ,  $b_3 = (b_{1,2} + b_{2,1})/2$ , and  $b_4 = (b_{1,3} + b_{3,1} + b_{2,2})/2$  (note, one has  $b_{2,1} = b_{1,2}$  and  $b_{3,1} = b_{1,3}$ ). It is convenient to write the virial coefficients  $b_{n_1, n_2}$  as

$$b_{n_1, n_2} = \Delta b_{n_1, n_2} + b_{n_1, n_2}^{\text{ref}}, \quad (8.6)$$

where  $b_{n_1, n_2}^{\text{ref}}$  is determined by the virial coefficients  $b_{j_1, j_2}$  and the canonical partition functions  $Q_{j_1, j_2}$  with  $j_1 + j_2 < n_1 + n_2$ . The term  $\Delta b_{n_1, n_2} = (Q_{n_1, n_2} - Q_{n_1, n_2}^{\text{ni}})/Q_{1,0}$ , where  $Q_{n_1, n_2}^{\text{ni}} = Q_{n_1, 0} Q_{0, n_2}$ , in contrast, accounts for the “new” physics introduced by the interacting  $(n_1, n_2)$  clusters [328].

### 8.3 Contradicting literature results for $b_4$

Two independent experiments find consistent values for the fourth-order virial coefficient, namely,  $b_4^{\text{hom}} = 0.096(15)$  [320] and  $0.096(10)$  [11], or  $b_4^0 = 0.01200(188)$  and  $b_4^0 = 0.01203(125)$ . The theoretical literature results, however, disagree with these experimental results [329], reflecting the fact that the fourth-order problem is highly non-trivial analytically and numerically. Using a sum-over-states approach with an energy cutoff, Ref. [2] obtained the low-temperature behavior of  $b_4$ . Assuming a monotonic temperature depen-

dence and extrapolating to the  $T \rightarrow \infty$  limit, Ref. [2] obtained  $b_4^0 = -0.0020(5)$ . It was concluded that more four-body energies would need to be calculated explicitly to obtain  $b_4$  reliably at high temperature. Applying a conjecture inspired by analytical three-body results, Refs. [322, 323] found  $b_4^0 = -0.007875(125)$ . Last, a diagrammatic approach [321], which included only a subset of the four-body free-space diagrams, obtained  $b_4^{\text{hom}} = 0.06$  or  $b_4^0 = 0.0075$ .

## 8.4 Customized PIMC algorithm

$\Delta b_{n_1, n_2}$  is determined by the partition function  $Q_{n_1, n_2}$  of the interacting  $(n_1, n_2)$  system ( $Q_{n_1, n_2}$  is not known in general) and the partition function  $Q_{n_1, n_2}^{\text{ni}}$  of the non-interacting  $(n_1, n_2)$  system ( $Q_{n_1, n_2}^{\text{ni}}$  is known analytically). We calculate the ratio of the partition functions  $Q_{n_1, n_2}^{\text{ni}}/Q_{n_1, n_2}$  using the PIMC technique. Specifically, the simulation generates configurations according to  $Q_{n_1, n_2}$  and accumulates the ratio  $Q_{n_1, n_2}^{\text{ni}}/Q_{n_1, n_2}$  as a weight. The reason for using the partition function of the unitary Fermi gas and not that of the non-interacting gas as the “guiding function” is the following. The probability density to find two unlike particles with vanishing interparticle spacing is finite at unitarity and zero in the non-interacting limit. If we used  $Q_{n_1, n_2}^{\text{ni}}$  as the guiding function, configurations in which two unlike particles are at the same spatial position would be absent and the standard deviation of  $Q_{n_1, n_2}/Q_{n_1, n_2}^{\text{ni}}$  would be infinite, rendering the expectation value meaningless [330].

In the PIMC formulation, the partition function  $Q_{n_1, n_2}^{\text{boltz}}(\beta)$  for Boltzmann particles (no exchange symmetries) at inverse temperature  $\beta$ ,  $\beta = (k_B T)^{-1}$ , is written in terms of a product over density matrices at imaginary time  $\tau$ ,

$$Q_{n_1, n_2}^{\text{boltz}}(\beta) = \int \dots \int \prod_{i=1}^N \rho(\mathbf{R}_i, \mathbf{R}_{i+1}; \tau) d\mathbf{R}_1 \dots d\mathbf{R}_N, \quad (8.7)$$

where  $\mathbf{R}_i$  collectively denotes the particle configurations at time slice  $i$ ,  $\mathbf{R}_N = \mathbf{R}_1$ , and

$N = \beta/\tau$ . For the two-component Fermi gas, the standard PIMC approach writes the partition function as  $Q_{n_1, n_2} = \mathcal{A}Q_{n_1, n_2}^{\text{boltz}}$ , where  $\mathcal{A}$  is the anti-symmetrizer [19, 331]. For the two-component Bose gas, the anti-symmetrizer  $\mathcal{A}$  is replaced by the symmetrizer  $\mathcal{S}$ .  $\mathcal{A}$  and  $\mathcal{S}$  contain the same number and types of terms; however, while all terms in  $\mathcal{S}$  enter with a plus sign,  $\mathcal{A}$  contains alternating plus and minus signs. Since the symmetrizer and anti-symmetrizer are, in the standard PIMC approach, evaluated stochastically, the two-component Fermi and Bose gases are simulated using the same paths. Expectation values, however, are accumulated with plus and minus signs for fermions and with plus signs only for bosons. We refer to this standard approach as post-symmetrization. The bosonic system with interspecies two-body zero-range interactions but without a three-body regulator would collapse to a single point; this is the well-known Thomas collapse [43]. Correspondingly, the fermionic paths would also collapse, rendering the simulation meaningless. To get around this problem, we developed a customized on-the-fly anti-symmetrization scheme, which explicitly anti-symmetrizes the density matrix at each imaginary time step,

$$Q_{n_1, n_2}(\beta) = \int \dots \int \prod_{i=1}^N \mathcal{A}\rho(\mathbf{R}_i, \mathbf{R}_{i+1}; \tau) d\mathbf{R}_1 \dots d\mathbf{R}_N. \quad (8.8)$$

The observable is then calculated using

$$\frac{Q_{n_1, n_2}^{\text{ni}}}{Q_{n_1, n_2}} = \left\langle \prod_{i=1}^N \frac{\mathcal{A}\rho^{\text{ni}}(\mathbf{R}_i, \mathbf{R}_{i+1}; \tau)}{\mathcal{A}\rho(\mathbf{R}_i, \mathbf{R}_{i+1}; \tau)} \right\rangle, \quad (8.9)$$

where  $\rho^{\text{ni}}$  denotes the density matrix for the non-interacting system and  $\langle \dots \rangle$  the thermal average using paths generated for the unitary Fermi gas using the on-the-fly anti-symmetrization scheme. Our simulation uses the pair-product approximation [19, 329] with the exact two-body density matrix for zero-range interactions. The on-the-fly scheme employed here is related to earlier works [325, 332], which anti-symmetrized, as we do, at each time slice. The key difference is that we employ a density matrix that accounts for the

interactions while the earlier works employed the non-interacting density matrix together with the Trotter (or improved Trotter) formula.

The on-the-fly anti-symmetrization scheme treats the  $n_1!n_2!$  permutations explicitly at each time slice, eliminating the need of the standard stochastic “permute move”. As a consequence, the scheme is computationally prohibitively demanding for large systems. For small systems, however, it is quite efficient for three reasons: (i) The number of permutations is manageable for small  $n_1 + n_2$ . (ii) The use of the zero-range interactions eliminates the need to perform calculations for several different ranges of the underlying two-body potential. (iii) Compared to finite-range interactions [10], the number of time slices needed to reach convergence for the zero-range interacting systems considered here is rather small; e.g., our scheme yields  $Q_{3,1}^{\text{ni}}/Q_{3,1}$  at  $E_{\text{ho}}/(k_B T) = 0.8$  with 0.1% error using only  $N = 9$  imaginary time slices (here,  $E_{\text{ho}} = \hbar\omega$ ). Within our approach, the key challenge in determining  $b_4$  reliably at high temperature comes from the fact that  $\Delta b_{2,2}$ ,  $\Delta b_{3,1}$ ,  $b_{2,2}^{\text{ref}}$ , and  $b_{3,1}^{\text{ref}}$  diverge, to leading order, as  $(k_B T/E_{\text{ho}})^6$ . This implies that  $b_{2,2}$  and  $b_{3,1}$  are, at high temperature, obtained by adding two numbers of opposite sign and nearly equal magnitude. Thus, to obtain reliable values at high temperature, we need to determine our observables with high accuracy. In practice, our available computer time limits us to  $k_B T \leq 2E_{\text{ho}}$  for the (2,2) and (3,1) systems.

## 8.5 PIMC results

To benchmark our customized PIMC algorithm, we apply it to the (2,1) system at unitarity, for which  $Q_{2,1}^{\text{ni}}/Q_{2,1}$  and  $b_3$  can be calculated with high accuracy for all temperatures using the sum-over-states approach [88]. As an example, circles in Fig. 8.1(a) show the quantity  $Q_{2,1}^{\text{ni}}/Q_{2,1}$  for  $k_B T = E_{\text{ho}}$ , obtained using our PIMC algorithm, as a function of the imaginary time step  $\tau$ . The  $\tau$  considered correspond to between  $N = 4$  and 10 time slices. The simulation is exact in the  $\tau \rightarrow 0$  (or equivalently,  $N \rightarrow \infty$ ) limit. To extrapolate to the

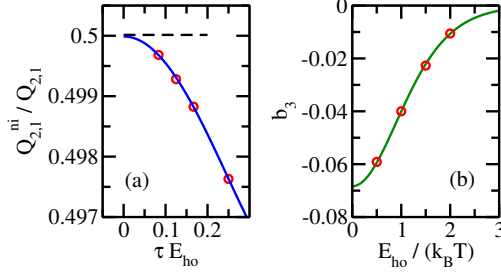


Figure 8.1: Benchmarking our PIMC results (circles) for the (2,1) system at unitarity through comparison with sum-over-states results. (a) The observable  $Q_{2,1}^{\text{ni}}/Q_{2,1}$  as a function of the imaginary time step  $\tau$  at  $k_B T = E_{\text{ho}}$ . The circles show our PIMC results. The error bars (not shown) are smaller than the symbol size. The solid line shows the fourth-order polynomial fit of the form  $a + b\tau^2 + c\tau^4$ . The dashed line shows the sum-over-states results. (b)  $b_3$  as a function of  $1/(k_B T)$ . The circles show our PIMC results while the solid line shows the sum-over-states results.

$\tau \rightarrow 0$  limit, we fit a fourth-order polynomial of the form  $a + b\tau^2 + c\tau^4$  to the PIMC data [solid line in Fig. 8.1(a)]. Our extrapolated result of 0.499989(26) agrees within error bars with the value of 0.500014 [dashed line in Fig. 8.1(a)] obtained by the sum-over-states approach. Using the extrapolated  $\tau \rightarrow 0$  values for  $Q_{2,1}^{\text{ni}}/Q_{2,1}$  at various temperatures, we obtain  $b_3$  as a function of  $T$  [circles in Fig. 8.1(b)]. The agreement with the sum-over-states results [solid line in Fig. 8.1(b)] is excellent for all  $T$  considered, demonstrating the reliability and accuracy of our PIMC approach.

We now discuss the determination of  $b_4$ . The extrapolation of the raw data to the  $\tau \rightarrow 0$  limit is discussed in the supplemental material [329]. Circles in Figs. 8.2(a) and 8.2(b) show our PIMC results for  $b_{3,1}$  and  $b_{2,2}$ , respectively, as a function of the inverse temperature. At low temperature, the PIMC results agree with the sum-over-states results (solid lines), obtained using the data provided in Ref. [2]. At all temperatures,  $b_{3,1}$  is positive and  $b_{2,2}$  is negative. To obtain  $b_{3,1}^0$  and  $b_{2,2}^0$ , we fit the data points for the four highest temperatures to the form  $a + b[E_{\text{ho}}/(k_B T)]^2$ . The dashed lines in Figs. 8.2(a) and 8.2(b) show the fits. Since the data points at  $k_B T = 2E_{\text{ho}}$  have much larger error bars than those at lower temperatures, the data points contribute comparatively little to the fit, which weighs each data point by the inverse of the square of its error bar. We find  $b_{3,1}^0 = 0.0212(8)$  and  $b_{2,2}^0/2 = -0.0115(8)$ , where

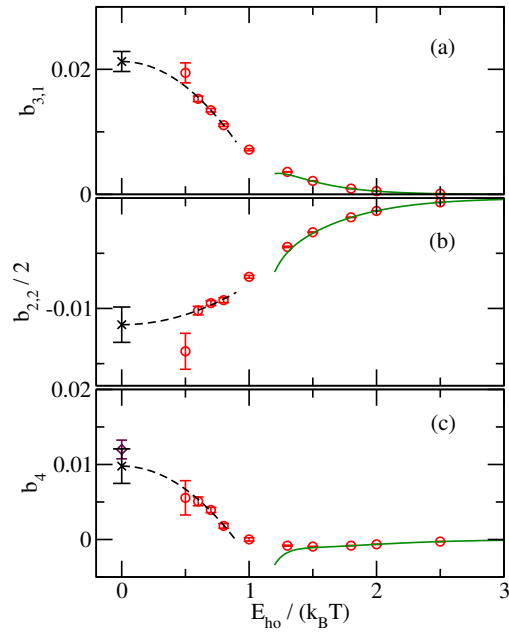


Figure 8.2: PIMC determination of the fourth-order virial coefficient. Circles in panels (a), (b), and (c) show  $b_{3,1}$ ,  $b_{2,2}/2$ , and  $b_4$ , respectively, determined by our PIMC approach. The crosses in (a) and (b) show the  $T \rightarrow \infty$  limit of the two-parameter fit (dashed line) to the PIMC data at the four highest temperatures. The dashed line and the cross in (c) show the sum of the fits from (a) and (b). The error bar in (c) is obtained by error propagation. The diamond with error bar shows the experimental result from Ref. [11].

the error bars reflect the uncertainty of the fit. We unfortunately do not have sufficiently many data to include a  $(k_B T)^{-4}$  term in the fit. Since the inclusion of a  $(k_B T)^{-4}$  term in the fit could alter the  $T \rightarrow \infty$  result, we add a systematic error of 0.0008 to  $b_{3,1}^0$  and  $b_{2,2}^0/2$ , yielding  $b_{3,1}^0 = 0.0212(16)$  and  $b_{2,2}^0/2 = -0.0115(16)$  [crosses in Figs. 8.2(a) and 8.2(b)]. To obtain  $b_4$  [see Fig. 8.2(c)], we combine  $b_{3,1}$  and  $b_{2,2}$ . Specifically, the circles and the fit are obtained by adding the data of Figs. 8.2(a) and 8.2(b) while the cross at  $T \rightarrow \infty$  is obtained using standard error propagation.  $b_4$  displays an interesting temperature dependence: It is negative at low temperature due to the dominance of  $b_{2,2}$ , vanishes at  $k_B T \approx E_{\text{ho}}$  due to a cancellation of  $b_{3,1}$  and  $b_{2,2}/2$ , and is positive at high temperature due to the dominance of  $b_{3,1}$ . Our results resolve the discrepancy of the sign of  $b_4$  between Ref. [2] and the experiments [11, 320]. Our extrapolated  $b_4$  at infinite temperature is  $b_4^0 = 0.0098(23)$ , which agrees with the experimental results of  $b_4^0 = 0.01203(125)$  [11] [diamond in Fig. 8.2(c)] and  $b_4^0 = 0.01200(188)$  [320]. Using the LDA, we find  $b_4^{\text{hom}} = 0.078(18)$ .

We now compare our results for  $b_{3,1}^0$  and  $b_{2,2}^0$  with the literature. The diagrammatic approach [321] yields  $b_{3,1}^0 = 0.025$ , which is within 2.5 standard deviations of our value, and  $b_{2,2}^0/2 = -0.018$ , which differs by a factor of about 1.5 (or many standard deviations) from our value. This comparison suggests that the convergence of the diagrammatic approach is slower for the (2,2) system than for the (3,1) system. The conjecture-based approach [322, 323] yields  $b_{3,1}^0 = 0.02297(4)$ , which agrees within error bars with our value, and  $b_{2,2}^0/2 = -0.0309(1)$ , which differs by about a factor of 3 from our value. While the conjecture put forward in Refs. [322, 323] is clearly invalidated for the (2,2) system, it remains an open question if the agreement observed here for the (3,1) system should be interpreted as supporting the conjecture or as being accidental.

## 8.6 Conclusion

This letter presented the PIMC determination of the fourth-order virial coefficient of the trapped unitary two-component Fermi gas. Our extrapolated infinite temperature result was found to agree with experiments within error bars, which, to the best of our knowledge, is the first numerical confirmation of the experimental determination of  $b_4$ . The customized PIMC scheme, which allows for the treatment of Fermi gases with zero-range interactions, can be applied to a variety of other situations. Since the zero-range density matrix can be constructed for arbitrary  $s$ -wave scattering length  $a_s$ , the scheme can be used to study the finite-temperature characteristics of the BEC-BCS crossover of few-body Fermi gases. Moreover, the algorithmic developments can be integrated into PIMC ground state calculations, providing a viable alternative to basis set expansion approaches.

*Acknowledgement:* We are grateful to Kevin M. Daily for valuable correspondence. Support by the National Science Foundation (NSF) through Grant No. PHY-1415112 is gratefully acknowledged. This work used the Extreme Science and Engineering Discovery Environment (XSEDE), which is supported by NSF Grant No. OCI-1053575, and the WSU HPC.

## 8.7 Supplemental material

The notation employed in this Supplemental Material follows that introduced in the main text.

### 8.7.1 Literature values of $b_4$

Table 8.1 summarizes the literature results for the fourth-order virial coefficient. The non-interacting contribution to the total fourth-order virial coefficient  $b_4^{\text{hom,tot}}$  of the homogeneous

system is given by

$$b_n^{\text{hom,ni}} = (-1)^{n+1}/n^{5/2}; \quad (8.10)$$

the interacting part of the fourth-order virial coefficient  $b_4^{\text{hom}}$  of the homogeneous system is defined through

$$b_n^{\text{hom}} = b_n^{\text{hom,tot}} - b_n^{\text{hom,ni}}. \quad (8.11)$$

The interacting part of the fourth-order virial coefficient  $b_4^0$  of the harmonically trapped system at high temperature and  $b_4^{\text{hom}}$  are related via (see also the main text),

$$b_n^{\text{hom}} = n^{3/2}b_n^0. \quad (8.12)$$

### 8.7.2 Pair product approximation and zero-range density matrix

Equation (9) of the main text writes the observable  $Q_{n_1,n_2}^{\text{ni}}/Q_{n_1,n_2}$  in terms of the density matrices  $\rho^{\text{ni}}(\mathbf{R}_i, \mathbf{R}_{i+1}; \tau)$  and  $\rho(\mathbf{R}_i, \mathbf{R}_{i+1}; \tau)$  of the non-interacting and unitary  $(n_1, n_2)$ -particle systems. To evaluate the density matrix by the PIMC approach, we use the pair product

Table 8.1: Summary of literature results. The value reported in the respective reference is underlined. The conversion to other “representations” is done using Eqs. (8.10)-(8.12). The column labeled “Ref.” refers to the bibliography of the main text.

$b_4^{\text{hom}}$	$b_4^{\text{hom,tot}}$	$b_4^0$	Ref.	comment
<u>0.096(15)</u>	0.065(15)	0.01200(188)	[320]	experiment
<u>0.096(10)</u>	<u>0.065(10)</u>	0.01203(125)	[11]	experiment
-0.016(4)	-0.04725(40)	<u>-0.0020(5)</u>	[2]	sum-over-states approach
<u>0.06</u>	0.02875	<u>0.0075</u>	[321]	diagrammatic
<u>-0.063(1)</u>	-0.09425(10)	-0.007875(125)	[322]	3-body inspired conjecture

approximation [19],

$$\rho(\mathbf{R}, \mathbf{R}'; \tau) \approx \left( \prod_{j=1}^{n_1+n_2} \rho^{\text{sp}}(\mathbf{r}_j, \mathbf{r}'_j; \tau) \right) \times \left( \prod_{j=1}^{n_1} \prod_{k=n_1+1}^{n_1+n_2} \bar{\rho}^{\text{rel}}(\mathbf{r}_j - \mathbf{r}_k, \mathbf{r}'_j - \mathbf{r}'_k; \tau) \right), \quad (8.13)$$

where  $\rho^{\text{sp}}(\mathbf{r}, \mathbf{r}'; \tau)$  is the single-particle density matrix [19],

$$\rho^{\text{sp}}(\mathbf{r}, \mathbf{r}'; \tau) = a_{\text{ho}}^{-3} [2\pi \sinh(\tau \hbar \omega)]^{-3/2} \times \exp\left(-\frac{(\mathbf{r}^2 + \mathbf{r}'^2) \cosh(\tau \hbar \omega) - 2\mathbf{r} \cdot \mathbf{r}'}{2 \sinh(\tau \hbar \omega) a_{\text{ho}}^2}\right), \quad (8.14)$$

and  $\bar{\rho}^{\text{rel}}(\mathbf{r}, \mathbf{r}'; \tau)$  is the reduced pair density matrix of the relative two-body problem with zero-range interaction [289],

$$\bar{\rho}^{\text{rel}}(\mathbf{r}, \mathbf{r}'; \tau) = 1 + \frac{2\hbar^2\tau}{mrr'} \exp\left(-\frac{m(rr' + \mathbf{r} \cdot \mathbf{r}')}{2\hbar^2\tau}\right). \quad (8.15)$$

The density matrix  $\rho^{\text{ni}}$  of the non-interacting system is given by Eq. (8.13) with  $\bar{\rho}^{\text{rel}}$  replaced by 1.

### 8.7.3 Extrapolation to the $\tau \rightarrow 0$ limit and selected raw data

As mentioned in the main text, to determine  $b_n$  with comparable percentage accuracy at all temperatures,  $Q_{n_1, n_2}^{\text{ni}}/Q_{n_1, n_2}$  has to be determined with increasing percentage accuracy with increasing temperature. To ensure that our results are free of systematic errors, the error introduced by the  $\tau \rightarrow 0$  extrapolation has to be smaller than the error of the extrapolation that arises from the statistical error of the individual PIMC data points. To illustrate this, we consider the (2,1) system at the highest temperature considered, i.e., at  $k_B T = 2E_{\text{ho}}$ .

Circles in Fig. 8.3(a) show  $Q_{2,1}^{\text{ni}}/Q_{2,1}$ , obtained by our PIMC approach, as a function of

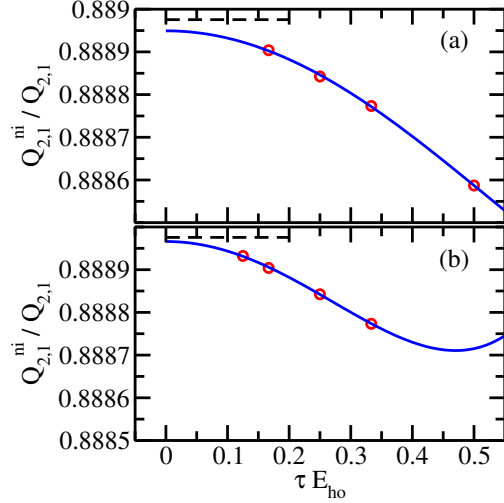


Figure 8.3: Benchmarking our PIMC results (circles) for the (2,1) system at unitarity through comparison with sum-over-states results. The observable  $Q_{2,1}^{im}/Q_{2,1}^{re}$  as a function of the imaginary time step  $\tau$  at temperature  $k_B T = 2E_{ho}$ . The error bars (not shown) are smaller than the symbol size. In (a), the time steps correspond to  $N = 2, 3, 4$ , and  $6$ . In (b), the time steps correspond to  $N = 3, 4, 6$ , and  $8$ . The solid line shows the fourth-order polynomial fit of the form  $a + b\tau^2 + c\tau^4$ . The dashed line shows the sum-over-states results.

the imaginary time step  $\tau$  (the data correspond to  $N = 2, 3, 4$ , and  $6$ ). The solid line shows a fourth-order fit of the form  $a + b\tau^2 + c\tau^4$  to our PIMC data. The extrapolated  $\tau \rightarrow 0$  value of  $0.888949(8)$ , where the error bar accounts for the statistical uncertainty of the PIMC data, deviates by about 3 standard deviations (or  $0.003\%$ ) from the sum-over-states result of  $0.8889755$ . We attribute the discrepancy to the fact that the  $\tau$  considered are not small enough for the fourth-order fit to be fully reliable. To corroborate this interpretation, we (i) employ a sixth-order fit and (ii) apply the fourth-order fit to PIMC data for smaller  $\tau$ . The sixth-order fit (using, as before, the data corresponding to  $N = 2, 3, 4$ , and  $6$ ) yields  $0.888964(19)$ , in agreement with the sum-over-states result. Note, however, that the error bar is much larger than that resulting from the fourth-order fit; the reason is that we are attempting to determine four fit parameters using just four data points. Performing a fourth-order fit to the PIMC data for  $N = 3, 4, 6$ , and  $8$  yields  $0.888966(8)$ , which almost agrees with the sum-over-states approach within error bar and with an error bar that is comparable to our previous fourth-order fit [see Fig. 8.3(b)]. This analysis suggests that our PIMC

Table 8.2: Selected PIMC raw data. Columns 1 and 2 show the inverse temperature  $E_{\text{ho}}/(k_B T)$  and the number of imaginary time slices  $N$ , respectively. Columns 3 and 4 show the observables  $Q_{3,1}^{\text{ni}}/Q_{3,1}$  and  $Q_{2,2}^{\text{ni}}/Q_{2,2}$  for the (3,1) and (2,2) systems, respectively.

$E_{\text{ho}}/(k_B T)$	$N$	$Q_{3,1}^{\text{ni}}/Q_{3,1}$	$Q_{2,2}^{\text{ni}}/Q_{2,2}$
0.5	2	0.8413081(35)	0.7940517(46)
0.5	3	0.8418155(43)	0.7946990(43)
0.5	4	0.8420157(41)	0.7949482(45)
0.5	6	0.8421806(41)	0.7951732(53)
0.6	3	0.754475(16)	0.686274(11)
0.6	4	0.754955(12)	0.686860(11)
0.6	5	0.755218(12)	0.687174(14)
0.6	7	0.755450(13)	0.687445(14)
0.6	9	0.755591(15)	0.687587(14)
0.7	3	0.658547(24)	0.571429(24)
0.7	4	0.659464(22)	0.572473(14)
0.7	6	0.660203(26)	0.573329(22)
0.7	9	0.660583(29)	0.573764(23)
0.8	4	0.563935(34)	0.462752(36)
0.8	5	0.564662(35)	0.463530(33)
0.8	7	0.565379(36)	0.464433(32)
0.8	9	0.565708(38)	0.464757(33)

calculations are free of systematic errors provided we go to sufficiently small  $\tau$ .

Table 8.2 lists the PIMC raw data for the (3,1) and (2,2) systems at various temperatures (the data for low temperatures are not shown). We report the observables  $Q_{3,1}^{\text{ni}}/Q_{3,1}$  and  $Q_{2,2}^{\text{ni}}/Q_{2,2}$  for various time slices. For  $E_{\text{ho}}/(k_B T) = 0.6, 0.7,$  and  $0.8$ , the largest number of time slices considered is  $N_{\text{max}} = 9$ . For  $E_{\text{ho}}/(k_B T) = 0.5$ , our available computing resources limit us to  $N_{\text{max}} = 6$ , resulting in reduced accuracy of the observables.

For  $E_{\text{ho}}/(k_B T) = 0.6, 0.7,$  and  $0.8$ , we perform fourth-order fits to the  $\tau$ -dependent  $Q_{3,1}^{\text{ni}}/Q_{3,1}$  and  $Q_{2,2}^{\text{ni}}/Q_{2,2}$  data listed in Table 8.2, yielding extrapolated  $\tau \rightarrow 0$  values with error bars between 0.0024% and 0.016%. We estimate, based on our tests for the three-body system, that these statistical errors are larger than the systematic error, which arises from the use of the fourth-order fit. Hence the systematic uncertainty can be neglected. For  $E_{\text{ho}}/(k_B T) = 0.5$ , a fourth-order fit to the data given in Table 8.2 yields error bars of 0.0008%

Table 8.3: Selected extrapolated PIMC results. Columns 1 and 2 show the inverse temperature  $E_{\text{ho}}/(k_B T)$  and the order used in the extrapolation, respectively. Columns 3 and 5 show the extrapolated  $\tau \rightarrow 0$  observables  $Q_{3,1}^{\text{ni}}/Q_{3,1}$  and  $Q_{2,2}^{\text{ni}}/Q_{2,2}$  for the (3,1) and (2,2) systems, respectively. Columns 4 and 6 show the resulting subcluster contributions  $b_{3,1}$  and  $b_{2,2}/2$ , respectively, to the fourth-order virial coefficient.

$E_{\text{ho}}/(k_B T)$	order	$Q_{3,1}^{\text{ni}}/Q_{3,1}$	$b_{3,1}$	$Q_{2,2}^{\text{ni}}/Q_{2,2}$	$b_{2,2}/2$
0.5	6	0.842330(15)	0.0194(16)	0.795393(18)	-0.0139(16)
0.6	4	0.755751(18)	0.0153(4)	0.687775(18)	-0.0102(4)
0.7	4	0.660877(39)	0.0135(3)	0.574108(30)	-0.0095(2)
0.8	4	0.566227(82)	0.0111(2)	0.465415(73)	-0.0093(2)

and 0.001% for  $Q_{3,1}^{\text{ni}}/Q_{3,1}$  and  $Q_{2,2}^{\text{ni}}/Q_{2,2}$ , respectively. Since we estimate the systematic fit uncertainty to be, based on our analysis for the (2,1) system, about 0.003%, we deem the fourth-order fit unreliable. Using a sixth-order fit (which yields a larger error bar), we find the values listed in Table 8.3.

# Chapter 9

## Conclusions

This thesis utilized the PIMC method and considered ultracold Bose and Fermi gases consisting of up to fifteen particles with interspecies short-range interactions. A scheme to incorporate the zero-range interaction was developed, which enables direct PIMC simulations for contact interactions in continuous space. Different systems at unitarity were considered: i) Bose and Fermi gases with two-body finite-range interactions, ii) Bose gases with two-body zero-range interaction and three-body repulsive interaction, and iii) Fermi gases with two-body zero-range interaction. For systems with short-range interactions, we investigated finite-temperature properties, extending our understanding of few-body systems beyond zero temperature. For systems with zero-range interactions, we performed calculations for the ground state of Bose droplets at unitarity with three-body repulsive interaction. This study constitutes one of the few exploratory studies of the generalization of three-body Efimov physics to  $N$  ( $N > 3$ ) particles. We also performed calculations for few fermions with zero-range interactions at unitarity, deepening our understanding of the unitary Fermi gas.

*Zero-range interaction:* Zero-range potentials have been widely used in analytical calculations to model the interactions between ultracold atoms [3, 32, 76, 145, 202]. Numerically, however, short-range potentials are more commonly used than zero-range potentials. If finite-range potentials are used, accurate calculations need to extrapolate to the zero-range limit

from a series of finite-range calculations. This thesis presented a general scheme to treat zero-range interactions in position space for simulations that utilize two-body propagators. We provided several benchmark tests for the implementation in the PIMC algorithm. Although not discussed in this thesis, the scheme was also found to work well within the PIGS algorithm. The scheme has been incorporated into a real time propagation algorithm [333]. In independent works, the propagator has been applied to DMC simulations [268, 334]. The approach developed in this thesis is based on the idea that, for short time or at high temperature, the propagator is dominated by two-body physics. One natural question to ask is: if we can fully solve the three-body problem, can we add a three-body correction to the propagator in an elegant way? Because the particle statistics plays a huge role in the three-body problem (e.g. there exist Efimov states at unitarity for equal-mass bosons but not for equal-mass two-component fermions), an open question is: if and how will the statistics enter into the three-body propagator?

*PIMC for fermions:* The PIMC method has been widely used to simulate bosonic systems at finite temperature. For bosons, the algorithm shows a favorable scaling with increasing system size. This thesis treated up to fifteen bosons. The calculation can be extended to more particles with fairly tolerable increase of the computer time. For fermions, because of the Fermi sign problem, there exist few exact PIMC simulations [332]. Most PIMC simulations make approximations and one commonly employed approximate approach is the restricted path integral Monte Carlo approach [335]. It should be noted that one-dimensional systems can, typically, be treated exactly due to the simplicity of the nodal topology. This thesis considered fermions in three dimensions with either finite- or zero-range interactions. The studies presented add to the small number of exact PIMC treatments of small fermionic systems. Furthermore, this thesis presented the first PIMC calculations for fermions with zero-range interactions. Since the complexity of the problem scales exponentially with the number of particles, the number of fermions that we treated is limited. If some controlled ap-

proximation to the “anti-symmetrizer” could be made—using, e.g., group theoretical ideas—, then simulations for fermions with zero-range interactions could be extended to more than 10 particles. If such an approach could be developed, it could be used to study the ground state energy of the spin-balanced Fermi gas at unitarity and gain further insight into the Bertsch parameter, which relates the scale invariant unitary Fermi gas to the non-interacting gas [336, 337].

*Other estimators:* The PIMC method employed here considered canonical ensembles, which means that all the paths are closed. With additional “moves”, the PIMC algorithm can be generalized to grand canonical ensembles. This generalization, sometimes known as worm algorithm, includes open paths [102]. Importantly, the worm algorithm is not only capable of treating systems in the grand canonical ensemble but also in the canonical ensemble. The “trick” of using worms in the canonical ensemble is to restrict the moves such that the closed paths sampled always correspond to the desired number of particles. The use of open paths improves the ergodicity of the sampling [102]. It is, however, an open question whether the use of open paths would improve the numerical efficiency for the small systems considered in this thesis. Moreover, utilizing open paths (one open path and  $N - 1$  closed paths), the condensate fraction can be extracted from the long-range correlations of the two ends of the open path (ODLRO of the one-body density matrix) [19]. Similarly, one might be able to extract the pair momentum distribution from the two-body density matrix by using two open paths and  $N - 2$  closed paths [338]. The pair momentum distribution could be used to analyze Fulde-Ferrell-Larkin-Ovchinnikov states [264, 313–315] of small systems. Other estimators that can be calculated by the PIMC approach include the Rényi entanglement entropy [339, 340], which is important in quantum information science and, very recently, stimulated research in few-body cold atom systems [341].

*Extended Efimov scenario:* The three-body Borromean state predicted by Efimov has been verified in ultracold experiments [80, 295, 296, 300, 342–345]. For  $N > 3$ , there exist

$N$ -body bound states attached to each three-body state. The ratio of the energies of the  $N$ -body resonance state (i.e., an  $N$ -body state attached to a highly excited three-body bound state) to the three-body state should be independent of the details of the interaction potential [41]. Both Nicholson [9] and Gattobigio *et al.* [1] predicted that the energy of an  $N$ -body resonance state scales, to leading order, quadratically with the number of particles. This thesis determined the lowest  $N$ -body bound state attached to the three-body ground state for systems at unitarity consisting of bosons with two-body zero-range interactions and three-body repulsive interactions. In contrast to earlier work [7], we found that the  $N$ -body ground state energy depends on the three-body regulator. The dependence on the three-body regulator is expected to decrease for the higher-lying resonance states. To calculate the energy of  $N$ -body resonance states, alternative techniques have to be employed because the PIMC approach is only capable of treating systems in the ground state or at finite temperature.

*Virial coefficient:* The third-order virial coefficient  $b_3$  of the unitary equal-mass two-component Fermi gas has been calculated numerically [88] and verified experimentally [320]. None of the previous numerical calculations [2, 321–323] for the fourth-order virial coefficient  $b_4$  agree with the experimentally determined results [11, 320]. This thesis determined  $b_4$  numerically and found, for the first time, agreement with the experimentally determined results. This verification could provide a benchmark for further refinement of  $b_4$  and stimulate the experimental determination of even higher-order virial coefficients. Recently [346], Endo *et al.* updated their earlier conjecture [322, 323]. The updated conjecture agrees with our calculations at high and low temperatures. If the newly proposed conjecture can be proved, it would yield a more accurate value of  $b_4$ .

*Other physical systems:* Using the tools developed in this thesis, many interesting problems not considered in this thesis can be simulated. Systems of interest include: i) A single particle immersed in a BEC background with interspecies interactions. This problem directly

relates to the original Fröhlich polaron model [347]. ii) Fermions with zero-range interaction and finite scattering length. For this system, the finite-temperature properties of the BEC-BCS crossover would be of particular interest. iii) Systems with unequal masses. For example, it would be interesting to calculate the virial coefficients for the two-component Li-K Fermi gas at unitarity.

# Bibliography

- [1] M. Gattobigio and A. Kievsky, “Universality and scaling in the  $N$ -body sector of Efimov physics,” *Phys. Rev. A* **90**, 012502 (2014).
- [2] D. Rakshit, K. M. Daily, and D. Blume, “Natural and unnatural parity states of small trapped equal-mass two-component Fermi gases at unitarity and fourth-order virial coefficient,” *Phys. Rev. A* **85**, 033634 (2012).
- [3] K. Huang and C. N. Yang, “Quantum-Mechanical Many-Body Problem with Hard-Sphere Interaction,” *Phys. Rev.* **105**, 767 (1957).
- [4] C. Chin, R. Grimm, P. Julienne, and E. Tiesinga, “Feshbach resonances in ultracold gases,” *Rev. Mod. Phys.* **82**, 1225 (2010).
- [5] R. J. Donnelly and C. F. Barenghi, “The Observed Properties of Liquid Helium at the Saturated Vapor Pressure,” *J. Phys. Chem. Ref. Data* **27**, 1217 (1998).
- [6] For the (4, 1) system, the results derived from the basis set expansion approach cover the temperature range  $k_B T \lesssim 0.1 E_{\text{ho}}$ . The results derived from the PIMC approach cover the temperature range  $k_B T \gtrsim E_{\text{ho}}$ . For this system, we did not treat the temperature regime between  $0.1 E_{\text{ho}} \lesssim k_B T \lesssim E_{\text{ho}}$ . Nevertheless, our results suggest that  $C_{4,1}$  exhibits a maximum at finite  $T$ , like the other maximally polarized systems considered in this paper.
- [7] J. von Stecher, “Weakly bound cluster states of Efimov character,” *J. Phys. B* **43**, 101002 (2010).
- [8] A. Deltuva, R. Lazauskas, and L. Platter, “Universality in Four-Body Scattering,” *Few-Body Syst.* **51**, 235 (2011).
- [9] A. N. Nicholson, “ $N$ -Body Efimov States from Two-Particle Noise,” *Phys. Rev. Lett.* **109**, 073003 (2012).
- [10] Y. Yan and D. Blume, “Temperature dependence of small harmonically trapped atom systems with Bose, Fermi, and Boltzmann statistics,” *Phys. Rev. A* **90**, 013620 (2014).
- [11] M. J. Ku, A. T. Sommer, L. W. Cheuk, and M. W. Zwierlein, “Revealing the superfluid lambda transition in the universal thermodynamics of a unitary Fermi gas,” *Science* **335**, 563 (2012).

- [12] D. R. Tilley and J. Tilley, *Superfluidity and Superconductivity*, 3rd ed. (Institute of Physics Publishing, Bristol and Philadelphia, 1990).
- [13] P. Kapitza, “Viscosity of liquid Helium below the  $\lambda$ -point,” *Nature (London)* **141**, 74 (1938).
- [14] J. F. Allen and A. D. Misener, “Flow Phenomena in Liquid Helium II,” *Nature (London)* **142**, 643 (1938).
- [15] H. E. Hall and W. F. Vinen, “The Rotation of Liquid Helium II. II. The Theory of Mutual Friction in Uniformly Rotating Helium II,” *Proc. R. Soc. London, Ser. A* **238**, 215 (1956).
- [16] D. D. Osheroff, R. C. Richardson, and D. M. Lee, “Evidence for a New Phase of Solid  $\text{He}^3$ ,” *Phys. Rev. Lett.* **28**, 885 (1972).
- [17] D. D. Osheroff, W. J. Gully, R. C. Richardson, and D. M. Lee, “New Magnetic Phenomena in Liquid  $\text{He}^3$  below 3 mK,” *Phys. Rev. Lett.* **29**, 920 (1972).
- [18] A. J. Leggett, “Interpretation of Recent Results on  $\text{He}^3$  below 3 mK: A New Liquid Phase?” *Phys. Rev. Lett.* **29**, 1227 (1972).
- [19] D. M. Ceperley, “Path integrals in the theory of condensed helium,” *Rev. Mod. Phys.* **67**, 279 (1995).
- [20] W. Krauth, *Statistical Mechanics: Algorithms and Computations*, Oxford Master Series in Physics (Oxford University Press, Oxford, UK, 2006).
- [21] Bose, “Plancks Gesetz und Lichtquantenhypothese,” *Zeitschrift fur Physik* **26**, 178 (1924).
- [22] Einstein, A., “Quantentheorie des einatomigen idealen Gases,” *Sitzungsberichte der Preussischen Akademie der Wissenschaften* **1**, 3 (1925).
- [23] F. Pereira Dos Santos, J. Léonard, J. Wang, C. J. Barrelet, F. Perales, E. Rasel, C. S. Unnikrishnan, M. Leduc, and C. Cohen-Tannoudji, “Bose-Einstein Condensation of Metastable Helium,” *Phys. Rev. Lett.* **86**, 3459 (2001).
- [24] A. Robert, O. Sirjean, A. Browaeys, J. Poupard, S. Nowak, D. Boiron, C. I. Westbrook, and A. Aspect, “A Bose-Einstein Condensate of Metastable Atoms,” *Science* **292**, 461 (2001).
- [25] S. Moal, M. Portier, J. Kim, J. Dugué, U. D. Rapol, M. Leduc, and C. Cohen-Tannoudji, “Accurate Determination of the Scattering Length of Metastable Helium Atoms Using Dark Resonances between Atoms and Exotic Molecules,” *Phys. Rev. Lett.* **96**, 023203 (2006).
- [26] J. Stärck and W. Meyer, “Long-range interaction potential of the  $^3\Sigma_g^+$  state of  $\text{He}_2$ ,” *Chem. Phys. Lett.* **225**, 229 (1994).

- [27] J. Weiner, V. S. Bagnato, S. Zilio, and P. S. Julienne, “Experiments and theory in cold and ultracold collisions,” *Rev. Mod. Phys.* **71**, 1 (1999).
- [28] M. Przybytek, W. Cencek, J. Komasa, G. Łach, B. Jeziorski, and K. Szalewicz, “Relativistic and Quantum Electrodynamics Effects in the Helium Pair Potential,” *Phys. Rev. Lett.* **104**, 183003 (2010).
- [29] O. Penrose and L. Onsager, “Bose-Einstein Condensation and Liquid Helium,” *Phys. Rev.* **104**, 576 (1956).
- [30] A. J. Leggett, *Quantum Liquids* (Oxford Univ. Press, 2006).
- [31] M. Girardeau, “Relationship between Systems of Impenetrable Bosons and Fermions in One Dimension,” *J Math. Phys.* **1**, 516 (1960).
- [32] S. Giorgini, L. P. Pitaevskii, and S. Stringari, “Theory of ultracold atomic Fermi gases,” *Rev. Mod. Phys.* **80**, 1215 (2008).
- [33] M. H. Anderson, J. R. Ensher, M. R. Matthews, C. E. Wieman, and E. A. Cornell, “Observation of Bose-Einstein Condensation in a Dilute Atomic Vapor,” *Science* **269**, 198 (1995).
- [34] B. DeMarco and D. S. Jin, “Onset of Fermi Degeneracy in a Trapped Atomic Gas,” *Science* **285**, 1703 (1999).
- [35] J. J. Sakurai and J. Napolitano, *Modern quantum mechanics* (Addison-Wesley, 2011).
- [36] H. Stanley, *Introduction to Phase Transitions and Critical Phenomena*, International series of monographs on physics (Oxford University Press, 1971).
- [37] H. Peitgen, H. Jürgens, and D. Saupe, *Chaos and Fractals: New Frontiers of Science* (Springer New York, 2004).
- [38] L. P. Pitaevskii and A. Rosch, “Breathing modes and hidden symmetry of trapped atoms in two dimensions,” *Phys. Rev. A* **55**, R853 (1997).
- [39] M. Olshanii, H. Perrin, and V. Lorent, “Example of a Quantum Anomaly in the Physics of Ultracold Gases,” *Phys. Rev. Lett.* **105**, 095302 (2010).
- [40] C.-L. Hung, X. Zhang, N. Gemelke, and C. Chin, “Observation of scale invariance and universality in two-dimensional Bose gases,” *Nature (London)* **470**, 236 (2011).
- [41] E. Braaten and H.-W. Hammer, “Universality in few-body systems with large scattering length,” *Phys. Rep.* **428**, 259 (2006).
- [42] B. Claude Cohen-Tannoudji, *Quantum Mechanics*, vol. 1 (Hermann, Paris).
- [43] L. H. Thomas, “The Interaction Between a Neutron and a Proton and the Structure of H<sub>3</sub>,” *Phys. Rev.* **47**, 903 (1935).

- [44] N. F. Ramsey, “Electron Coupled Interactions between Nuclear Spins in Molecules,” *Phys. Rev.* **91**, 303 (1953).
- [45] E. Epelbaum, H.-W. Hammer, and U.-G. Meißner, “Modern theory of nuclear forces,” *Rev. Mod. Phys.* **81**, 1773 (2009).
- [46] Y. N. Demkov and V. N. Ostrovskiĭ, *Zero-Range Potentials and Their Applications in Atomic Physics* (Plenum Press, New York, 1988).
- [47] P. S. Krstić, D. B. Milošević, and R. K. Janev, “Zero-range potential model for the description of atomic and molecular systems in a laser field,” *Phys. Rev. A* **44**, 3089 (1991).
- [48] N. L. Manakov, M. V. Frolov, A. F. Starace, and I. I. Fabrikant, “Interaction of laser radiation with a negative ion in the presence of a strong static electric field,” *J. Phys. B* **33**, R141 (2000).
- [49] S. Tan, “Energetics of a strongly correlated Fermi gas,” *Ann. Phys. (N. Y.)* **323**, 2952 (2008).
- [50] S. Tan, “Large momentum part of a strongly correlated Fermi gas,” *Ann. Phys. (N. Y.)* **323**, 2971 (2008).
- [51] S. Tan, “Generalized virial theorem and pressure relation for a strongly correlated Fermi gas,” *Ann. Phys. (N. Y.)* **323**, 2987 (2008).
- [52] J. T. Stewart, J. P. Gaebler, T. E. Drake, and D. S. Jin, “Verification of Universal Relations in a Strongly Interacting Fermi Gas,” *Phys. Rev. Lett.* **104**, 235301 (2010).
- [53] E. D. Kuhnle, H. Hu, X.-J. Liu, P. Dyke, M. Mark, P. D. Drummond, P. Hannaford, and C. J. Vale, “Universal Behavior of Pair Correlations in a Strongly Interacting Fermi Gas,” *Phys. Rev. Lett.* **105**, 070402 (2010).
- [54] E. D. Kuhnle, S. Hoinka, P. Dyke, H. Hu, P. Hannaford, and C. J. Vale, “Temperature Dependence of the Universal Contact Parameter in a Unitary Fermi Gas,” *Phys. Rev. Lett.* **106**, 170402 (2011).
- [55] Y. Sagi, T. E. Drake, R. Paudel, and D. S. Jin, “Measurement of the Homogeneous Contact of a Unitary Fermi Gas,” *Phys. Rev. Lett.* **109**, 220402 (2012).
- [56] S. Hoinka, M. Lingham, K. Fenech, H. Hu, C. J. Vale, J. E. Drut, and S. Gandolfi, “Precise Determination of the Structure Factor and Contact in a Unitary Fermi Gas,” *Phys. Rev. Lett.* **110**, 055305 (2013).
- [57] D. Blume and K. M. Daily, “Universal relations for a trapped four-fermion system with arbitrary  $s$ -wave scattering length,” *Phys. Rev. A* **80**, 053626 (2009).
- [58] F. Werner, L. Tarruell, and Y. Castin, “Number of closed-channel molecules in the BEC-BCS crossover,” *Eur. Phys. J. B* **68**, 401 (2009).

- [59] Z. Yu, G. M. Bruun, and G. Baym, “Short-range correlations and entropy in ultracold-atom Fermi gases,” *Phys. Rev. A* **80**, 023615 (2009).
- [60] F. Palestini, A. Perali, P. Pieri, and G. C. Strinati, “Temperature and coupling dependence of the universal contact intensity for an ultracold Fermi gas,” *Phys. Rev. A* **82**, 021605(R) (2010).
- [61] J. E. Drut, T. A. Lähde, and T. Ten, “Momentum Distribution and Contact of the Unitary Fermi Gas,” *Phys. Rev. Lett.* **106**, 205302 (2011).
- [62] K. Van Houcke, F. Werner, E. Kozik, N. Prokof’ev, and B. Svistunov, “Contact and Momentum Distribution of the Unitary Fermi Gas by Bold Diagrammatic Monte Carlo,” (2013), arXiv:1303.6245 .
- [63] I. Boettcher, S. Diehl, J. M. Pawłowski, and C. Wetterich, “Tan contact and universal high momentum behavior of the fermion propagator in the BCS-BEC crossover,” *Phys. Rev. A* **87**, 023606 (2013).
- [64] M. Barth and W. Zwerger, “Tan relations in one dimension,” *Ann. Phys. (N. Y.)* **326**, 2544 (2011).
- [65] T. Enss, R. Haussmann, and W. Zwerger, “Viscosity and scale invariance in the unitary Fermi gas,” *Ann. Phys. (N. Y.)* **326**, 770 (2011).
- [66] E. V. H. Doggen and J. J. Kinnunen, “Energy and Contact of the One-Dimensional Fermi Polaron at Zero and Finite Temperature,” *Phys. Rev. Lett.* **111**, 025302 (2013).
- [67] H. Hu, X.-J. Liu, and P. D. Drummond, “Universal contact of strongly interacting fermions at finite temperatures,” *New J. Phys.* **13**, 035007 (2011).
- [68] R. Weiss, B. Bazak, and N. Barnea, “Nuclear Neutron-Proton Contact and the Photoabsorption Cross Section,” *Phys. Rev. Lett.* **114**, 012501 (2015).
- [69] O. Hen, L. B. Weinstein, E. Piasetzky, G. A. Miller, M. M. Sargsian, and Y. Sagi, “Correlated fermions in nuclei and ultracold atomic gases,” *Phys. Rev. C* **92**, 045205 (2015).
- [70] P. O. Fedichev, M. W. Reynolds, and G. V. Shlyapnikov, “Three-Body Recombination of Ultracold Atoms to a Weakly Bound  $s$  Level,” *Phys. Rev. Lett.* **77**, 2921 (1996).
- [71] D. S. Petrov, “Three-body problem in Fermi gases with short-range interparticle interaction,” *Phys. Rev. A* **67**, 010703(R) (2003).
- [72] J. P. D’Incao and B. D. Esry, “Scattering Length Scaling Laws for Ultracold Three-Body Collisions,” *Phys. Rev. Lett.* **94**, 213201 (2005).
- [73] K. O’hara, S. Hemmer, M. Gehm, S. Granade, and J. Thomas, “Observation of a strongly interacting degenerate Fermi gas of atoms,” *Science* **298**, 2179 (2002).

- [74] D. Blume, S. T. Rittenhouse, J. von Stecher, and C. H. Greene, “Stability of inhomogeneous multicomponent Fermi gases,” *Phys. Rev. A* **77**, 033627 (2008).
- [75] C. D. Lin, “Hyperspherical coordinate approach to atomic and other Coulombic three-body systems,” *Phys. Rep.* **257**, 1 (1995).
- [76] D. Blume, “Few-body physics with ultracold atomic and molecular systems in traps,” *Rep. Prog. Phys.* **75**, 046401 (2012).
- [77] J. Wang, J. P. D’Incao, B. D. Esry, and C. H. Greene, “Origin of the Three-Body Parameter Universality in Efimov Physics,” *Phys. Rev. Lett.* **108**, 263001 (2012).
- [78] P. Naidon, S. Endo, and M. Ueda, “Microscopic Origin and Universality Classes of the Efimov Three-Body Parameter,” *Phys. Rev. Lett.* **112**, 105301 (2014).
- [79] F. Ferlaino and R. Grimm, “Trend: Forty years of Efimov physics: How a bizarre prediction turned into a hot topic,” *Physics* **3**, 9 (2010).
- [80] T. Kraemer, M. Mark, P. Waldburger, J. G. Danzl, C. Chin, B. Engeser, A. D. Lange, K. Pilch, A. Jaakkola, H.-C. Nägerl, and R. Grimm, “Evidence for Efimov quantum states in an ultracold gas of caesium atoms,” *Nature (London)* **440**, 315 (2006).
- [81] R. D. Amado and F. C. Greenwood, “There Is No Efimov Effect for Four or More Particles,” *Phys. Rev. D* **7**, 2517 (1973).
- [82] L. Platter, H.-W. Hammer, and U.-G. Meißner, “Four-boson system with short-range interactions,” *Phys. Rev. A* **70**, 052101 (2004).
- [83] H.-W. Hammer and L. Platter, “Universal properties of the four-body system with large scattering length,” *Euro. Phys. J. A* **32**, 113 (2007).
- [84] F. Ferlaino, S. Knoop, M. Berninger, W. Harm, J. P. D’Incao, H.-C. Nägerl, and R. Grimm, “Evidence for Universal Four-Body States Tied to an Efimov Trimer,” *Phys. Rev. Lett.* **102**, 140401 (2009).
- [85] J. von Stecher, J. P. D’Incao, and C. H. Greene, “Signatures of universal four-body phenomena and their relation to the Efimov effect,” *Nat. Phys.* **5**, 417 (2009).
- [86] A. Zenesini, B. Huang, M. Berninger, S. Besler, H.-C. Ngerl, F. Ferlaino, R. Grimm, C. H. Greene, and J. von Stecher, “Resonant five-body recombination in an ultracold gas of bosonic atoms,” *New J. Phys.* **15**, 043040 (2013).
- [87] K. Huang, *Statistical Mechanics*, 2nd ed. (Wiley, New York, 1987).
- [88] X.-J. Liu, H. Hu, and P. D. Drummond, “Virial Expansion for a Strongly Correlated Fermi Gas,” *Phys. Rev. Lett.* **102**, 160401 (2009).
- [89] X.-J. Liu, “Virial expansion for a strongly correlated Fermi system and its application to ultracold atomic Fermi gases,” *Phys. Rep.* **524**, 37 (2013).

- [90] F. Serwane, G. Zürn, T. Lompe, T. B. Ottenstein, A. N. Wenz, and S. Jochim, “Deterministic Preparation of a Tunable Few-Fermion System,” *Science* **332**, 336 (2011).
- [91] G. Zürn, F. Serwane, T. Lompe, A. N. Wenz, M. G. Ries, J. E. Bohn, and S. Jochim, “Fermionization of Two Distinguishable Fermions,” *Phys. Rev. Lett.* **108**, 075303 (2012).
- [92] G. Zürn, A. Wenz, S. Murmann, A. Bergschneider, T. Lompe, and S. Jochim, “Pairing in Few-Fermion Systems with Attractive Interactions,” *Phys. Rev. Lett.* **111**, 175302 (2013).
- [93] G. Zürn, *Few-fermion systems in one dimension*, Ph.D. thesis, Ruperto-Carola-University of Heidelberg, Germany (2012).
- [94] P. Sindzingre, M. L. Klein, and D. M. Ceperley, “Path-integral Monte Carlo study of low-temperature  $^4\text{He}$  clusters,” *Phys. Rev. Lett.* **63**, 1601 (1989).
- [95] Y. Kwon, D. M. Ceperley, and K. B. Whaley, “Path integral Monte Carlo study of  $\text{SF}_6$ -doped helium clusters,” *J. Chem. Phys.* **104**, 2341 (1996).
- [96] M. W. Cole, V. H. Crespi, G. Stan, C. Ebner, J. M. Hartman, S. Moroni, and M. Boninsegni, “Condensation of Helium in Nanotube Bundles,” *Phys. Rev. Lett.* **84**, 3883 (2000).
- [97] E. Y. Loh, J. E. Gubernatis, R. T. Scalettar, S. R. White, D. J. Scalapino, and R. L. Sugar, “Sign problem in the numerical simulation of many-electron systems,” *Phys. Rev. B* **41**, 9301 (1990).
- [98] R. Stratonovich, “On a method of calculating quantum distribution functions,” *Sov. Phys. Dokl.* **2**, 416 (1957).
- [99] D. Ceperley and B. Alder, “Quantum Monte Carlo,” *Science* **231**, 555 (1986).
- [100] B. Hetényi, E. Rabani, and B. J. Berne, “Path-integral diffusion Monte Carlo: Calculation of observables of many-body systems in the ground state,” *J. Chem. Phys.* **110**, 6143 (1999).
- [101] A. Sarsa, K. E. Schmidt, and W. R. Magro, “A path integral ground state method,” *J. Chem. Phys.* **113**, 1366 (2000).
- [102] M. Boninsegni, N. V. Prokof’ev, and B. V. Svistunov, “Worm algorithm and diagrammatic Monte Carlo: A new approach to continuous-space path integral Monte Carlo simulations,” *Phys. Rev. E* **74**, 036701 (2006).
- [103] L. Pollet, “Recent developments in quantum Monte Carlo simulations with applications for cold gases,” *Rep. Prog. Phys.* **75**, 094501 (2012).

- [104] B. Capogrosso-Sansone, N. V. Prokof'ev, and B. V. Svistunov, "Phase diagram and thermodynamics of the three-dimensional Bose-Hubbard model," *Phys. Rev. B* **75**, 134302 (2007).
- [105] K. Van Houcke, E. Kozik, N. Prokof'ev, and B. Svistunov, "Diagrammatic Monte Carlo," (2008), arXiv:0802.2923 .
- [106] E. Burovski, N. Prokof'ev, B. Svistunov, and M. Troyer, "The Fermi-Hubbard model at unitarity," *New J. Phys.* **8**, 153 (2006).
- [107] J. Kolorenč and L. Mitas, "Applications of quantum Monte Carlo methods in condensed systems," *Rep. Prog. Phys.* **74**, 026502 (2011).
- [108] R. Feynman and A. Hibbs, *Quantum mechanics and path integrals*, International series in pure and applied physics (McGraw-Hill, New York, 1965).
- [109] D. Chandler and P. G. Wolynes, "Exploiting the isomorphism between quantum theory and classical statistical mechanics of polyatomic fluids," *J. Chem. Phys.* **74**, 4078 (1981).
- [110] H. F. Trotter, "On the product of semi-groups of operators," *Proc. Amer. Math. Soc.* **10**, 545 (1959).
- [111] W. Rossmann, *Lie Groups: An Introduction Through Linear Groups*, Oxford graduate texts in mathematics (Oxford University Press, Oxford, UK, 2006).
- [112] S. A. Chin, "Symplectic integrators from composite operator factorizations," *Phys. Lett. A* **226**, 344 (1997).
- [113] B. Gaveau and L. S. Schulman, "Explicit time-dependent Schrodinger propagators," *J. Phys. A* **19**, 1833 (1986).
- [114] S. M. Blinder, "Green's function and propagator for the one-dimensional  $\delta$ -function potential," *Phys. Rev. A* **37**, 973 (1988).
- [115] S. V. Lawande and K. V. Bhagwat, "Feynman propagator for the  $\delta$ -function potential," *Phys. Lett. A* **131**, 8 (1988).
- [116] K. Wódkiewicz, "Fermi pseudopotential in arbitrary dimensions," *Phys. Rev. A* **43**, 68 (1991).
- [117] J. A. Barker, "A quantumstatistical Monte Carlo method; path integrals with boundary conditions," *J Chem. Phys.* **70**, 2914 (1979).
- [118] J. Cao and B. J. Berne, "A new quantum propagator for hard sphere and cavity systems," *J Chem. Phys.* **97**, 2382 (1992).
- [119] R. E. Zillich, J. M. Mayrhofer, and S. A. Chin, "Extrapolated high-order propagators for path integral Monte Carlo simulations," *J. Chem. Phys.* **132**, 044103 (2010).

- [120] M. Nava, D. E. Galli, M. W. Cole, and L. Reatto, “Adsorption of He isotopes on fluorographene and graphane: Fluid and superfluid phases from quantum Monte Carlo calculations,” *Phys. Rev. B* **86**, 174509 (2012).
- [121] G. Baym, *Lectures on Quantum Mechanics*, Advanced Book Program (Addison-Wesley, 1990).
- [122] In *Mathematica*, the number of inversions  $N_1(\sigma)$  is represented by the function `Inversions`.
- [123] W. Press, *Numerical Recipes 3rd Ed.: The Art of Scientific Computing* (Cambridge University Press, Cambridge, UK, 2007).
- [124] B. L. Hammond, W. A. Lester, and P. J. Reynolds, *Monte Carlo Methods in Ab Initio Quantum Chemistry*, Lecture and Course Notes In Chemistry Series, Vol. 1 (World Scientific, Singapore, 1994).
- [125] J. Salas, *Applied Modeling of Hydrologic Time Series*, Water Resources publication (Water Resources Publications, Highlands Ranch, 1980).
- [126] L. Gonick, *Cartoon Guide to Statistics*, Cartoon Guide Series (HarperCollins, New York, 1993).
- [127] G. E. P. Box and M. E. Muller, “A Note on the Generation of Random Normal Deviates,” *Ann. Math. Statist.* **29**, 610 (1958).
- [128] T. A. B. G. Marsaglia, “A Convenient Method for Generating Normal Variables,” *SIAM Review* **6**, 260 (1964).
- [129] G. Marsaglia and W. W. Tsang, “The Ziggurat Method for Generating Random Variables,” *J. Stat. Softw.* **5**, 1 (2000).
- [130] B. Nadler, “Design Flaws in the Implementation of the Ziggurat and Monty Python methods (and some remarks on Matlab randn),” [arXiv:math/0603058](https://arxiv.org/abs/math/0603058) .
- [131] R. Bellman and R. Corporation, *Dynamic Programming*, Rand Corporation research study (Princeton University Press, Princeton, 1957).
- [132] B. Berg, *Markov Chain Monte Carlo Simulations and Their Statistical Analysis: With Web-based Fortran Code* (World Scientific, Singapore, 2004).
- [133] M. Boninsegni, “Permutation Sampling in Path Integral Monte Carlo,” *J. Low Temp. Phys.* **141**, 27 (2005).
- [134] D. M. Ceperley, “Path integral Monte Carlo methods for fermions,” in *The Proceedings of the Les Houches Summer School, Session 56, Strongly Interacting Fermions and High  $T_c$  Superconductivity*, edited by B. Douçot and J. Zinn-Justin (Elsevier, Amsterdam, 1995) p. 427.

- [135] D. Ceperley, “Fermion nodes,” *J. Stat. Phys.* **63**, 1237 (1991).
- [136] In *Mathematica*, the function `Partition(N)` is represented by the function `PartitionsP`.
- [137] A. P. Lyubartsev and P. N. Vorontsov-Velyaminov, “Path-integral Monte Carlo method in quantum statistics for a system of  $N$  identical fermions,” *Phys. Rev. A* **48**, 4075 (1993).
- [138] M. A. Voznesenskiy, P. N. Vorontsov-Velyaminov, and A. P. Lyubartsev, “Path-integral–expanded-ensemble Monte Carlo method in treatment of the sign problem for fermions,” *Phys. Rev. E* **80**, 066702 (2009).
- [139] J. L. DuBois, E. W. Brown, and B. J. Alder, “Overcoming the fermion sign problem in homogeneous systems,” [arXiv:1409.3262](https://arxiv.org/abs/1409.3262) .
- [140] G. L. Jones, “On the Markov chain central limit theorem,” *Probab. Surveys* **1**, 299 (2004).
- [141] F. Werner and Y. Castin, “General relations for quantum gases in two and three dimensions: Two-component fermions,” *Phys. Rev. A* **86**, 013626 (2012).
- [142] E. Braaten and L. Platter, “Exact Relations for a Strongly Interacting Fermi Gas from the Operator Product Expansion,” *Phys. Rev. Lett.* **100**, 205301 (2008).
- [143] T.-L. Ho and E. J. Mueller, “High Temperature Expansion Applied to Fermions near Feshbach Resonance,” *Phys. Rev. Lett.* **92**, 160404 (2004).
- [144] The virial expansion is derived in the grand canonical ensemble and works with an average number of particles. In the small particle limit, where 1 is not small compared to  $N$ , the virial expansion is not expected to yield accurate results.
- [145] T. Busch, B.-G. Englert, K. Rzażewski, and M. Wilkens, “Two Cold Atoms in a Harmonic Trap,” *Found. Phys.* **28**, 549 (1998).
- [146] F. Werner and Y. Castin, “Unitary Quantum Three-Body Problem in a Harmonic Trap,” *Phys. Rev. Lett.* **97**, 150401 (2006).
- [147] Y. Suzuki and K. Varga, *Stochastic Variational Approach to Quantum Mechanical Few-Body Problems* (Springer-Verlag, Berlin, 1998).
- [148] K. M. Daily and D. Blume, “Energy spectrum of harmonically trapped two-component Fermi gases: Three- and four-particle problem,” *Phys. Rev. A* **81**, 053615 (2010).
- [149] K. M. Daily, X. Y. Yin, and D. Blume, “Occupation numbers of the harmonically trapped few-boson system,” *Phys. Rev. A* **85**, 053614 (2012).
- [150] J. P. Kestner and L.-M. Duan, “Level crossing in the three-body problem for strongly interacting fermions in a harmonic trap,” *Phys. Rev. A* **76**, 033611 (2007).

- [151] I. Stetcu, B. R. Barrett, U. van Kolck, and J. P. Vary, “Effective theory for trapped few-fermion systems,” *Phys. Rev. A* **76**, 063613 (2007).
- [152] J. von Stecher, C. H. Greene, and D. Blume, “Energetics and structural properties of trapped two-component Fermi gases,” *Phys. Rev. A* **77**, 043619 (2008).
- [153] E. Pulvirenti and D. Tsagkarogiannis, “Cluster Expansion in the Canonical Ensemble,” *Commun. Math. Phys.* **316**, 289 (2012).
- [154] E. Braaten, D. Kang, and L. Platter, “Universal Relations for Identical Bosons from Three-Body Physics,” *Phys. Rev. Lett.* **106**, 153005 (2011).
- [155] The three-body contact [154] should not be confused with the two-body contact  $C_{N_1, N_2}$  of the two-, three- and higher-body systems. For the Fermi systems considered in this work, the three-body contact vanishes identically.
- [156] Y. Kwon and K. Birgitta Whaley, “Atomic-Scale Quantum Solvation Structure in Superfluid Helium-4 Clusters,” *Phys. Rev. Lett.* **83**, 4108 (1999).
- [157] N. Blinov and P.-N. Roy, “Effect of exchange on the rotational dynamics of doped helium clusters,” *J. Low Temp. Phys.* **140**, 253 (2005).
- [158] S. Jang, S. Jang, and G. A. Voth, “Applications of higher order composite factorization schemes in imaginary time path integral simulations,” *J. Chem. Phys.* **115**, 7832 (2001).
- [159] R. Stock, A. Silberfarb, E. L. Bolda, and I. H. Deutsch, “Generalized Pseudopotentials for Higher Partial Wave Scattering,” *Phys. Rev. Lett.* **94**, 023202 (2005).
- [160] S. T. Rittenhouse, N. P. Mehta, and C. H. Greene, “Green’s functions and the adiabatic hyperspherical method,” *Phys. Rev. A* **82**, 022706 (2010).
- [161] S. Moroz, “Scale-invariant Fermi gas in a time-dependent harmonic potential,” *Phys. Rev. A* **86**, 011601 (2012).
- [162] L. A. Sidorenkov, M. K. Tey, R. Grimm, Y.-H. Hou, L. Pitaevskii, and S. Stringari, “Second sound and the superfluid fraction in a Fermi gas with resonant interactions,” *Nature (London)* **498**, 78 (2013).
- [163] D. Page, M. Prakash, J. M. Lattimer, and A. W. Steiner, “Prospects of Detecting Baryon and Quark Superfluidity from Cooling Neutron Stars,” *Phys. Rev. Lett.* **85**, 2048 (2000).
- [164] D. Page, M. Prakash, J. M. Lattimer, and A. W. Steiner, “Rapid Cooling of the Neutron Star in Cassiopeia A Triggered by Neutron Superfluidity in Dense Matter,” *Phys. Rev. Lett.* **106**, 081101 (2011).
- [165] M. R. Matthews, B. P. Anderson, P. C. Haljan, D. S. Hall, C. E. Wieman, and E. A. Cornell, “Vortices in a Bose-Einstein Condensate,” *Phys. Rev. Lett.* **83**, 2498 (1999).

- [166] K. W. Madison, F. Chevy, W. Wohlleben, and J. Dalibard, “Vortex Formation in a Stirred Bose-Einstein Condensate,” *Phys. Rev. Lett.* **84**, 806 (2000).
- [167] J. R. Abo-Shaeer, C. Raman, J. M. Vogels, and W. Ketterle, “Observation of vortex lattices in Bose-Einstein condensates,” *Science* **292**, 476 (2001).
- [168] M. W. Zwierlein, J. R. Abo-Shaeer, A. Schirotzek, C. H. Schunck, and W. Ketterle, “Vortices and superfluidity in a strongly interacting Fermi gas,” *Nature (London)* **435**, 1047 (2005).
- [169] P. Ring and P. Schuck, *The Nuclear Many-Body Problem* (Springer Verlag, New York, 1980).
- [170] L. Pitaevskii and S. Stringari, *Bose-Einstein Condensation* (Oxford University Press, Oxford, UK, 2003).
- [171] C. J. Pethick and H. Smith, *Bose-Einstein Condensation in Dilute Gases*, 2nd ed. (Cambridge University Press, Cambridge, UK).
- [172] J. P. Toennies and A. F. Vilesov, “Superfluid Helium Droplets: A Uniquely Cold Nanomatrix for Molecules and Molecular Complexes,” *Angewandte Chemie International Edition* **43**, 2622 (2004).
- [173] S. Grebenev, J. P. Toennies, and A. F. Vilesov, “Superfluidity Within a Small Helium-4 Cluster: The Microscopic Andronikashvili Experiment,” *Science* **279**, 2083 (1998).
- [174] S. Grebenev, B. Sartakov, J. P. Toennies, and A. F. Vilesov, “Evidence for Superfluidity in Para-Hydrogen Clusters Inside Helium-4 Droplets at 0.15 Kelvin,” *Science* **289**, 1532 (2000).
- [175] J. Tang, Y. Xu, A. R. W. McKellar, and W. Jäger, “Quantum Solvation of Carbonyl Sulfide with Helium Atoms,” *Science* **297**, 2030 (2002).
- [176] Y. Kwon and K. B. Whaley, “Nanoscale Molecular Superfluidity of Hydrogen,” *Phys. Rev. Lett.* **89**, 273401 (2002).
- [177] F. Paesani, Y. Kwon, and K. B. Whaley, “Onset of Superfluidity in Small  $\text{CO}_2(^4\text{He})_N$  Clusters,” *Phys. Rev. Lett.* **94**, 153401 (2005).
- [178] A. Bohr, B. R. Mottelson, and D. Pines, “Possible Analogy between the Excitation Spectra of Nuclei and Those of the Superconducting Metallic State,” *Phys. Rev.* **110**, 936 (1958).
- [179] S. T. Belyaev, “Effect of pairing correlations on nuclear properties,” *Mat. Fys. Medd. Dan. Vid. Selsk.* **31** (1959), no. 11.
- [180] A. Migdal, “Superfluidity and the moments of inertia of nuclei,” *Nucl. Phys.* **13**, 655 (1959).

- [181] D. J. Dean and M. Hjorth-Jensen, “Pairing in nuclear systems: from neutron stars to finite nuclei,” *Rev. Mod. Phys.* **75**, 607 (2003).
- [182] R. A. Broglia and V. Zelevinsky, *Fifty Years of Nuclear BCS: Pairing in Finite Systems* (World Scientific, 2013).
- [183] Y. Alhassid, G. F. Bertsch, L. Fang, and S. Liu, “Nuclear moment of inertia and spin distribution of nuclear levels,” *Phys. Rev. C* **72**, 064326 (2005).
- [184] H. Saarikoski, S. M. Reimann, A. Harju, and M. Manninen, “Vortices in quantum droplets: Analogies between boson and fermion systems,” *Rev. Mod. Phys.* **82**, 2785 (2010).
- [185] P. A. Dirac, “Quantised singularities in the electromagnetic field,” *Proc. R. Soc. A* **133**, 60 (1931).
- [186] J. O. Hirschfelder, C. J. Goebel, and L. W. Bruch, “Quantized vortices around wavefunction nodes. II,” *J. Chem. Phys.* **61**, 5456 (1974).
- [187] D. Dagnino, N. Barberán, M. Lewenstein, and J. Dalibard, “Vortex nucleation as a case study of symmetry breaking in quantum systems,” *Nat. Phys.* **5**, 431 (2009).
- [188] A. J. Leggett, “Can a Solid Be “Superfluid”?” *Phys. Rev. Lett.* **25**, 1543 (1970).
- [189] G. Baym, in *Mathematical Methods in Solid State and Superfluid Theory*, edited by R. Clark and E. Derrick (Oliver and Boyd, Edinburgh, 1969) Chap. The Microscopic Description of Superfluidity.
- [190] A. J. Leggett, “Topics in the theory of helium,” *Phys. Fenn.* **8**, 125 (1973).
- [191] E. L. Pollock and D. M. Ceperley, “Path-integral computation of superfluid densities,” *Phys. Rev. B* **36**, 8343 (1987).
- [192] T. Paananen, “Superfluid density of the ultra-cold Fermi gas in optical lattices,” *J. Phys. B* **42**, 165304 (2009).
- [193] The distance  $r_{n,\perp}$  between  $\vec{r}_n$  and the axis  $\hat{z}$  can be expressed as  $r_{n,\perp} = |\vec{r}_n \times \hat{z}|$ .
- [194] Y. Yan and D. Blume, “Harmonically trapped Fermi gas: Temperature dependence of the Tan contact,” *Phys. Rev. A* **88**, 023616 (2013).
- [195] Y. Kwon, F. Paesani, and K. B. Whaley, “Local superfluidity in inhomogeneous quantum fluids,” *Phys. Rev. B* **74**, 174522 (2006).
- [196] J. M. Blatt and S. T. Butler, “Superfluidity of an Ideal Bose-Einstein Gas,” *Phys. Rev.* **100**, 476 (1955).

- [197] The partition function of the non-interacting  $N$ -particle system can be obtained by symmetrizing (anti-symmetrizing) the single-particle partition function for bosons (fermions) [20]. By the virial theorem [348],  $I_c$  is equal to  $2\langle E \rangle_{\text{th}}/(3\omega^2)$ . To calculate  $I_q$ , we note that  $\langle M^2 \rangle_{\text{th}} = \langle (\sum_n M_n)^2 \rangle_{\text{th}}$  simplifies to  $\langle \sum_n M_n^2 \rangle_{\text{th}}$  since the cross terms cancel; here,  $M_n$  is the projection quantum number of the  $n$ th particle.
- [198] S. Stringari, “Moment of Inertia and Superfluidity of a Trapped Bose Gas,” *Phys. Rev. Lett.* **76**, 1405 (1996).
- [199]  $\rho_s(\mathbf{r})$  satisfies  $I_c - I_q = m \int \rho_s(\mathbf{r}) r_{\perp}^2 d^3\mathbf{r}$ , where  $r_{\perp}$  denotes the distance to the  $z$ -axis.
- [200] P. O. Bugnion, J. A. Lofthouse, and G. J. Conduit, “Inhomogeneous State of Few-Fermion Superfluids,” *Phys. Rev. Lett.* **111**, 045301 (2013).
- [201] N. R. Cooper and Z. Hadzibabic, “Measuring the Superfluid Fraction of an Ultracold Atomic Gas,” *Phys. Rev. Lett.* **104**, 030401 (2010).
- [202] F. Dalfovo, S. Giorgini, L. P. Pitaevskii, and S. Stringari, “Theory of Bose-Einstein Condensation in Trapped Gases,” *Rev. Mod. Phys.* **71**, 463 (1999).
- [203] I. Bloch, J. Dalibard, and W. Zwerger, “Many-body physics with ultracold gases,” *Rev. Mod. Phys.* **80**, 885 (2008).
- [204] M. Greiner, C. A. Regal, and D. S. Jin, “Emergence of a molecular Bose-Einstein condensate from a Fermi gas,” *Nature (London)* **426**, 537 (2003).
- [205] M. W. Zwierlein, C. A. Stan, C. H. Schunck, S. M. F. Raupach, S. Gupta, Z. Hadzibabic, and W. Ketterle, “Observation of Bose-Einstein Condensation of Molecules,” *Phys. Rev. Lett.* **91**, 250401 (2003).
- [206] P. Ring and P. Schuck, *The Nuclear Many-Body Problem* (Springer, 2004).
- [207] R. Pathria, *Statistical Mechanics* (Elsevier, Amsterdam, 1996).
- [208] H. B. Callen, *Thermodynamics and an Introduction to Thermostatistics* (John Wiley & Sons, 2006).
- [209] J. Carlson, S.-Y. Chang, V. R. Pandharipande, and K. E. Schmidt, “Superfluid Fermi Gases with Large Scattering Length,” *Phys. Rev. Lett.* **91**, 050401 (2003).
- [210] G. E. Astrakharchik, J. Boronat, J. Casulleras, and S. Giorgini, “Equation of State of a Fermi Gas in the BEC-BCS Crossover: A Quantum Monte Carlo Study,” *Phys. Rev. Lett.* **93**, 200404 (2004).
- [211] V. Efimov, “Energy levels arising from resonant two-body forces in a three-body system,” *Phys. Lett. B* **33**, 563 (1970).
- [212] For the two-component system, normalization to the number of particles in each component would be a more natural choice.

- [213] M. A. Cirone, K. Góral, K. Rzażewski, and M. Wilkens, “Bose-Einstein condensation of two interacting particles,” *J. Phys. B* **34**, 4571 (2001).
- [214] A. Cherny, J.-S. Caux, and J. Brand, “Theory of superfluidity and drag force in the one-dimensional Bose gas,” *Frontiers of Physics* **7**, 54 (2012).
- [215] I. Carusotto, “Sorting superfluidity from Bose-Einstein condensation in atomic gases,” *Physics* **3**, 5 (2010).
- [216] A. Wairegi, A. Gamboa, A. D. Burbanks, E. A. Lee, and D. Farrelly, “Microscopic Superfluidity in  $^4\text{He}$  Clusters Stirred by a Rotating Impurity Molecule,” *Phys. Rev. Lett.* **112**, 143401 (2014).
- [217] F. Mezzacapo and M. Boninsegni, “Structure, superfluidity, and quantum melting of hydrogen clusters,” *Phys. Rev. A* **75**, 033201 (2007).
- [218] F. Mezzacapo and M. Boninsegni, “Local Superfluidity of Parahydrogen Clusters,” *Phys. Rev. Lett.* **100**, 145301 (2008).
- [219] E. W. Draeger and D. M. Ceperley, “Superfluidity in a Doped Helium Droplet,” *Phys. Rev. Lett.* **90**, 065301 (2003).
- [220] F. Werner and Y. Castin, “Unitary gas in an isotropic harmonic trap: Symmetry properties and applications,” *Phys. Rev. A* **74**, 053604 (2006).
- [221] S. Jonsell, H. Heiselberg, and C. J. Pethick, “Universal Behavior of the Energy of Trapped Few-Boson Systems with Large Scattering Length,” *Phys. Rev. Lett.* **89**, 250401 (2002).
- [222] J. Portegies and S. Kokkelmans, “Efimov Trimers in a Harmonic Potential,” *Few-Body Syst.* **51**, 219 (2011).
- [223] Note that the range of the three-body phase  $\theta_b$  in Fig. 9 of Ref. [76] is incorrect: The unique  $\theta_b$  values span a range of  $\pi$  instead of  $2\pi$ .
- [224] A. Kievsky and M. Gattobigio, “Universal nature and finite-range corrections in elastic atom-dimer scattering below the dimer breakup threshold,” *Phys. Rev. A* **87**, 052719 (2013).
- [225] D. M. Ceperley and E. L. Pollock, “Path-integral computation of the low-temperature properties of liquid  $^4\text{He}$ ,” *Phys. Rev. Lett.* **56**, 351 (1986).
- [226] For identical fermions, our  $S$  is equal to the quantity  $\langle S \rangle_{\bar{P}}$  of Ref. [97].
- [227] X. Waintal, G. Fleury, K. Kazymyrenko, M. Houzet, P. Schmitteckert, and D. Weinmann, “Persistent Currents in One Dimension: The Counterpart of Leggett’s Theorem,” *Phys. Rev. Lett.* **101**, 106804 (2008).

- [228] Y. Yan and D. Blume, “Abnormal Superfluid Fraction of Harmonically Trapped Few-Fermion Systems,” *Phys. Rev. Lett.* **112**, 235301 (2014).
- [229] Y. Kwon, P. Huang, M. V. Patel, D. Blume, and K. B. Whaley, “Quantum solvation and molecular rotations in superfluid helium clusters,” *J. Chem. Phys.* **113**, 6469 (2000).
- [230] E. Lee, D. Farrelly, and K. B. Whaley, “Rotational Level Structure of SF<sub>6</sub>-Doped 4He<sub>N</sub> Clusters,” *Phys. Rev. Lett.* **83**, 3812 (1999).
- [231] W. K. Wootters, “Entanglement of Formation of an Arbitrary State of Two Qubits,” *Phys. Rev. Lett.* **80**, 2245 (1998).
- [232] A. Peres, “Separability Criterion for Density Matrices,” *Phys. Rev. Lett.* **77**, 1413 (1996).
- [233] B. Sun, D. L. Zhou, and L. You, “Entanglement between two interacting atoms in a one-dimensional harmonic trap,” *Phys. Rev. A* **73**, 012336 (2006).
- [234] I. Talmi, “Nuclear Spectroscopy with Harmonic Oscillator Wave-Functions,” *Helv. Phys. Acta* **25**, 185 (1952).
- [235] M. Moshinsky, “Transformation brackets for harmonic oscillator functions,” *Nucl. Phys.* **13**, 104 (1959).
- [236] M. H. W. Chan, K. I. Blum, S. Q. Murphy, G. K. S. Wong, and J. D. Reppy, “Disorder and the Superfluid Transition in Liquid He<sub>4</sub>,” *Phys. Rev. Lett.* **61**, 1950 (1988).
- [237] E. Burovski, E. Kozik, A. Kuklov, N. Prokof’ev, and B. Svistunov, “Superfluid Interfaces in Quantum Solids,” *Phys. Rev. Lett.* **94**, 165301 (2005).
- [238] Ş. G. Söyler, B. Capogrosso-Sansone, N. V. Prokof’ev, and B. V. Svistunov, “Superfluid-insulator and roughening transitions in domain walls,” *Phys. Rev. A* **76**, 043628 (2007).
- [239] A. Deltuva, “Properties of Universal Bosonic Tetramers,” *Few-Body Syst.* **54**, 569 (2012).
- [240] Note that Refs. [1, 9] propose that the  $N$ -boson droplet energy scales as  $N(N - 1)$  in the universal regime.
- [241] S. Piątekki and W. Krauth, “Efimov-driven phase transitions of the unitary Bose gas,” *Nat. Comm.* **5**, 3503 (2014).
- [242] P. Naidon, S. Endo, and M. Ueda, “Physical Origin of the Universal Three-body Parameter in Atomic Efimov Physics,” arXiv:1208.3912 .
- [243] V. Efimov, “Level Spectrum of Three Resonantly Interacting Particles,” *JETP Lett.* **16**, 34 (1972).

- [244] V. Efimov, “Energy levels of three resonantly interacting particles,” *Nuclear Physics A* **210**, 157 (1973).
- [245] M. Brewczyk, M. Gajda, and K. Rzażewski, “Classical fields approximation for bosons at nonzero temperatures,” *J. Phys. B* **40**, R1 (2007).
- [246] N. P. Proukakis and B. Jackson, “Finite-temperature models of BoseEinstein condensation,” *J. Phys. B* **41**, 203002 (2008).
- [247] S.-J. Jiang, W.-M. Liu, G. W. Semenoff, and F. Zhou, “Universal Bose gases near resonance: A rigorous solution,” *Phys. Rev. A* **89**, 033614 (2014).
- [248] P. Nikolić and S. Sachdev, “Renormalization-group fixed points, universal phase diagram, and 1N expansion for quantum liquids with interactions near the unitarity limit,” *Phys. Rev. A* **75**, 033608 (2007).
- [249] J. J. R. M. van Heugten and H. T. C. Stoof, “Theory of unitary Bose gases,” arXiv:1302.1792 .
- [250] M. Rossi, L. Salasnich, F. Ancilotto, and F. Toigo, “Monte Carlo simulations of the unitary Bose gas,” *Phys. Rev. A* **89**, 041602(R) (2014).
- [251] P. Makotyn, C. E. Klauss, D. L. Goldberger, E. A. Cornell, and D. S. Jin, “Universal dynamics of a degenerate unitary Bose gas,” *Nature Phys.* **10**, 116 (2014).
- [252] T. Sowiński, T. Grass, O. Dutta, and M. Lewenstein, “Few interacting fermions in a one-dimensional harmonic trap,” *Phys. Rev. A* **88**, 033607 (2013).
- [253] T. Sowiński, M. Gajda, and K. Rzażewski, “Emergence of pairing in a system of a few strongly attractive fermions in a one-dimensional harmonic trap,” arXiv:1406.0400 .
- [254] E. Fermi, “Sopra lo spostamento per pressione delle righe elevate delle serie spettrali,” *Nuovo Cimento* **11**, 157 (1934).
- [255] E. H. Lieb and W. Liniger, “Exact Analysis of an Interacting Bose Gas. I. The General Solution and the Ground State,” *Phys. Rev.* **130**, 1605 (1963).
- [256] M. Gaudin, “Un systeme a une dimension de fermions en interaction,” *Phys. Lett. A* **24**, 55 (1967).
- [257] C. N. Yang, “Some Exact Results for the Many-Body Problem in one Dimension with Repulsive Delta-Function Interaction,” *Phys. Rev. Lett.* **19**, 1312 (1967).
- [258] C. N. Yang and C. P. Yang, “Thermodynamics of a OneDimensional System of Bosons with Repulsive DeltaFunction Interaction,” *J. Math. Phys.* **10**, 1115 (1969).
- [259] W. Jones and N. H. March, *Theoretical Solid State Physics*, vol. 2 (Dover Publications, New York, 1985).

- [260] D. V. Fedorov, A. S. Jensen, and K. Riisager, “Three-body halos: Gross properties,” *Phys. Rev. C* **49**, 201 (1994).
- [261] J. E. Cuervo, P.-N. Roy, and M. Boninsegni, “Path integral ground state with a fourth-order propagator: Application to condensed helium,” *J. Chem. Phys.* **122**, 114504 (2005).
- [262] M. Rossi, M. Nava, L. Reatto, and D. E. Galli, “Exact ground state Monte Carlo method for Bosons without importance sampling,” *J. Chem. Phys.* **131**, 154108 (2009).
- [263] Equation (6.9) is to be interpreted as follows:  $\int[\psi_k^s(x)]^*\psi_{k'}^s(x) dx = \delta(k - k')$ ,  $\int[\psi_k^a(x)]^*\psi_{k'}^a(x) dx = \delta(k - k')$ , and  $\int[\psi_k^a(x)]^*\psi_{k'}^s(x) dx = 0$  (due to symmetry).
- [264] M. Casula, D. M. Ceperley, and E. J. Mueller, “Quantum Monte Carlo study of one-dimensional trapped fermions with attractive contact interactions,” *Phys. Rev. A* **78**, 033607 (2008).
- [265] M. Olshanii, “Atomic Scattering in the Presence of an External Confinement and a Gas of Impenetrable Bosons,” *Phys. Rev. Lett.* **81**, 938 (1998).
- [266] M. D. Girardeau, H. Nguyen, and M. Olshanii, “Effective interactions, FermiBose duality, and ground states of ultracold atomic vapors in tight de Broglie waveguides,” *Opt. Commun.* **243**, 3 (2004).
- [267] See entry 3.954 of I. S. Gradshteyn and I. M. Ryzhik, *Table of Integrals, Series, and Products*, 6th Ed., Academic Press.
- [268] R. Pessoa, S. A. Vitiello, and K. E. Schmidt, “Monte Carlo Calculations for Fermi Gases in the Unitary Limit with a Zero-Range Interaction,” *J. Low Temp. Phys.* **180**, 168 (2015).
- [269] S. E. Gharashi, K. M. Daily, and D. Blume, “Three s-wave-interacting fermions under anisotropic harmonic confinement: Dimensional crossover of energetics and virial coefficients,” *Phys. Rev. A* **86**, 042702 (2012).
- [270] B. S. Rem, A. T. Grier, I. Ferrier-Barbut, U. Eismann, T. Langen, N. Navon, L. Khaykovich, F. Werner, D. S. Petrov, F. Chevy, and C. Salomon, “Lifetime of the Bose Gas with Resonant Interactions,” *Phys. Rev. Lett.* **110**, 163202 (2013).
- [271] R. J. Fletcher, A. L. Gaunt, N. Navon, R. P. Smith, and Z. Hadzibabic, “Stability of a Unitary Bose Gas,” *Phys. Rev. Lett.* **111**, 125303 (2013).
- [272] A. G. Sykes, J. P. Corson, J. P. D’Incao, A. P. Koller, C. H. Greene, A. M. Rey, K. R. A. Hazzard, and J. L. Bohn, “Quenching to unitarity: Quantum dynamics in a three-dimensional Bose gas,” *Phys. Rev. A* **89**, 021601(R) (2014).
- [273] D. H. Smith, E. Braaten, D. Kang, and L. Platter, “Two-Body and Three-Body Contacts for Identical Bosons near Unitarity,” *Phys. Rev. Lett.* **112**, 110402 (2014).

- [274] The ground state wave function is obtained by transforming to hyperspherical coordinates. The hyperangular wave function, which separates from the hyperradial portion, is known analytically [41, 211] and the hyperradial wave function is found numerically.
- [275] Y. Yan and D. Blume, see Chapter 7.
- [276] J. B. Kogut, “The lattice gauge theory approach to quantum chromodynamics,” *Rev. Mod. Phys.* **55**, 775 (1983).
- [277] D. Lee, “Lattice simulations for few- and many-body systems,” *Progress in Particle and Nuclear Physics* **63**, 117 (2009).
- [278] J. E. Drut and A. N. Nicholson, “Lattice methods for strongly interacting many-body systems,” *J. Phys. G* **40**, 043101 (2013).
- [279] B. D. Esry and C. H. Greene, “Validity of the shape-independent approximation for Bose-Einstein condensates,” *Phys. Rev. A* **60**, 1451 (1999).
- [280] Y. Alhassid, G. F. Bertsch, and L. Fang, “New Effective Interaction for the Trapped Fermi Gas,” *Phys. Rev. Lett.* **100**, 230401 (2008).
- [281] M. Rontani, J. R. Armstrong, Y. Yu, S. Åberg, and S. M. Reimann, “Cold Fermionic Atoms in Two-Dimensional Traps: Pairing versus Hund’s Rule,” *Phys. Rev. Lett.* **102**, 060401 (2009).
- [282] C. A. Regal, M. Greiner, and D. S. Jin, “Observation of Resonance Condensation of Fermionic Atom Pairs,” *Phys. Rev. Lett.* **92**, 040403 (2004).
- [283] M. W. Zwierlein, C. A. Stan, C. H. Schunck, S. M. F. Raupach, A. J. Kerman, and W. Ketterle, “Condensation of Pairs of Fermionic Atoms near a Feshbach Resonance,” *Phys. Rev. Lett.* **92**, 120403 (2004).
- [284] G. J. Hanna and D. Blume, “Energetics and structural properties of three-dimensional bosonic clusters near threshold,” *Phys. Rev. A* **74**, 063604 (2006).
- [285] A. Deltuva, “Efimov physics in bosonic atom-trimer scattering,” *Phys. Rev. A* **82**, 040701 (2010).
- [286] M. R. Hadizadeh, M. T. Yamashita, L. Tomio, A. Delfino, and T. Frederico, “Scaling Properties of Universal Tetramers,” *Phys. Rev. Lett.* **107**, 135304 (2011).
- [287] J. von Stecher, “Five- and Six-Body Resonances Tied to an Efimov Trimer,” *Phys. Rev. Lett.* **107**, 200402 (2011).
- [288] T. Frederico, A. Delfino, M. Hadizadeh, L. Tomio, and M. Yamashita, “Universality in Four-Boson Systems,” *Few-Body Syst.* **54**, 559 (2013).
- [289] Y. Yan and D. Blume, “Incorporating exact two-body propagators for zero-range interactions into  $N$ -body Monte Carlo simulations,” *Phys. Rev. A* **91**, 043607 (2015).

- [290] A. Kievsky, N. K. Timofeyuk, and M. Gattobigio, “ $N$ -boson spectrum from a discrete scale invariance,” *Phys. Rev. A* **90**, 032504 (2014).
- [291] M. Gattobigio, A. Kievsky, and M. Viviani, “Spectra of helium clusters with up to six atoms using soft-core potentials,” *Phys. Rev. A* **84**, 052503 (2011).
- [292] J. Voigtsberger, S. Zeller, J. Becht, N. Neumann, F. Sturm, H.-K. Kim, M. Waitz, F. Trinter, M. Kunitski, A. Kalinin, J. Wu, W. Schöllkopf, D. Bressanini, A. Czasch, J. B. Williams, K. Ullmann-Pfleger, L. P. H. Schmidt, M. S. Schöffler, R. E. Grisenti, T. Jahnke, and R. Dörner, “Imaging the structure of the trimer systems  $^4\text{He}_3$  and  $^3\text{He}^4\text{He}_2$ ,” *Nat. Comm.* **5**, 5765 (2014).
- [293] M. Kunitski, S. Zeller, J. Voigtsberger, A. Kalinin, L. P. H. Schmidt, M. Schöffler, A. Czasch, W. Schöllkopf, R. E. Grisenti, T. Jahnke, D. Blume, and R. Dörner, “Observation of the Efimov state of the helium trimer,” *Science* **348**, 551 (2015).
- [294] M. Berninger, A. Zenesini, B. Huang, W. Harm, H.-C. Nägerl, F. Ferlaino, R. Grimm, P. S. Julienne, and J. M. Hutson, “Universality of the Three-Body Parameter for Efimov States in Ultracold Cesium,” *Phys. Rev. Lett.* **107**, 120401 (2011).
- [295] S. E. Pollack, D. Dries, and R. G. Hulet, “Universality in Three- and Four-Body Bound States of Ultracold Atoms,” *Science* **326**, 1683 (2009).
- [296] N. Gross, Z. Shotan, S. Kokkelmans, and L. Khaykovich, “Observation of Universality in Ultracold  $^7\text{Li}$  Three-Body Recombination,” *Phys. Rev. Lett.* **103**, 163202 (2009).
- [297] T. B. Ottenstein, T. Lompe, M. Kohnen, A. N. Wenz, and S. Jochim, “Collisional Stability of a Three-Component Degenerate Fermi Gas,” *Phys. Rev. Lett.* **101**, 203202 (2008).
- [298] J. H. Huckans, J. R. Williams, E. L. Hazlett, R. W. Stites, and K. M. O’Hara, “Three-Body Recombination in a Three-State Fermi Gas with Widely Tunable Interactions,” *Phys. Rev. Lett.* **102**, 165302 (2009).
- [299] R. J. Wild, P. Makotyn, J. M. Pino, E. A. Cornell, and D. S. Jin, “Measurements of Tan’s Contact in an Atomic Bose-Einstein Condensate,” *Phys. Rev. Lett.* **108**, 145305 (2012).
- [300] M. Zaccanti, B. Deissler, C. D’Errico, M. Fattori, M. Jona-Lasinio, S. Müller, G. Roati, M. Inguscio, and G. Modugno, “Observation of an Efimov spectrum in an atomic system,” *Nat. Phys.* **5**, 586 (2009).
- [301] D. Blume, “Efimov physics and the three-body parameter for shallow van der Waals potentials,” *arXiv:1506.05668* .
- [302] K. B. Whaley, “Structure and dynamics of quantum clusters,” *International Reviews in Physical Chemistry* **13**, 41 (1994).

- [303] D. Blume, B. D. Esry, C. H. Greene, N. N. Klausen, and G. J. Hanna, “Formation of Atomic Tritium Clusters and Bose-Einstein Condensates,” *Phys. Rev. Lett.* **89**, 163402 (2002).
- [304] The Supplemental Material contains tables for the energies for the models 2bZR+3bRp with  $p = 4 - 8$ , He-He(scale), and He-He(arctan).
- [305] S. Y. Chang and G. F. Bertsch, “Unitary Fermi gas in a harmonic trap,” *Phys. Rev. A* **76**, 021603 (2007).
- [306] D. Blume, J. von Stecher, and C. H. Greene, “Universal Properties of a Trapped Two-Component Fermi Gas at Unitarity,” *Phys. Rev. Lett.* **99**, 233201 (2007).
- [307] In practice, the structural properties are obtained by calculating thermal averages at low temperature, where the excitations of the relative degrees of freedom are negligible. This implies that thermally averaged structural properties that are independent of the center of mass degrees of freedom coincide, to a very good approximation, with the corresponding quantum mechanical expectation values with respect to the ground state wave function.
- [308] A. S. Jensen, K. Riisager, D. V. Fedorov, and E. Garrido, “Structure and reactions of quantum halos,” *Rev. Mod. Phys.* **76**, 215 (2004).
- [309] C. J. Pethick and D. G. Ravenhall, “Matter at Large Neutron Excess and the Physics of Neutron-Star Crusts,” *Annu. Rev. Nucl. Part. Sci.* **45**, 429 (1995).
- [310] P. A. Lee, N. Nagaosa, and X.-G. Wen, “Doping a Mott insulator: Physics of high-temperature superconductivity,” *Rev. Mod. Phys.* **78**, 17 (2006).
- [311] J. Bardeen, L. N. Cooper, and J. R. Schrieffer, “Microscopic Theory of Superconductivity,” *Phys. Rev.* **106**, 162 (1957).
- [312] R. B. Laughlin, “Anomalous Quantum Hall Effect: An Incompressible Quantum Fluid with Fractionally Charged Excitations,” *Phys. Rev. Lett.* **50**, 1395 (1983).
- [313] P. Fulde and R. A. Ferrell, “Superconductivity in a Strong Spin-Exchange Field,” *Phys. Rev.* **135**, A550 (1964).
- [314] A. Larkin and Y. N. Ovchinnikov, “Nonuniform state of superconductors,” *Zh. Eksperim. i Teor. Fiz.* **47**, 1136 (1964).
- [315] A. Larkin and I. Ovchinnikov, “Inhomogeneous state of superconductors,” *Soviet Physics-JETP* **20**, 762 (1965).
- [316] H. Heiselberg, “Fermi systems with long scattering lengths,” *Phys. Rev. A* **63**, 043606 (2001).
- [317] T.-L. Ho, “Universal Thermodynamics of Degenerate Quantum Gases in the Unitarity Limit,” *Phys. Rev. Lett.* **92**, 090402 (2004).

- [318] D. B. Kaplan and S. Sun, “New Field-Theoretic Method for the Virial Expansion,” *Phys. Rev. Lett.* **107**, 030601 (2011).
- [319] X. Leyronas, “Virial expansion with Feynman diagrams,” *Phys. Rev. A* **84**, 053633 (2011).
- [320] S. Nascimbene, N. Navon, K. Jiang, F. Chevy, and C. Salomon, “Exploring the thermodynamics of a universal Fermi gas,” *Nature (London)* **463**, 1057 (2010).
- [321] V. Ngampruetikorn, M. M. Parish, and J. Levinsen, “High-temperature limit of the resonant Fermi gas,” *Phys. Rev. A* **91**, 013606 (2015).
- [322] S. Endo and Y. Castin, “Absence of a four-body Efimov effect in the  $2 + 2$  fermionic problem,” *Phys. Rev. A* **92**, 053624 (2015).
- [323] S. Endo and Y. Castin, “The interaction-sensitive states of a trapped two-component ideal Fermi gas,” (2015), arXiv:1512.06543 .
- [324] G. V. Skorniakov and K. A. Ter-Martirosian, “Three Body Problem for Short Range Forces. I. Scattering of Low Energy Neutrons by Deuterons,” *Zh. Eksp. Teor. Fiz.* **31**, 775 (1956), [*Sov. Phys. JETP* **4**, 648 (1957)].
- [325] M. Takahashi and M. Imada, “Monte Carlo Calculation of Quantum Systems,” *J. Phys. Soc. Japan* **53**, 963 (1984).
- [326] X.-J. Liu and H. Hu, “Virial expansion for a strongly correlated Fermi gas with imbalanced spin populations,” *Phys. Rev. A* **82**, 043626 (2010).
- [327] K. M. Daily and D. Blume, “Thermodynamics of the two-component Fermi gas with unequal masses at unitarity,” *Phys. Rev. A* **85**, 013609 (2012).
- [328] The explicit expressions for  $b_{n_1, n_2}^{\text{ref}}$  with  $n_1 + n_2 = 4$  read  $b_{3,1}^{\text{ref}} = -b_3 Q_{1,0} - 2b_2 Q_{2,0}$  and  $b_{2,2}^{\text{ref}} = -2b_3 Q_{1,0} - 2(b_2)^2 Q_{1,0} - 2b_2 (Q_{1,0})^2$ .
- [329] The supplemental material contains (i) a summary of the literature values of the fourth-order virial coefficient; (ii) information on the pair product approximation and the two-body density matrix for zero-range interactions; and (iii) PIMC simulation details and tables containing selected raw data.
- [330] For a simulation of finite length  $l$ , the standard deviation would not be following a Gaussian distribution, implying that the standard deviation would not decrease as  $1/\sqrt{l}$  with increasing simulation length  $l$ .
- [331] For the (2,2) system, e.g.,  $\mathcal{A}$  reads  $(1 - P_{12} - P_{34} + P_{12}P_{34})/4$ , where  $P_{ij}$  permutes the coordinates of particles  $i$  and  $j$ .
- [332] S. A. Chin, “High-order path-integral Monte Carlo methods for solving quantum dot problems,” *Phys. Rev. E* **91**, 031301(R) (2015).

- [333] S. E. Gharashi and D. Blume, “Tunneling dynamics of two interacting one-dimensional particles,” *Phys. Rev. A* **92**, 033629 (2015).
- [334] R. Pessoa, S. Gandolfi, S. A. Vitiello, and K. E. Schmidt, “Contact interaction in a unitary ultracold Fermi gas,” *Phys. Rev. A* **92**, 063625 (2015).
- [335] V. K. Akkineni, D. M. Ceperley, and N. Trivedi, “Pairing and superfluid properties of dilute fermion gases at unitarity,” *Phys. Rev. B* **76**, 165116 (2007).
- [336] M. M. Forbes, S. Gandolfi, and A. Gezerlis, “Resonantly Interacting Fermions in a Box,” *Phys. Rev. Lett.* **106**, 235303 (2011).
- [337] M. G. Endres, D. B. Kaplan, J.-W. Lee, and A. N. Nicholson, “Lattice Monte Carlo calculations for unitary fermions in a finite box,” *Phys. Rev. A* **87**, 023615 (2013).
- [338] Ş. G. Söyler, B. Capogrosso-Sansone, N. V. Prokof’ev, and B. V. Svistunov, “Sign-alternating interaction mediated by strongly correlated lattice bosons,” *New J. Phys.* **11**, 073036 (2009).
- [339] M. B. Hastings, I. González, A. B. Kallin, and R. G. Melko, “Measuring Renyi Entanglement Entropy in Quantum Monte Carlo Simulations,” *Phys. Rev. Lett.* **104**, 157201 (2010).
- [340] C. M. Herdman, S. Inglis, P.-N. Roy, R. G. Melko, and A. Del Maestro, “Path-integral Monte Carlo method for Rényi entanglement entropies,” *Phys. Rev. E* **90**, 013308 (2014).
- [341] R. Islam, R. Ma, P. M. Preiss, M. E. Tai, A. Lukin, M. Rispoli, and M. Greiner, “Measuring entanglement entropy through the interference of quantum many-body twins,” *arXiv:1509.01160* .
- [342] S. Knoop, F. Ferlaino, M. Mark, M. Berninger, H. Schöbel, H.-C. Nägerl, and R. Grimm, “Observation of an Efimov-like trimer resonance in ultracold atom-dimer scattering,” *Nat. Phys.* **5**, 227 (2009).
- [343] A. N. Wenz, T. Lompe, T. B. Ottenstein, F. Serwane, G. Zürn, and S. Jochim, “Universal trimer in a three-component Fermi gas,” *Phys. Rev. A* **80**, 040702 (2009).
- [344] J. R. Williams, E. L. Hazlett, J. H. Huckans, R. W. Stites, Y. Zhang, and K. M. O’Hara, “Evidence for an Excited-State Efimov Trimer in a Three-Component Fermi Gas,” *Phys. Rev. Lett.* **103**, 130404 (2009).
- [345] S. Nakajima, M. Horikoshi, T. Mukaiyama, P. Naidon, and M. Ueda, “Measurement of an Efimov Trimer Binding Energy in a Three-Component Mixture of  ${}^6\text{Li}$ ,” *Phys. Rev. Lett.* **106**, 143201 (2011).
- [346] S. Endo and Y. Castin, private communication (Feb. 2016).

- [347] H. Fröhlich, “Electrons in lattice fields,” *Advances in Physics* **3**, 325 (1954).
- [348] W. Greiner, *Quantum Mechanics: an Introduction*, 4th ed. (Springer-Verlag; Berlin, Heidelberg, New York, 2001).